

University of Windsor

## Scholarship at UWindsor

---

Electronic Theses and Dissertations

Theses, Dissertations, and Major Papers

---

2018

# Formability Enhancement of AA5182-O During Electro-Hydraulic Forming

Arash Jenab  
*University of Windsor*

Follow this and additional works at: <https://scholar.uwindsor.ca/etd>

---

### Recommended Citation

Jenab, Arash, "Formability Enhancement of AA5182-O During Electro-Hydraulic Forming" (2018).  
*Electronic Theses and Dissertations*. 7365.  
<https://scholar.uwindsor.ca/etd/7365>

This online database contains the full-text of PhD dissertations and Masters' theses of University of Windsor students from 1954 forward. These documents are made available for personal study and research purposes only, in accordance with the Canadian Copyright Act and the Creative Commons license—CC BY-NC-ND (Attribution, Non-Commercial, No Derivative Works). Under this license, works must always be attributed to the copyright holder (original author), cannot be used for any commercial purposes, and may not be altered. Any other use would require the permission of the copyright holder. Students may inquire about withdrawing their dissertation and/or thesis from this database. For additional inquiries, please contact the repository administrator via email ([scholarship@uwindsor.ca](mailto:scholarship@uwindsor.ca)) or by telephone at 519-253-3000ext. 3208.

# **Formability Enhancement of AA5182-O During Electro-Hydraulic Forming**

by

**Arash Jenab**

A Dissertation  
Submitted to the Faculty of Graduate Studies  
through the Department of Mechanical, Automotive, and Materials Engineering  
in Partial Fulfilment of the Requirements for  
the Degree of Doctor of Philosophy  
at the University of Windsor

Windsor, Ontario, Canada

2018

© 2018 Arash Jenab

# Formability Enhancement of AA5182-O During Electro-Hydraulic Forming

by

**Arash Jenab**

Approved by:

---

**S. Yue**, External Examiner  
Materials Engineering Department, McGill University

---

**V. Stoilov**  
Department of Mechanical, Automotive & Materials Engineering

---

**D. O. Northwood**  
Department of Mechanical, Automotive & Materials Engineering

---

**A. Edrisy**  
Department of Mechanical, Automotive & Materials Engineering

---

**S. F. Golovashchenko**  
School of Engineering and Computer Science, Oakland University

---

**K. Boyle**  
CanmetMATERIALS, Natural Resources Canada

---

**D. E. Green**, Co-Advisor  
Department of Mechanical, Automotive & Materials Engineering

---

**A. T. Alpas**, Co-Advisor  
Department of Mechanical, Automotive & Materials Engineering

December 18, 2017

# Declaration of Co-Authorship and Previous Publication

## I. Co-Authorship Declaration

I hereby declare that this dissertation incorporates material that is the result of joint research undertaken in collaboration with Prof. Sergey F. Golovashchenko, Prof. Michael Worswick, Dr. Babak Shalchi Amirkhiz, Dr. Kevin P. Boyle, Dr. Iman Sari Sarraf, Dr. Javad Samei, Dr. Amir Hassannejadasl, Mr. Taamjeed Rahmaan, Mr. Christopher Maris, under the supervision of Prof. Daniel E. Green and Prof. Ahmet T. Alpas, University of Windsor. In addition, the experimental tensile tests used in Chapter 4, were carried by Mr. Taamjeed Rahmaan at University of Waterloo under the supervision of Prof. Michael Worswick, Dr. Iman Sari Sarraf performed the regression analysis published in Chapter 4, electro-hydraulic forming experiments were carried out by Mr. Alan Gillard at Ford Research Advanced Engineering (Ford Motor Company) under the supervision of Dr. Sergey F. Golovashchenko, quasi-static Marciniak tests was carried out by Lucian Blaga at CanmetMATERIALS under the supervision of Dr. Kevin P. Boyle and transmission electron microscopy was performed by Dr. Babak Shalchi-Amirkhiz at CanmetMATERIALS used in Chapter 4 and Appendix A.

In all cases, the key ideas, the primary contributions, simulations and data analysis and interpretations were performed by the author of this dissertation. The contributions of the co-authors were primarily focused on the provision of the study and suggesting possible directions. Results related to this research are reported in Chapters 3 through 6, inclusively and Appendices A through B.1. I am aware of the University of Windsor Senate Policy on Authorship and I certify that I have properly acknowledged contribution of other researchers to my thesis, and have obtained written permission from each of the co-author(s) to include the above material(s) in my

thesis.

I certify that, with the above qualification, this thesis, and the research to which it refers, is the product of my own work.

## II. Declaration of Previous Publication

This dissertation was prepared according to the guidelines for a manuscript-based thesis published by the Graduate Studies office of University of Windsor.

The present dissertation includes unpublished results and four original papers; three of which were published and one was accepted for publication;

- **A. Jenab**, D. E. Green, A. T. Alpas, and K. P. Boyle, "Formability of AA5182-O Sheet during Electro-Hydraulic Forming: Influence of Input Energy", in *Materials Science and Technology (MS&T)*, pp. 535-542, 2015.
- **A. Jenab**, I. Sari Sarraf, D. E. Green, T. Rahmaan, and M. J. Worswick, "The Use of Genetic Algorithm and Neural Network to Predict Rate-dependent Tensile Flow Behaviour of AA5182-O Sheets", *Materials & Design*, vol. 94, pp. 262-273, Mar 2016.
- **A. Jenab**, D. E. Green, A. T. Alpas,, "Microscopic Investigation of Failure Mechanisms in AA5182-O Sheets Subjected to Electro-hydraulic Forming", *Materials Science & Engineering A*, vol. 691, pp. 31-41, Mar 2017.
- **A. Jenab**, D. E. Green, A. T. Alpas, S. F. Golovashchenko, "Experimental and Finite Element Modelling of Formability Improvement of AA5182-O Sheet during Electro-Hydraulic Forming", Accepted for publication in "Journal of Materials Processing Technology".

I certify that I have obtained a written permission from the copyright owners to include the above published materials in my dissertation. I certify that the above material describes work completed during my registration as graduate student at the University of Windsor.

I declare that, to the best of my knowledge, my dissertation does not infringe upon anyone's copyright nor violates any proprietary rights and that any ideas, techniques, quotations, or any other material from the work of other people included in my dissertation, published or otherwise, are fully acknowledged in accordance with the standard referencing practices. Furthermore, to the extent that I have included copyrighted material that surpasses the bounds of fair dealing within the meaning of the Canada Copyright Act, I certify that I have obtained a written permission from the copyright owners to include such materials in my dissertation.

I declare that this is a true copy of my dissertation, including any final revisions, as approved by my dissertation committee and the Graduate Studies office, and that this dissertation has not been submitted for a higher degree to any other University or Institution.

# Abstract

In this research, formability improvement of AA5182-O aluminium sheet during electrohydraulic forming (EHF) was investigated by means of experimental and finite element analysis. Free and conical die formed EHF was carried out on grid sheet blanks and formability improvement was measured by comparing grid analysis results at each EHF condition with different forming limit curves (FLCs). It is found that AA5182-O shows minor improvement in formability when formed freely into EHF. But a significant rise in effective strain in safe grids is observed when EHF into 34, 40 and 45° conical dies provided a critical threshold of input energy has been used. In order to understand the mechanical aspects of formability improvement, related factors such as strain rate, stress triaxiality, and compressive through-thickness stress were studied using finite element simulation with an accurate description of the hardening behaviour of AA5182-O. Another advantage of the numerical simulation carried out in this work is that unlike previously published works, the driving force for EHF deformation was not simplified as uniform pressure and it resembles the actual process of EHF. Ignition and growth model was used in conjunction with Coupled Eulerian-Lagrangian (CEL) approach to simulate the EHF pulse formation. Moreover, 3D solid elements were used instead of shell elements and this facilitated measurement of stress in elements located in the bulk of sheet material. The tensile flow behaviour of AA5182-O sheet was investigated in the strain rate range of 0.001 to 1000s<sup>-1</sup> and at different material directions (RD, DD, and TD) by means of both phenomenological models and neural networks (NNs). Genetic algorithm (GA) and linear regression analysis methods were used to calculate the constants in Johnson-Cook (JC), Khan-Huang-Liang (KHL) and modified Voce hardening functions, and user-material subroutines were developed and used in FE software. Moreover, in order to predict the rheological behaviour of AA5182-O without the limitations of a mathematical function, two types of feed-forward back-propagation neural networks were trained and used in the FE

model. Simulation results were compared with experimental tensile flow curves and the most accurate method is used to predict the mechanical response of AA5182-O in FE simulations of the EHF process. FE results suggested that a combination of EHF process related parameters including compressive through-thickness stress (negative stress triaxiality) generated during the deformation could postpone the failure, when specimens are formed into a die cavity (EHDF). Also, the increased velocity and significant impact pressure at the final stage of deformation not only prevent strain localization but also help in further suppressing the damage. It is found that very high peak strain rates develop in the sheet as it contacts the die surface which further postpone the failure since AA5182-O exhibits positive strain rate sensitivity at such high-strain rates. Moreover, damage mechanisms of AA5182-O sheets were investigated during EHF tests and are compared with those occur during quasi-static (QS) deformation. The results confirm that void nucleation, growth and coalescence are the main damage mechanisms of AA5182-O at both high and low strain rates. It is found that  $Mg_2Si$  particles do not significantly influence void formation and the main source of void nucleation is cracking of  $Al_3(Fe-Mn)$  intermetallic particles. More importantly, it is found that specimens deformed under QS conditions contained more voids in areas away from the sub-fracture surface but EHF specimens exhibit higher rate of void growth close to sub-fracture areas. Optical microscopy results confirmed that void formation is suppressed by increasing the applied energy in EHF. And more importantly, the growth of voids is suppressed due to the high-velocity impact of the sheet against the die which plays an important role in increasing formability of AA5182-O aluminium sheet in EHF. Optical microscopy showed that AA5182-O grains experience significant shearing strain during the EHF deformation in the apex area of conical EHDF specimens. The results of transmission electron microscopy showed that dislocation density increases when specimens are formed using EHF process but the magnitude of this increase is not significantly greater than in quasi-static deformations. Finally, it is concluded that the combination of high strain rate deformation and compressive through-thickness stress during the deformation, leads to formability improvement of AA5182-O in EHDF.



## Acknowledgements

First of all, I would like to acknowledge my advisers, Dr. Daniel Green and Prof. Ahmet Alpas for their guidance, support, personality, patience and insistence on excellence. It was a pleasure and constant learning experience for me to work with them not only in the academic field but also in many other aspects.

I would like to express my appreciation to Prof. Sergey Golovashchenko who not only technically guided me during this project but also facilitated performing EHF tests at Ford Motor Company. His continued help and support well after the project termination was really amazing.

Special thanks are due to CanmetMATERIAL's personnel and most importantly, Dr. Mark Kozdras, Dr. Kevin Boyle and especially Dr. Babak Shalchi Amirkhiz for their generous contribution and their exceptional knowledge and expertise.

I also would like to thank Dr. Richard Burrows and Dr. Richard Hammerton from Novelis Inc. for their support during this project. Moreover, Novelis Inc. personnel especially Tudor Piroteala are greatly appreciated for facilitating the tests carried out during our OCE-Auto21 project.

Also, I would also like to express my gratitude to my best friend/colleague, Iman Sari Sarraf for his kind and unbelievable support and assistance. Iman; I am very lucky to have such a nice and mature friend by my side in the last decade of my life.

I am also grateful to my close friends and colleagues, Dr. Javad Samei, Dr. Amir Hassannejadasl, and Dr. Mehdi Sanjari for sharing their knowledge and expertise not only on technical terms of this project but also on the diplomatic aspect of working as a graduate student.

I also would like to express my appreciation to Gina Succi and Emil Radoslov from Westhill Innovation Inc. for their constant support and providing me with flexibility to work on my project to its completion.

I am always grateful for my parents, enduring support and encouragement in every step in my life, career and studies. This work would not have been possible without their endless love and support.

Last, but not least, I would like to express my warm gratitude to my better half, Mehrnaz, for her unconditional love and encouragement, which always motivated me to strive for something better.

# Table of Content

<b>Declaration of Co-Authorship and Previous Publication</b>	<b>iii</b>
<b>Abstract</b>	<b>vi</b>
<b>Acknowledgements</b>	<b>viii</b>
<b>List of Tables</b>	<b>xii</b>
<b>List of Figures</b>	<b>xiii</b>
<b>Nomenclature and Abbreviations</b>	<b>xvii</b>
<b>1 Introduction</b>	<b>1</b>
1.1 Motivation for the industrial use of aluminium alloys . . . . .	1
1.2 Objective of the research . . . . .	2
1.3 Structure of the dissertation . . . . .	3
1.4 References . . . . .	4
<b>2 Literature Survey</b>	<b>6</b>
2.1 5xxx-series aluminium alloys . . . . .	6
2.1.1 Chemical composition of AA5182 . . . . .	8
2.1.2 Forming limits of AA5182-O sheets . . . . .	8
2.2 High strain rate metal forming processes . . . . .	10
2.2.1 Explosive Forming . . . . .	10
2.2.2 Electro-magnetic forming . . . . .	11
2.2.3 Electro-hydraulic forming (EHF) . . . . .	11
2.2.4 Comparison of EHF with other high-strain rate forming processes . .	14
2.3 Mechanisms of Hyperplasticity in High Strain Rate Forming . . . . .	16
2.3.1 Changes in hardening behaviour of material . . . . .	17
2.3.2 Inertial effect and importance of input energy . . . . .	26
2.3.3 Die effects . . . . .	28
2.3.4 Effect of hydrostatic pressure and die . . . . .	28
2.4 Hardening properties of AA5182-O . . . . .	30
2.4.1 Constitutive Equations . . . . .	30
2.4.2 Genetic Algorithm (GA) . . . . .	34
2.4.3 Artificial Neural Network (ANN) . . . . .	36
2.4.4 Basics of neural networks . . . . .	38
2.4.5 The ANN used for AA5182 . . . . .	39
2.5 Fracture Mechanism of AA5182 . . . . .	40
2.5.1 Localized Shear Bands; at QS strain rates . . . . .	41
2.5.2 Void Nucleation, Growth and Coalescence; High strain rates . . . . .	43
2.6 References . . . . .	46

<b>3</b>	<b>Formability of AA5182-O Sheet during Electro Hydraulic Forming: Influence of Input Energy</b>	<b>55</b>
3.1	Introduction . . . . .	56
3.2	Experimental Procedure . . . . .	57
3.2.1	EHF Experiments and Grid Analysis . . . . .	57
3.2.2	Formability Improvement Index . . . . .	58
3.3	Results and Discussion . . . . .	59
3.3.1	EHF Experiments: Effect of Die and Input Voltage . . . . .	59
3.3.2	Formability Improvement . . . . .	60
3.4	Conclusions . . . . .	62
3.5	Acknowledgements . . . . .	64
3.6	References . . . . .	64
<b>4</b>	<b>The Use of Genetic Algorithm and Neural Network to Predict Rate-dependent Tensile Flow Behaviour of AA5182-O Sheets</b>	<b>66</b>
4.1	Introduction . . . . .	68
4.1.1	Constitutive equations . . . . .	70
4.1.2	Genetic algorithm method . . . . .	71
4.1.3	Artificial neural network . . . . .	72
4.2	Experimental and Computational Procedures . . . . .	73
4.2.1	Genetic algorithm approach . . . . .	74
4.2.2	Artificial neural network approach . . . . .	75
4.2.3	Simulation procedure . . . . .	78
4.3	Results and Discussion . . . . .	79
4.3.1	Flow behaviour of AA5182-O . . . . .	79
4.3.2	Determination of accuracy . . . . .	82
4.3.3	Predictions of strain hardening rate and flow stress at different strain values . . . . .	85
4.3.4	Simulation results . . . . .	88
4.4	Conclusions . . . . .	92
4.5	Acknowledgements . . . . .	93
4.6	References . . . . .	94
<b>5</b>	<b>Experimental and Numerical Analyses of Formability Improvement of AA5182-O Sheet during Electro-Hydraulic Forming</b>	<b>98</b>
5.1	Introduction . . . . .	101
5.2	Experimental and Computational Procedures . . . . .	105
5.2.1	EHF experiments and grid analysis . . . . .	105
5.2.2	Finite element modelling procedure . . . . .	106
5.3	Results and Discussion . . . . .	110
5.3.1	EHF experimental results . . . . .	110
5.3.2	Deformation history . . . . .	113
5.3.3	Strain distribution and strain path . . . . .	116
5.3.4	Strain rate . . . . .	118
5.3.5	Equivalent strain, stress triaxiality and strain rate history . . . . .	121
5.3.6	Sheet Velocity . . . . .	122
5.3.7	Compressive through-thickness stresses . . . . .	124
5.3.8	Impact stress . . . . .	126

5.4	Conclusions . . . . .	130
5.5	Acknowledgements . . . . .	132
5.6	References . . . . .	132
<b>6</b>	<b>Microscopic investigation of failure mechanisms in AA5182-O sheets sub- jected to electro-hydraulic forming</b>	<b>136</b>
6.1	Introduction . . . . .	137
6.2	Experimental and Analysis Procedures . . . . .	141
6.3	Results and Discussion . . . . .	144
6.3.1	Strain distribution in EHF specimens . . . . .	144
6.3.2	Fracture Mechanism . . . . .	145
6.3.3	Void Nucleation; Intermetallic Particles . . . . .	146
6.3.4	Void Growth . . . . .	154
6.4	Conclusions . . . . .	158
6.5	Acknowledgements . . . . .	159
6.6	References . . . . .	159
<b>7</b>	<b>General Discussion and Conclusions</b>	<b>162</b>
7.1	General Discussion . . . . .	162
7.2	Conclusions . . . . .	164
7.3	Originality of the research . . . . .	168
7.4	Future Work . . . . .	168
7.5	References . . . . .	170
	<b>Appendices</b>	<b>171</b>
A	Further Microscopic Material Studies; OM, TEM . . . . .	172
A.1	Microscopic deformation of grains . . . . .	173
A.1.1	Polished and anodized surface of as-received AA5182 . . . . .	173
A.1.2	Deformed specimens . . . . .	173
A.2	Transmission electron microscopy . . . . .	176
A.2.1	The effect of beam orientation . . . . .	178
A.2.2	Dislocation Density Measurements . . . . .	178
A.2.3	Dislocation-second phase particles interaction . . . . .	181
B	Optical metallography sample preparation . . . . .	184
B.1	Grinding and Polishing . . . . .	184
B.2	Anodizing, Etching and Electro-polishing . . . . .	185
C	Appendix References . . . . .	186
C.1	Appendix References . . . . .	186
	<b>Vita Auctoris</b>	<b>188</b>

# List of Tables

2.1	Chemical composition of various AA5182 alloys from literature, wt% . . . . .	8
2.2	Comparison between high-strain rate metal forming processes [39]. . . . .	15
2.3	Constants of Johnson-Cook constitutive equation for AA5182 sheet calculated by different sources. . . . .	32
3.1	FI% of selected samples compared to different FLCs. . . . .	62
4.1	Boundary values of each parameter . . . . .	75
4.2	Neural Network structures used . . . . .	77
4.3	AA5182-O parameters calculated by GA and regression analysis . . . . .	82
5.1	Ignition-and-growth parameters for explosive material. . . . .	109
5.2	FI% of selected samples compared to different FLCs. . . . .	113
5.3	Steel and aluminium properties. . . . .	128
6.1	Chemical composition of the as-received AA5182-O aluminium, wt%. . . . .	142
6.2	Deformation history, status and maximum safe strains measured in studied specimens. . . . .	143
6.3	Chemical composition and description of second phases existing on the frac- ture surface of AA5182-O subject to either quasi-static or high-strain rate forming. . . . .	149
B.1	AA5182-O sample polishing steps . . . . .	184
B.2	Most common etchant used for AA5xxx-series metallography observation . .	185

# List of Figures

2.1	Comparison of (a) tensile strength and (b) specific tensile strength of aluminium alloys with those of other major industrial alloys [2]. . . . .	7
2.2	Forming limit curves of AA5182-O replotted from literature [15, 21–24]. . . . .	9
2.3	Schematic of EF process to form (a) a large workpiece into final shape (b) a flat panel and (c) a cylindrical workpiece [30]. . . . .	11
2.4	Schematic of EMF process to (a) form sheet metals and (b) expand tube-shaped metals [31]. . . . .	12
2.5	Schematic of EHF process (revised) [36]. . . . .	13
2.6	Schematic of (a) EHFF and (b) EHDF processes [37]. . . . .	14
2.7	Changes of (a) maximum flow stress and (b) yield stress with strain rate for different Mg containing aluminium alloys [66]. . . . .	21
2.8	Changes of normalized failure elongation with strain rate for different aluminium alloys; $E_0$ denotes the elongation to failure at QS strain rate [63]. . . . .	23
2.9	Variation of (a) uniform and (b) total elongation with strain rate and magnesium content [66]. . . . .	24
2.10	(a) variation of AA5182 flow stress with strain rates at different strain values [64]. . . . .	25
2.11	Variation of $FLD_0$ with (a) J-C parameter constant $C$ , (b) hardening exponent $n$ , and (c) thermal softening exponent $m$ [51]. . . . .	26
2.12	(a) Comparison of AA6061-T4 elongation in uniaxial and ring expansion tests [43] and (b) comparison of QS and EHDF Vicker’s hardness for AA6061-T4 and a copper alloy [33]. . . . .	27
2.13	GA Process [112]. . . . .	35
2.14	NN Basics & Process [121]. . . . .	37
2.15	Feed Forward NN Basics [121]. . . . .	38
2.16	Overview of neural network structure used in this study . . . . .	39
2.17	Void nucleation by (a) plastic deformation (interaction of shear with a barrier), (b) coalescence of cavities around hard particles in a soft matrix, and (c) grain boundary sliding at high temperature [86]. . . . .	41
2.18	(a) Occurrence of shear bands in AA5754 before damage, and (b) damage on shear bands in AA5182 [12]. . . . .	42
2.19	Nucleation of voids around inclusions by (a) matrix decohesion, (b) fracture of brittle particles, and (c) shear deformation [86]. . . . .	44
2.20	(a) $Al_3(Fe,Mn)$ and (b) $Al_m(Fe,Mn)$ particles observed in as cast and heat treated AA5182 [130]. . . . .	45
2.21	(a) Mode 1: schematic of equiaxed void growth, (b) Mode 2: parabola-shaped dimples in shear deformation areas [86]. . . . .	46
3.1	Schematic of EHDF apparatus. . . . .	57
3.2	Top and side view of (a) EHFF; top: 6.0 kV, bottom: 5.5 kV, (b) EHDF-34° die; top: 8.4 kV, bottom: 8.0 kV, (c) EHDF-40° die; top: 8.0 kV, bottom: 12.0 kV, and (d) EHDF-45° die; top: 11.5 kV, bottom: 12.0 kV. . . . .	61

3.3	(a) Formability improvement of samples showing highest increase in safe strain and FLCs and (b) variation of improvement of formability with input energy (compared with Ref. [16]). . . . .	63
4.1	Schematic of (a) GA and (b) ANN structure used in this study. . . . .	76
4.2	Specimen used to simulate (a) QS and (b) high strain rate tensile tests. . . .	80
4.3	Comparison of calculated AA5182-O flow stress with experimental data for (a) RD: $0.001s^{-1}$ , (b) DD: $1s^{-1}$ , and (c) TD: $1000s^{-1}$ . . . . .	81
4.4	Comparison of calculated true stress values with experimental data for (a) JC, (b) KHL, (c) VM, and (d) ANN. . . . .	83
4.5	Comparison of accuracies of JC, KHL, VM and NN structures based on (a) adjusted R-square, (b) overall MSE values. . . . .	85
4.6	Variation of the slope of the true stress vs. true plastic strain curve for (a) RD: $1000s^{-1}$ , (b) TD: $0.001s^{-1}$ . . . . .	86
4.7	Variation of AA5182-O flow stress with strain rate at (a) 0.02 strain in RD, (b) 0.02 strain in DD, (c) 0.14 strain in DD, and (d) 0.14 strain in TD. . . .	88
4.8	Contours of effective strain values predicted by different hardening models at the onset of necking for specimens deformed at (a) $0.1s^{-1}$ and (b) $100s^{-1}$ strain rates. . . . .	90
4.9	Experimental strain distribution at the onset of instability for specimen formed under (a) quasi-static and (b) $100s^{-1}$ strain rate. . . . .	91
4.10	(a) Comparison of simulation accuracies and (b) Computational cost vs accuracies. . . . .	92
5.1	Schematic of FE model used to simulate (a) EHFF and (b) EHDF- $40^{\circ}$ . . . .	111
5.2	Top view of (a) EHFF; top: 6.0 kV, bottom: 5.5 kV, (b) EHDF- $34^{\circ}$ die; top: 8.4 kV, bottom: 8.0 kV, (c) EHDF- $40^{\circ}$ die; top: 12.0 kV, bottom: 8.0 kV. . .	112
5.3	Progress of EHF deformation at different times, calculated from the FE model, compared with experimental results for (a) EHFF specimen formed with 4.8kJ input energy, (b) EHDF- $34^{\circ}$ specimen formed with 6.4kJ input energy and (c) EHDF- $40^{\circ}$ specimen formed with 14.4kJ input energy. . . . .	115
5.4	Comparison of experimental and predicted strain distributions for (a) EHFF specimen formed with 4.8kJ input energy, (b) EHDF- $34^{\circ}$ specimen formed with 6.4kJ input energy and (c) EHDF- $40^{\circ}$ specimen formed with 14.4kJ input energy; major ( $e_1$ ) and minor ( $e_2$ ) strains are shown as blue and green points, respectively, where experimental measurements in the RD and TD are shown as square and diamond points. . . . .	117
5.5	Comparison of experimental grid measurement of EHF formed specimens with quasi-static FLC derived from Ref. Wu et al. (2003) and deformation strain path at different locations of (a) EHFF specimen formed with 4.8kJ input energy, (b) EHDF- $34^{\circ}$ specimen formed with 6.4kJ input energy and (c) EHDF- $40^{\circ}$ specimen formed with 14.4kJ input energy; + and $\times$ denote measurements carried out in the RD and TD directions, respectively. The reported distance on FEM lines is relative to the apex of each specimen. . . .	119

5.6	Comparison of peak strain rates predicted at different locations from the apex and averaged through the thickness of AA5182-O specimens; EHFF specimen (yellow line) was formed with 4.8kJ input energy, EHDF-34° specimen (blue line) formed with 6.4kJ input energy and EHDF-40° specimen (red line) formed with 14.4kJ input energy. . . . .	121
5.7	Variations of normalized equivalent plastic strain, strain rate and stress tri-axiality at the apex for (a) EHFF specimen formed with 4.8kJ input energy, (b) EHDF-34° specimen formed with 6.4kJ input energy and (c) EHDF-40° specimen formed with 14.4kJ input energy. . . . .	123
5.8	Variation of velocities for elements located (a) 40mm from the apex and (b) at the apex during EHFF and EHDF processes. . . . .	125
5.9	Evolution of the through-thickness stress at different radial distances from the apex for (a) EHFF specimen formed with 4.8kJ input energy, (b) EHDF-34° specimen formed with 6.4kJ input energy and (c) EHDF-40° specimen formed with 14.4kJ input energy; values were taken from elements located at the mid-thickness of the sheet. . . . .	127
5.10	The effect of input energy on void evolution in safely formed EHDF specimens brought from Jenab et al. (2017). . . . .	128
5.11	Comparison between impact pressure and maximum through thickness stress generated upon impact of the sheet against the die; lines with filled markers are calculated based on the analytical approach, Eq.5.3, and lines with open markers are derived directly from FE model ( $\sigma_{3max}$ ). . . . .	129
6.1	Schematic of (a) EHFF and (b) EHDF apparatuses. . . . .	138
6.2	Void nucleation around inclusions; (a) matrix decohesion, (b) cracked brittle particles, and (c) shear deformation (adapted from Ref. [20]). . . . .	141
6.3	Major ( $e_1$ ), minor ( $e_2$ ) and effective ( $\varepsilon_{eff}$ ) strain distributions of EHDF-34° specimens deformed at (a) 7.4kJ (fractured) and (b) 8.1kJ (safe) input energies; RD and TD refer to measurements carried out at rolling and transverse directions of the as-received rolled sheet, respectively. . . . .	145
6.4	Polished subfracture and low magnification fractography of (a) QS Marciniak ( $e_1 = 34.3\%$ , $e_2 = 33.0\%$ ), (b) EHFF; 4.9kJ ( $e_1 = 36.8\%$ , $e_2 = 28.2\%$ ), and (c) EHDF-40°; 10kJ ( $e_1 = 48.4\%$ , $e_2 = 39.3\%$ ). . . . .	147
6.5	Fracture surface of AA5182-O aluminium at 800× magnification deformed under biaxial strain state in (a) QS Marciniak, (b) EHFF; 4.9kJ, (c) EHDF-34°; 7.4kJ, and (d) EHDF-40°; 10kJ conditions. . . . .	148
6.6	Fracture surface of EHFF specimens deformed at 19.4kJ showing different dimple sizes and cracked second phase particles at 2000× magnification; (a) at side of dimples and (b) at the bottom of dimples. . . . .	149
6.7	Void nucleation sites from sub-fracture surface of (a) EHFF; 4.9kJ ( $e_1 = 36.8\%$ , $e_2 = 28.2\%$ ) and (b) EHDF-45°; 12.1kJ ( $e_1 = 56.0\%$ , $e_2 = 34.2\%$ ) specimens. . . . .	151
6.8	Transmission electron microscopy results of AA5182-O aluminium showing void nucleation by (a,b) cracking of (Fe,Mn)-containing particle in QS Marciniak specimen ( $e_1 = 29.9\%$ , $e_2 = 29.5\%$ ), (c,d) particle debonding from interface of Mg <sub>2</sub> Si and (Fe,Mn)-containing intermetallic particle in EHDF-45°; 19.6kJ specimen ( $e_1 = 61.0\%$ , $e_2 = 24.2\%$ ), and (e,f) particle-matrix debonding in EHDF-40°; 14.4kJ specimen( $e_1 = 62.4\%$ , $e_2 = 22.8\%$ ). . . . .	153



6.9	Variation in void percentage with distance from the fracture surface in specimens formed at low and high-strain rates in (a) biaxial and (b) uniaxial tension. . . . .	155
6.10	(a) The effect of input energy on void evolution in safely formed EHDF specimens, (b) effect of die presence on void formation in different EHFed specimens. . . . .	157
A.1	As-received microstructure of AA5182 in RD, TD, and ND, (a) polished and (b) anodized. . . . .	174
A.2	Mosaic images of subfracture surface of (a) QS Marciniak specimen and (b) EHFF specimen deformed with at 6.0kV input voltage. . . . .	175
A.3	Mosaic images of EHDF specimens formed into (a) 40° conical die with 10kV input voltage and (b) into 45° conical die with 14kV input voltage. Both images were taken at the apex, where greatest levels of major and minor strain were measured. . . . .	176
A.4	Microstructure of specimens formed using (a) QS Marciniak, (b) EHFF at 6kV input voltage, (c) 34° die formed EHF using 9kV input voltage, (d) 40° die formed EHF using 10kV input voltage, (e) and (f) 45° die formed EHF using 14kV input voltage. Images were taken at largest values of strain shown in Fig. 3.3 of Chapter 3. . . . .	177
A.5	The effect of beam alignment on the observation of dislocation lines; (a) diffraction pattern, (b) DF image at plane A, (c) DF image at plane B, (d) DF image at [011] plane and (e) BF image from [011] plane. . . . .	179
A.6	Measurement of dislocation densities in as-received AA5182-O . . . . .	180
A.7	Variation of dislocation densities of as-received AA5182-O sheet and specimens deformed under QS Marciniak, EHDF-40 safely formed with 10kV input voltage and EHDF-45 safely formed with 14kV input voltage with effective strain in different specimens. . . . .	181
A.8	(a) Dislocations interaction with second phase particles (b) chemical analysis of second phases showing Fe-Mn and Mg-Si enriched second phases. . . . .	182
A.9	Initiation of a void by cracking of an Fe-Mn enriched second phase particle; (a) bright field image showing the void as a dark spot and (b) chemical analysis showing the void by the absence of aluminium matrix. . . . .	182

# Nomenclature and Abbreviations

## Nomenclature

$\zeta$	Strain rate related multiplicative factor
$\rho$	Material density or density of dislocations
$\rho_0$	Density of the explosive material
$\rho_p$	Density of the detonation products
$C_i$	Longitudinal wave speed in $i$ material
$c$	Capacity of EHF capacitors
$e_1$	Major engineering strain
$e_2$	Minor engineering strain
$E_m$	Initial energy of explosive material per unit mass
$FI$	Formability improvement factor
$I$	Vector of biases in each layer of neural network
$K$	The strength coefficient or bulk modulus
$m$	Strain rate sensitivity exponent
$n$	Strain hardening exponent
$P_i$	Impact pressure
$P$	A pixel in a given image
$p$	Pressure generated upon explosion
$t_{\alpha/2}$	The probability distribution
$U$	The discharged energy of EHF process
$v$	Input voltage of EHF
$VP$	Void percentage
$W$	Vector of weights in each layer of neural network

## Abbreviations

CGA	Circle grid analysis
BF	Bright field image (TEM)
DSA	Dynamic strain ageing
DF	Dark field image (TEM)
EELS	Electron energy loss spectroscopy
EF	Explosive forming
EHDF	Electro-hydraulic die forming
EHF	Electro-hydraulic forming
EHFF	Electro-hydraulic free forming
EMF	Electro-magnetic forming
FLC	Forming limit curve
FLD	Forming limit diagram
HAADF	High angle annular dark field
JC	Johnson-Cook hardening function
KHL	Khan-Huang-Liang hardening function
MSE	Mean squared error
NN1	Simplified neural network
NN2	Complex structured neural network
OM	Optical microscopy
QS	Quasi-static
SEM	Scanning electro microscopy
SRS	Strain rate sensitivity
TEM	Transmission electron microscopy
VM	Modified-Voce hardening function

# Chapter 1

## Introduction

### 1.1 Motivation for the industrial use of aluminium alloys

The use of aluminium alloys in the automotive industry is attractive since it allows the weight of a vehicle body to be reduced by 50% [1]. By reducing the weight of a passenger vehicle by even 10%, Joost [2] showed that fuel efficiency can improve by 6-8%. Besides, the low density of aluminium alloys and their excellent corrosion resistance as compared to steels, make them a material of choice for automotive body and structure components. Highly formable 5xxx-series aluminium alloys are generally used for inner panel applications whereas 6xxx-series alloys which are heat-treatable are preferred for outer panel applications [3]. However, in comparison with steel which can show more than 50% elongation, aluminium alloys typically exhibit lower formability at low temperatures [4, 5]. Moreover, the cost of aluminium alloys and their manufactured parts is greater than that of steels [3].

Another difficulty is that impurities and second phase particles in aluminium alloys lead to localized shear and final failure [6]. Besides, these alloys have low strain hardening exponent which limit their ductilities compared to commercial steels especially at room temperature deformations. Therefore, in the last decades, researchers have focused on improving the formability of aluminium alloys [5].

Among the many aluminium alloys that are commercially produced, fully annealed 5182 aluminium alloys (AA5182-O) is of great interest to the automotive industry due to their good formability and production price compared to 6xxx or 7xxx-series aluminium alloys. AA5182-O is a good material for inner parts of vehicles mainly due to its cost. However, AA5182-O low formability as compared to many commercial

grade steels prevents the extensive use of this alloy in automotive industry.

Forming at elevated temperatures could lead to better formability improvement of AA5182-O but has its own drawbacks including additional costs of lubrication, higher energy consumption of heating and post forming cleaning [7]. Alternatively, high strain rate deformation processes can be used but there are several uncertainties regarding high strain rate forming. A clear understanding of the deformation history and the materials' response to high-strain rate deformation would remove hindrances to a broad implementation of such forming processes in the automotive industry.

## 1.2 Objective of the research

The ultimate objective of this research was to explain the micro-mechanisms and mechanical factors that are the root cause of the formability enhancement of AA5182-O when it is subject to EHF. The following were secondary objectives of this research;

1. Quantitative analysis of deformation of AA5182-O sheets deformed under different EHF conditions; electro-hydraulic die form (EHDF) and electro-hydraulic free form (EHFF) and with different levels of input energy. The purpose of the quantitative analyses was to determine the magnitude of formability improvement in each case.
2. Due to the technical difficulties related to EHF experiments, it was needed to obtain reliable numerical simulation of the EHF process especially to understand the effect of factors influencing the formability of the sheets; including hydrostatic stresses. The first step toward this goal was to obtain work hardening behaviour of AA5182-O at different strain rates ranging from QS to high-strain rates and implement this work hardening properties to numerical simulation. Also, this investigation helped us to understand if changes in mechanical properties could lead to any improvement in formability of the alloy at high-strain rates.
3. Observation and quantification of failure mechanisms of AA5182-O under dif-

ferent EHF conditions to determine the void nucleation process. Moreover, the quantitative analysis of void growth indicated if the void growth could be influenced by the EHF process.

### 1.3 Structure of the dissertation

This dissertation consists of seven chapters. The following is a brief description of the contents of each chapter;

**Chapter 2** presents a literature review on 5xxx-series aluminium alloys, their important alloying components. High strain rate processes including EHF are then discussed as well as the mechanisms of hyperplasticity and changes in material constitutive behaviour. Different hardening functions and two approaches to determine phenomenological hardening functions for the alloy, genetic algorithm and artificial neural network, are discussed briefly. Finally, fracture mechanisms by void nucleation and growth are presented.

**Chapter 3** describes the experimental measurement of formability improvement during EHF. The importance of the die effect and input energy are discussed in this chapter. This chapter is published in *Materials Science and Technology (MS&T)*.

**Chapter 4** discusses the constitutive behaviour of AA5182-O during quasi-static and high-strain rate deformation. Tensile test data were fitted to various hardening functions and the constants of Johnson-Cook, KHL and modified-Voce were determined using two different approaches; regression analysis and genetic algorithm optimization. Also, the hardening properties of the alloy are studied using different structures of artificial neural networks. All hardening functions are implemented as ABAQUS VUMATs and used to simulate simple tensile tests to determine the most accurate constitutive function. This chapter is published in *Journal of Materials and Design*.

**Chapter 5** discusses the extent of formability improvement of AA5182-O during the EHF process by means of experimental and finite element modelling. Finite element

(FE) analysis was performed using coupled Eulerian-Lagrangian elements and the ignition and growth of an explosive material submerged in water. FE simulations were conducted using obtained artificial neural network to describe the hardening behaviour of AA5182-O and reveals the importance of strain rate, sheet velocity, stress triaxiality and impact stress on free and die formed EHF specimens. This chapter is accepted for publication in *Journal of Materials Processing Technology*.

**Chapter 6** discusses the findings on fracture mechanisms of the AA5182-O sheet. Sources of void nucleation as well as the effect of EHF process on void growth is discussed. The work in this chapter is published in the journal of *Materials Science and Engineering A*. Further material characterization performed during this work is presented; optical microscopy of anodized specimens revealing grain structure as well as transmission electron microscopy results including interaction of dislocations with second-phases and intermetallic particles and dislocation density measurements are presented in appendices A and B.

**Chapter 7** presents the general discussion and concluding remarks from this research. At the end of this chapter, suggestions are made for future research.

## 1.4 References

- [1] E. M. Taleff, P. J. Nevland, and P. E. Krajewski, "Tensile ductility of several commercial aluminum alloys at elevated temperatures," *Metallurgical and Materials Transactions a-Physical Metallurgy and Materials Science*, vol. 32, no. 5, pp. 1119–1130, 2001.
- [2] W. J. Joost, "Reducing Vehicle Weight and Improving U.S. Energy Efficiency Using Integrated Computational Materials Engineering," *Jom*, vol. 64, pp. 1032–1038, Aug 2012.
- [3] W. Miller, L. Zhuang, J. Bottema, A. Wittebrood, P. De Smet, A. Haszler, and A. Vieregge, "Recent development in aluminium alloys for the automotive industry," *Materials Science and Engineering: A*, vol. 280, pp. 37–49, mar 2000.
- [4] E. M. Taleff, P. J. Nevland, and P. E. Krajewski, "Solute-drag creep and tensile ductility in aluminum alloys," in *Creep Behavior of Advanced Materials for the 21st Century*, pp. 349–358, The Mineral, Metals & Materials Society, 1999.
- [5] J.-Y. Jeon, H.-T. Son, K.-D. Woo, and K.-J. Lee, "Texture and mechanical properties of Al-0.5Mg-1.0Si-0.5Cu alloy sheets manufactured via a cross rolling method," *Metals and Materials International*, vol. 18, pp. 295–301, apr 2012.
- [6] B. M. Dariani, G. H. Liaghat, and M. Gerdooei, "Experimental investigation of sheet metal formability under various strain rates," *Proceedings of the Institution of Mechan-*

*ical Engineers, Part B: Journal of Engineering Manufacture*, vol. 223, pp. 703–712, jun 2009.

- [7] A. Rohatgi, E. V. Stephens, R. W. Davies, M. T. Smith, A. Soulami, and S. Ahzi, “Electro-hydraulic forming of sheet metals: Free-forming vs. conical-die forming,” *Journal of Materials Processing Technology*, vol. 212, pp. 1070–1079, may 2012.



## Chapter 2

### Literature Survey

#### 2.1 5xxx-series aluminium alloys

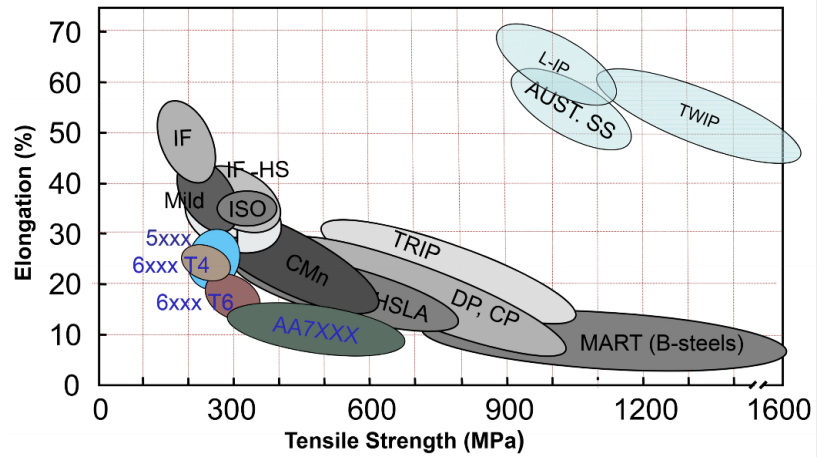
5xxx-series aluminium-magnesium (Al-Mg) alloys were first developed in the 1930s when there was a need for sheet materials with higher strengths, weldability, good formability and higher levels of corrosion resistance [1]. Fig. 2.1 shows a comparison of mechanical properties of 5xxx-series alloys with those of other major industrial alloys [2]. Although these alloys are not typically heat-treatable and derive their mechanical properties from solid solution hardening of magnesium atoms in the aluminium matrix, the mentioned favourable properties in conjunction with their ease of being manufactured, physical properties and low cost results in their extensive usage in the automotive, aerospace, and shipbuilding industries [3].

According to the binary Al-Mg phase diagram, 3% (mass fraction) of magnesium (Mg) could be completely dissolved at temperatures over 190°C in the aluminium matrix, which contributes to the solute-drag effect. The linear misfit factor between Mg and Al is +0.12. High stacking-fault energy of Al-3Mg makes cross-slip and climb easier and helps provide a uniform dislocation distribution [4].

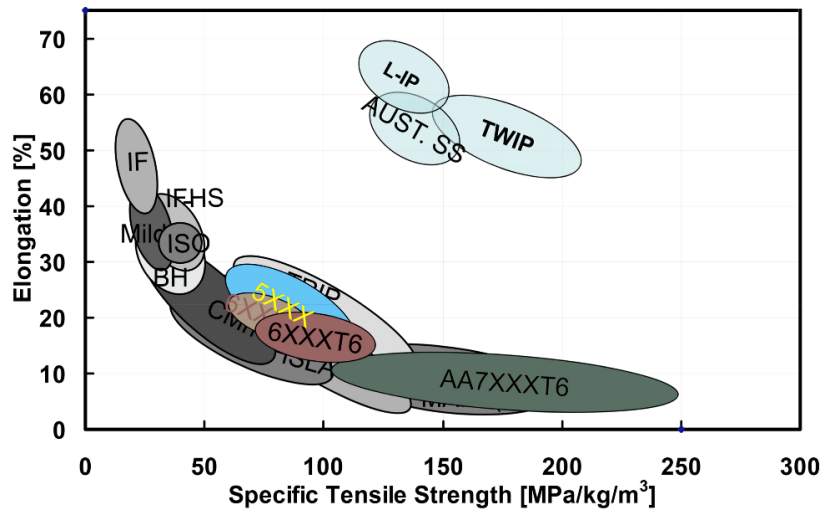
Korbel et al. [5] compared shear band formation of a pure aluminium and Al-4.5Mg alloys and concluded that straining by shear localization inversely changes with the magnesium content.

Manganese is usually added to aluminium alloys to provide strength and grain size control [6, 7]. The addition of Mn can help to increase the formability of 5xxx alloys above that of 6xxx-series alloys; Li and Ghosh [8] found better formability for strain-hardened AA5182+Mn as compared to AA6111-T4.

Other alloying elements, such as Fe and Si, can significantly influence the damage



(a)



(b)

Figure 2.1: Comparison of (a) tensile strength and (b) specific tensile strength of aluminium alloys with those of other major industrial alloys [2].

mechanisms and fracture behaviour. In alloys with low Fe content, voids play a major role in damage whereas for alloys with high-Fe content, shear bands are more prevalent. For example, Spencer [9] showed that by increasing the Fe content, the effective plastic strain up to fracture (fracture strain) reduces in most testing conditions.

A large variety of second-phase particles with various size distribution are present in the microstructure of a typical commercial AA5xxx where their size and distribution are influenced by the casting and hot rolling processes. These particles are the result of Mg and other alloying elements, mainly Fe and Si, and impurities in the aluminium and consist mainly of  $Mg_2Si$ ,  $Al_{12}(Fe,Mn)_3Si$ ,  $Al_6(Fe,Mn)$  and  $Al_3Fe$  [10]. Kaibyshev et al. [11] observed the presence of incoherent second-phase particles of  $Al_3Zr$ ,  $Al_3Cr$  and  $Al_6Mn$  using TEM investigation. These incoherent particles do not contribute to the strength or work hardening of the alloy [9].

Hadianfard et al. [12] detected three groups of second phases in AA5182; the first category consists of mainly Al, Mg, and Si, the second category contains 10% Fe, Mg and Mn, and finally, less common second phases contain only aluminium oxides.

### 2.1.1 Chemical composition of AA5182

AA5182 alloy has a range of chemical composition, as indicated in Table 2.1.

Table 2.1: Chemical composition of various AA5182 alloys from literature, wt%.

Al	Mg	Mn	Fe	Si	Cr	Cu	Zn	Ti	Detail
Bal.	4.0-5.0	0.20-0.50	<0.35	<0.2	<0.10	<0.015	<0.10	<0.05	Accepted range
Bal.	4.30	0.34	0.21	0.03	-	0.01	<0.01	<0.01	[13-15]
Bal.	4.40	0.36	0.18	0.11	0.04	0.10	0.02	0.02	[16]
Bal.	4.51	0.34	0.18	0.08	0.02	0.05	-	0.02	[17]
Bal.	4.60	0.35	0.21	0.11	0.01	0.04	-	-	[18]

### 2.1.2 Forming limits of AA5182-O sheets

The concept of a forming limit diagram (FLD) was introduced by Keeler and Backhofen (1964) and then further developed by Goodwin (1968). Since then FLDs have become the primary tool to evaluate the formability of sheet materials [19]. The

forming limit curve (FLC) represents the locus of all combinations of plastic strains beyond which there is a risk of necking in sheet materials [7].

A review of the literature shows that there is significant scatter between the experimental FLC of AA5182-O sheets. This is due to the difficulty of identifying the onset of necking as well as the range of mechanical properties. This difficulty is more prominent for aluminium alloys because they tend to develop highly localized deformation areas following by rapid cracking. This is also confirmed by damage analysis for aluminium alloys such as in Ref. [20]. Figure 2.2 shows different experimental FLCs of AA5182-O developed at room temperature and reported in the literature [15, 21–24].

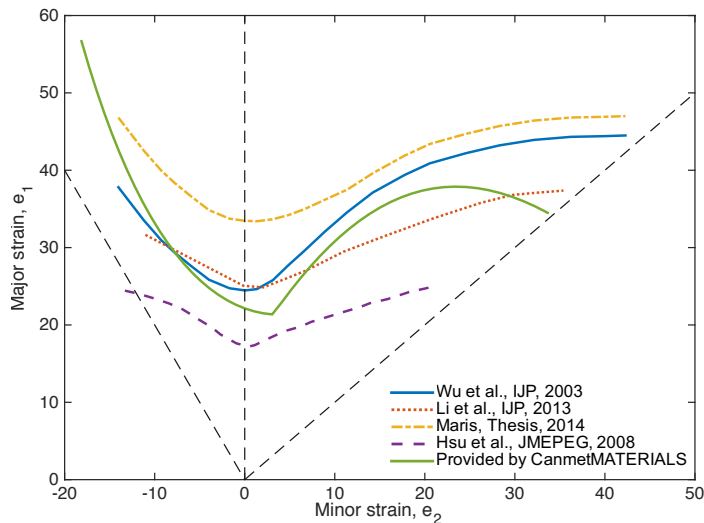


Figure 2.2: Forming limit curves of AA5182-O replotted from literature [15, 21–24].

Li et al. [25] predicted the FLC of AA5182-O using FE analysis and Barlat’s Yld89 yield criterion. They observed that the minor and major strain of elements just outside the necking area do not change significantly after the occurrence of necking, and hence the strains at these locations are suitable to determine the FLC especially when capturing the onset of necking is not possible.

According to Dariani et al. [26] who investigated the effect of strain rate on FLC, 6xxx-series aluminium alloys exhibit substantially improved formability at a strain rate of  $1000\text{s}^{-1}$  when compared to (AISI 1045) steel specimens. Also, Dariani et al. [26] noticed that more formability improvement can be seen in AA6061-T6 during

explosive forming for positive minor strain values (i.e. biaxial stretching). Consequently, it is expected that the formability of AA5182-O could be improved at high strain rate deformation.

## **2.2 High strain rate metal forming processes**

The most common defects in conventional quasi-static sheet metal forming are shape inaccuracy and localized deformation. The former is mostly due to wrinkling or springback while the latter leads to localized thinning and rupture [20]. High strain rate metal forming processes offer the potential of increasing the formability of sheet materials.

Explosive forming (EF), electro-magnetic forming (EMF) and electro-hydraulic forming (EHF) are three well-known high-strain rate, or pulse, forming processes.

In these unconventional forming processes, parts are formed into a single die surface thus eliminating the need for matching dies. Hence, as compared to conventional forming processes, not only the cost of production dies is significantly reduced but friction is also eliminated from one side of the blank [27]. This elimination of friction helps to reduce the strain localization in corners of the workpiece [28]. As a result, sharper corner radii can be manufactured in pulse forming compared to quasi-static forming processes [29]. Besides, due to the nature of pulse forming techniques, strain can be redistributed across a much broader area of the workpiece [28].

### **2.2.1 Explosive Forming**

Explosive Forming (EF) is perhaps the most commonly used high-strain rate forming process especially in the aerospace industry, which was the main driver to explore the use of EF [27]. In EF, the pressure needed to form the workpiece is generated by an explosive charge usually submerged in a liquid medium that is usually water. After detonation, pressure waves propagate through the liquid medium and reach the sheet surface forming it either into a die or into free space [30] (Fig. 2.3).

Because of its high reproducibility and the ability to form large and geometrically

complex parts with good accuracy, EF is commonly used in different industries to form a wide range of parts from high strength steel to various aluminium alloys [27].

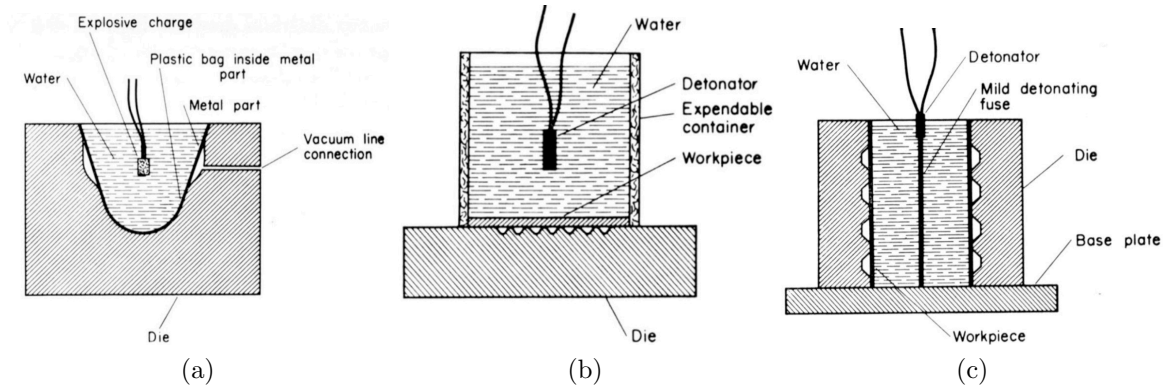


Figure 2.3: Schematic of EF process to form (a) a large workpiece into final shape (b) a flat panel and (c) a cylindrical workpiece [30].

## 2.2.2 Electro-magnetic forming

Electro-magnetic forming (EMF) is another high-strain rate process that is used to form sheet and tubular parts and also in impact welding processes. Fig. 2.4 shows a schematic of the EMF process used to form sheet metal parts and tubular parts. During EMF, once the electrical energy stored in capacitors is released, an extremely strong transient magnetic field is produced in the coil located close to the workpiece. This magnetic field creates eddy currents in the conductive sheet metal blank in the opposite direction of the primary current. The resulting repulsive electromagnetic force generated will push the sheet away from the coil and either toward a die or into free space with significant speed. Since a pulsed magnetic field is used, the process is limited to metals with a high electrical conductivity [30, 31]. For an in-depth review of the EMF process, readers are referred to the article by Psyk [31].

## 2.2.3 Electro-hydraulic forming (EHF)

Electro-hydraulic forming (EHF) is a high-strain rate forming process in which electrical energy is converted into work without involving a magnetic field. The principles

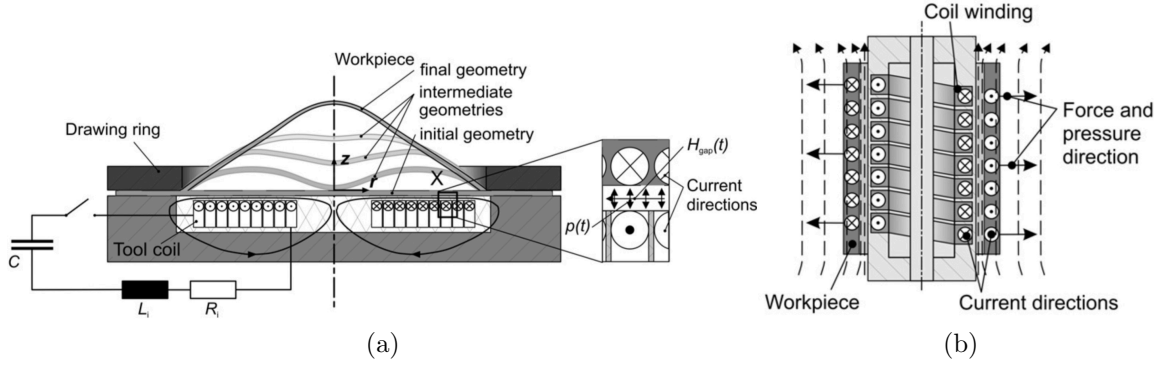


Figure 2.4: Schematic of EMF process to (a) form sheet metals and (b) expand tube-shaped metals [31].

of EHF and EF processes are similar except that instead of using a chemical explosive as the driving force, the electrical discharge between two electrodes is used in EHF. Early and Dow [32] were perhaps the first researchers to present the concept of EHF to form sheet metals. Soon after that, EHF was investigated by many researchers not only for sheet metal forming but also for bulging process. The technology of EHF rapidly developed in the 1960s.

The schematic design of EHF machines is shown in Fig. 2.5. During the electrical discharge, most of the energy stored in capacitors is released in a short period of time (typically around  $100\mu\text{s}$ ). As a result, the liquid surrounding the bridge wire connecting the electrodes vaporizes and produces a high-velocity shock wave. This shock wave propagates through the water in the chamber and forces the sheet metal into the die [33]. Gilchrist and Crossland [34] explained the initiation and expansion of the plasma channel without employing a wire-bridge; without the wire-bridge, a low impedance spark channel has to be formed first and then the remaining electrical energy in the capacitors is rapidly dissipated between the electrodes. The result is a sudden rise in spark channel pressure generating shock waves radiating from the channel. This creates a hot gas bubble which continues to expand into a circular-elliptical shape [34]. This shockwave propagates towards the work-piece at very high speed and the momentum of the water forms the sheet metal into either free space or into a die cavity [28]. The discharged energy, released from capacitors, can be

calculated from Eq.2.1 [35];

$$U = \frac{1}{2}cv^2 \quad (2.1)$$

where  $c$  is the capacitor capacitance and  $v$  is the input voltage. However, under optimum testing conditions the overall conversion of electrical energy into plastic work was found to be only around 12% without the use of a wire bridge [34].

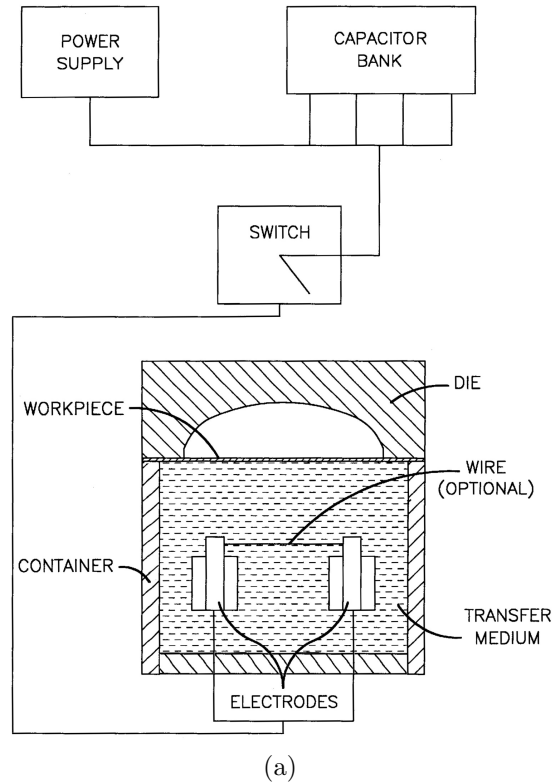


Figure 2.5: Schematic of EHF process (revised) [36].

The EHF process can be carried out either into free space, electro-hydraulic free forming (EHFF), or with the presence of a die which is called electro-hydraulic die forming (EHDF). Schematics of EHFF and EHDF processes are shown in Fig. 2.6. In EHFF, the workpiece decelerates at the end of the forming process and hence the strain rates at the end of the process are quasi-static (QS). The same QS deformation can happen even in EHDF process when the initial energy is not sufficient to fully form the part. In this case, the blank speed reduces before the die cavity is completely filled and no formability improvement would be observed. However, as discussed in



detail in Section 2.3, the EHF process should be designed in a way that the specimen reaches a high-impact velocity in order to obtain superior formability. Golovashchenko et al. [28] reported that the highest possible strain rates are achieved when the sheet contacts the die at high velocity and hence enhanced formability can only be achieved during the EHDF process [28].

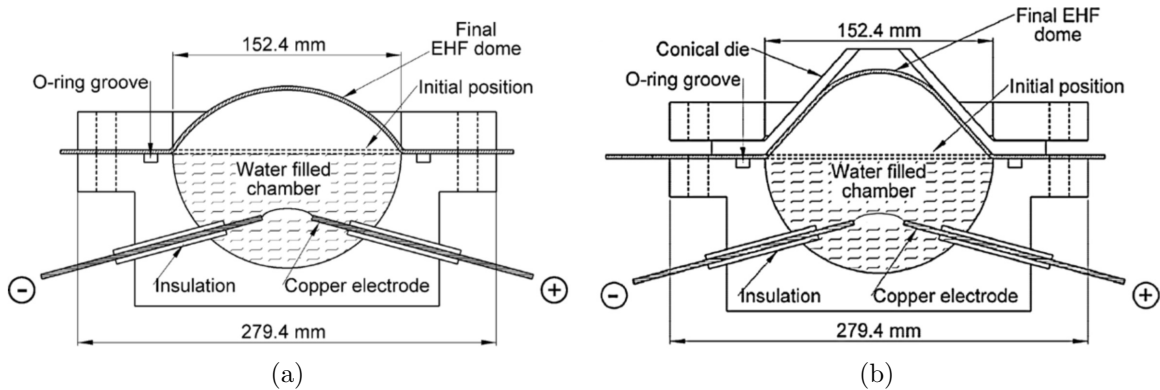


Figure 2.6: Schematic of (a) EHFF and (b) EHDF processes [37].

## 2.2.4 Comparison of EHF with other high-strain rate forming processes

Among the mentioned high-strain rate forming processes, EHF seems to be the most promising technique because it is a more flexible manufacturing process than EMF. In EHF, several successive discharges can be used to fill the die completely or to calibrate springback without removing the die [28]. Besides, the repeatability of the EHF can be improved significantly by using a wire bridge between electrodes. And most importantly, experiments suggested that higher strains can be achieved in EHF process [28]. As suggested by Noland et al. [38], when compared with EMF, larger specimens can be manufactured with EHF process (1.2m diameter compared to 0.3m diameter). Moreover, the tooling and capital costs are usually less in the case of EHF even though the production speed may be less than EMF [39]. Also, during EHF the greatest amount of formability improvement was observed in plane strain. Since local areas close to relatively sharp corners are the most prone to failure, EHF seems

to be a good candidate in corner filling processes [28]. Table 2.2 tabulates the main differences between EF, EMF and EHF. Interested readers are referred to Daehn [30] who published an in-depth review of various high-rate forming processes including EF, EMF and EHF.

Table 2.2: Comparison between high-strain rate metal forming processes [39].

	EF	EMF	EHF	
	Confined		Bridgewire	Spark Discharge
Diameter limit,m	1.5	0.3	1.2	1.2
Shape complexity	Complex	Complex	Complex	Complex
Capital cost	Low	Moderate to high	Moderate	Moderate
Tooling cost	Moderate	Moderate to high	Low	Low
Production rate	2-12 pts/hr	up to 1000pts/min	4-12 pts/hr	up to 50pts/hr

Tobe et al. [40] studied the deformation of several aluminium alloys during EHFF tests and found that the forming limit of relatively strain rate dependent alloys can be increased by 35%. Balanethiram et al. [33] performed EHDF experiments in which AA6061-T4 sheets with a 1.6mm thickness were formed into a die with a 90° apex. Results of EHDF were compared to QS forming into the same die. The specimens deformed in EHDF filled the dies, whereas the QS process was unable to cause the sheets to fill the die completely. Their circle grid analysis (CGA) showed significant improvement in major strain; at a constant minor strain of 3.0% the major strain increased from 21.5% in QS to 122.1% in EHDF [33].

According to Balanethiram et al. [33], during the EHDF process, the high velocity impact of the work-piece is expected to increase the formability and not only the high-strain rate deformation itself. Therefore, even for materials whose strain rate sensitivity is not positive or does not change significantly with strain rate, enhanced formability might still be observed in EHDF conditions [33].

Golovashchenko et al. [28] investigated the formability improvement and crack geometries of DP600 steels in QS, EHFF, EHDF with conical and V-shaped dies. Based on their simulations, a peak strain rate of 20,000s<sup>-1</sup> was achieved in EHDF conditions in the apex area of the conical and V-shaped specimens [28].

Rohatgi and his co-workers performed EHFF and EHDF experiments on AA5182-O with 1mm thickness and published their work in Ref. [35, 37, 41]. They experimentally

measured strains using a DIC system and reported that the duration of the EHF process was in the range of 600-700 $\mu$ s for aluminium alloys. They also noticed that by increasing the input energy, the velocity and plastic strain increased with almost a proportional relation during forming [35]. Using their facility, the maximum sheet-normal velocity was calculated to be 146 ms<sup>-1</sup> in EHFF. This led to a maximum in-plane engineering strain-rate of 3900s<sup>-1</sup> during their EHFF tests. However, a peak strain rate of 4230s<sup>-1</sup> was measured in EHDF experiments [41]. Rohatgi et al. [41] emphasized that a formability enhancement is possible even under EHFF conditions; the local minor strains of 0.1 and 0.05 were enhanced by 2.5 and 6.5 times under EHFF and EHDF conditions, respectively [41].

Moreover, they observed that during the EHF process, the sheet profile is generally convex [37] as opposed to EMF process where a concave-convex profile was reported by Takastu et al. [42]. Their results show that strain path in the apex region of conical specimens is linear and equi-biaxial. Even though this linearity was observed in both EHDF and EHFF tests, it is more noticeable in case of EHFF because of the non-symmetrical friction condition of EHDF. Perhaps, the EHDF condition is also similar to the equi-biaxial because during the majority of the deformation time, the sheet material in the apex region does not contact the die and hence it is deforming without the presence of die-sheet frictional effects.

## **2.3 Mechanisms of Hyperplasticity in High Strain Rate Forming**

Potentially higher strains can be achieved in high-energy rate forming processes when compared to conventional QS forming processes. Besides the work published by Balanethiram and co-workers [33, 43] on AA6061-T4, in which 568% increase in major strain was observed in near plane-strains conditions (from 21.5% in QS to 122.1% in EHDF), hyperplasticity of another aluminium alloy (AA6111-T4) is also reported by Golovashchenko et al. [44]. They observed that by implementing EHF deformation process, overall formability can be improved by 11 to 29% and local deformation can

be extended by 40 to 90%. In another work, Oliveira and Worswick [45] performed EMF experiments on AA5182 and AA5754 sheets and measured significant engineering strains of 40-50% for AA5754 when formed into a rectangular die. Moreover, Imbert and his co-authors [46, 47] investigated the effect of free and die forming EMF processes on AA5754 and AA5182 sheets. They reported that the maximum engineering strains for AA5754 is 20-30% but in the QS condition this improved to 35-45% in EMDF for a 112° apex angle die [46] and 65% for a 100° apex angle die [47].

Other researchers also observed hyperplasticity: the numerical results of Gerdooei et al. [48] indicate that the formability of AA6061 can be improved 146% at high-strain rates. Rohatgi's final strain in x-direction of EHDF samples are 64% more than EHFF samples [35].

To explain the reasons of this improved formability, three major mechanisms are mentioned in the literature to explain this improved formability:

**I** The increase in flow stress (i.e. the change in material constitutive behaviour) at high-strain rate regimes which can lead to enhanced formability [49–52] (section 2.3.1).

**II** Inertial effects [33, 48, 53, 54] which lead to a reduction in the growth rate of geometric imperfections, such as voids or cracks, at high speed deformation due to enhanced inertial forces. This effect is also called "inertial ironing" in the literature (section 2.3.2) and is influenced by the velocity rather than the strain rate imposed on material [33].

**III** Die effects [46] which are explained in detail in Section 2.3.3.

### **2.3.1 Changes in hardening behaviour of material**

Plastic instability and neck formation occur when the work-hardening rate of the sheet specimen is not sufficient to prevent strain localization. According to Considère's criterion, diffuse necking occurs in uniaxial tension when the rate of work hardening is balanced out with the true stress ( $d\sigma/d\varepsilon = \sigma$ ). As a result of this, deformation

will be focused on localized regions which will deform more rapidly and consequently, material deformation changes drastically from uniform to non-uniform.

Perhaps, the most important mechanical property which can influence the achievable uniform elongation is the material strain rate sensitivity (SRS) [55, 56]. Also, the post-uniform elongation is determined by SRS so that enhanced post-uniform elongation can be achieved with higher SRS values [55]. When the flow stress of a material obeys the power law relation ( $\sigma = k\varepsilon^n\dot{\varepsilon}^m$ ) [8], SRS is noted as  $m$  and can be calculated by  $m = \left. \frac{d \ln \sigma}{d \ln \dot{\varepsilon}} \right|_{\varepsilon, T}$ .

Since this parameter can affect the total elongation (fracture strain) and formability of AA5182-O sheets significantly, the SRS of aluminium alloys is discussed in detail in this section.

### **At QS strain rates; negative SRS**

Generally, aluminium alloys show little dependency on strain rate and exhibit insignificant and sometimes negative values of SRS especially at QS strain rates. To exemplify, Chung et al. [57] showed that AA7075 (Al-Zn-Mg) exhibit negative SRSs and the failure occurred by shear localization before the onset of necking. Jenab et al. [58–60] also observed negative SRS at QS strain rates even at warm forming temperatures in the temperature range of 200–250°C. In case of 5xxx-series aluminium alloys, Lloyd [61] tested 5052, 5154 and 5083 Al-Mg alloys and observed that at initial stages of deformation the SRS has a positive value, but as the plastic strain continues, it gradually decreases. Also, Wagenhofer et al. [62] observed negative strain rate dependency for AA5086 alloy at QS strain rates ( $<0.36\text{s}^{-1}$ ). Moreover, Li and Ghosh [8] showed that by increasing strain rates up to  $1.5\text{s}^{-1}$ , the total elongation of different Al-Mg alloys (AA5754, AA5182+Mn and AA6111-T4) decreases. Also, Hadianfard et al. [12] observed a reduction in ultimate strength for AA5182 and AA5754 by increasing the strain rate from QS to  $1500\text{s}^{-1}$ . This reduction of ultimate strength and total elongation was measured to be 10.6% and 14% for AA5182, respectively. Hence, by increasing the strain, both AA5182 and AA5754 sheets soften and further deformation leads to more shear band formation [12]. But perhaps the most comprehensive

studies were carried out by Higashi et al. [63–65] and Mukai et al. [66–69]; they observed the same behaviour up to moderate strain rates (lower than  $1 \times 10^2 \text{s}^{-1}$ ) for different aluminium alloys [63], 5xxx-series containing different Mg concentrations [66] and different grain size [67, 68].

When the strain rate is increased an aluminium alloy which exhibits negative SRS requires lower flow stress to deform, in another words, it tends to soften with increasing strain rate. Therefore, once the deformation localizes in an area of the workpiece, it concentrates to the same region and hence the alloy exhibits low overall formability [10, 70]. This negative SRS not only provides conditions for further localization by reducing the flow stress in areas where stress is concentrated (localized areas). Hence, failure occurs rapidly and with little evidence of damage before final failure [57]. Consequently, the low SRS of Al-Mg alloys is the reason for their sudden failure after the onset of necking which was observed by project partners during the QS Marciniak tests [71].

The negative sensitivity to strain rate in 5xxx-series aluminium alloys is the result of interactions between solute atoms and the mobile dislocations and is associated with the occurrence of dynamic strain ageing (DSA). This phenomena is also associated with the Portevin-Le Chatelier (PLC) effect which can be seen as large serrations on the flow curve and the formation and propagations of Luders bands in the workpiece [72]. As a result of DSA, clusters of solute atoms resist the motion of dislocations [73, 74]. At QS strain rates, formation of large clusters is easier and hence they can resist the motion of dislocations which lead to an increase in strain hardening. However, at moderate strain rates (up to  $1 \text{s}^{-1}$ ) as discussed by Khan et al. [74] the effective size of clusters becomes smaller and they offer less resistance to the motion of dislocations. Higashi et al. [64] suggested another mechanism for this serrated flow using the periodic interaction of dislocations with solute atoms. Their TEM observations of AA5182 specimens revealed that at QS and moderate strain rates (below  $10^2 \text{s}^{-1}$ ), due to the rearrangement of dislocations (formation of network-like deformation bands), the density of dislocations decreases. Consequently, the material requires less applied stress to deform further when the strain rate increases [64].

The occurrence of serrated flow (due to DSA and PLC) was observed for many different Mg containing aluminium alloys in QS deformation. For example, Lademo et al. [75] observed this behaviour in Al-Zn-Mg and Al-Mg-Si alloys, Clausen et al. [76] observed serrated flow in AA5083, Bazarnik et al. [77] reported it for both AA5083 and AA5483 alloys and Picu et al. [73] observed it in AA5182. Moreover, Higashi et al. [63] observed that only Mg containing aluminium alloys (AA3004: 1.21%Mg, AA5182: 4.52%Mg, 7N01: 1.71%Mg) show negative strain rate sensitivity at moderate strain rates and AA3003, AA1050 only exhibit an increase in flow stress with increasing strain rates [63]. Similarly, Mukai et al. [67, 68] observed serrated flow due to the periodic interaction of mobile dislocations and Mg solute atoms in IN905XL aluminium alloy (containing 4wt% Mg). In other work, Mukai et al. [66] studied the flow behaviour of different Al-Mg alloys with different Mg concentrations ranging from 1.8 to 8.4 wt% and observed serrated flow in the strain range from  $10^{-3}$  to  $10^{-1}\text{s}^{-1}$  in all cases.

Since DSA is the result of interaction of rapidly diffusing solute atoms (Mg in 5xxx-series) with moving dislocations [62, 72] it is therefore temperature and strain-rate dependant; the effect of DSA can be diminished by increasing the strain rate.

As a result of formation of PLC bands, the necking strain of Al-Mg alloys are less than what Considère's criterion predicts [78]. Also, geometric inhomogeneity increases with propagation of PLC bands which contributes to decreasing the fracture strain and hence leads to lower formability of AA5xxx [75].

### **At moderate strain rates; minimum flow stress**

In several Al-Mg aluminium alloys the flow stress reduces to its minimum at moderate strain rates (between  $10^{-1}$  and  $10^3\text{s}^{-1}$ ) as shown in Fig. 2.7(a). Also, elongation and ductility decrease in this range of strain rates [66].

According to Dorward and Hasse [79] the decrease of elongation and ductility is due to adiabatic heating in specimens. At moderate strain rates a thermal gradient exists due to the transition of isothermal to adiabatic conditions and consequently ductility decreases. Mukai et al. [67, 68] also explained the reduced flow stress due to

the adiabatic temperature rise (adiabatic heating) which becomes more significant at moderate strain rates than the increase in stress due to strain rate effects.

It is significant that yield stress (0.2% proof stress) only shows a positive trend with strain rate and increases sharply at high-strain rates, as shown in Fig. 2.7(b).

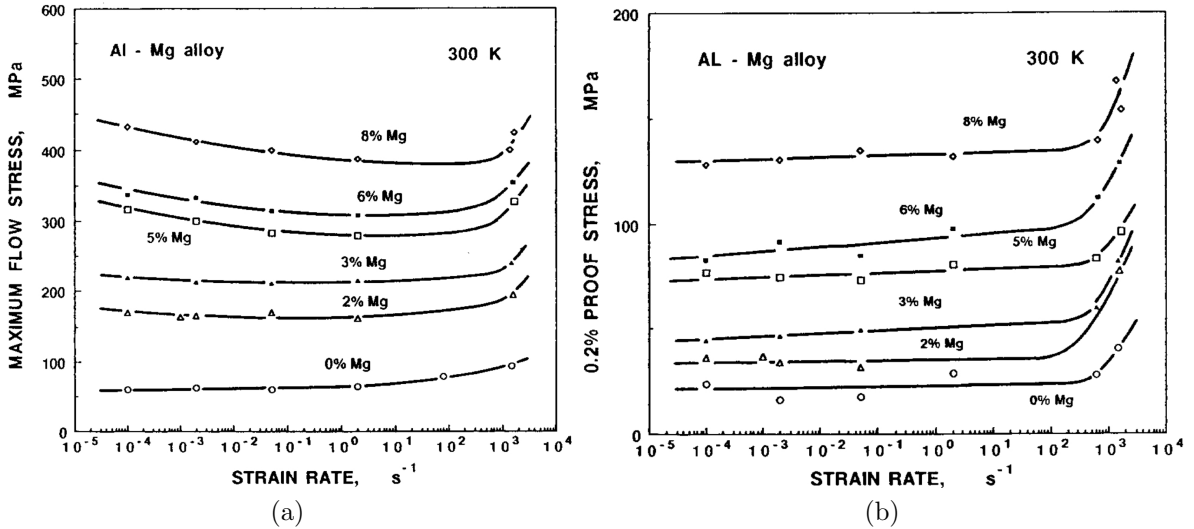


Figure 2.7: Changes of (a) maximum flow stress and (b) yield stress with strain rate for different Mg containing aluminium alloys [66].

### At High strain rates; positive SRS and increased elongation

Several researchers have shown that the flow stress of various aluminium alloys increases with strain rate, showing a positive SRS at high-strain rates (above  $10^3\text{s}^{-1}$ ). This positive SRS delays the onset of diffuse necking [80] and hence total elongation and formability, can be improved at high-strain rates. For instance, binary Al-Mg alloys show a positive dependency of elongation and flow stress on strain rate at high-strain rates ( $10^3\text{s}^{-1}$ ) as shown in Fig. 2.7. Similarly, Dorward et al. [79] observed the same trend for the ductility of AA2024 and AA7075 sheets (containing 1.4 and 2.5 wt% Mg) at strain rates above  $0.1\text{s}^{-1}$ . Mukai et al. [67] observed an increase in flow stress of Al-4Mg-1.5Li at 0.06 strain at the highest tested strain rates ( $10^3\text{s}^{-1}$ ). Sakino [81] observed a step increase in SRS of AA2017-O at strain rates greater than  $3 \times 10^3\text{s}^{-1}$ . Wagenhofer [62] also observed a positive SRS of AA5086 at strain rates



above  $1\text{s}^{-1}$ . And Hadianfard et al. [12] noticed a mild positive SRS for AA5182 and AA5754 at dynamic strain rates (above  $600\text{s}^{-1}$ ).

According to Mukai et al. [67], at high-strain rates, the strengthening mechanisms due to an increase in strain rate overcome the reduction in stress due to adiabatic heating and consequently, the flow stress of aluminium alloys tends to increase with strain rate in the high-strain rate domain. Dorward et al. [79] also noted that at high-strain rates, the hardening effects become dominant and hence the flow stress and elongation increase with increasing strain rates.

Mukai et al. [66], studied the changes in yield stress (0.2% proof stress) with strain rate and found that the yield stress is a weak function of strain rate in the strain rate range of  $10^{-4}$  to  $10^2\text{s}^{-1}$  where it remains almost linear with strain rate. However, As shown in Fig. 2.7(b) at higher strain rates (above  $10^2\text{s}^{-1}$ ) the 0.2% proof stress increases sharply with strain rate [66].

As a result of this increased flow stress, many researchers observed improved elongation in high-strain rate deformation. For example, Dorward and Hasse [79] measured almost 40% increase in normalized elongation from QS to  $100\text{s}^{-1}$  for AA2024-O and AA7075-O alloys, containing 1.4 and 2.5 wt% Mg, respectively. In case of 5xxx-series aluminium alloys, Clausen et al. [76] observed an increased elongation in AA5083 at strain rates above  $1\text{s}^{-1}$  and Smerd et al. [82] for AA5182 at relatively high-strain rate tests performed by modified split Hopkinson bar test. Mukai et al. observed a significant increase in total elongation for IN905XL [67] and for AA5056-O (contains 4.8 wt% Mg) [69] at high-strain rate ( $> 10^3\text{s}^{-1}$ ).

Figure 2.8 shows the changes of normalized failure elongation ( $r_e = \varepsilon/\varepsilon_f$ ) with strain rate for different aluminium alloys where  $\varepsilon_f$  is the elongation to failure at QS strain rate ( $10^{-3}\text{s}^{-1}$ ) [63]. It can be seen that by increasing the strain rate the ratio of elongation increases for most alloys (except 7N01) and by increasing the Mg content, this ratio increases more significantly. Based on this figure, AA5182-O would exhibit better response to high-strain rate deformation as compared to other studied aluminium alloys and this makes it a good candidate for high-strain rate deformation processes.

This increased elongation is mostly due to post-uniform elongation as the uniform

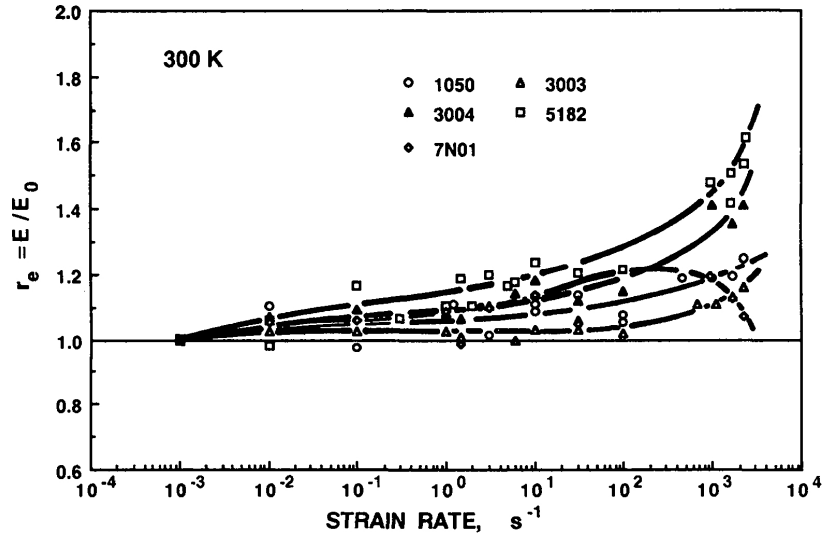


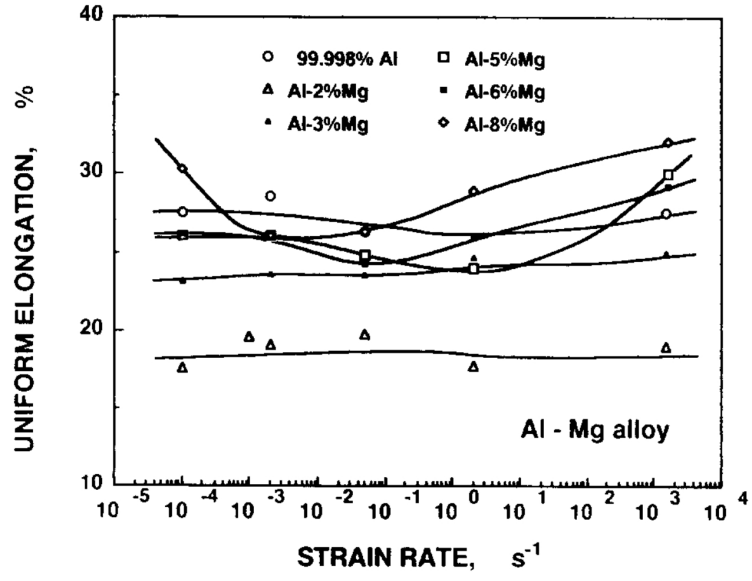
Figure 2.8: Changes of normalized failure elongation with strain rate for different aluminium alloys;  $E_0$  denotes the elongation to failure at QS strain rate [63].

elongation remains almost constant with increases in strain rate. Positive strain hardening in regions of localized strain is the main reason for enhanced post-uniform elongation [79]. This is true for many alloys including AA5454-O and AA5454-H34 as Lindholm et al. [83] indicated and also AA2024 and AA7075 as noted by Dorward and Hasse [79].

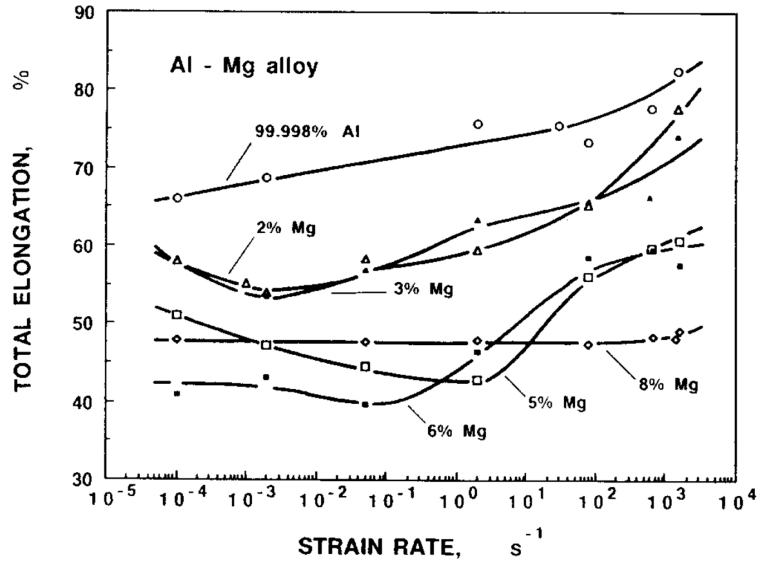
Figure 2.9 shows the variation of total and uniform elongation of different Al-Mg alloys. Obviously, for Mg contents of 5-6% (which is relatively close to AA5182) both elongations decrease at intermediate strain rates but increase at high-strain rates. However, it should be noted that in case of high Mg concentration alloys (more than 5%) even uniform elongation increases with increasing strain rate [66].

Higashi et al. [63, 64] showed that by increasing the strain rate in AA5182-O specimens, the elongation to failure increases and hence the failure is postponed. At QS strain rates ( $10^{-3}\text{s}^{-1}$ ) the material exhibited 30% elongation whereas it increased to more than 40% at strain rates above  $2 \times 10^3\text{s}^{-1}$ .

Higashi et al. [64] reported the variation of flow stress of AA5182-O at different strain values of 0.002, 0.05, 0.1, 0.15 and 0.20 [64]; their results are shown in Fig. 2.10. In the early stages of deformation ( $\varepsilon = 0.002$ ) the flow stress is almost independent of strain rate, but increases rapidly at high-strain rates (above  $10^2\text{s}^{-1}$ ). As the deforma-



(a)



(b)

Figure 2.9: Variation of (a) uniform and (b) total elongation with strain rate and magnesium content [66].

tion continues ( $\varepsilon > 0.05$ ) the flow stress decreases with increasing strain rate in the intermediate strain rate range (up to  $10^2\text{s}^{-1}$ ) and then increases again at high-strain rate, showing positive strain rate sensitivity [64].

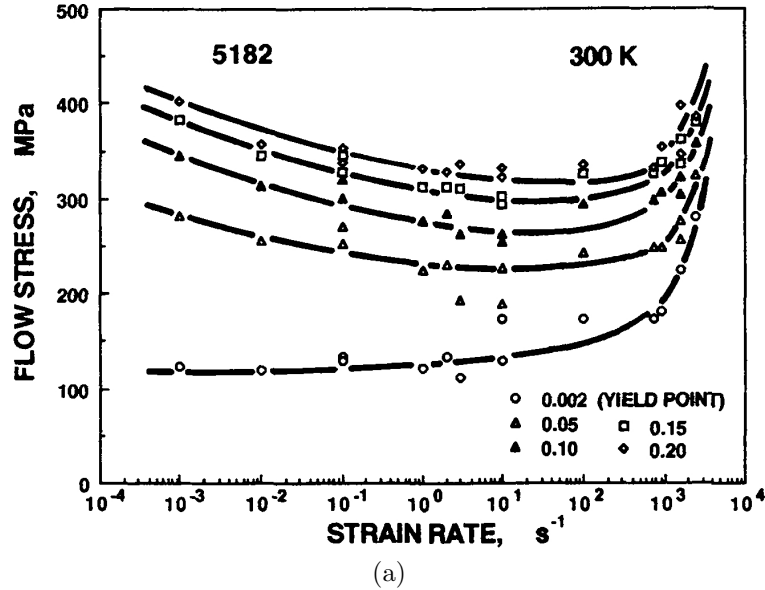


Figure 2.10: (a) variation of AA5182 flow stress with strain rates at different strain values [64].

Changes in material behaviour at high-strain rates were also observed by Gerdooei and Dariani [51]. They developed analytical FLDs over a wide range of strain rates from  $0.01$  (QS) to  $500\text{s}^{-1}$  (intermediate) and reported that the shape and position of the FLC changes with strain rate. The  $\text{FLD}_0$ , which represents the lowest limit strains in a plane strain mode of deformation, increases after a certain critical strain rate at any given  $C$  value (strain rate exponent in Johnson-Cook hardening function), strain hardening exponent ( $n$ ) or thermal softening exponent ( $m$ ) and is more sensitive to strain hardening exponent. For more information regarding Johnson-Cook equation and explanation, readers are referred to Section 2.4.1. The variation of  $\text{FLD}_0$  with these parameters is illustrated in Fig. 2.11.

Consequently, by increasing the strain rate beyond a certain critical level, the formability improves and localized necking is delayed. Gerdooei and Dariani reported that this increase in formability is due to inertial effects. As the density of material increases, inertial effects increase, especially at high accelerations. The stress in areas

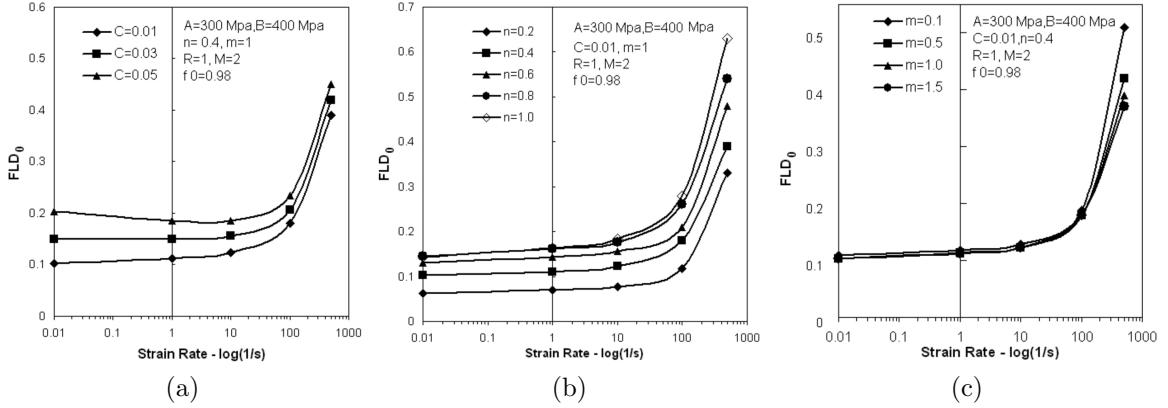


Figure 2.11: Variation of  $FLD_0$  with (a) J-C parameter constant  $C$ , (b) hardening exponent  $n$ , and (c) thermal softening exponent  $m$  [51].

of localized strain increases as a result of this inertial force and hence the deformation is distributed to the entire sheet and neck growth stabilize.

### 2.3.2 Inertial effect and importance of input energy

When the input voltage is increased in EHDF, the discharge energy increases and as a result the initial velocity of the sheet also increases. In fact, Balanethiram et al. [33, 43] explained that in order to achieve enhanced formability, the workpiece velocity must exceed a critical threshold. Golovashchenko et al. [28] also noticed that by increasing the discharge energy of EHF tests, the sheet material could safely deform to higher strains and hence the fracture strain increases with discharge energy. Figure 2.12(a) shows the changes of elongation with workpiece velocity for AA6061-T4 based on ring expansion and uniaxial tension results [33, 43]. Figure 2.12(b) shows a comparison of material hardness in QS testing conditions and in EHDF for different values of true thickness strain. Both AA6061-T4 and copper show a slight increase in hardness at high-strain rates. However, the increase is insignificant since at any given strain it is always less than 20%. As a result, Balanethiram et al. concluded that shock hardening could not contribute to the enhanced formability and the changes in strain rate sensitivity are not the cause of the increase in elongation. Instead, they discussed that the inertial effects have a more significant effect [33, 43].

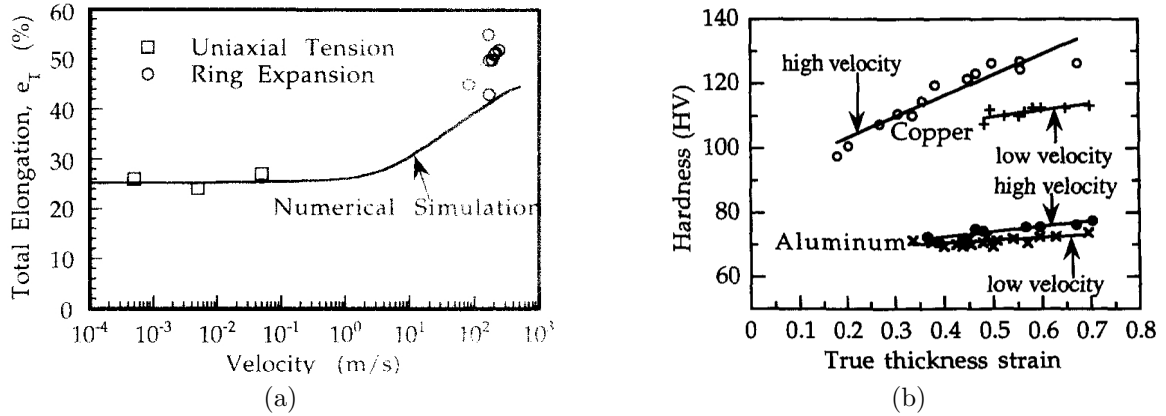


Figure 2.12: (a) Comparison of AA6061-T4 elongation in uniaxial and ring expansion tests [43] and (b) comparison of QS and EHDF Vicker's hardness for AA6061-T4 and a copper alloy [33].

After testing different materials at different input energy levels and studying their fracture behaviour, Golovashchenko et al. [28] concluded that at low energy levels, even in EHDF process, cracks occur in the apex region of conical specimens. Also, moderate increases in such input energy do not improve the occurrence of failure and only widens the initially formed cracks. This is basically a QS failure mode and hence the presence of the die, could not significantly improve the formability of the workpiece. However, once the input energy and the consequent pressure of the pulse reached a threshold velocity of the workpiece, the strain rate, and the hydrostatic pressure generated at the moment of impact against the die contributed to increase the level of safe strains that were achievable before the occurrence of any fracture [28]. Oliveira et al. [84] also reported that some AA5182 and AA5754 specimens formed with EMF fractured well before the cavity of the die could be completely filled which is likely due to insufficient pressure and energy of deformation. Moreover, Golovashchenko et al. [28] noticed that aluminium specimens showed greater formability enhancement in EHF compared to steel specimens using the same apparatus. In case of steel, much higher voltages are required in order to overcome the critical velocity of the sheet and observe formability enhancement as compared to aluminium.

The results of Balanethiram et al. [43] also show that inertial forces generated at high velocities (above  $5 \text{ ms}^{-1}$ ) can spread the deformation away from the localized areas

in specimens which contributes to increased post-uniform strain of 5% even in sheet metals with limited sensitivity to strain rate [43].

### **2.3.3 Die effects**

### **2.3.4 Effect of hydrostatic pressure and die**

The presence of a die in EHDF can result in the generation of significant hydrostatic stresses in the sheet upon impact with the die. According to Price [85] the presence of a state of triaxial tension promotes failure mechanisms in ductile materials such as void nucleation (also noted in Ref. [86]) and growth which are pressure-dependent mechanisms. Consequently, the existence of a superimposed hydrostatic pressure can prevent failure by suppressing void nucleation and growth in the deforming material [82]. According to French and Weinrich [87] strain localization in ductile materials can be changed from void nucleation and growth to localized shear by increasing the superimposed hydrostatic pressure. Also, Korbil and his co-workers [5] experimentally showed that the onset of localization of AA7075 in the tension is influenced by the hydrostatic pressure.

#### **Effect of die on void initiation and growth**

The interaction between the workpiece and the die has a significant effect on formability enhancement during high-strain rate forming processes. Imbert et al. [46] performed EMF on AA5754(1mm) and observed that during free forming (EMFF) formability improves for a narrow region on FLC whereas in the case of die forming (EMDF) specimens showed a wide range of strain path formability improvement as compared to QS deformation. They concluded that the die-sheet interaction causes a complex stress state which includes compressive hydrostatic stresses that can potentially suppress the damage that occurs during the deformation. Optical metallographic observations support this proposition as the EMFF specimens contained significantly more damage and localization as compared to EMDF specimens.

Moreover, Oliveira [84] also observed that the formability enhancement during EMFF of aluminium alloys was almost insignificant, which again supports the idea that tool-sheet interaction plays an important role in formability enhancement in high-strain rate forming. Dariani et al. [26] also noticed that formability of both AA6061-T6 and AISI 1045 steel sheets improved under the effect of die impact.

However, it is worth emphasizing that the presence of the die itself is not sufficient to improve formability. Golovashchenko et al. [28] observed that some specimens fail well before the sheet specimens fill the die cavity, especially when a high-apex angle die is used (40° conical die). Hence, in this case the failure should really be considered to occur in free-forming rather than die-forming conditions. Similarly, in the early stages of EHDF sheet specimens are formed into open space without the influence of any die-impact force. Therefore, the initial forming should be considered as free forming [28].

### **Effect of die on strain rate**

In many EHDF studies, the maximum strain rates were measured in areas close to the apex of the conical specimens and hence the presence of the die can significantly increase the strain rate and the material's corresponding response. For example, numerical simulation results from Golovashchenko et al. [28] shows peak strain rates up to  $20,000\text{s}^{-1}$  in EHDF whereas in EHFF strain rates of only  $6900\text{s}^{-1}$  were predicted. The reason is that the conical geometry of the die focuses the kinetic energy progressively into smaller area in the centre of the specimen and this increases the effective strain rate that is attained [28]. Golovashchenko et al. [28] also observed that the failure mode in EHFF specimens is very similar to failures observed in hydro-bulging tests carried out by Smith et al. [88] and concluded that without the presence of a die, the failure mode should be considered as QS even in EHFF.



## 2.4 Hardening properties of AA5182-O

### 2.4.1 Constitutive Equations

Constitutive equations describe a complex combination of strengthening and softening mechanisms that occur in sheet materials. Strengthening due to lattice resistance (Peierls-Nabarro barriers), dislocation interactions, interstitial and solute atoms, second phases and dispersoids and grain boundaries all tend to increase the flow stress of aluminium sheet materials. Also, thermally activated processes can result in softening of a material. Consequently, material flow stress is the product of both athermal and thermally activated phenomena [89]. The development of such constitutive equations is complex and beyond the scope of this work, nevertheless, many existing phenomenological constitutive equations provide a suitable mathematical relationship between the flow stress and the effective plastic strain, strain rate and temperature. Since it is necessary to use a hardening function during numerical simulations of the deformation of aluminium sheets, different phenomenological hardening equations discussed in this section are used and calibrated in Chapter 4. Several hardening equations are considered in this study based on their acceptance and wide usage in the simulation of the forming processes. Also, another aim of this research was to compare the outcome and accuracy of various constitutive equations so as to be able to perform accurate simulations of EHF as described in Chapter 5.

#### Power-law

Fields and Backofen [90] proposed one of the earliest phenomenological models, also known as the power law function, to determine the flow behaviour of different materials using Eq.2.2;

$$\sigma = K\varepsilon^n \dot{\varepsilon}^m \tag{2.2}$$

where  $\sigma$  is the effective true stress,  $\varepsilon$  is the effective true plastic strain and  $\dot{\varepsilon}$  is the true

strain rate. Also,  $K$ ,  $n$ , and  $m$  are the strength coefficient, strain hardening exponent and strain rate sensitivity exponent, respectively. The power law constitutive equation is of interest especially because of its material-mechanical justifications: in other words, power law parameters have been used extensively to determine, predict and investigate the properties of materials. As discussed, strain rate sensitivity ( $m$ ) is a critical parameter in formability analysis, in flow localization [91, 92], in dynamic material model [93, 94] and it is also linked to material deformation mechanisms such as dynamic strain ageing of aluminium alloys [61, 95, 96]. This equation might be used as is (i.e. in [97]) or a part of it as in warm or hot forming processes (i.e. in [98, 99]). Moreover, mobile dislocation velocity varies with the strain rate sensitivity exponent ( $m$ ) and the strain hardening exponent ( $n$ ) as explained by Dieter [100]. The implementation of the power law for simulation of forming processes with AA5182-O sheets are rare in the literature. Although this hardening function can be calibrated with high accuracy to the wide range of strains and strain rates tested in this study, its accuracy in numerical simulation is well below other constitutive equation used in Chapter 4.

### Johnson-Cook (JC)

Johnson and Cook [101] developed one of the most widely used constitutive hardening equations in metal forming literature. The JC constitutive equation is shown in Eq. 2.3;

$$\sigma = (A + B\varepsilon_p^n)(1 + C \ln \dot{\varepsilon}_p^*)(1 - T^{*m}) \quad (2.3a)$$

$$\dot{\varepsilon}_p^* = \frac{\dot{\varepsilon}}{\dot{\varepsilon}_0} \quad (2.3b)$$

$$T^* = \frac{T - T_{\text{room}}}{T_{\text{melt}} - T_{\text{room}}} \quad (2.3c)$$

where  $\varepsilon_p$  is the equivalent plastic strain,  $\dot{\varepsilon}_p^*$  is a dimensionless strain rate equal to

$\dot{\epsilon}_p/\dot{\epsilon}_0$ ,  $\dot{\epsilon}_0$  is the reference strain rate,  $T^{*m}$  is the homologous temperature equal to  $(T - T_{\text{room}})/(T_{\text{melt}} - T_{\text{room}})$  in Kelvin. In this study a reference strain rate ( $\dot{\epsilon}$ ) of  $1\text{s}^{-1}$  is used and the temperature effect was not considered since the mechanical tests and EHF experiments were performed at room temperature ( $T = T_{\text{room}}$ ) and consequently  $T^* = 0$ .

Table 2.3 presents the parameters in the JC equation calculated by Rohatgi [41] and Smerd [82] for AA5182 sheets. Rohatgi et al. [41] did not mention the rolling direction of the specimens and considered  $\dot{\epsilon}_0$  as  $1\text{s}^{-1}$  and carried out tensile tests on AA5182-O sheet with 1mm thickness at strain rates ranging from 1000 to  $2400\text{s}^{-1}$ . Smerd et al. [82] calculated these constants based on a non-linear regression procedure for AA5182-O sheets with 1.6mm thickness and tested in uniaxial tension in the rolling direction at different strain rates ranging from  $3.3 \times 10^{-3}$  to  $1.5 \times 10^3\text{s}^{-1}$ . Knowing that the AA5182 alloy tested in this research has different alloying concentrations and thickness (and hence different size and distributions of second phase particles broken during cold rolling) an attempt was made to recalculate these parameters for JC equations so that more accurate results could be achieved in numerical simulations of EHF (see Chapter 5).

Table 2.3: Constants of Johnson-Cook constitutive equation for AA5182 sheet calculated by different sources.

	$A(\text{MPa})$	$B(\text{MPa})$	$n$	$C$	$m$	Ref.
Estimate	109	522	0.4	0.0012	3.19	[41]
Estimate	106.737	569.120	0.485	-0.001	3.261	[82]
95% lower	96.077	554.512	0.450	-0.02	3.088	[82]
95% upper	117.398	583.728	0.519	0	3.433	[82]

### **Khan-Huang-Liang (KHL)**

This constitutive equation was first introduced by Khan and his co-workers in 1999 [102] for BCC materials and then further developed for Ti-6Al-4V [103, 104] and AA5754 [105]

as:

$$\sigma = \left( A + B \left[ 1 - \frac{\ln(\dot{\varepsilon}_p)}{\ln(D_0^p)} \right]^{n_1} \varepsilon_p^{n_0} \right) \left( \frac{\dot{\varepsilon}_p}{\dot{\varepsilon}^*} \right)^m \left( \frac{T_m - T}{T_m - T_{\text{ref}}} \right)^\beta \quad (2.4)$$

where  $D_p = 10^6$ , and the reference strain rate ( $\dot{\varepsilon}^*$ ) is considered to be one. In case of AA5182, the parameters were calculated for QS range ( $10^{-4}$  to  $1\text{s}^{-1}$ ) but were not reported in Ref. [74].

### Modified Voce

The original Voce hardening function [106] is one of the most convenient equations used to predict the flow behaviour of different materials [107, 108]. It is inherently simple and shows remarkable fitting performance for many different materials including aluminium alloys [109]. However, the Voce hardening function does not consider the effect of strain rate on deformation behaviour in its original form. In order to take both strain and strain rate sensitivity into account, it is possible to combine the Voce strain hardening function with a strain rate hardening function in a multiplicative manner. Hence, two multiplicative methods were used and the Voce equation was combined with a Power-law or with a Logarithmic strain rate expression. The latter was proposed by Rahmaan et al. [110] and showed reasonable accuracy at different strain rates (see Chapter 4. These modified Voce equations, Voce-Power law (VP) and Voce-Logarithmic (VL) are expressed in Eq. 2.5.

$$\sigma = \left[ B - (B - A) \left( \exp(-m_1 \varepsilon) \right) \right] \times \zeta(\dot{\varepsilon}) \quad (2.5a)$$

$$\zeta_{VP}(\dot{\varepsilon}) = k(\dot{\varepsilon})^{m_2} \quad (2.5b)$$

$$\zeta_{VL}(\dot{\varepsilon}) = \left[ C \ln(\dot{\varepsilon}) + (1 + \dot{\varepsilon})^D \right] \quad (2.5c)$$

where  $A$ ,  $B$ ,  $m_1$ ,  $K$ ,  $m_2$ ,  $C$  and  $D$  are material constants to be calculated for each

testing condition. It is noteworthy that for JC, KHL and VP equations,  $A$  and  $B$  ideally represent the yield and ultimate true stress of the material, but none of the calculated values found in the literature correlated exactly with the experimental values. It is worth noting that the early attempts made to calculate these constants, showed that the power law multiplicative function (Eq.2.5(a) and (b)) exhibit less accuracy at high-strain rates when compared to Voce-Logarithmic function (Eq.2.5(a) and (c)). It can be noted that in the VP function the  $m_2$  parameter can only increase or decrease the flow stress with increased strain rate since it will have either a positive or negative value. However, in the VL equation, since  $C$  and  $D$  constants are assigned to logarithmic and exponential terms, adjusting them can lead to positive or negative strain rate sensitivity of flow stress. For this reason it is expected that the VL function generally leads to better results.

### 2.4.2 Genetic Algorithm (GA)

In this work and in Chapter 4 Genetic Algorithm (GA) optimization method is used to calculate constants of phenomenological hardening functions. Since the 1960s, John Holland [111] worked on artificial system which has properties similar to natural systems and published the idea of GA in 1975. Since then, GA has been widely used in scientific studies as a successful tool for search and optimization problems [112]. GA, unlike most conventional optimization techniques, operates on a whole population of data points; during its search, GA uses the populations of solutions rather than a single solution. This, improves the robustness of GA and gives it the capability to reach the global optimum while avoiding local optima [112].

The basics of GA and its terminology are summarized below;

The first step is to define a *fitness function* which will be *optimized* during the GA process. In case of hardening functions, the fitness function which should be minimized is the absolute difference between the experimental flow stress and that predicted by the constitutive equation.

GA process starts with an initial population of chromosomes which should be large enough to contain a wide diversity of the gene pool so that the solution can be

generated within. This initial and total population should be defined randomly for the GA optimization within the predefined boundary conditions (BC). The main limitation of GA comes from the determination of an appropriate BC; if the BC is extensively wide, the GA can converge to the optima but with a high computational cost.

Once the GA process starts with the initial population, in each iteration it follows a sequence of selection, reproduction, evaluation and replacement processes. Fig. 2.13 shows the relation of these steps in each GA iteration.

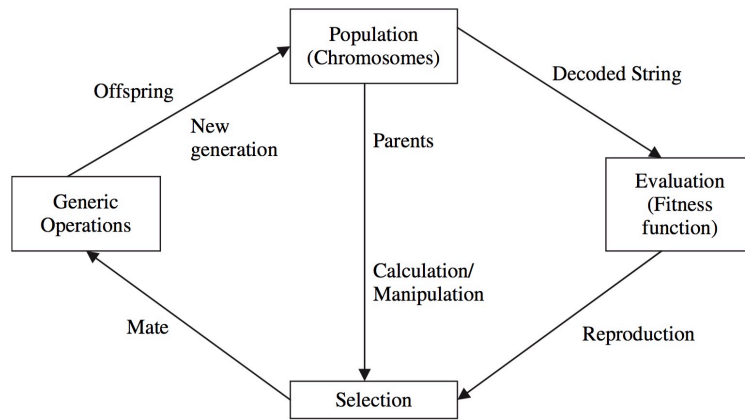


Figure 2.13: GA Process [112].

During the selection stage, individuals are selected randomly to reproduce new generations. The randomization is biased toward the relative fitness of individuals so that better individuals are often chosen rather than poor ones.

Reproduction is the next step which contains *crossover* and *mutation*. A crossover function is used to create new offspring from the parent population as without it offspring would be the exact copy of the parents. This stage is critical to GA process as it allows characteristics from parents to be assorted. A simple function to crossover new populations is to convert all parameters into binary data and exchange a different portion of zeros and ones between each parent. However, it is important to maintain the genetic chromosome and create diversity of answers so that the result converges to the minimum value more efficiently. A mutation function is responsible for providing diversity by creating new genomes and offspring from the previous population. The mutation function facilitates exploring the search space within the BC more quickly.

The next stage is to evaluate the fitness of the newly made generation. To maintain population size, individuals with higher difference with the optima will be *eliminated*. Generating populations is continued until the total *number of generations* is reached or when the population converges toward the optimal solution. This is usually determined when the difference between optimal value of a certain amount of generations is less than a predefined value (e.g.  $10^{-6}$  within 50 generation intervals).

It is important that GA exhibit reasonable reliability and ease to discover global optima within a wide BC. Also, mainly due to mutation process, unlike many other optimization processes, GA resists being trapped in local optima. The process can be easily modified to be used in different problems as long as the evaluated function can be defined. The search space and input data can be large and contain noisy data. Interested readers are referred to Ref. [112] for further details on the usage of GA.

In view of its versatility, GA method was used to calculate the constants of each phenomenological hardening function discussed in section 2.4.1 and is presented in Chapter 4. In short, it is found that the constants calculated using GA optimization give more accurate results than regression analysis when compared with experimental results.

### 2.4.3 Artificial Neural Network (ANN)

Although constitutive equations represent non-linear relations between mechanical parameters ( $\sigma$ ,  $\varepsilon$ ,  $\dot{\varepsilon}$ ,  $T$ , rolling direction and etc.), they are usually limited to specific deformation mechanisms and break down when the deformation is extended beyond the domain for which they were determined. As a result, to represent data over large domains (i.e. large strain rate or temperature ranges), different equation parameters and separate equations are required.

In order to overcome the limitations of mathematical problems, artificial neural network (ANN) was introduced and showed very good performance in different applications. In ANNs, rather than relying on predetermined assumptions (i.e. constitutive equations) data is used to form the model. The idea was derived from simplified biological neurons, Fig. 2.14(a). An ANN is a computational model of neural pro-

cessing or logical structure with multiprocessing elements (Fig. 2.14(b)), which are linked through interconnection weights. The knowledge is presented by the interconnection weights which should be adjusted during the learning phase. This makes ANNs capable of handling complex and mathematically unresolvable relations between parameters and a suitable tool to be used in a wide range of applications. In metal forming, many researchers utilized ANN to predict the forming behaviour of sheet metals [113–118] either solely, or in combination with finite element simulations [119, 120].

The most important benefit of neural networks is realized when a complete understanding of the physical mechanisms is very difficult, or even impossible to acquire [113]. In case of hardening properties of aluminium alloys, as explained in Section 2.3.1, AA5182-O sheet alloys will behave differently at QS, medium and high-strain rates. Consequently, it is expected that the accuracy of most constitutive equations, where one parameter usually dictates the sensitivity to increased strain rate, would be low. Hence, an attempt was made in this study to use ANN to describe material behaviour rather than relying on pre-defined mathematical equations, and to implement it into finite element simulation of the EHF process.



Figure 2.14: NN Basics & Process [121].



## 2.4.4 Basics of neural networks

The first step in designing an ANN is to decide on the network architecture. There are different classifications for neural networks but the one used mostly in engineering field is a fully-connected, layered feed-forward neural network (FFNN). As shown in Fig. 2.15, in FFNNs, layers of the network are connected in feed-forward manner without any feed-back between them. Also, neurons within each layer have no connection between them. The term "fully connected" in FFNN denotes that each node in any layer has a connection to every node in its immediate adjacent layer, as shown in Fig. 2.15 [121].

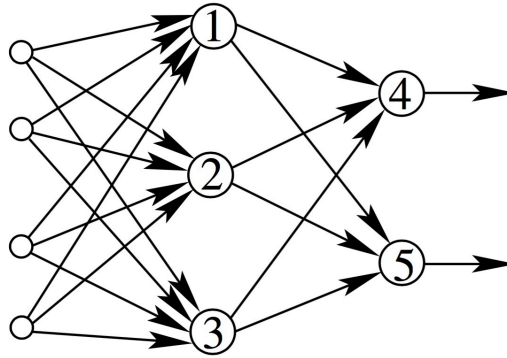


Figure 2.15: Feed Forward NN Basics [121].

When the network structure, which contains a number of layers, a number of neurons in each layer and a transfer function between each layer is determined, the network is ready to be trained. During the supervised training stage the input variables are supplied and the resultant output is compared with the desired output. The network then adjusts the interconnection weights between layers to increase its performance. This is done by the training algorithm. At each iteration during the training stage, called *epoch*, all training examples are presented to the network once and their outcomes are calculated. This process is repeated until the network performs well on the training set. To control and terminate the learning process, a performance criterion is needed which is usually the mean squared error (MSE). After training, the network can be introduced to some new input and reasonable output is produced.

Interested readers are referred to Ref. [121] for further details and different architec-

tures of ANNs.

### 2.4.5 The ANN used for AA5182

In order to implement NN to predict the flow behaviour of AA5182-O sheets, the input parameters of the network was defined as the orientation to the rolling direction [0, 45, 90°], strain rate [0.001, 0.1, 1, 10, 100, 1000s<sup>-1</sup>], and true plastic strain obtained from tensile tests carried out by project partners at the University of Waterloo [110]. The output of the network was the flow stress of the material. Many different structures of FFNN were used and compared with each other and two optimum cases were chosen for further study: a simplified NN called NN1 and a more complex one named NN2. Figure 2.16 illustrates a brief overview of the neural network structure used in Chapter 4.

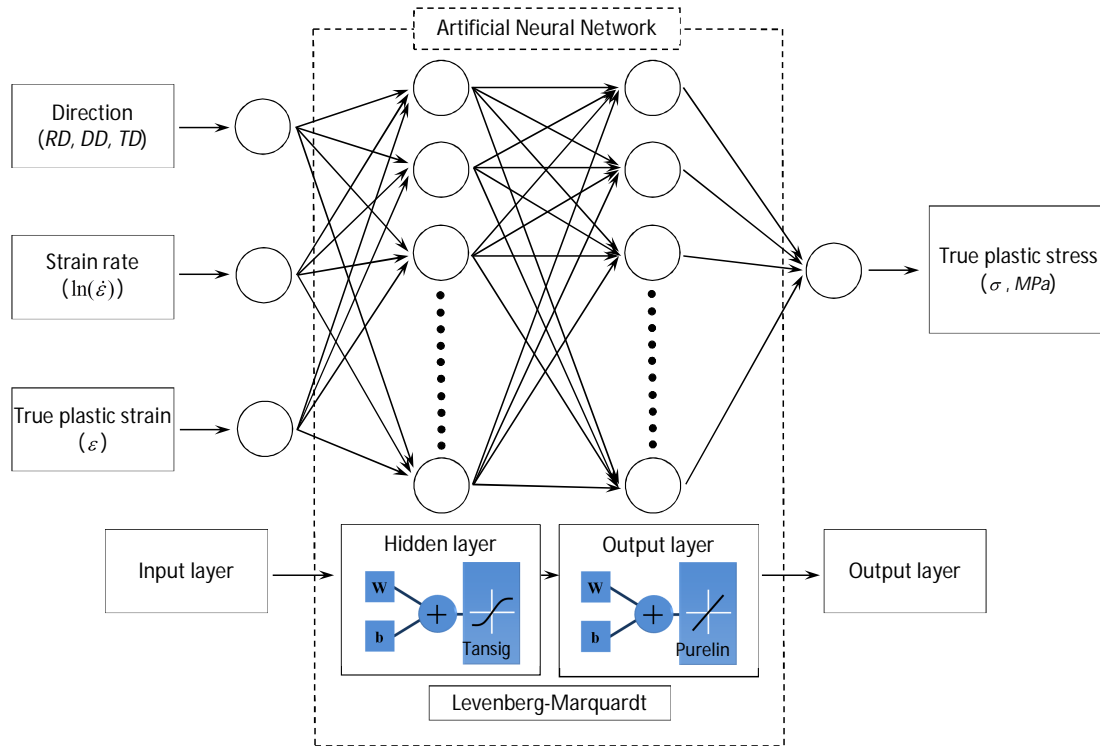


Figure 2.16: Overview of neural network structure used in this study

The structure of the network consists of a symmetric sigmoid transfer function capable of producing outputs in the range of -1 to +1 and a linear transfer function to scale

outputs up or down. Eq. 2.6 shows the matrix form of the NN1 model used;

$$S = \begin{bmatrix} w2_1 & w2_1 & \dots & w2_s \end{bmatrix} \cdot \text{tansig} \left( \begin{bmatrix} w1_{11} & w1_{12} & w1_{13} \\ w1_{21} & w1_{22} & w1_{23} \\ \dots & \dots & \dots \\ w1_{s1} & w1_{s2} & w1_{s3} \end{bmatrix} \times \begin{bmatrix} I_1 \\ I_2 \\ I_3 \end{bmatrix} + \begin{bmatrix} b1_1 \\ b1_2 \\ \dots \\ b1_s \end{bmatrix} \right) + b_2 \quad (2.6)$$

where  $I_1$  to  $I_3$  are normalized values of the angle to the rolling direction, strain rate in logarithmic scale and strain and  $S$  is the normalized stress calculated based on input weights and biases. Data were normalized using  $2 \times \frac{x-x_{\min}}{x_{\max}-x_{\min}} - 1$  and *tansig* of a parameter ( $x$ ) is calculated from Eq.2.7;

$$\text{tansig}(x) = \frac{2}{1 + e^{-2x}} - 1 \quad (2.7)$$

Backpropagation training method was used according to the Levenberg–Marquardt [122] (LM) algorithm; LM was shown to be very successful in many engineering applications and is the training algorithm that converges the fastest. The other algorithm that was used to train the complex network (NN2) was the Bayesian training algorithm. The Bayesian framework was developed by MacKay [123, 124] and used successfully to train many neural networks [125]; in the Bayesian algorithm, weights and biases are updated according to LM optimization.

More details on the structure of NN used are discussed in Chapter 4.

## 2.5 Fracture Mechanism of AA5182

Although material composition (alloying elements and second phases), microstructure, strain rate and temperature have a significant influence on the failure mechanisms of aluminium alloys [12], in general, the damage of ductile materials includes void nucleation and propagation [86]. Interaction of shear bands and barriers, coalescence of voids and grain boundary sliding are the most common void nucleation mechanisms for metals which are shown schematically in Fig. 2.17 [86]. Since in this study the EHF and QS experiments were carried out at room temperature, the occurrence of

grain boundary sliding (Fig. 2.17(c)) is unlikely to be a dominant failure mechanism.

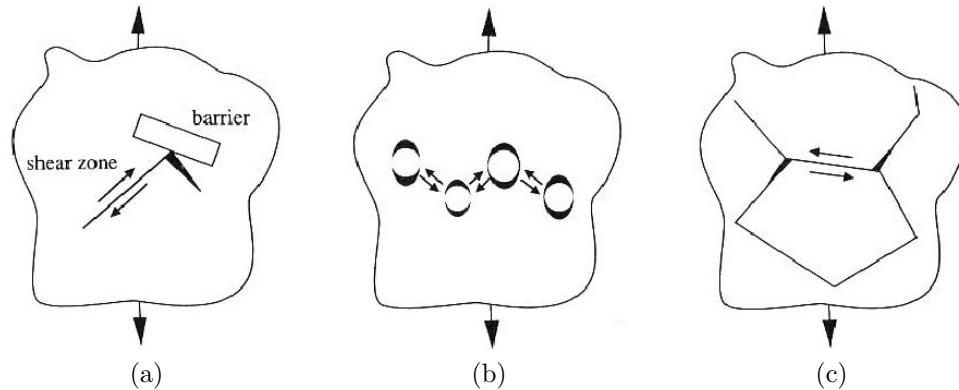


Figure 2.17: Void nucleation by (a) plastic deformation (interaction of shear with a barrier), (b) coalescence of cavities around hard particles in a soft matrix, and (c) grain boundary sliding at high temperature [86].

### 2.5.1 Localized Shear Bands; at QS strain rates

At QS strain rates, many studies have shown that aluminium alloys fail as a result of shear band formation prior to necking. Lademo et al. [75] observed this phenomenon for AlZnMg alloys (AA7xxx and AA6xxx) and Pedersen et al. [126] observed this in AA7xxx series alloys.

According to Korbil et al. [5], dynamic recovery mechanisms are due to the cooperative motion of unpinned dislocations which result in localized softening and are responsible for the occurrence of shear localization in Al-Mg alloys [5].

Once formed, these shear bands are preferential locations for void nucleation especially because of the large strains present in shear bands. Carlson et al. [127] estimated that in QS deformation of AA5182 alloys, once the necking is formed due to shear bands and the related thermal softening, the local strain rate increases by a factor of 1000 and this may result in a 20MPa reduction in flow stress. They also concluded that the softening process is influenced much more by negative strain rate sensitivity than by the rise in temperature due to localized adiabatic heating [127].

Spencer [9] showed that the failure of notched AA5754 tensile specimens does not mainly involve nucleation, growth and linkage of voids since there is insignificant

damage prior to fracture. Also, rapid failure occurs immediately after the strain reaches the failure strain of notched specimen. According to Hadianfard et al. [12], in QS strain rates, the competition between strain hardening and thermal softening mechanisms governs the shear fracture. During QS experiments of AA5182 and AA5754, localization occurred in form of intense shear bands before the final fracture; as shown in Fig. 2.18(a). Highly damaged areas are localized inside these shear bands or within a short distance from these shear bands, as shown in Fig. 2.18(b) [12].

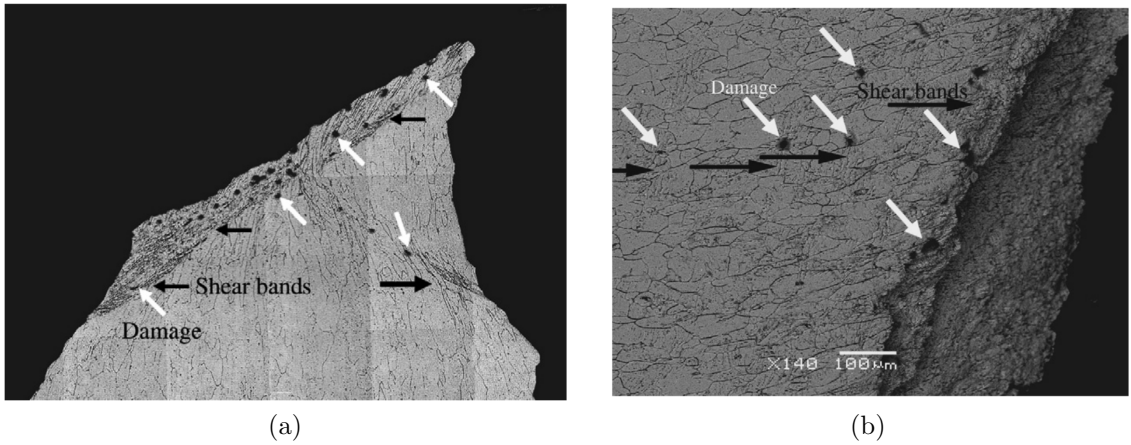


Figure 2.18: (a) Occurrence of shear bands in AA5754 before damage, and (b) damage on shear bands in AA5182 [12].

Hadianfard et al. [12] concluded that in QS conditions, strain localization occurs by shear band formation which leads to damage development and final failure. They also observed that large particles have more tendency to cause damage as compared to smaller ones.

According to Voyiadjis [128] at low strain rates, dislocation motion suppresses local stress concentration zones (areas where micro-defects could lead to void nucleation), and as a result the controlling factor for failure is plastic deformation. However, at moderate strain rates, since more dislocations become immobilized, the local stress increases and becomes sufficient to nucleate micro-cracks, voids or shear bands from pre-existing weak spots such as inclusions, second-phase particles or grain boundaries.

## 2.5.2 Void Nucleation, Growth and Coalescence; High strain rates

Void nucleation, growth and coalescence are the main failure mechanisms in AA5182 at high-strain rate. At high-strain rates ranges, if any shear localization is observed, it appears to be the result of void nucleation from inhomogenities, growth and coalescence and hence shear localization effect on final failure is insignificant compared to void nucleation mechanism [12].

Worswick et al. [80] observed both necking and void coalescence in necked AA5182 specimens deformed at dynamic strain rates. They concluded that damage mechanisms play a more important role at high-strain rates and damage intensity increases with increasing strain rate where deeper necking is observed prior to fracture under high strain loadings [80]. Hadianfard et al. [12] also confirms that most of the damage occurred outside the shear bands in high-strain rate forming and were associated with second phase particles. They concluded that just before localization of deformation, the dominant failure mode is based on void nucleation around second phase particles, growth and coalescence. By increasing strain rates, the average size of damaged particles decreases (in contrast with QS regimes). Hence, the critical localized strain necessary for failure decreases with increasing strain rate.

However, according to Mukai et al. [66] who investigated fracture mechanisms of different Al-Mg alloys using tensile tests in a strain rate range of  $10^{-4}$  to  $2 \times 10^3 \text{s}^{-1}$ , the main failure mechanism for Al-Mg alloys is void nucleation, growth and coalescence. Mukai et al. [66] indicated that the main difference between fracture surfaces in specimens deformed at QS and high-strain rates is that at high-strain rates dimples are larger and deeper compared to those observed in specimens that fractured at QS strain rates. Also, the specimens deformed at high-strain rate showed enhanced elongation, as compared to QS due to the change in void growth mechanisms [66].

## Void nucleation

Nucleation of voids in metals mostly occurs at or around micro-structural inhomogeneities. Pre-existing flaws such as voids or cracks, second-phase particles and inclusions, grain boundaries and subgrains are typical nucleation sites [129].

Decohesion of the particle-matrix interface, fracture of brittle particles, or shear deformation are possible mechanisms for the nucleation of voids and are illustrated schematically in Fig. 2.19. According to Hull [86], the first two mechanisms shown in Fig.2.19(a) and (b) mostly lead to spherical and ellipsoidal voids whereas the last one (Fig. 2.19(c)) will result in parabola-shaped dimples on the fracture surface.

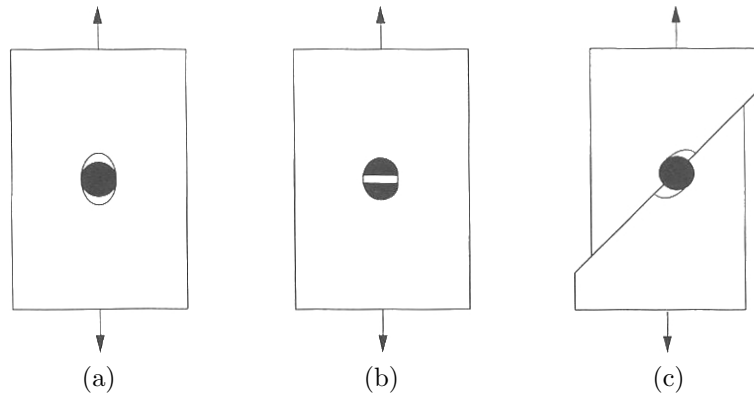


Figure 2.19: Nucleation of voids around inclusions by (a) matrix decohesion, (b) fracture of brittle particles, and (c) shear deformation [86].

Intermetallic particles have a significant influence on the mechanical behaviour and formability of aluminium alloys. The existence of precipitates and inclusions may cause micro-defects (micro-voids or micro-cracks) during the forming process which may lead to the final failure [20]. White skeletal or plate shaped iron-bearing particles (i.e.  $\text{Al}_6(\text{Fe},\text{Mn})$ ) and dark skeletal  $\text{Mg}_2\text{Si}$  phases reside at grain boundaries and are considered as primary particles in 5xxx-series aluminium alloys [130]. A small fraction of particles are also  $\text{Al}_8\text{Mg}_5$  particles [131]. Existence of such heterogeneous particles and inclusions leads to strain localization in AA5182 and AA5754 alloys [132].

Li and his co-workers [130, 133] performed several microstructural analyses on as-cast AA5182 (before cold rolling) and after different heat treatment conditions. They found that the dominant iron-bearing primary particles are not simply  $\text{Al}_6(\text{Fe},\text{Mn})$  particles

but instead the ratio of Al/(Fe,Mn) is between 4.0-4.4 and hence they named these particles  $Al_m(Fe,Mn)$  particles [130]. They also concluded that  $Al_m(Fe,Mn)$  particles transform to  $Al_3(Fe,Mn)$  by a eutectoid process during heat treatment of as-cast ingots at 520 or 470°C which is believed to be beneficial for further forming as the latter particles break up from large primary particles more easily [133]. Finally, as shown in Fig. 2.20,  $Al_3(Fe,Mn)$  particles have a long rod-like shape, whereas  $Al_m(Fe,Mn)$  particles have a skeletal shape.

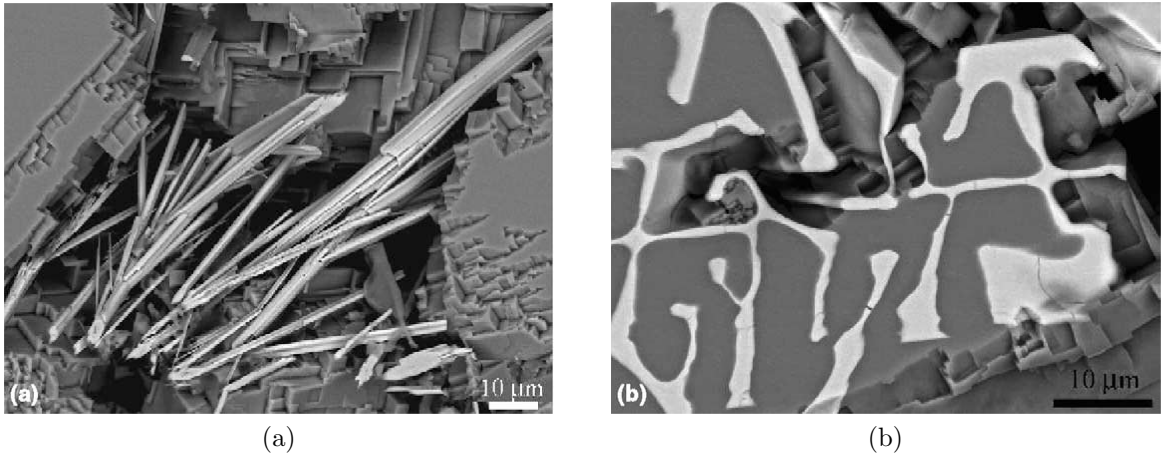


Figure 2.20: (a)  $Al_3(Fe,Mn)$  and (b)  $Al_m(Fe,Mn)$  particles observed in as casted and heat treated AA5182 [130].

### Void Growth; equi-axed and parabola

The most common void growth mechanisms in metals are in either equiaxed or parabola-shaped dimples. The growth of equiaxed voids usually occurs when the deformation is uniform in the sample and parabola-shaped voids are due to shear deformation or to the separation at a major crack tip [86]. Fig. 2.21(a) represents the mechanism of void growth in case of uniform deformation supposing that all voids nucleate and grow at the same stress and rate. The final fracture surface shows an array of equiaxed and matching dimples with heterogeneities inside them. However, in case of voids nucleated during shear deformation (i.e. shear bands) cavities are elongated at an angle of 45° to the applied stress which is the direction of the shear bands [86]. This will lead to parabola-shaped dimples on the fracture surface, as



shown in Fig. 2.21(b). It is important to note that large voids grow more preferably and faster as compared to small voids so they cause more damage [66, 86].

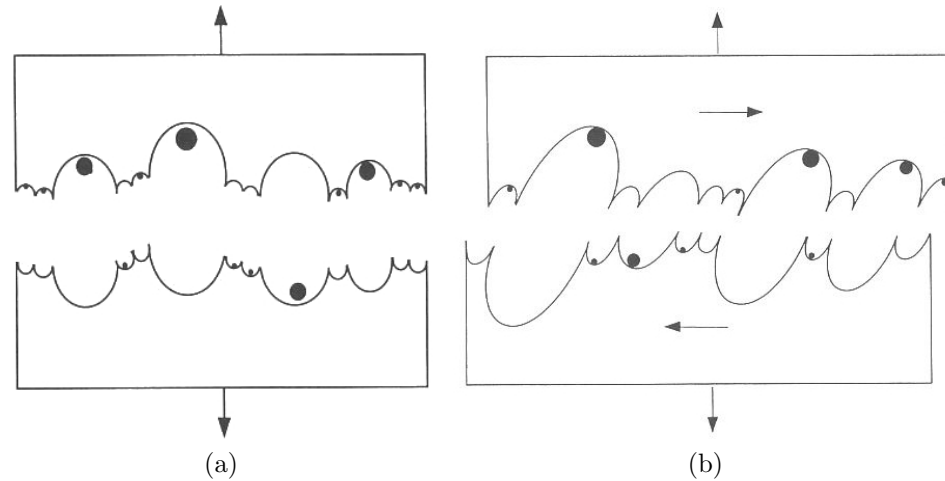


Figure 2.21: (a) Mode 1: schematic of equiaxed void growth, (b) Mode 2: parabola-shaped dimples in shear deformation areas [86].

## 2.6 References

- [1] I. J. Polmear, *Light Alloys From Traditional Alloys to Nanocrystals*. Oxford: Butterworth-Heinemann-Elsevier, 2006.
- [2] D. V. Nieuwerburgh, “Aluminium Sheet Developments for current and future BIW concepts,” tech. rep., 2011.
- [3] C. N. Panagopoulos and E. P. Georgiou, “Cold rolling and lubricated wear of 5083 aluminium alloy,” *Materials & Design*, vol. 31, no. 3, pp. 1050–1055, 2010.
- [4] Q. Jun and E. M. Taleff, “Superplasticity-like creep behavior of coarse grained ternary Al alloys,” *Transactions of Nonferrous Metals Society of China*, vol. 20, p. 564571, 2010.
- [5] A. Korbøl, J. Embury, M. Hatherly, P. Martin, and H. Erbsloh, “Microstructural aspects of strain localization in Al-Mg alloys,” *Acta Metallurgica*, vol. 34, no. 10, pp. 1999–2009, 1986.
- [6] Z. Horita and T. G. Langdon, “The creep behavior of a commercial Al-5%Mg-0.25%Fe (5083) alloy,” in *Deformation of Multi-Phase and Particle Containing Materials*, (Roskilde, Denmark), pp. 307–312, 1983.
- [7] P. Kazanowski, “Forming of Aluminum Alloys,” in *Metalworking: Sheet Forming*, pp. 583–599, ASM Handbook, ASM International, 2006.
- [8] D. Li and A. K. Ghosh, “Tensile deformation behavior of aluminum alloys at warm forming temperatures,” *Materials Science and Engineering: A*, vol. 352, pp. 279–286, jul 2003.
- [9] K. R. Spencer, *Evolution of fracture in an automotive aluminum alloy under plane strain tension*. PhD thesis, University of Waterloo, 2000.

- [10] D. Zdravecky, *Formability and Failure of Automotive Sheet Material AA5754*. Msc, McMaster University, 2007.
- [11] R. Kaibyshev, F. Musin, E. Avtokratova, and Y. Motohashi, “Deformation behavior of a modified 5083 aluminum alloy,” *Materials Science and Engineering a-Structural Materials Properties Microstructure and Processing*, vol. 392, no. 1-2, pp. 373–379, 2005.
- [12] M. Hadianfard, R. Smerd, S. Winkler, and M. J. Worswick, “Effects of strain rate on mechanical properties and failure mechanism of structural Al–Mg alloys,” *Materials Science and . . .*, vol. 492, pp. 283–292, sep 2008.
- [13] J. Li, *Characterization of post-annealing mechanical behavior of preformed aluminum alloy 5182-O*. Phd thesis, University of Michigan, 2011.
- [14] N. Abedrabbo, F. Pourboghrat, and J. Carsley, “Forming of AA5182-O and AA5754-O at elevated temperatures using coupled thermo-mechanical finite element models,” *International Journal of Plasticity*, vol. 23, pp. 841–875, may 2007.
- [15] E. Hsu, J. E. J. E. J. E. Carsley, and R. Verma, “Development of forming limit diagrams of aluminum and magnesium sheet alloys at elevated temperatures,” *Journal of Materials Engineering and . . .*, vol. 17, pp. 288–296, jan 2008.
- [16] J.-K. Chang, K. Takata, K. Ichitani, and E. M. Taleff, “Abnormal Grain Growth and Recrystallization in Al-Mg Alloy AA5182 Following Hot Deformation,” *Metallurgical and Materials Transactions A*, vol. 41, pp. 1942–1953, may 2010.
- [17] K. Kim, D. Kim, S. Choi, K. Chung, K. Shin, F. Barlat, K. Oh, and J. Youn, “Formability of AA5182/polypropylene/AA5182 sandwich sheets,” *Journal of Materials Processing Technology*, vol. 139, pp. 1–7, aug 2003.
- [18] J. Li, W. C. Liu, T. Zhai, and E. Kenik, “Comparison of recrystallization texture in cold-rolled continuous cast AA5083 and 5182 aluminum alloys,” *Scripta Materialia*, vol. 52, pp. 163–168, feb 2005.
- [19] B. M. Dariani and H. D. Azodi, “Finding the optimum Hill index in the determination of the forming limit diagram,” *Proceedings of the Institution of Mechanical Engineers, Part B: Journal of Engineering Manufacture*, vol. 217, pp. 1677–1683, jan 2003.
- [20] M. Brunet, F. Morestin, and H. Walter-Leberre, “Failure analysis of anisotropic sheet-metals using a non-local plastic damage model,” *Journal of Materials Processing Technology*, vol. 170, pp. 457–470, dec 2005.
- [21] P. D. Wu, M. Jain, J. Savoie, S. MacEwen, P. Tugcu, and K. W. Neale, “Evaluation of anisotropic yield functions for aluminum sheets,” *International Journal of Plasticity*, vol. 19, pp. 121–138, jan 2003.
- [22] J. Li, J. E. Carsley, T. B. Stoughton, L. G. Hector, and S. J. Hu, “Forming limit analysis for two-stage forming of 5182-O aluminum sheet with intermediate annealing,” *International Journal of Plasticity*, vol. 45, pp. 21–43, jun 2013.
- [23] C. Maris, “Experimental determination of the forming limits of DP600 and AA5182 sheets in electrohydraulic free forming,” Master’s thesis, Windsor, 2014.
- [24] CanmetMATERIALS, “Internal communications,” tech. rep., 2014.
- [25] J. Li, W. C. Liu, H. Yuan, and Y. K. Gao, “Comparison of earing behavior between continuous cast and direct chill cast AA 5182 aluminum alloys during cold rolling and annealing,” *Journal of Materials Processing Technology*, vol. 210, pp. 2007–2015, nov 2010.
- [26] B. M. Dariani, G. H. Liaghat, and M. Gerdooei, “Experimental investigation of sheet metal formability under various strain rates,” *Proceedings of the Institution of Mechan-*

- ical Engineers, Part B: Journal of Engineering Manufacture*, vol. 223, pp. 703–712, jun 2009.
- [27] D. J. Mynors and B. Zhang, “Applications and capabilities of explosive forming,” *Journal of materials processing technology*, vol. 126, no. February, pp. 1–25, 2002.
- [28] S. F. Golovashchenko, A. J. Gillard, and A. V. Mamutov, “Formability of dual phase steels in electrohydraulic forming,” *Journal of Materials Processing Technology*, vol. 213, pp. 1191–1212, jul 2013.
- [29] J. Imbert and M. J. Worswick, “Electromagnetic reduction of a pre-formed radius on AA 5754 sheet,” *Journal of Materials Processing Technology*, vol. 211, pp. 896–908, may 2011.
- [30] G. S. Daehn, “High-velocity metal forming,” *Metalworking: Sheet Forming(ASM Handbook Volume . . .*, vol. 14, pp. 405–418, 2006.
- [31] V. Psyk, D. Risch, B. Kinsey, A. Tekkaya, M. Kleiner, and A. Tekkaya, “Electromagnetic forming—A review,” *Journal of Materials Processing Technology*, vol. 211, pp. 787–829, may 2011.
- [32] C. Early and W. G. Dow, “Experimental Studies and applications of Explosive Pressures Produced by Sparks in Confined Channels,” in *A.I.E.E.*, (New York), 1953.
- [33] V. Balanethiram and G. S. Daehn, “Hyperplasticity: Increased forming limits at high workpiece velocity,” *Scripta Metallurgica et Materialia*, vol. 30, pp. 515–520, feb 1994.
- [34] I. Gilchrist and B. Crossland, “The Forming of Sheet Metal Using Underwater Electrical Discharges,” *IEE Conference Publication*, pp. 1–14, 1967.
- [35] A. Rohatgi, E. V. Stephens, A. Soulami, R. W. Davies, and M. T. Smith, “Experimental characterization of sheet metal deformation during electro-hydraulic forming,” *Journal of Materials Processing Technology*, vol. 211, pp. 1824–1833, nov 2011.
- [36] G. S. Daehn and V. J. Vohnout, “Hybrid Matched Tool-Hydraulic Forming Methods,” 2001.
- [37] A. Rohatgi, E. V. Stephens, R. W. Davies, M. T. Smith, A. Soulami, and S. Ahzi, “Electro-hydraulic forming of sheet metals: Free-forming vs. conical-die forming,” *Journal of Materials Processing Technology*, vol. 212, pp. 1070–1079, may 2012.
- [38] M. C. Noland, *High-velocity Metalworking: A Survey*. NASA, Technology Utilization Division, National Aeronautics and Space Administration, 1967.
- [39] G. F. Benedict, *Nontraditional Manufacturing Processes*. Manufacturing Engineering and Materials Processing, Taylor & Francis, 1987.
- [40] T. Tobe, M. Kato, and H. Obara, “Metal Forming by Underwater Wire Explosion : 1. An Analysis of Plastic Deformation of Circular Membranes Under Impulsive Loading,” *Bulletin of JSME*, vol. 22, no. 164, pp. 271–278, 1979.
- [41] A. Rohatgi, A. Soulami, E. V. Stephens, R. W. Davies, and M. T. Smith, “An investigation of enhanced formability in AA5182-O Al during high-rate free-forming at room-temperature: Quantification of deformation history,” *Journal of Materials Processing Technology*, vol. 214, pp. 722–732, mar 2014.
- [42] N. Takatsu, M. Kato, K. Sato, and T. Tobe, “High speed forming of metal sheets by electromagnetic force (3rd report, Free bulging of circular aluminum plates by spiral flat coils),” *Nippon Kikai Gakkai Ronbunshu, C Hen/Transactions of the Japan Society of Mechanical Engineers, Part C*, vol. 53, no. 496, pp. 2717–2723, 1987.
- [43] V. Balanethiram, X. Hu, M. Altynova, and G. S. Daehn, “Hyperplasticity: Enhanced formability at high rates,” *Journal of Materials Processing Technology*, vol. 45, pp. 595–600, sep 1994.

- [44] S. F. Golovashchenko, V. Mamutov, V. Dmitriev, and A. Sherman, "Formability of sheet metal with pulsed electromagnetic and electrohydraulic technologies," in *TMS Annual Meeting* (D. S.K., ed.), (San Diego, CA), pp. 99–110, 2003.
- [45] D.A. Oliveira and M. Worswick, "Electromagnetic forming of aluminium alloy sheet," *J. Phys. IV France*, vol. 110, pp. 293–298, 2003.
- [46] J. M. Imbert, S. L. Winkler, M. J. Worswick, D. Oliveira, and S. F. Golovashchenko, "The effect of tool–sheet interaction on damage evolution in electromagnetic forming of aluminum alloy sheet," *Journal of Engineering Materials and Technology*, vol. 127, no. 1, pp. 145–153, 2005.
- [47] J. M. Imbert, M. J. Worswick, S. Winkler, S. F. Golovashchenko, and V. Dmitriev, "Analysis of the increased formability of aluminum alloy sheet formed using electromagnetic forming," *SAE Technical Papers 2005-01-0082*, apr 2005.
- [48] M. Gerdooei, B. M. Dariani, and G. H. Liaghat, "Effect of Material Models on Formability of Sheet Metals in Explosive Forming," in *Proceedings of the World Congress on Engineering*, vol. II, 2009.
- [49] H. Yu, Y. Guo, and X. Lai, "Rate-dependent behavior and constitutive model of DP600 steel at strain rate from 10<sup>-4</sup> to 10<sup>3</sup> s<sup>-1</sup>," *Materials and Design*, vol. 30, no. 7, pp. 2501–2505, 2009.
- [50] M. Jie, C. H. Cheng, L. C. Chan, and C. L. Chow, "Forming limit diagrams of strain-rate-dependent sheet metals," vol. 51, pp. 269–275, 2009.
- [51] M. Gerdooei and B. M. Dariani, "Strain-rate-dependent forming limit diagrams for sheet metals," *Proceedings of the Institution of Mechanical Engineers, Part B: Journal of Engineering Manufacture*, vol. 222, pp. 1651–1659, dec 2008.
- [52] A. Jenab, I. Sari Sarraf, D. E. Green, T. Rahmaan, and M. J. Worswick, "The Use of genetic algorithm and neural network to predict rate-dependent tensile flow behaviour of AA5182-O sheets," *Materials & Design*, vol. 94, pp. 262–273, mar 2016.
- [53] X. Hu and G. S. S. Daehn, "Effect of velocity on flow localization in tension," *Acta Materialia*, vol. 44, no. 3, pp. 1021–1033, 1996.
- [54] G. Daehn, "High velocity sheet metal forming: state of the art and prognosis for advanced commercialization," . . . *Science and Engineering, the Ohio State . . .*, pp. 1–29, 2002.
- [55] A. K. Ghosh, "Influence of strain hardening and strain-rate sensitivity on sheet metal forming," *Journal of Engineering Materials and Technology, Transactions of the ASME*, vol. 99 Ser H, no. 3, pp. 264–274, 1977.
- [56] A. K. Ghosh and C. H. Hamilton, "Influences of material parameters and microstructure on superplastic forming," *Metallurgical Transactions A*, vol. 13, pp. 733–743, may 1982.
- [57] N. Chung, J. D. Embury, J. D. Evensen, R. G. Hoagland, and C. M. Sargent, "Unstable shear failure in a 7075 aluminum alloy," *Acta Metallurgica*, vol. 25, no. 4, pp. 377–381, 1977.
- [58] A. Jenab and A. Karimi Taheri, "Evaluation of low strain rate constitutive equation of 7075 aluminium alloy at high temperature," *Materials Science and Technology*, vol. 27, pp. 1067–1072, jun 2011.
- [59] A. Jenab, A. Karimi Taheri, and K. Karimi Taheri, "Development of Hot Deformation Processing Map of 7075 Aluminum Alloy Using Dynamic Material Model," *International Journal of Agile Manufacturing*, vol. 12, no. 1, pp. 41–49, 2012.
- [60] A. Jenab and A. Karimi Taheri, "Experimental investigation of the hot deformation behavior of AA7075: Development and comparison of flow localization parameter

- and dynamic material model processing maps,” *International Journal of Mechanical Sciences*, vol. 78, pp. 97–105, jan 2014.
- [61] D. J. Lloyd, “The deformation of commercial aluminum-magnesium alloys,” *Metallurgical Transactions A*, vol. 11, no. 8, pp. 1287–1294, 1980.
- [62] M. Wagenhofer, M. Erickson-Natishan, R. W. Armstrong, and F. J. Zerilli, “Influences of strain rate and grain size on yield and serrated flow in commercial Al-Mg alloy 5086,” *Scripta Materialia*, vol. 41, pp. 1177–1184, nov 1999.
- [63] K. Higashi, T. Mukai, K. Kaizu, S. Tsuchida, and S. Tanimura, “Strain rate Dependence on Mechanical Properties in Some Commercial Aluminum Alloys,” *Le Journal de Physique IV*, vol. 01, pp. C3–341–C3–346, oct 1991.
- [64] K. Higashi, T. Mukai, K. Kaizu, S. Tsuchida, and S. Tanimura, “The microstructural evolution during deformation under several strain rates in a commercial 5182 aluminium alloys,” *Le Journal de Physique IV*, vol. 01, pp. C3–347–C3–352, oct 1991.
- [65] K. Higashi, T. Okada, T. Mukai, and S. Tanimura, “Superplastic deformation mechanisms at high strain rates in mechanically alloyed aluminum IN905XL,” *Funtai Oyobi Fumatsu Yakin/Journal of the Japan Society of Powder and Powder Metallurgy*, vol. 40, no. 3, pp. 337–340, 1993.
- [66] S. T. T. Mukai K. Higashi, T. Mukai, K. Higashi, and S. Tanimura, “Influence of the magnesium concentration on the relationship between fracture mechanism and strain rate in high purity Al-Mg alloys,” *Materials Science and Engineering: A*, vol. 176, no. 1-2, pp. 181–189, 1994.
- [67] T. Mukai, K. Ishikawa, and K. Higashi, “Influence of strain rate on the mechanical properties in fine-grained aluminum alloys,” *Materials Science and Engineering: A*, vol. 204, pp. 12–18, dec 1995.
- [68] T. Mukai, K. Ishikawa, and K. Higashi, “Strength and ductility under dynamic loading in fine-grained IN905XL aluminum alloy,” *Metallurgical and Materials Transactions A*, vol. 26, pp. 2521–2526, oct 1995.
- [69] T. Mukai, M. Kawazoe, and K. Higashi, “Strain-rate dependence of mechanical properties in AA5056 Al-Mg alloy processed by equal-channel-angular-extrusion,” *Materials Science and Engineering: A*, vol. 247, pp. 270–274, jun 1998.
- [70] J. Pan, M. Saje, and A. Needleman, “Localization of deformation in rate sensitive porous plastic solids,” *International Journal of Fracture*, vol. 21, no. 4, pp. 261–278, 1983.
- [71] J. Cheng, *Investigation of the Formability Enhancement of DP600 Steel Sheets in Electrohydraulic Die Forming*. PhD thesis, 2015.
- [72] M. Abbadi, P. Hähner, and A. Zeghloul, “On the characteristics of Portevin - Le Chatelier bands in aluminum alloy 5182 under stress-controlled and strain-controlled tensile testing,” *Materials Science and Engineering A*, vol. 337, no. 1-2, pp. 194–201, 2002.
- [73] R. Picu, G. Vincze, F. Ozturk, J. J. Gracio, F. Barlat, a. M. Maniatty, and R. C. Picua, “Strain rate sensitivity of the commercial aluminum alloy AA5182-O,” *Materials Science and Engineering A*, vol. 390, pp. 334–343, jan 2005.
- [74] A. S. Khan and M. Baig, “Anisotropic responses, constitutive modeling and the effects of strain-rate and temperature on the formability of an aluminum alloy,” *International Journal of Plasticity*, vol. 27, pp. 522–538, apr 2011.
- [75] O.-G. Lademo, K. O. Pedersen, T. Berstad, T. Furu, and O. S. Hopperstad, “An experimental and numerical study on the formability of textured AlZnMg alloys,” *European Journal of Mechanics - A/Solids*, vol. 27, pp. 116–140, mar 2008.

- [76] A. H. Clausen, T. Børvik, O. S. Hopperstad, and A. Benallal, “Flow and fracture characteristics of aluminium alloy AA5083–H116 as function of strain rate, temperature and triaxiality,” *Materials Science and Engineering: A*, vol. 364, pp. 260–272, jan 2004.
- [77] P. Bazarnik, M. Lewandowska, and K. Kurzydłowski, “Mechanical behaviour of ultrafine grained Al-Mg alloys obtained by different processing routes,” *Archives of Metallurgy and Materials*, vol. 57, pp. 869–876, jan 2012.
- [78] J. Kang, D. S. Wilkinson, J. D. Embury, M. Jain, and A. J. Beaudoin, “Effect of type-B Portevin-Le Chatelier bands on the onset of necking in uniaxial tension of strip cast AA5754 sheets,” *Scripta Materialia*, vol. 53, no. 5, pp. 499–503, 2005.
- [79] R. C. Dorward and K. R. Hasse, “Strain rate effects on tensile deformation of 2024-0 and 7075-0 aluminum alloy sheet,” *Journal of Materials Engineering and Performance*, vol. 4, pp. 216–220, apr 1995.
- [80] M. J. Worswick, R. Smerd, C. Salisbury, S. Winkler, and D. J. Lloyd, “High Strain Rate Behaviour of Aluminium Alloy Sheet,” *Materials Science Forum*, vol. 519-521, no. PART 1, pp. 139–146, 2006.
- [81] K. Sakino, “Strain rate dependence of dynamic flow stress of 2017 aluminum alloy at very high strain rates,” *International Journal of Modern Physics B*, vol. 22, no. 9-11, pp. 1209–1214, 2008.
- [82] R. Smerd, S. Winkler, C. Salisbury, M. J. Worswick, D. J. Lloyd, and M. Finn, “High strain rate tensile testing of automotive aluminum alloy sheet,” *International Journal of Impact Engineering*, vol. 32, pp. 541–560, dec 2005.
- [83] U. Lindholm, R. Bessey, and G. Smith, “Effect of strain rate on yield strength, tensile strength, and elongation of three aluminum alloys,” *Journal of Materials*, vol. 6, no. 1, pp. 119–133, 1971.
- [84] D. Oliveira, M. J. Worswick, M. Finn, and D. Newman, “Electromagnetic forming of aluminum alloy sheet: Free-form and cavity fill experiments and model,” *Journal of Materials Processing Technology*, vol. 170, pp. 350–362, dec 2005.
- [85] R. J. Price and A. Kelly, “Deformation of age-hardened aluminium alloy crystals—II. Fracture,” *Acta Metallurgica*, vol. 12, no. 9, pp. 979–992, 1964.
- [86] D. Hull, *Fractography: Observing, Measuring and Interpreting Fracture Surface Topography*. Cambridge University Press, 1999.
- [87] I. E. French and P. F. Weinrich, “The shear mode of ductile fracture in commercial copper,” *Scripta Metallurgica*, vol. 11, no. 11, pp. 965–968, 1977.
- [88] L. Smith, C. Wanintrudal, W. Yang, and S. Jiang, “A new experimental approach for obtaining diffuse-strain flow stress curves,” *Journal of Materials Processing Technology*, vol. 209, pp. 3830–3839, apr 2009.
- [89] G. T. (Rusty) Gray, “High-Strain-Rate Deformation: Mechanical Behavior and Deformation Substructures Induced,” *Annual Review of Materials Research*, vol. 42, pp. 285–303, aug 2012.
- [90] D. Fields and J. W. Backofen, “Determination of Strain-Hardening Characteristics By Torsion Testing,” in *ASTM Proceeding*, vol. 57, pp. 14 (1259 – 1272), Am Soc Test Mater, 1957.
- [91] J. J. Jonas, R. Holt, and C. Coleman, “Plastic stability in tension and compression,” *Acta Metallurgica*, vol. 24, pp. 911–918, oct 1976.
- [92] S. L. Semiatin and J. J. Jonas, *Formability and Workability of Metals*. ASM series in metal processing, American Society for Metals, 1984.

- [93] Y. Prasad and S. Sasidhara, *Hot Working Guide: A Compendium of Processing Maps*. Ohio: ASM International, 1997.
- [94] S. V. S. N. Murty, S. V. S. Narayana Murty, B. Nageswara Rao, and B. P. Kashyap, "Development and validation of a processing map for AFNOR 7020 aluminium alloy," *Materials science and ...*, vol. 20, no. 6, pp. 772–782, 2004.
- [95] F. Kabirian, A. S. Khan, and A. Pandey, "Negative to positive strain rate sensitivity in 5xxx series aluminum alloys: Experiment and constitutive modeling," *International Journal of Plasticity*, vol. 55, pp. 232–246, apr 2014.
- [96] K. Peng, W. Chen, and K. Qian, "Study on dynamic strain aging phenomenon of 3004 aluminum alloy," *Materials Science and Engineering: A*, vol. 415, pp. 53–58, jan 2006.
- [97] Y. Aoura, D. Ollivier, A. Ambari, and P. D. Santo, "Determination of material parameters for 7475 Al alloy from bulge forming tests at constant stress," *Journal of Materials Processing Technology*, vol. 145, pp. 352–359, feb 2004.
- [98] H. McQueen and N. D. Ryan, "Constitutive analysis in hot working," *Materials Science and Engineering a-Structural Materials Properties Microstructure and Processing*, vol. 322, pp. 43–63, jan 2002.
- [99] Q. Lei, Z. Li, J. Wang, S. Li, L. Zhang, and Q. Dong, "High-temperature deformation behavior of Cu–6.0Ni–1.0Si–0.5Al–0.15 Mg–0.1Cr alloy," *Journal of Materials Science*, vol. 47, pp. 6034–6042, may 2012.
- [100] G. E. Dieter and D. Bacon, *Mechanical metallurgy*. New York: McGraw-Hill, 1988.
- [101] G. R. Johnson, W. H. Cook, H. S. Rates, and H. Temperatures, "A constitutive model and data for metals subjected to large strains, high strain rates and high temperatures," in *Proceedings of the 7th International Symposium on Ballistics*, vol. 21, pp. 541–547, The Hague, Netherlands: International Ballistics Committee, 1983.
- [102] A. S. Khan and R. Liang, "Behaviors of three BCC metal over a wide range of strain rates and temperatures: experiments and modeling," *International Journal of Plasticity*, vol. 15, pp. 1089–1109, jan 1999.
- [103] A. S. Khan, Y. Sung Suh, and R. Kazmi, "Quasi-static and dynamic loading responses and constitutive modeling of titanium alloys," *International Journal of Plasticity*, vol. 20, pp. 2233–2248, dec 2004.
- [104] A. S. Khan, R. Kazmi, and B. Farrokh, "Multiaxial and non-proportional loading responses, anisotropy and modeling of Ti–6Al–4V titanium alloy over wide ranges of strain rates and temperatures," *International Journal of Plasticity*, vol. 23, pp. 931–950, jun 2007.
- [105] A. Pandey, A. S. Khan, E.-Y. Kim, S.-H. Choi, and T. Gnäupel-Herold, "Experimental and numerical investigations of yield surface, texture, and deformation mechanisms in AA5754 over low to high temperatures and strain rates," *International Journal of Plasticity*, vol. 41, pp. 165–188, feb 2013.
- [106] E. Voce, "The relationship between stress and strain for homogeneous deformation," *Journal of the Institute of Metals*, vol. 74, pp. 537–562, 1948.
- [107] H. J. Kleemola and M. a. Nieminen, "On the strain-hardening parameters of metals," *Metallurgical Transactions*, vol. 5, no. 8, pp. 1863–1866, 1974.
- [108] G. Sainath, B. Choudhary, J. Christopher, E. Isaac Samuel, and M. Mathew, "Applicability of Voce equation for tensile flow and work hardening behaviour of P92 ferritic steel," *International Journal of Pressure Vessels and Piping*, vol. 132-133, pp. 1–9, 2015.

- [109] C. Zhang and B. Wang, "Identification of the hardening behavior of solids described by three-parameter Voce law using spherical indentation," *Journal of Materials Research*, vol. 27, no. 20, pp. 2624–2629, 2012.
- [110] T. Rahmaan, A. Bardelcik, J. Imbert, C. Butcher, and M. J. Worswick, "Effect of strain rate on flow stress and anisotropy of DP600 , TRIP780 , and AA5182-O sheet metal alloys," *International Journal of Impact Engineering*, vol. 88, pp. 72–90, 2016.
- [111] J. H. Holland, *Adaptation in Natural and Artificial Systems: An Introductory Analysis with Applications to Biology, Control and Artificial Intelligence*. Cambridge, MA, USA: MIT Press, 1975.
- [112] S.N.Sivanandam and S.N.Deepa, *An introduction to genetic algorithms*. New York: Springer Berlin Heidelberg, 2008.
- [113] K. Elangovan, C. S. Narayanan, R. Narayanasamy, and C. Sathiya Narayanan, "Modelling of forming limit diagram of perforated commercial pure aluminium sheets using artificial neural network," *Computational Materials Science*, vol. 47, pp. 1072–1078, feb 2010.
- [114] K. Elangovan, C. S. Narayanan, and R. Narayanasamy, "Modelling the correlation between the geometrical features and the forming limit strains of perforated Al 8011 sheets using artificial neural network," *International Journal of Material Forming*, vol. 4, pp. 389–399, nov 2010.
- [115] A. Derogar and F. Djavanroodi, "Artificial Neural Network Modeling of Forming Limit Diagram," *Materials and Manufacturing Processes*, vol. 26, pp. 1415–1422, nov 2011.
- [116] H. Aguir, H. BelHadjSalah, and R. Hambli, "Parameter identification of an elasto-plastic behaviour using artificial neural networks–genetic algorithm method," *Materials & Design*, vol. 32, pp. 48–53, jan 2011.
- [117] G. Ambrogio, L. Filice, F. Guerriero, R. Guido, and D. Umbrello, "Prediction of incremental sheet forming process performance by using a neural network approach," *The International Journal of Advanced Manufacturing Technology*, vol. 54, pp. 921–930, nov 2010.
- [118] A. Forcellese, F. Gabrielli, and M. Simoncini, "Prediction of flow curves and forming limit curves of Mg alloy thin sheets using ANN-based models," *Computational Materials Science*, vol. 50, pp. 3184–3197, oct 2011.
- [119] Z. Fu, J. Mo, L. Chen, and W. Chen, "Using genetic algorithm-back propagation neural network prediction and finite-element model simulation to optimize the process of multiple-step incremental air-bending forming of sheet metal," *Materials & Design*, vol. 31, pp. 267–277, jan 2010.
- [120] B. S. Kessler, a. S. El-Gizawy, and D. E. Smith, "Incorporating Neural Network Material Models Within Finite Element Analysis for Rheological Behavior Prediction," *Journal of Pressure Vessel Technology*, vol. 129, no. 1, p. 58, 2007.
- [121] K. Du and M. Swamy, *Neural networks in a softcomputing framework*. Germany: Springer-Verlag London Limited, 2006.
- [122] D. W. Marquardt, "An Algorithm for Least-Squares Estimation of Nonlinear Parameters," *Journal of the Society for Industrial and Applied Mathematics*, vol. 11, no. 2, pp. 431–441, 1963.
- [123] D. J. C. MacKay, "Bayesian Interpolation," *Neural Computation*, vol. 4, no. 3, pp. 415–447, 1992.
- [124] D. J. C. MacKay, "A Practical Bayesian Framework for Backpropagation Networks," *Neural Computation*, vol. 4, no. 3, pp. 448–472, 1992.



- [125] H. K. D. H. Bhadeshia, C. MacKay, and E. Svensson, "Impact toughness of C-Mn steel arc welds: Bayesian neural network analysis," *Materials science and technology*, vol. 11, no. 10, pp. 1046–1051, 1995.
- [126] K. O. Pedersen, H. J. Roven, O.-G. Lademo, and O. S. Hopperstad, "Strength and ductility of aluminium alloy AA7030," *Materials Science and Engineering A*, vol. 473, no. 1-2, pp. 81–89, 2008.
- [127] J. M. Carlson and J. E. Bird, "Thermal and strain rate softening in Al-Mg sheet during necking and shear band formation," *Metallurgical Transactions A*, vol. 22, no. 1, pp. 1154–1156, 1991.
- [128] G. Voyiadjis, A. Palazotto, and X.-L. Gao, "Modeling of metallic materials at high strain rates with continuum damage mechanics," *Applied Mechanics Reviews*, vol. 55, no. 5, pp. 481–492, 2002.
- [129] D. R. Curran, L. Seaman, and D. A. Shockey, "Dynamic failure of solids," *Physics Reports*, vol. 147, no. 5, pp. 253–388, 1987.
- [130] Y. Li and L. Arnberg, "Solidification structures and phase selection of iron-bearing eutectic particles in a DC-cast AA5182 alloy," *Acta Materialia*, vol. 52, pp. 2673–2681, may 2004.
- [131] C. J. Simensen and U. Sodervall, "Investigation of trace elements in an Al-4.8 wt.% Mg-0.3 wt.% Mn alloy," *Surface and Interface Analysis*, vol. 30, pp. 309–314, aug 2000.
- [132] M. Hadianfard and M. J. Worswick, "Influence of strain rate on shear localization during deformation and fracture of 5754 and 5182 aluminum alloy," *Aluminium Alloys 2006, Pts 1 and 2*, vol. 519-521, pp. 1047–1051, 2006.
- [133] Y. Li and L. Arnberg, "A eutectoid phase transformation for the primary intermetallic particle from Alm(Fe,Mn) to Al<sub>3</sub>(Fe,Mn) in AA5182 alloy," *Acta Materialia*, vol. 52, pp. 2945–2952, jun 2004.

## Chapter 3

# Formability of AA5182-O Sheet during Electro Hydraulic Forming: Influence of Input Energy

In this chapter the formability of electro-hydraulically formed AA5182-O aluminium sheet was investigated by means of grid analysis and by comparing with different forming limit curves (FLCs). Previously, many researchers claimed that the formability of aluminium alloys can be enhanced significantly during the EHFF and EHDF processes. However, it is found that free-formed AA5182-O specimens did not show any significant increase in formability. When specimens were electro-hydraulically formed with sufficient input energy into 34, 40 and 45° conical dies a maximum increase above the quasi-static FLC of 50, 70 and 90% were measured in the safe strains, respectively. These results suggest that AA5182-O exhibits improved formability in the conical dies once a critical threshold of 8-10 kJ input energy has been reached. This threshold input energy controls a number of factors which may influence formability including the impact velocity against the die surface and the subsequent strain rate of the material as it fills the die.

∴ This section has been published: A. Jenab, D. E. Green, A. T. Alpas, and K. P. Boyle, “Formability of AA5182- O Sheet during Electro-Hydraulic Forming: Influence of Input Energy”, in MS&T, pp. 535-542, 2015.

### 3.1 Introduction

The use of aluminium alloys in the automotive industry is attractive as it leads to body weight reduction [1]. The extensive use of Al-Mg alloys (5xxx-series) in automotive, aerospace and shipbuilding industries is due to their high specific strength, weldability and corrosion resistance [2]. However, in comparison to highly formable steel sheet such as extra deep drawing quality grades, Al-Mg alloys exhibit lower formability at room temperature [3]. To overcome this limitation, warm forming can be used [4, 5] but forming at elevated temperatures has its own drawbacks, including those associated with additional cost due to the use of specialized lubrication, high energy consumption and post-forming cleaning.

An alternative approach is to use high-strain-rate forming techniques such as explosive forming, electro-magnetic forming or electro-hydraulic forming (EHF) [6–10]. These high-rate forming techniques lead to improved formability that were attributed to “*inertial effects*” and changes in material behaviour which stabilize neck formation [11, 12]. The elimination of matching dies and a decrease in press size are some of the advantages of explosive forming techniques which result in a reduction in initial capital investment. Electro-hydraulic forming is of special interest because of the ease with which the process can be controlled, the ability to form non-magnetic sheets, good repeatability (especially with the use of a wire bridge) and the ability to reach very high strain rates ( $\sim 10^4 \text{ s}^{-1}$ ) [10]. To obtain the highest improvement in formability with the EHF process, both high strain rate and high hydrostatic stress are required [9]. The benefit of EHF AA5182-O sheet was demonstrated by Rohatgi et al. [13–15], who found an increase, from the quasi-static FLC, of 150% and 550% in the safe major strains in free-forming and conical die forming, respectively, depending on the strain path.

Forming limit curves are used to determine the onset of necking for a wide range of strain paths and to provide a quantitative assessment of sheet formability. In this study, free-formed EHF (EHFF) and die-formed EHF (EHDF) forming limits are compared with quasi-static and EHFF forming limit curves (FLCs) in order to quantify the formability enhancement of AA5182-O during high strain rate forming.

## 3.2 Experimental Procedure

### 3.2.1 EHF Experiments and Grid Analysis

AA5182-O sheet with a 1.5mm thickness was provided by Novelis Inc. The chemical composition of the alloy in weight percent was Al-5.02Mg-0.37Mn-0.24Fe-0.041Si-0.015Cu with traces of Cr, Zn and Ti as measured by spectrographic analysis. Prior to deformation 20×20 cm square samples were electro-etched using a 2.54 mm square grid.

The EHF experiments were performed using different input voltages and test conditions. At the moment of discharge, a high voltage current generates a pressure wave which forms the sheet into either free space (EHFF) or into a die (EHDF). Figure 3.1 shows a schematic of the EHDF apparatus. The EHDF experiments used conical dies with die angles of 34, 40 and 45° (see Fig. 3.1).

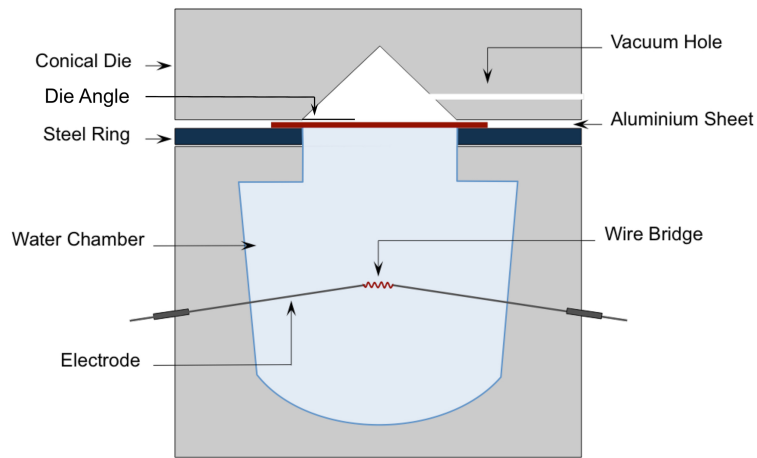


Figure 3.1: Schematic of EHDF apparatus.

After forming, major and minor strains were measured at the apex and radially from

the apex along the sheet rolling and transverse directions using a grid analyzer with a precision of 0.5% engineering strain. Safe, necked and cracked grids were identified as such prior to being measured. Cracked grids were stitched together by the optical strain measurement system so as to determine the principal strains just prior to fracture.

### 3.2.2 Formability Improvement Index

A formability improvement index was defined in order to compare the forming limit data from the EHF experiments with reference FLCs. A linear strain path  $\rho = e_2/e_1$  is assumed where  $e_1$  and  $e_2$  are the major and minor principal engineering strains. The formability improvement was calculated from the difference in magnitudes of in-plane principal strains from the EHF experiments and the reference FLC for equivalent strain paths. The magnitude of the in-plane principal engineering strain is given by  $|e| = e_1\sqrt{1 + \rho^2}$  and consequently, the formability improvement index may be expressed as,

$$FI\% = \frac{|e^{EHF}| - |e^{FLC}|}{|e^{FLC}|} \times 100 \quad (3.1a)$$

$$= \frac{e_1^{EHF} - e_1^{FLC}}{e_1^{FLC}} \times 100 \quad (3.1b)$$

where  $e_1^{EHF}$  is the major principal engineering strain measured from the EHF specimen and  $e_1^{FLC}$  is the major principal engineering strain from the reference FLC for an equivalent strain path. It is worth emphasizing that Eq. (3.1) determines the percent change in the forming limit for equivalent strain paths, and not for equivalent minor strains, as is more commonly used. To determine the formability improvement index for each specimen, the average value of three safe grids with the highest effective strains were chosen. Quasi-static FLCs were extracted from the work of Wu et al. [16] and from data provided by CanmetMATERIALS [17]. An EHF FLC from Maris [18] was also used for comparison.

## 3.3 Results and Discussion

### 3.3.1 EHF Experiments: Effect of Die and Input Voltage

Figure 3.2 shows selected samples formed under different EHF conditions. The EHFF experiments are quite sensitive to the input voltage. For example, an increase in input voltage of 0.5 kV, from 5.5 kV to 6.0 kV, consistently led to failure in EHFF specimens (Fig. 3.2 (a)). However, the sensitivity to the applied voltage reduces significantly with the presence of the die. Fig. 3.2(b) shows two specimens formed using the 34° die. Splitting was rarely observed and mostly located at the apex area in case of 34° dies (Fig. 3.2(b)-top) since the material could fill the die safely and reach a greater depth compared to EHFF.

Typical specimens deformed using the 40° die are shown in Fig. 3.2(c). All failed specimens showed failure in the apex area and some specimens exhibited signs of concentric circumferential localized deformation on the inside of the conical specimens. However, measured strain values suggest that much greater safe strains are reached at locations away from these localized deformation areas. It is worth emphasizing that the majority of cracked specimens were formed at lower input voltages (i.e. at 8.0 kV in Fig. 3.2(c)-top) and the safe specimens were formed at higher input voltages (i.e. at 12.0 kV in Fig. 3.2(c)-bottom).

Although many grids safely reached strain values higher than other EHDF specimens tested at lower die angles, all specimens formed in the 45° die failed by showing large cracks. An interesting observation is that the mode of failure and the location of crack initiation changed by increasing the input energy in EHDF-45° condition. At low applied voltages (11.5 kV or less) the crack nucleates and propagates radially at the apex (shown in Fig. 3.2(d)-top) but at high applied voltages circumferential cracks can be seen instead (i.e. with applied voltage of 12.0 kV in Fig. 3.2(d)-bottom).

In the EHDF experiments and at low voltages, cracks usually nucleate at the apex area and the specimens were unable to fill the die cavity completely (see Fig. 3.2(b)-(d)). Hence the cracks were formed in free forming state of the deformation. However,

at higher input voltages, which results in higher initial velocities, circumferential localization (in EHDF-40° shown in Fig. 3.2(c)-bottom) or splitting (in EHDF-45° shown in Fig. 3.2(d)-bottom) was observed. Similar observations were reported for DP500 and DP980 in Ref [9]. In the 40° die-formed specimens, formed using high input voltages, splitting was suppressed as the incipient circumferential neck hit the die and the active deformation region moved away allowing the sample to fill the die without occurrence of crack. However, due to the die geometry, localization of the incipient circumferential neck continued in the 45° die-formed specimens and consequently cracks nucleated before the die was hit. Hence, it is believed that a certain threshold of input energy is needed to be able to apply high velocities and strain rates in order to fill the die without cracking and safely reach high strains. It is noteworthy that most of the safely deformed grids in the apex area of EHDF specimens were removed as a result of either generated heat (of compressed air) or due to the friction with the die as shown in Fig. 3.2(b) and (c).

### 3.3.2 Formability Improvement

Table 3.1 shows calculated formability improvement of selected samples formed in EHFF and EHDF condition when compared with different FLCs. It can be seen that when formed by the EHFF process, the specimens do not show any significant improvement in formability. However, in case of EHDF, reasonable improvement can be seen. Maximum FI% calculated for EHDF is about 50, 70 and 90% for 34, 40, and 45° conical dies, respectively. Also, using low voltages with high angle dies does not result in enhanced formability in AA5182-O sheets. These formability improvements are less than results reported in Ref. [15], where an increase in safe major strains of 150% and 550% greater than quasi-static FLC were reported for EHFF and EHDF tests, respectively.

The input energy ( $U$ ) can be calculated from  $U = \frac{1}{2}cv^2$  where  $c$  is the capacitance of the circuit and  $v$  is the input voltage. Figure 3.3 shows the variation of FI% with input energy for EHDF specimens. It can clearly be seen that by increasing the input energy, above a threshold of 8-10 kJ, AA5182-O sheet was formed to higher safe

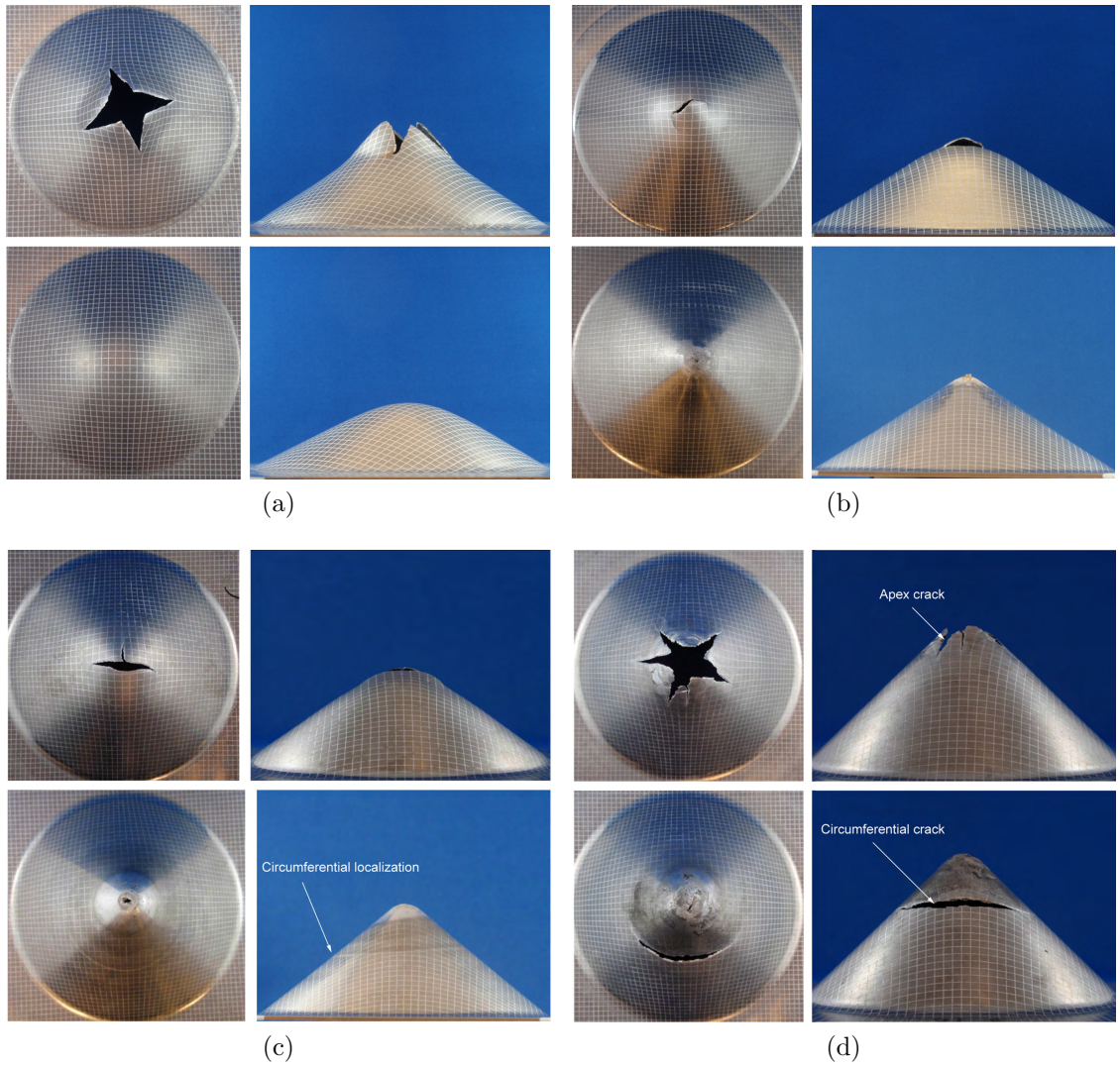


Figure 3.2: Top and side view of (a) EHFF; top: 6.0 kV, bottom: 5.5 kV, (b) EHDF-34° die; top: 8.4 kV, bottom: 8.0 kV, (c) EHDF-40° die; top: 8.0 kV, bottom: 12.0 kV, and (d) EHDF-45° die; top: 11.5 kV, bottom: 12.0 kV.



Table 3.1: FI% of selected samples compared to different FLCs.

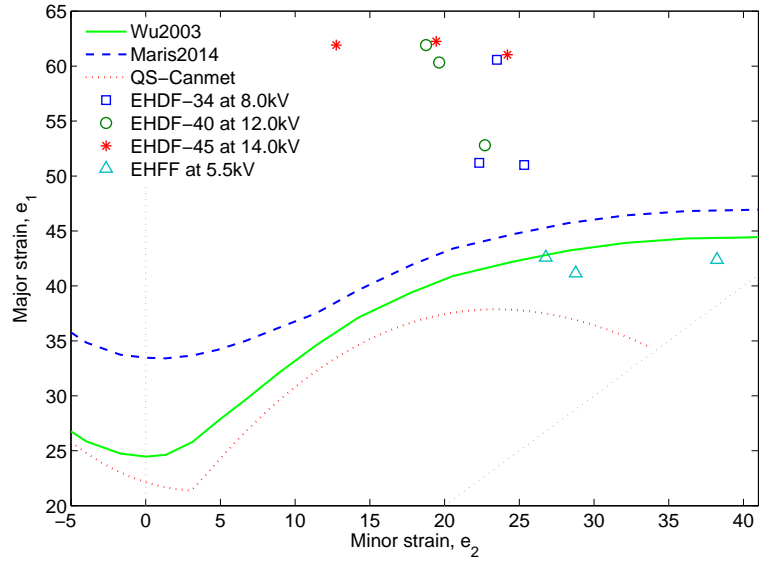
Test Cond.	Voltage, (kV)	Referenced FLD		
		QS [16]	QS-Canmet	EHFF [18]
EHFF	5.5	-3.67	13.82	-9.44
	6.0	-6.4	6.05	-12.4
	8.0	-6.98	9.29	-12.5
	11.0	-5.92	8.67	-11.69
EHDF-34°	8.0	50.15	66.02	37.06
	8.0	50.66	66.65	37.69
	9.0	32.52	45.93	22.32
	9.0	19.67	32.47	9.21
EHDF-40°	11.5	45.79	63.95	29.08
	12.0	69.67	88.71	53.22
	12.0	34.07	48.49	22.2
	9.0	5.9	24.02	-0.41
EHDF-45°	11.0	14.54	34.32	7.69
	12.0	35.32	48.99	25.13
	13.0	53.9	70.79	40.58
	14.0	87.21	114.08	62.98

strains. Hence, a number of factors influencing formability, including the strain rate and impact velocity against the die surface and the resulting hydrostatic stress of the material, are controlled by the input energy.

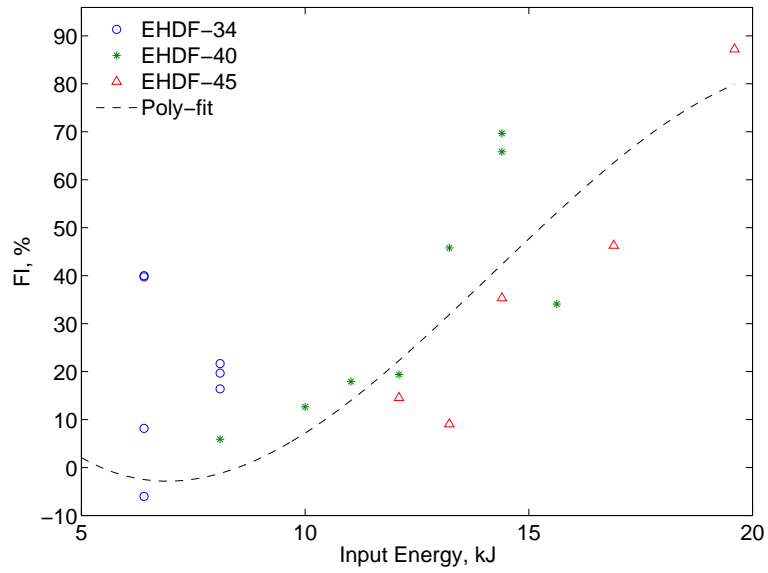
### 3.4 Conclusions

In this study, the formability of AA5182-O sheets was investigated during the EHFF and EHDF process. The following conclusions were obtained;

1. Formability increased slightly during EHFF; a 14% to 18% increase was observed when compared to more conservative quasi-static FLCs.
2. In case of EHDF process, a 50, 70 and 90% increase in safe strains were measured for 34, 40, and 45° conical dies, respectively, as compared to the quasi-static FLC.
3. An important factor in reaching high safe strain in EHDF process is the input



(a)



(b)

Figure 3.3: (a) Formability improvement of samples showing highest increase in safe strain and FLCs and (b) variation of improvement of formability with input energy (compared with Ref. [16]).

energy; once a certain energy threshold of 8-10 kJ is reached, AA5182-O sheet can be formed successfully into the conical dies.

## 3.5 Acknowledgements

This research was funded by NSERC’s Automotive Partnership Canada program with support from Amino North America Corp., ArcelorMittal Dofasco, Ford Motor Company, Natural Resources Canada and Novelis Inc. The authors are grateful to Dr. Mark Kozdras for his help reviewing the paper and Prof. Sergey Golovashchenko for his expert advice and facilitating the EHF experiments.

## 3.6 References

- [1] E. M. Taleff, P. J. Nevland, and P. E. Krajewski, “Tensile ductility of several commercial aluminum alloys at elevated temperatures,” *Metallurgical and Materials Transactions A-Physical Metallurgy and Materials Science*, vol. 32, no. 5, pp. 1119–1130, 2001.
- [2] I. J. Polmear, *Light Alloys From Traditional Alloys to Nanocrystals*. Oxford: Butterworth-Heinemann-Elsevier, 2006.
- [3] E. M. Taleff, P. J. Nevland, and P. E. Krajewski, “Solute-drag creep and tensile ductility in aluminum alloys,” in *Creep Behavior of Advanced Materials for the 21st Century*, pp. 349–358, The Mineral, Metals & Materials Society, 1999.
- [4] Y. C. Lin, L. T. Li, Y. C. Xia, and Y. Q. Jiang, “Hot deformation and processing map of a typical Al–Zn–Mg–Cu alloy,” *Journal of Alloys and Compounds*, vol. 550, pp. 438–445, 2013.
- [5] J. Li, J. E. Carsley, T. B. Stoughton, L. G. Hector, and S. J. Hu, “Forming limit analysis for two-stage forming of 5182-O aluminum sheet with intermediate annealing,” *International Journal of Plasticity*, vol. 45, pp. 21–43, June 2013.
- [6] V. S. Balanethiram and G. S. Daehn, “Enhanced formability of interstitial free iron at high strain rates,” *Scripta Metallurgica et Materialia*, vol. 27, no. 12, pp. 1783 – 1788, 1992.
- [7] V. S. Balanethiram and G. S. Daehn, “Hyperplasticity: Increased forming limits at high workpiece velocity,” *Scripta Metallurgica et Materialia*, vol. 30, pp. 515–520, Feb. 1994.
- [8] J. Imbert, M. Worswick, S. Winkler, S. Golovashchenko, and V. Dmitriev, “Analysis of the increased formability of aluminum alloy sheet formed using electromagnetic forming,” *SAE Technical Papers 2005-01-0082*, Apr. 2005.
- [9] S. F. Golovashchenko, A. J. Gillard, and A. V. Mamutov, “Formability of dual phase steels in electrohydraulic forming,” *Journal of Materials Processing Technology*, vol. 213, pp. 1191–1212, July 2013.
- [10] A. Hassannejadasl, D. E. Green, S. F. Golovashchenko, J. Samei, and C. Maris, “Numerical modelling of electrohydraulic free-forming and die-forming of DP590 steel,” *Journal of Manufacturing Processes*, vol. 16, pp. 391–404, Aug. 2014.

- [11] V. S. Balanethiram, X. Hu, M. Altynova, and G. S. Daehn, “Hyperplasticity: Enhanced formability at high rates,” *Journal of Materials Processing Technology*, vol. 45, pp. 595–600, Sept. 1994.
- [12] V. S. Balanethiram, *Hyperplasticity: Enhanced Formability of Sheet Metals at High Workpiece Velocity*. PhD thesis, 1996.
- [13] A. Rohatgi, E. V. Stephens, A. Soulami, R. W. Davies, and M. T. Smith, “Experimental characterization of sheet metal deformation during electro-hydraulic forming,” *Journal of Materials Processing Technology*, vol. 211, pp. 1824–1833, Nov. 2011.
- [14] A. Rohatgi, E. V. Stephens, R. W. Davies, M. T. Smith, A. Soulami, and S. Ahzi, “Electro-hydraulic forming of sheet metals: Free-forming vs. conical-die forming,” *Journal of Materials Processing Technology*, vol. 212, pp. 1070–1079, May 2012.
- [15] A. Rohatgi, A. Soulami, E. V. Stephens, R. W. Davies, and M. T. Smith, “An investigation of enhanced formability in AA5182-O Al during high-rate free-forming at room-temperature: Quantification of deformation history,” *Journal of Materials Processing Technology*, vol. 214, pp. 722–732, Mar. 2014.
- [16] P. D. Wu, M. Jain, J. Savoie, S. R. MacEwen, P. Tuğcu, and K. W. Neale, “Evaluation of anisotropic yield functions for aluminum sheets,” *International Journal of Plasticity*, vol. 19, pp. 121–138, Jan. 2003.
- [17] “Private communication.” 2014.
- [18] C. Maris, “Experimental determination of the forming limits of DP600 and AA5182 sheets in electrohydraulic free forming,” Master’s thesis, University of Windsor, 2014.

## Chapter 4

# The Use of Genetic Algorithm and Neural Network to Predict Rate-dependent Tensile Flow Behaviour of AA5182-O Sheets

In this chapter, the hardening properties of AA5182-O are investigated by means of tensile tests carried out by project partner, University of Waterloo, at different strain rates ranging from quasi-static to  $1000\text{s}^{-1}$ . The motivation to perform this study was to;

- know how the material behaves at moderate and high-strain rates. If the flow stress increases with strain rate, it could lead to strengthening in high-strain rate processes such as EHF and consequently to better formability.
- examine how the constitutive behaviour is predicted at high strains; for some sheet materials the flow stress saturates at high strains leading to extensive deformation in numerical simulations of the forming process.
- understand the effect of anisotropy on constitutive equation and flow behaviour of AA5182-O.
- obtain a reliable constitutive equation that can be used to accurately simulate the EHF process.

Hence, in this chapter, two approaches are taken, using the conventional JC, KHL and modified-Voce constitutive equations<sup>1</sup>, and more complex computational structures such as artificial neural networks. To determine the constants in constitutive

---

<sup>1</sup>Erratum: one of the methods used in the published manuscript was *non-linear regression analysis* and not *linear regression analysis*.

equations, a more advanced approach was taken which is the genetic algorithm optimization. It is worth noting that beside the constitutive equations reported in this chapter, different forms of modified-Voce and power-law equations were also investigated but were not included in the dissertation because they lead to less accurate predictions of the experimental flow stress.

In brief, this chapter discusses the tensile flow behaviour of AA5182-O sheet which was experimentally obtained in different material directions (RD, DD, and TD) at strain rates ranging from 0.001 to 1000s<sup>-1</sup> and predicted by means of both phenomenological models and neural networks (NNs). Constants in Johnson-Cook (JC), Khan-Huang-Liang (KHL), and modified Voce were calculated using genetic algorithm (GA) and linear regression analysis and used to simulate the uniaxial tension tests. Two types of feed-forward back-propagation neural networks were also trained and validated to predict the rheological behaviour of the alloy without the limitations of a mathematical function. The weights and bias values of each network were then used to simulate uniaxial tensile deformation. Subsequently, the results were compared with experimental flow curves and accuracy parameters were calculated. It was found that the modified Voce constitutive equation was able to predict the flow behaviour of AA5182-O with better accuracy than JC and KHL models. Also, the NN was found to be the most accurate method of predicting the anisotropic rate-dependant behaviour of AA5182-O.

∴ This section has been published: A. Jenab, I. Sari Sarraf, D. E. Green, T. Rahmaan, and M. J. Worswick, “The Use of genetic algorithm and neural network to predict rate-dependent tensile flow behaviour of AA5182-O sheets”, *Materials & Design*, vol. 94, pp. 262-273, Mar 2016.

## 4.1 Introduction

Aluminium alloys exhibit various properties that are advantageous for the manufacture of automobiles such as good corrosion resistance, high specific strength and especially low density as compared to steel. Additionally, it is estimated that each 10% reduction of weight in a passenger vehicle results in a 6-8% improvement in fuel efficiency [1]. Hence, aluminium sheets are increasingly being used to manufacture automotive body parts so as to reduce vehicle weight [2]. Due to their good mechanical properties, 5xxx-series sheet alloys are of special interest for inner panels and body-in-white components [3]. However, limited formability at low temperature [4] as compared to many steel grades, moderate strength and negative strain rate sensitivity are limitations that prevent wide-usage of these alloys in industry. In order to overcome these limitations, high temperature deformation [5] or high strain rate forming techniques [6, 7] can be used to produce automotive body parts because of their potential for increasing sheet formability. At low strain rates, many aluminium alloys including 5xxx-series exhibit negative strain rate sensitivity which is attributed to dynamic strain ageing and Portevin-Le Chatelier (PLC) effect [8, 9] where interactions between mobile dislocations and solute atoms result in inhomogeneity of plastic deformation and serrations in the flow curve. However, at moderate strain rates (i.e.  $10\text{-}100\text{s}^{-1}$ ) a transition from negative to positive rate sensitivity is observed for different Mg concentrated 5xxx-series aluminium alloys [10]. This transition is definitely beneficial for high rate forming processes since it promotes better post-uniform flow behaviour. But in view of the technical challenges, limited experimental data are available for these high-strain rate processes and consequently it is necessary to carry out numerical simulations in order to predict the outcome of the forming process.

Therefore, it is essential to accurately model the mechanical response of the sheet material.

Phenomenological constitutive functions are developed to implement material flow behaviour in numerical models, particularly in finite element models used for process simulation. Consequently, many researchers have used such rheological models to predict the behaviour of different alloys such as AA2124-T851 [11], AA5052 [12], AA5182 [13], AA6026 [14], and AA7075 [15, 16]. In this study, different approaches were utilized and compared to investigate the flow behaviour of AA5182-O sheets along different material directions (i.e. the rolling direction (RD), 45° to the rolling direction (DD) and transverse direction (TD)) from quasi-static ( $0.001\text{s}^{-1}$ ) to high strain rates ( $1000\text{s}^{-1}$ ). Genetic algorithm (GA) and linear regression (R.) methods were used to calculate the constants in widely-accepted phenomenological constitutive equations; Johnson-Cook (JC), Khan-Huang-Liang (KHL), and modified-Voce. These models were selected due to their common usage in simulation of metal forming and frequent citations in the literature.

Although constitutive equations represent non-linear relations between empirical parameters such as  $\sigma$ ,  $\varepsilon$ ,  $\dot{\varepsilon}$ , and  $T$ , they are usually limited to specific deformation mechanisms and break down when deformation domains change. Consequently, to overcome these limitations, different equation parameters or separate equations are required to represent data over large domains. Many researchers have also used neural networks to determine the rheological behaviour of materials [17, 18]. Consequently, in addition to the phenomenological approach, artificial neural networks were also utilized to predict the flow behaviour of AA5182-O in the same sheet orientations and strain rate range. A feed-forward back-propagation neural network was selected because it has previously been shown to accurately predict the flow stress for different materials subject to both warm and hot forming conditions in a range of strain rates [19] even when the material's dominant deformation mechanism was changed [5]. The accuracy of these different approaches will be compared to each other as well as with conventional linear regression calculations using well-known statistical errors, such as mean square error (MSE) and adjusted R-square error ( $R_{\text{adj}}^2$ ). Then, the



most accurate results will be used to simulate the mechanical response of AA5182-O using different user material subroutines that were developed to facilitate the use of JC, KHL, and modified-Voce constitutive equations and the trained neural networks. The advantages and disadvantages of the mentioned approaches will be discussed.

#### 4.1.1 Constitutive equations

The Johnson and Cook (JC) constitutive equation [20] is one of the hardening criteria mostly used in metal forming simulations, either in its original form shown in Eq.4.1, or with some modifications [21].

$$\sigma = \left( A + B\varepsilon^n \right) \left[ 1 + C \ln \left( \frac{\dot{\varepsilon}}{\dot{\varepsilon}_0} \right) \right] \left[ 1 - \left( \frac{T - T_r}{T_m - T_r} \right)^m \right] \quad (4.1)$$

where  $\dot{\varepsilon}_0$  is the reference strain rate and  $A$ ,  $B$ ,  $C$ ,  $n$  and  $m$  are material constants.  $T_r$ ,  $T_m$ , and  $T$  denote room, melting and test temperatures, respectively. Previously, the parameters in the JC constitutive equation were calculated by Rohatgi [22] and Smerd [23] in the rolling direction of AA5182-O sheets considering isotropic behaviour and primarily mostly in the quasi-static strain rate range. However, published research (e.g. [24–26]) suggests that AA5182-O exhibits anisotropic flow behaviour. Consequently, these parameters were calculated for different orientations to study the anisotropic behaviour of AA5182-O, as well as for a wide range of strain rates.

The Khan-Huang-Liang constitutive function [27] is shown in Eq. 4.2. Khan et al. [28] and Kabirian et al. [29] modified the original KHL phenomenological function to accommodate changes in strain rate sensitivity of AA5182-O at elevated temperatures.

$$\sigma = \left[ A + B \left( 1 - \frac{\ln \dot{\varepsilon}}{\ln D_p^p} \right)^{n_1} \varepsilon^{n_0} \right] \left( \frac{\dot{\varepsilon}}{\dot{\varepsilon}_0} \right)^c \left( \frac{T_m - T}{T_m - T_{\text{ref}}} \right)^m \quad (4.2)$$

where  $A$  and  $B$  are material constants and  $c$  is the overall factor for strain rate sensitivity.  $m$  is the temperature exponent and  $n_0$  and  $n_1$  represent the work hardening exponent and the strain rate sensitivity of the work hardening, respectively.  $D_p$  is an arbitrary upper bound strain-rate and is usually assumed to be  $10^6 \text{s}^{-1}$ .

The Voce hardening function [30] is one of the most convenient equations used to predict flow behaviour of different materials [31, 32]. It shows remarkable fitting performance and inherent simplicity for different materials including aluminium alloys [33]. However, the Voce hardening function does not consider the effect of strain rate on deformation behaviour in its original formulation. To consider both strain and strain rate sensitivity, a multiplicative method was used to combine the Voce equation with a Logarithmic-Exponential strain rate expression. This modified Voce equation (VM) is expressed in Eq. 4.3.

$$\sigma = \left[ B - (B - A) \left( \exp(-m_1 \varepsilon) \right) \right] \times \zeta(\dot{\varepsilon}) \quad (4.3a)$$

$$\zeta(\dot{\varepsilon}) = \left[ C \ln(\dot{\varepsilon}) + (1 + \dot{\varepsilon})^D \right] \quad (4.3b)$$

where  $A$ ,  $B$ ,  $m_1$ ,  $C$  and  $D$  are material constants to be calculated for each testing condition. It is worth noting that by adjusting  $C$  and  $D$  in Eq.4.3b according to the material's response,  $\zeta(\dot{\varepsilon})$  can be changed to accommodate variations in strain rate sensitivity for the wide range of strain rates used in this study. This model was shown to successfully predict increase of flow stress at high strain rate regimes for different materials in Ref. [13].

### 4.1.2 Genetic algorithm method

Genetic algorithm (GA) is an optimization method widely used in scientific and engineering studies because of its ability to reach optimum conditions, e.g. the global minimum. One advantage of the GA approach is the ease with which parameters can be calculated without the need to make the equation linear or to calculate each parameter separately using partial equations. The various GA parameters will briefly be defined and explained. The first step is to create a function, which will be minimized during the GA process. The initial population is a set of parameters used to calculate the first minimum value of the function randomized within a predefined boundary

condition. New generations are created from the parent population by crossover. However, it is important to maintain the genetic chromosome and create diversity of answers so that the result converges to the minimum value more efficiently; a mutation function is responsible for providing diversity during the crossover process. The populations that correspond to greater differences from the minimum values (constants) obtained are eliminated, and populations continue to be generated until the total number of generations is reached or the difference between the minimum value of a certain amount of generations is less than a specified value (i.e.  $1 \times 10^{-6}$  for 50 generation intervals). Readers are referred to Ref. [34] for further details on GA concepts and theory.

In particular, GA have been used to describe the behaviour of materials under a variety of conditions. For instance, Lin and Yang [35] determined the constitutive equation of Ti6Al4V super-plastic alloy using GA, Zain-ul-abedin et al. [36] used GA to study the thermo-mechanical behaviour of AA6056 at low strain rates, Yin et al. [37] implemented GA to optimize the parameters of microstructural evolution of GCr15 steel during hot compression and Aguir et al. [38] used GA-ANN hybrid model to calculate material parameters of an anisotropic material.

### **4.1.3 Artificial neural network**

Artificial neural networks (ANNs) are computational logical structures with multiprocessing elements, which are linked through interconnection weights. In NNs, rather than relying on predetermined assumptions (i.e. that a function is able to describe the constitutive behaviour) data is used to form the model. When the structure of the network is determined, the input variables are supplied during the training stage and the resulting output is compared with the desired output using a convergence criterion. The interconnection weights are then adjusted between layers to increase its performance. This process is repeated until the network performs well on the training set. In the validation stage, the trained network will be assessed on data not included in the training set to estimate its performance and adjust weights and biases if necessary. Consequently, ANNs are capable of handling complex and mathemat-

ically unresolvable relations between parameters and this makes this approach very useful for many applications. In the field of metal forming, many researchers have utilized ANN to predict the forming behaviour of different materials. To exemplify, Elangovan et al. [39], Derogar et al. [40], and Forcellese et al. [41] used NN to predict the forming limit of sheets and Fu et al. [42] used it in conjunction with GA to successfully design an air-bending punch. Kessler et al. [43] implemented ANN into finite element simulation and Abbasi et al. [44] identified mechanical ductile damage using NN.

## 4.2 Experimental and Computational Procedures

Tensile tests were performed on AA5182-O sheet specimens taken at 0, 45, and 90° with respect to the rolling direction (corresponding to RD, DD, and TD). Quasi-static tests ( $\dot{\epsilon} = 0.001, 0.1\text{s}^{-1}$ ) were performed on ASTM-E8 tensile specimens using an Instron 1331 servo-hydraulic testing machine. Intermediate strain rate tests ( $\dot{\epsilon} = 1, 10, 100\text{s}^{-1}$ ) were carried out using a specialized Hydraulic Intermediate Strain Rate apparatus, and a split Hopkinson bar apparatus was used for strain rate of approximately  $1000\text{s}^{-1}$  both using sub-size tensile specimens. The specimens were strained until fracture where load-displacement data were recorded and converted to stress-strain values according to standard methods. In order to measure experimental strain distributions, Digital Image Correlation (DIC) technique was used. First, each specimen was painted in white and then a black stochastic speckle pattern was applied. High speed image acquisition was used to record images of specimens being formed where the deformation of the applied speckle pattern was used as virtual extensometers to measure longitudinal and width strains. Data processing of the recorded images taken from quasi-static and high strain rate specimens were conducted using ARAMIS from GOM and VIC-2D from Correlated Solutions, respectively. More detailed information about testing procedures can be found in Ref. [13, 45].

### 4.2.1 Genetic algorithm approach

Different minimization functions were developed to calculate the parameters of phenomenological constitutive functions based on the fact that the final goal is to have zero difference between the flow stress ( $\sigma$ ) and the right hand side of each constitutive equation (Eqs. 4.1, 4.2, and 4.3). The mean square error (MSE) was chosen to measure the difference between predicted and measured stress values and it can be calculated using Eq.4.4;

$$\text{MSE} = \frac{1}{n} \sum_{i=1}^n (\sigma - \hat{\sigma})^2 \quad (4.4)$$

where  $\sigma$  represents the experimental true stress and  $\hat{\sigma}$  is the predicted stress. Each function will be considered as optimized when the minimum value of this difference for all samples tested in each material direction is reached. During the first trials, it was realized that this technique will provide much more reliable results specially when the experimental data contains noise or serrations and was obtained for a wide range of strain rates. To avoid complication, the reference strain rate ( $\dot{\epsilon}$  in JC and  $\dot{\epsilon}_0$  in KHL) was considered to be unity, and since tests were carried out at room temperature, the temperature-dependent term in the rheological equations was dismissed.

The population size and the fraction of parent-to-children populations were set to 50 and 0.35, respectively. Also, a migration fraction of 0.2 and 20 intervals were used. MATLAB (R2014a) default crossover fraction and mutation function was employed. The maximum number of generations in each optimization was decided by the number of constants to be calculated and a multiplier, and was equal to 250 for JC and 350 for KHL and VM hardening functions. The boundary condition shown in Table 4.1 were chosen based on values obtained from rough curve fitting. To avoid premature termination of the GA process and to obtain superior results, loops were designed to re-run the optimization several times; each loop ends if the value of the fitness function in each algorithm (800 for JC and KHL and 600 for VM), or the maximum number of 100 GAs is reached. Fig. 4.1(a) illustrates the GA process used in this study. The result of each GA was saved and the ones leading to minimum MSE were

Table 4.1: Boundary values of each parameter

JC	KHL	VM
A: 50 – 200	A: 0 – 120	A: 100 – 200
B: 300 – 800	B: 200 – 500	B: 300 – 400
$n$ : 0 – 0.5	$n_0$ : -0.5 – 0.5	$m_1$ : 5 – 15
C: -0.1 – 0.5	$n_1$ : 0 – 1	C: -1 – 0
	$c$ : -0.5 – 0.5	D: 0 – 0.1

chosen for further comparisons and are shown in Table 4.3.

## 4.2.2 Artificial neural network approach

Several structures of back-propagation neural networks with different transfer functions, layers, and numbers of neurons were tested and two networks with reasonable performances were selected to present in this study. The first and simplest network, "NN1" was trained with the Levenberg-Marquardt training algorithm. It consists of two layers; an input layer with the material orientation, the strain rate in logarithmic scale and the true plastic strain as input values and the output layer with true stress as the target. The other network, "NN2", consists of three layers with normalized orientation, logarithmic strain rate and strain values as the inputs and logarithmic stress as the output. In case of NN2, the Bayesian regulation backpropagation training algorithm was used as it produced better weights and biases than Levenberg-Marquardt. Basically, the Bayesian regulation takes place within the Levenberg-Marquardt algorithm and is capable of reaching a minimized combination of weights and errors. Table 4.2 summarizes the structure of networks used in this study where  $\theta$  and  $\tilde{\theta}$  represent orientation and normalized orientation of the specimens, respectively. The analytical form of NN1 and NN2 networks are shown in Eqs. 4.5a and 4.5b, respectively.

$$\tilde{\sigma}_{(1,1)} = w_{O(1,i)} \times f_1 \left( w_{I(i,j)} \times \tilde{I}_{(j,1)} + b_{I(i,1)} \right) + b_{O(1,1)} \quad (4.5a)$$

$$\log(\tilde{\sigma}_{(1,1)}) = w_{O(1,i)} \times f_1 \left[ w_{L1(i,i)} \times f_1 \left( w_{I(i,j)} \times \tilde{I}_{(j,1)} + b_{I(i,1)} \right) + b_{L1(i,1)} \right] + b_{O(1,1)} \quad (4.5b)$$

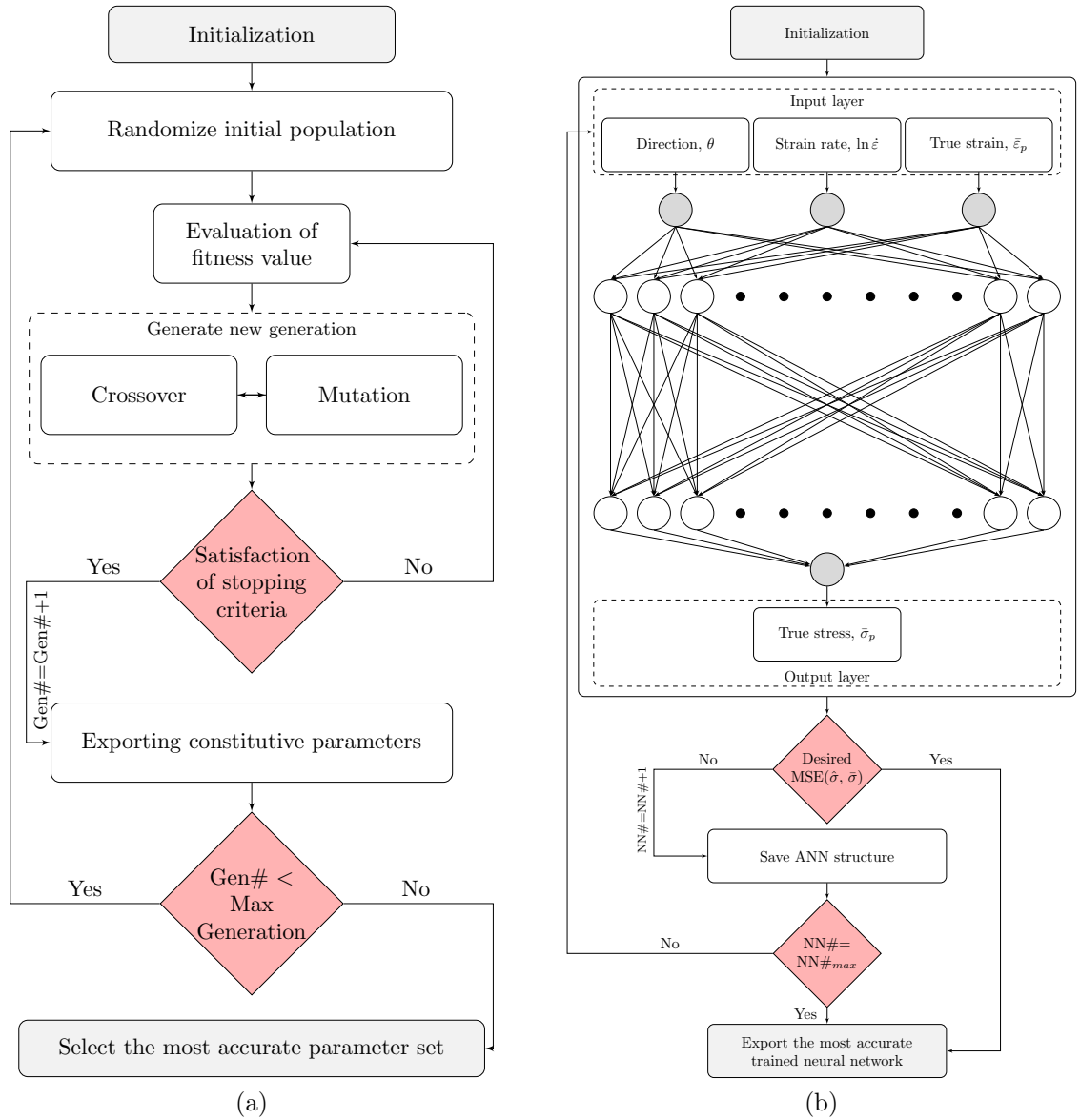


Figure 4.1: Schematic of (a) GA and (b) ANN structure used in this study.

Table 4.2: Neural Network structures used

	NN1	NN2
Number of layers	2	3
Inputs	$I = [\theta; \log(\dot{\varepsilon}); \varepsilon]$	$I = [\tilde{\theta}; \log(\dot{\varepsilon}); \log(\varepsilon)]$
Input range	$\begin{bmatrix} (0 : 90) \\ (-6.908 : 6.908) \\ (0.002 : 0.192) \end{bmatrix}$	$\begin{bmatrix} (0 : 1) \\ (-6.908 : 6.908) \\ (-6.215 : -1.650) \end{bmatrix}$
Output	$\sigma$	$\log(\sigma)$
Output range	(126.19:335.55)	(4.838:5.816)
Input layer	6	15
First hidden layer	-	15
NN <sub>max</sub>	1000	100
Target MSE	1	$1 \times 10^{-6}$
Training algorithm	Levenberg-Marquardt	Bayesian regulation

$$f_1(x) = \frac{2}{1 + e^{-2x}} - 1 \quad (4.5c)$$

where  $\tilde{I}$  and  $\tilde{\sigma}$  represent normalized inputs and stress values,  $W$  and  $b$  represent weights and biases, respectively. The subscripts  $I$ ,  $L_1$  and  $O$  denote input, first and output layers, respectively.  $i$  and  $j$  are the numbers of neurons in the input layer and the number of inputs, respectively.  $f_1$  is the hyperbolic tangent sigmoid transfer function (Eq. 4.5c) which is capable of producing outputs in a range of  $-1$  to  $+1$ . A pure linear transfer function is used in both NN structure to scale outputs up and down for the output layer.

Since the goal is to obtain a network with enhanced accuracies for further studies and specially for simulation purposes, 70% of randomly chosen data were used to train the network and the remaining 30% was used as new experimental data to validate and test its performance. To obtain better results, loops were generated to repeat the process until the desired mean square error (MSE) or the maximum number of training loops was reached. Fig. 4.1(b) graphically shows the neural network structure used in this study.



### 4.2.3 Simulation procedure

To further study the accuracy of each constitutive equation and calculated parameters, uniaxial tensile tests were simulated using ABAQUS dynamic explicit finite element software. The specimen geometries used in the simulations are shown in Fig. 4.2 and correspond with the experimental specimens for quasi-static (Fig. 4.2(a)) and moderate and high strain rates (Fig. 4.2(b)), respectively. In the simulation of quasi-static tests, a quarter symmetry was used (Fig. 4.2(a)) and the region of the specimen that would be locked in the grips was shortened in order to reduce computation time. The boundary condition along the symmetry line that is perpendicular to the specimen axis and in the centre of the gauge area was such that nodal displacements in the loading direction were prevented. Moreover, nodal displacements perpendicular to the loading direction were prevented along the entire symmetry line that is parallel with the specimen axis. A reference point located 10 mm above the top boundary of the specimen (Fig. 4.2(a)) and corresponding with the free edge of the grips was coupled with the top edge. The velocity of the grips measured experimentally in the tensile test was applied to this reference point to ensure that the specimen would deform at the same strain rate in the numerical simulation. For the specimen used to simulate high strain rate deformation (Fig. 4.2(b)), two reference points, each located at 10 mm from one end of the specimen in the region that would be held in the grips of the testing machine, were each coupled to one end of the specimen. For one of these reference points all degrees of freedom were locked and the required velocity was applied to the other reference point.

ABAQUS user material subroutines (VUMATs) were developed and tested accordingly to implement JC, KHL, and VM hardening functions as well as the developed NNs. It is worth pointing out that since the built-in JC constitutive function in ABAQUS does not accept negative strain rate sensitivities, the development of a VUMAT for JC was required. However, simulations were also performed using ABAQUS built-in JC function disregarding the strain rate exponent calculated from GA and Regression results. Python scripts were created and called from MATLAB to run

simulations and extract the required information from simulation results. Simulations were carried out at tensile head velocities that were equivalent to the experimental values and using the calculated constants in the hardening functions.

Mesh sensitivity was considered and the optimum conditions were used to simulate the tensile tests at different strain rates considering computational costs. The specimens were discretized using reduced-integration 8-node linear brick elements. Biased element sizes ranging from 0.05-0.175mm and 0.15-0.75mm were used along the gauge length of quasi-static and high strain rate specimens where the gauge widths were divided into 9 and 10 elements as shown in Fig. 4.2(a) and (b), respectively. Mass scaling was used to reduce computational costs, specially to simulate material behaviour at low strain rates. Instead of measuring stress-strain from a set of elements in the gauge area of specimens, the load-displacement data of the constrained reference point on top of the specimen were used to calculate the flow curve up to the onset of necking which was then compared with the experimental and calculated curves from Eq.4.1, 4.2, and 4.3. It is worth noting that the AA5182-O tested showed minimal variation of r-value with testing direction and strain rate [13]. Consequently, isotropy was assumed in the VUMAT at this stage of development in order to reduce computational complexity. Nevertheless, to minimize error in simulation due to this isotropic assumption, tensile tests were simulated in each direction using the corresponding calculated parameters in order to evaluate the overall performance of the hardening functions and the corresponding user material subroutines.

## 4.3 Results and Discussion

### 4.3.1 Flow behaviour of AA5182-O

The parameters calculated for each constitutive equation using Eqs.(4.1), (4.2), and (4.3) are shown in Table 4.3. The constants vary slightly with loading direction. Fig. 4.3 shows stress-strain curves of selected specimens obtained from experiments as well as constitutive functions and the trained neural network. In general, by utilizing

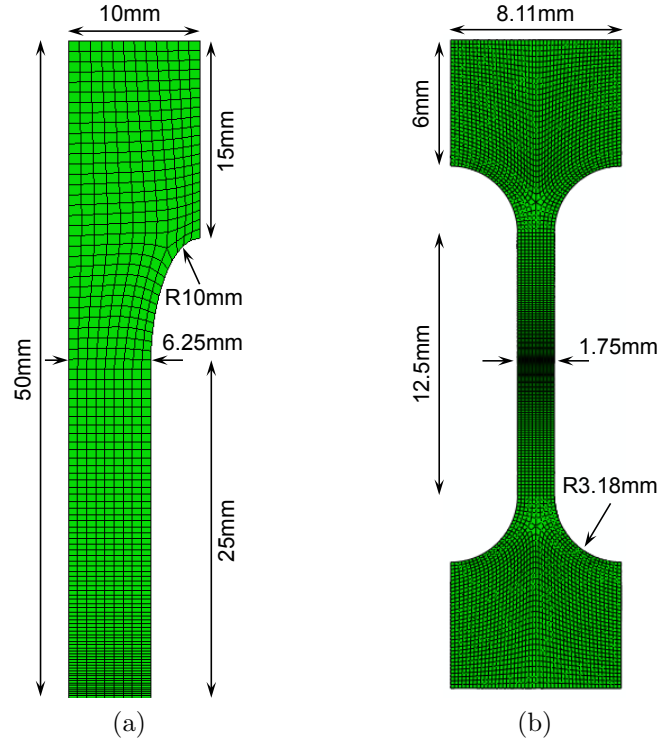


Figure 4.2: Specimen used to simulate (a) QS and (b) high strain rate tensile tests.

the calculated constants shown in Table 4.3, numerical methods successfully predict the flow behaviour of AA5182-O in any direction and strain rate tested. However, some discrepancies can be seen in case of phenomenological methods, especially at low and high strain values (Fig. 4.3(a) and (b)). These inaccuracies seem to diminish as a result of increased scatter in high strain rate experimental data ( $100-1000s^{-1}$ ) but JC and KHL calculated stress values tend to be larger at low strain and smaller at higher strains, as shown in Fig. 4.3(c).

Fig. 4.4 shows the predicted true stress determined by each method against the experimental values of all tested specimens. It can be seen that the selected methods are able to predict the flow behaviour of AA5182-O sufficiently well since the predicted results lie mostly on the line of exact fit. However, the predictions using phenomenological models lose their precision at low strain values, as evidenced by the difference in stress values in Fig. 4.4(a)-(c). Judging by the scattered data in Fig. 4.4(a) and (b), the prediction of the flow stress values using the JC and KHL models are less accurate when compared to the modified-Voce (VM) and ANN approaches. In fact, JC

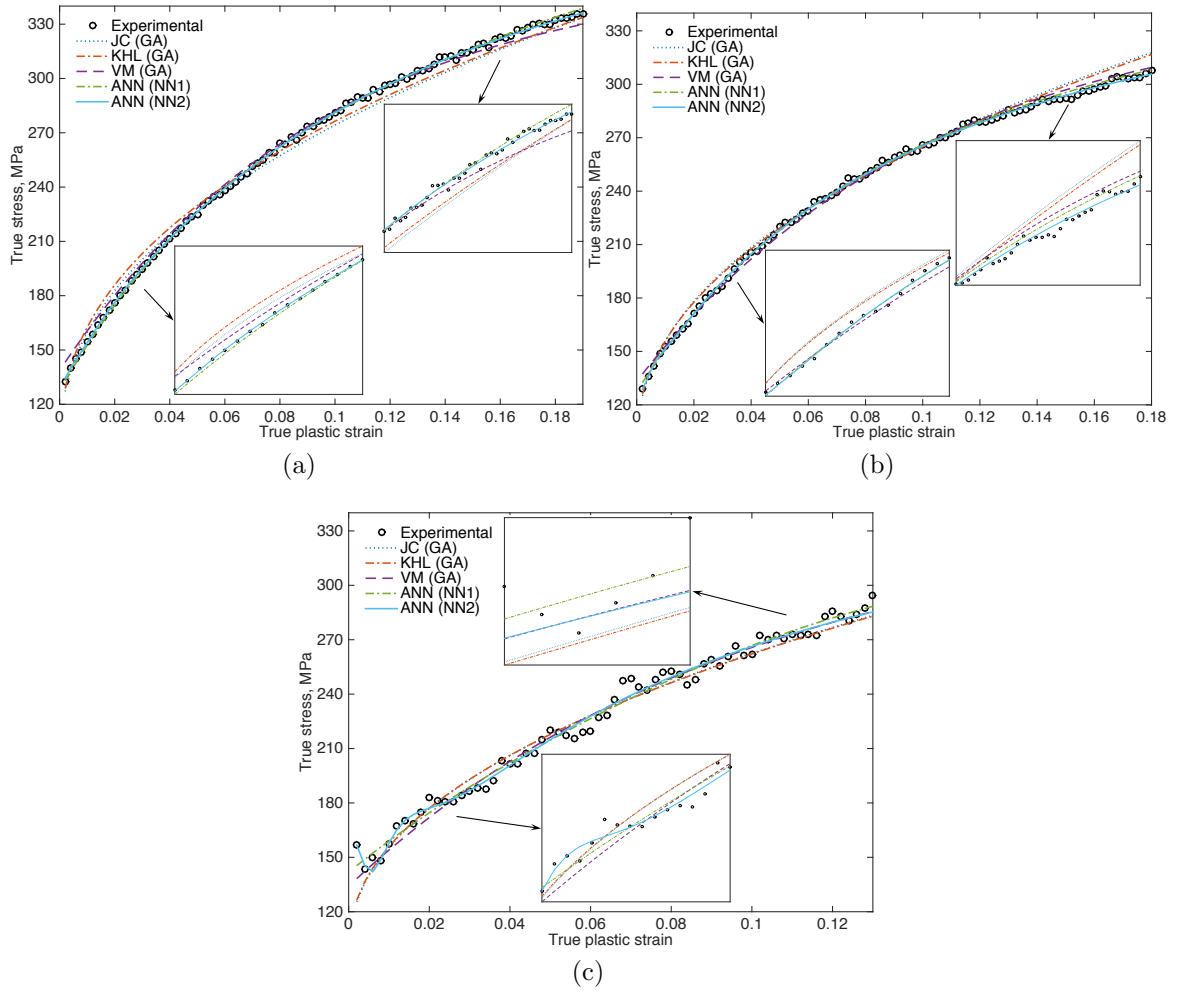


Figure 4.3: Comparison of calculated AA5182-O flow stress with experimental data for (a) RD: 0.001s<sup>-1</sup>, (b) DD: 1s<sup>-1</sup>, and (c) TD:1000s<sup>-1</sup>.

Table 4.3: AA5182-O parameters calculated by GA and regression analysis

		Genetic Algorithm			Regression analysis		
		RD	DD	TD	RD	DD	TD
JC	A	95.789	96.008	98.575	90.394	86.739	88.577
	B	497.051	481.434	473.433	492.812	479.7	464.872
	$n$	0.4488	0.4520	0.4571	0.4268	0.4194	0.4187
	C	-0.00086	-0.00134	-0.00073	-0.0014	-0.0021	-0.0017
KHL	A	89.739	98.695	99.715	85.8	79.4	82.5
	B	486.302	481.936	473.565	478.56	456.925	436.35
	$n_1$	-0.1274	-0.1077	0.0127	-0.2885	-0.2231	0.0641
	$n_0$	0.4271	0.4625	0.4601	0.4202	0.3968	0.3798
	$c$	-0.00748	-0.00659	-0.00017	-0.016	-0.014	0.0013
VM	A	133.383	132.422	134.952	134	128	136
	B	347.445	344.597	343.478	342	339	328
	$m1$	10.327	9.700	10.091	11.11	10.31	11.11
	C	-0.00574	-0.00624	-0.00094	-0.003	-0.006	-0.003
	D	0.00876	0.00873	0.00004	0.008	0.012	0.009

(Eq. 4.1) and KHL (Eq. 4.2) underestimate the flow curve at low strain values whereas VM (Eq. 4.3) overestimates it. However, both trained neural network structures were able to calculate the flow stress of AA5182-O within the entire strain domain with a smaller and almost constant deviation from perfect fit (Fig. 4.4(d)).

### 4.3.2 Determination of accuracy

The accuracy of each method to calculate the flow curves of AA5182-O was examined using adjusted R-squared given in Eq. 4.6 and MSE parameter (Eq. 4.4).

$$R_{\text{adj}}^2 = R^2 - (1 - R^2) \frac{p}{n - p - 1} \quad (4.6a)$$

$$R^2 = 1 - \frac{\sum_{i=1}^n (\sigma - \hat{\sigma})^2}{\sum_{i=1}^n (\sigma - \bar{\sigma})^2} \quad (4.6b)$$

where  $\sigma$ ,  $\hat{\sigma}$ , and  $\bar{\sigma}$  represent the experimental, predicted and mean stress values.  $R$ ,  $n$  and  $p$  in Eq.4.6 are the regression coefficient, sample size and total number of regressors in a given model, respectively. In case of ANN,  $p$  was considered to be the number of neurons in the input layer. When accuracies are compared together

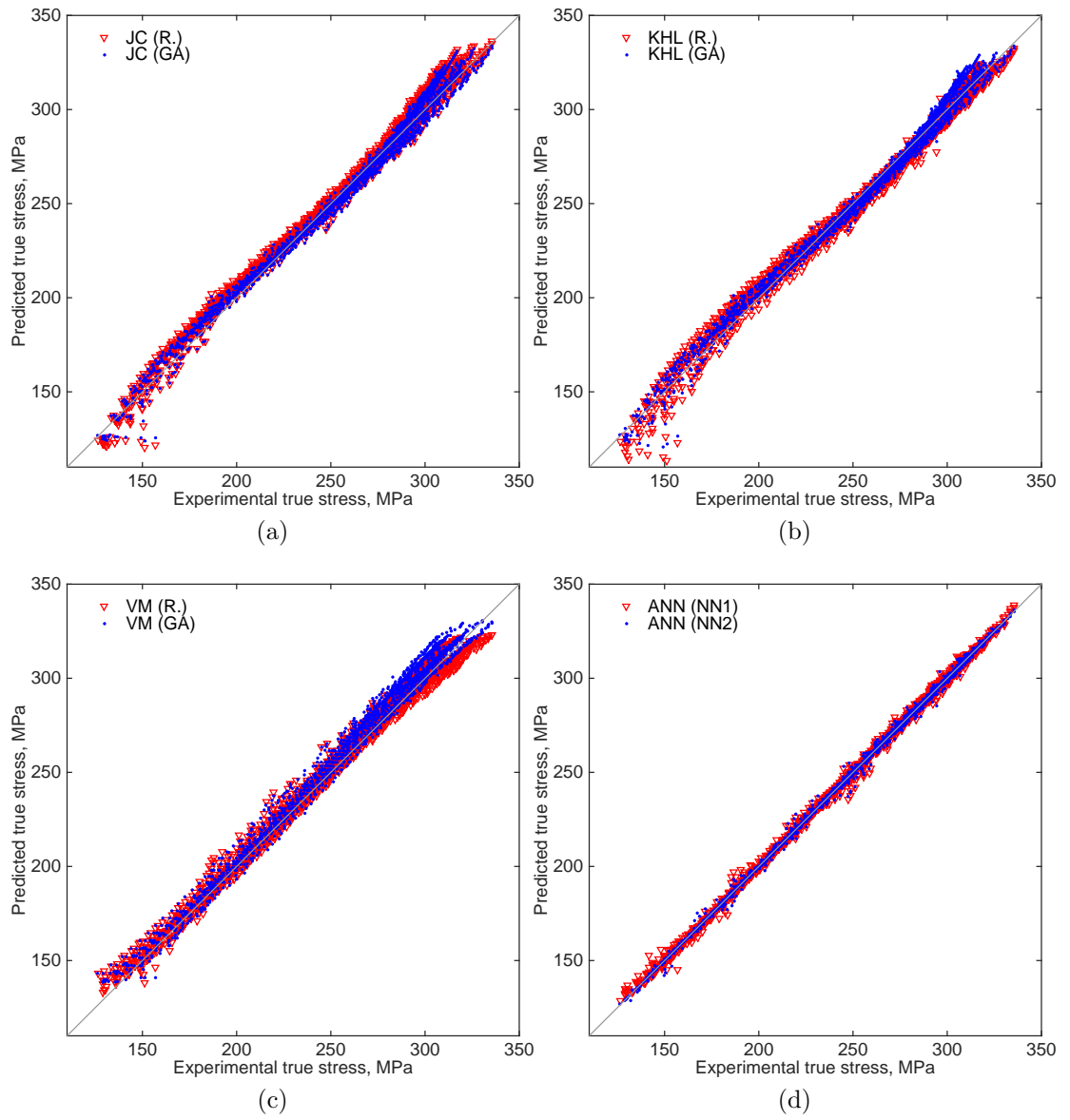


Figure 4.4: Comparison of calculated true stress values with experimental data for (a) JC, (b) KHL, (c) VM, and (d) ANN.

using adjusted R-squared error, all methods exhibit their ability to determine the flow behaviour of AA5182-O for any direction with calculated values always above 0.98, as shown in Fig. 4.5(a).

The overall comparison of accuracy for each of the prediction methods using MSE is shown in Fig. 4.5(b). It can be seen that the modified-Voce equation leads to more accurate predictions when compared with the other hardening functions studied. However, the difference between predictions with JC and KHL is insignificant and they both exhibit reasonable accuracies when used with the GA-calculated constants. In fact all GA calculations lead to more accurate results when compared to parameters derived by regression analysis. In the case of the modified-Voce GA calculations improved the adjusted R-squared from 0.983 to 0.998 for the transverse direction. The superiority of GA compared to the regression method for determining constants, as shown in Fig. 4.5, is due to the calculation procedure taken to determine these parameters; in order to use the regression method, constants related to strain hardening were calculated first and then the strain rate related constants were calculated to avoid the necessity of making the equation linear. In fact, it is a common approach to calculate parameters of such equations separately (e.g. in Ref. [29]). However, in case of GA, all parameters were calculated at the same time and change relative to each other in order to maximize the overall performance. The other obvious advantage of the GA method is the ease of mathematical calculations for the operator. Consequently, the usage of GA to determine the parameters in complex equations is preferable for engineering studies and hence for further analysis of AA5182-O flow behaviour, only GA-calculated parameters will be used.

Besides, Fig. 4.5(b) suggests that the trained simple (NN1) and the more complex (NN2) structures were able to calculate the flow behaviour of AA5182-O better than the rheological constitutive equations. However, the more complex NN2 structure with logarithmic scaled input-output values leads to enhanced accuracy as seen in Fig. 4.5(b). Although only one network was trained on a range of sheet directions in each case, their outcomes show the most accurate agreement with experimentally determined values when compared to individual directions. This ability of NNs to

study the mechanical behaviour of materials makes them useful tools.

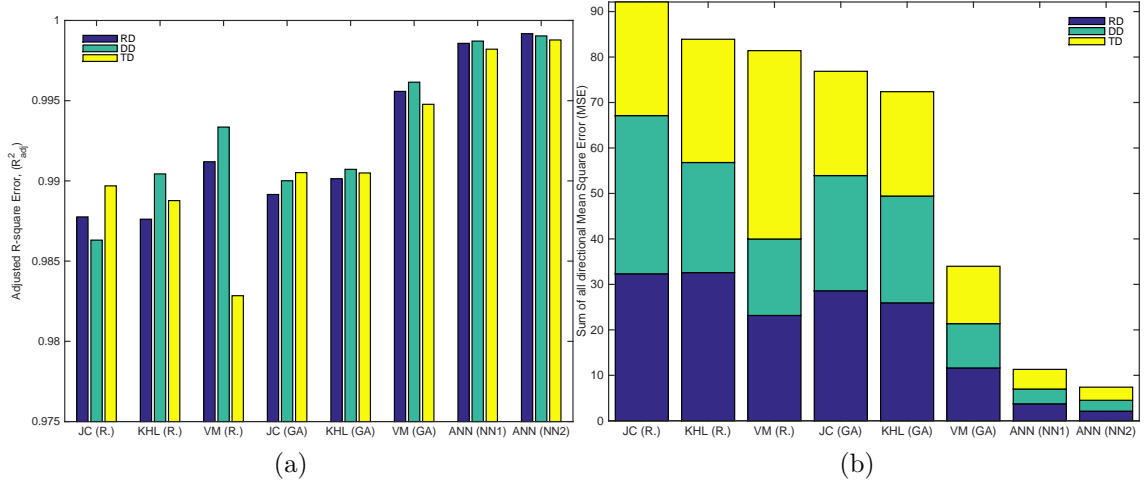


Figure 4.5: Comparison of accuracies of JC, KHL, VM and NN structures based on (a) adjusted R-square, (b) overall MSE values.

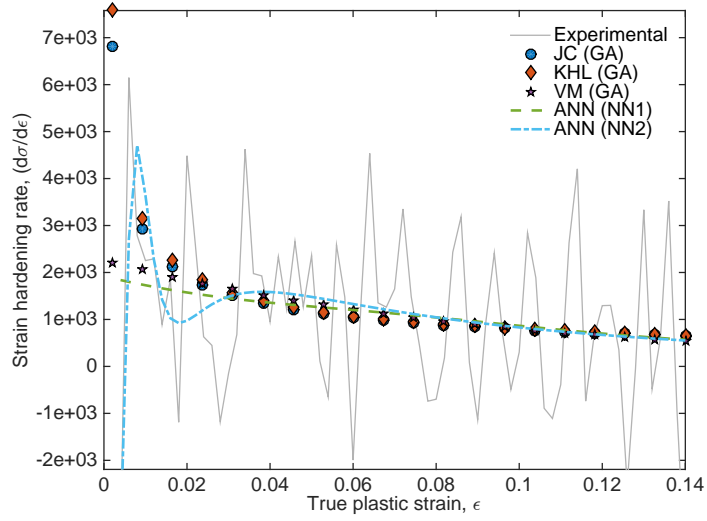
### 4.3.3 Predictions of strain hardening rate and flow stress at different strain values

Fig. 4.6 shows examples of the evolution of strain hardening rate  $(d\sigma/d\varepsilon)|_{\dot{\varepsilon},\theta}$  calculated by each method with true plastic strain in selected specimens. Serrations in experimental values at high strain rates are due to the experimental noise (Fig. 4.6(a)), however, at low strain rates, the serrations are due to plastic strain inhomogeneity caused by the PLC effect, as shown in Fig. 4.6(b).

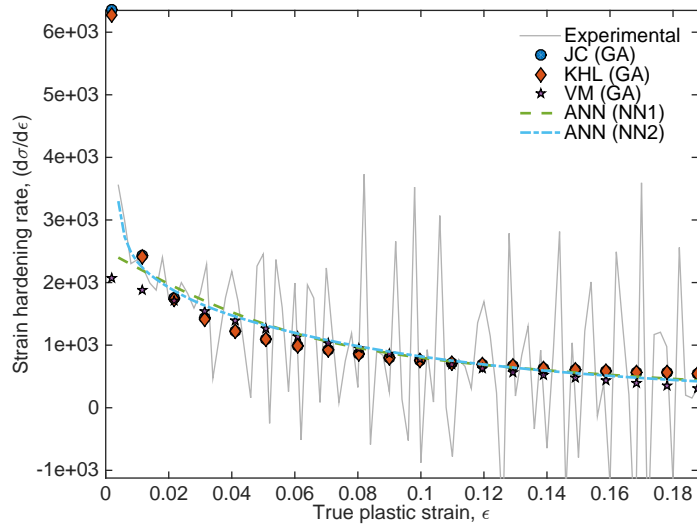
It can be seen in Fig. 4.6(a)-(b) that, although all approaches used in this study are able to satisfactorily calculate the overall strain hardening behaviour of AA5182-O at low and high strain rates, the accuracy is inadequate at low strain values. Although experimental data contain serrations, the inaccuracy of JC and KHL can be seen by their excessively high work hardening rate values at low plastic strains. Consequently, among all prediction methods, VM and the trained NN structures exhibited the most accurate determination of the work hardening rate at low strains whereas the JC and KHL showed the least accuracy.

Fig. 4.7(a) to (d) show the flow stress of AA5182-O at true strains of 0.02 and 0.14,





(a)



(b)

Figure 4.6: Variation of the slope of the true stress vs. true plastic strain curve for (a) RD:  $1000\text{s}^{-1}$ , (b) TD:  $0.001\text{s}^{-1}$ .

respectively, corresponding to low and high ends of the reliable range of true stress in split-Hopkinson bar experiments. The error bars in experimental curves shown in Fig. 4.7 were derived from maximum and minimum measured flow stress from repeated tests.

The difference between the calculated and experimental stress values is of importance in process simulations and hence the preferred approach is the one leading to the minimum difference. A significant observation from Fig. 4.7 is that the flow stress corresponding to the 0.02 to 0.14 strain range decreases to a minimum at low strain rates and then increases at higher strain rates. This trend suggests that the material exhibits negative strain rate sensitivity at low- to moderate-strain rates but positive, although small, values at higher strain rates. This is consistent with the observations of Higashi et al. [46, 47], Mukai et al. [10, 48–50] and Rahmaan et al. [13] for Al-Mg alloys. However, the amount of decrease in flow stress at lower strain rates can be more or less significant, as seen for the DD specimens at 0.02 strain in Fig. 4.7(b).

It can be seen from Fig. 4.7(a)-(d) that the NN structures were able to accurately predict the transition in strain rate sensitivity of AA5182-O at a given strain for the entire range of strain rates. Although NN2 calculations seem to fluctuate somewhat with strain rate, these variations are within the experimental accuracy represented by the error bars. In fact, for experimental strain rates NN2 predictions were so close to the experimental results that the curves almost lie on top of each other. NN1 predictions were also very close to the experimental flow stress making it superior than all phenomenological approaches studied. Phenomenological approaches were able to estimate the flow curves reasonably well but when a single strain rate expression is used (such as in JC Eq. 4.1) they fail to predict its variation with strain rate. However, for most loading directions and strain values, the VM hardening function was also able to replicate the increased stress values at high strain rates (i.e. as shown in Fig. 4.7(a)-(c)).

It is worth emphasizing that the increased stress level of AA5182-O at high strain rates is of importance as it may lead to improved formability [7] considering a simple JC damage model [20]. In fact, the AA5182-O sheets used showed increased formability

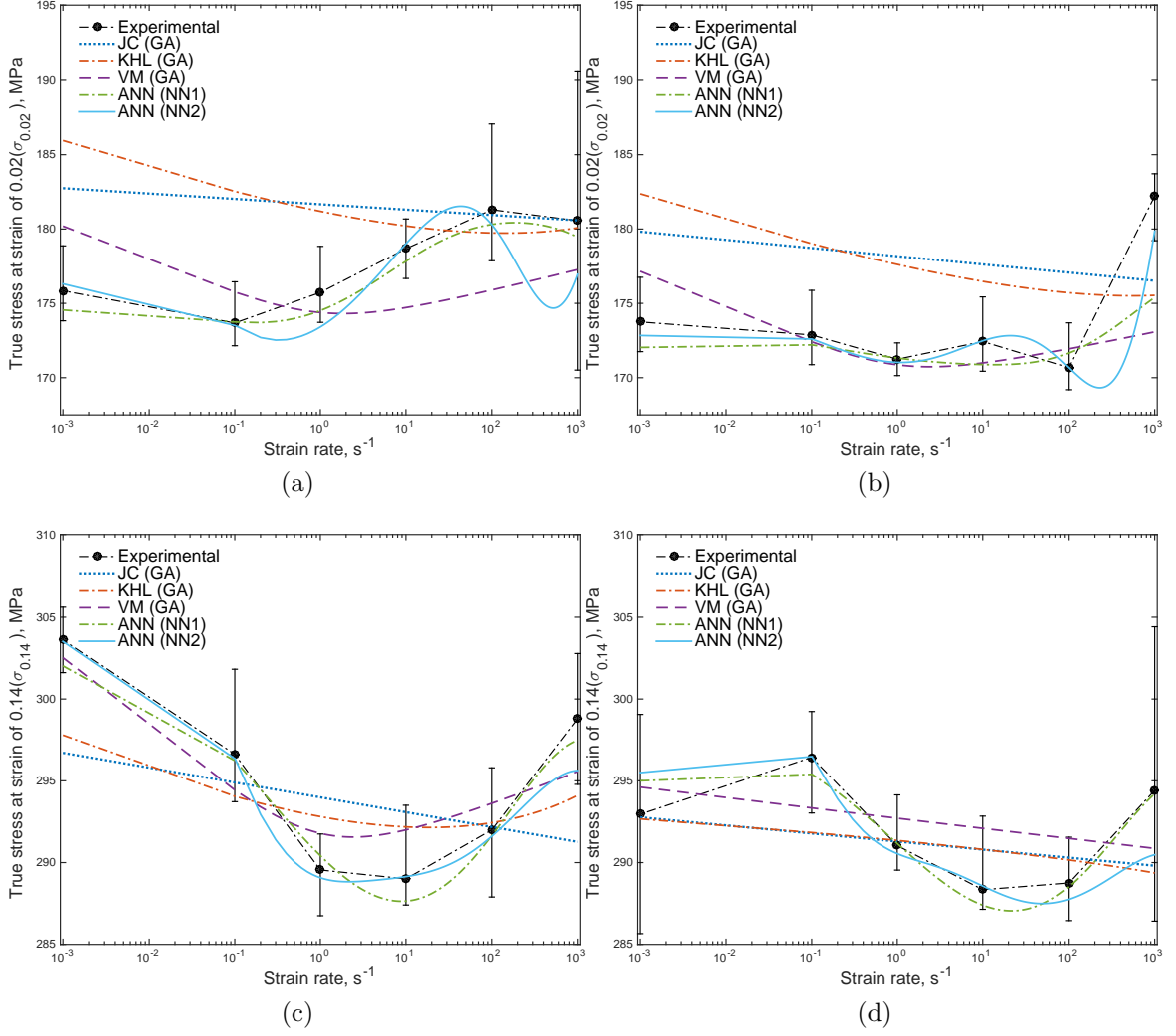


Figure 4.7: Variation of AA5182-O flow stress with strain rate at (a) 0.02 strain in RD, (b) 0.02 strain in DD, (c) 0.14 strain in DD, and (d) 0.14 strain in TD.

when deformed in an electro-hydraulic forming process which can locally reach strain rates above  $1 \times 10^4 \text{s}^{-1}$  [51]. Consequently, the use of NN in finite element simulations can be very useful in that they are capable of predicting flow curves without the limitation of a single strain rate exponent. Further analyses of the changes of stress with strain rate are beyond the scope of this paper and will be discussed elsewhere.

#### 4.3.4 Simulation results

FEM simulations were carried out as explained in section 4.2.3 and the region which exhibits the onset of necking is investigated in more detail. Fig. 4.8 shows contours of

effective strain in tensile specimens at the onset of localized necking predicted by FE simulations using the different approaches studied. In order to increase the clarity of these images, the mesh lines were removed from Fig. 4.8. Fig. 4.8(a) corresponds to quasi-static ( $0.1\text{s}^{-1}$ ) and Fig. 4.8(b) represents specimens deformed at moderate strain rates ( $100\text{s}^{-1}$ ). Severe shear bands can be seen in quasi-static specimens but their severity reduces at high strain rates. The diffused neck is observable in all cases but the intensity of localization differs depending on the method used to define the work hardening behaviour. In case of JC and KHL models, the deformation is more uniform in the gauge area since at the onset of necking, the sample experienced larger strains overall. On the other hand, results from NN2, NN1 and especially VM suggest that necking is very localized in a specimen that, overall, was strained less when necking occurred. In other words, strains localized earlier when VM or NNs user subroutines were used. In both cases, judging by the intensity of the effective strains, failure is expected to start inside the gauge area where shear bands intersect. Fig. 4.9 shows the strain distribution at the onset of necking in a tensile specimen formed under quasi-static strain rates. It can be seen that not only the strain distribution around the localized area are close to VM, NN1 and NN2 predictions, but the equivalent strain values are also very close to the simulation results for VM, NN1 and NN2 (Fig. 4.8(a)).

In order to quantify the accuracy of each approach in modelling the tensile behaviour, the flow curves calculated from the load-displacement data predicted by finite element analysis at different strain rates and material orientations were compared with the experimental flow curves, and the MSE was calculated in each case. Fig. 4.10(a) shows overall MSE using each method used. It can be seen from Fig. 4.10(a) that the developed subroutines were able to predict the mechanical response of this sheet material with acceptable accuracy especially when compared with the ABAQUS built-in JC hardening function. Also, disregarding the negative but insignificant strain rate exponent in JC will result in 14.7% less accuracy in the predicted flow curve. Furthermore, the KHL formulation leads to the most accurate simulation results among the phenomenological hardening functions considered, followed by VM and JC which

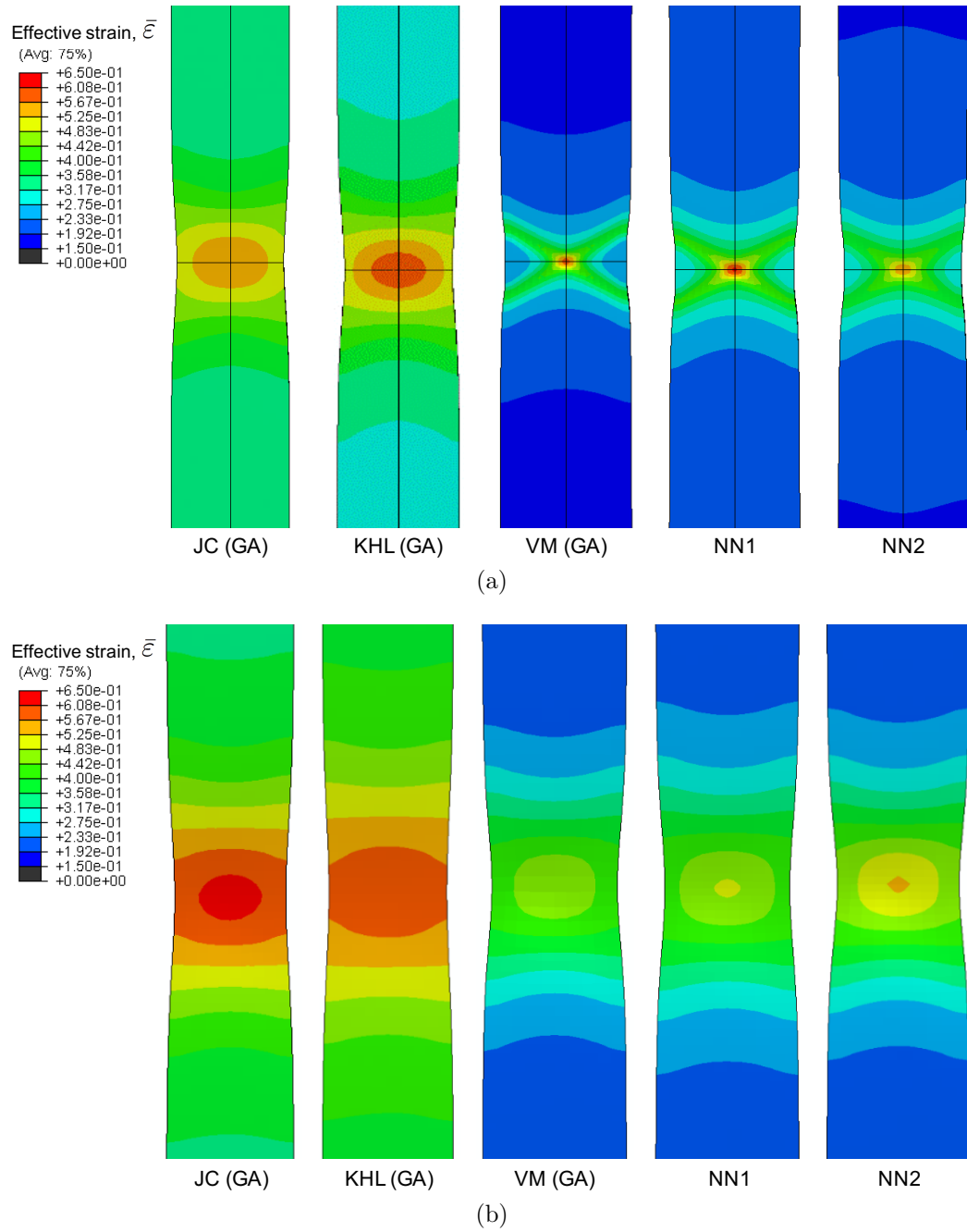


Figure 4.8: Contours of effective strain values predicted by different hardening models at the onset of necking for specimens deformed at (a)  $0.1\text{s}^{-1}$  and (b)  $100\text{s}^{-1}$  strain rates.

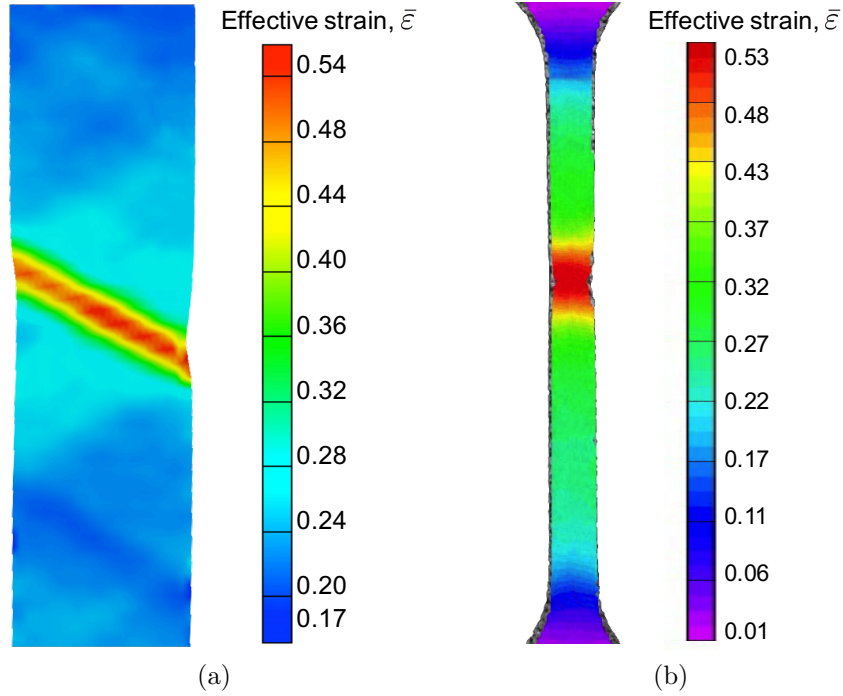


Figure 4.9: Experimental strain distribution at the onset of instability for specimen formed under (a) quasi-static and (b)  $100\text{s}^{-1}$  strain rate.

also show reasonable accuracy. The NN2 structure was the most accurate method used, with 19.5% better performance than KHL. The NN1 overall performance was between that of KHL and NN2.

Fig. 4.10(b) shows the average computational cost and MSE that were achieved in order to carry out the simulation of the complete tensile test with each hardening function. All tests were performed on a computer with an 8-core 3.40GHz CPU and the run time was measured by MATLAB which was used to create, submit and finalize the simulation. It can be seen that JC and KHL were the most cost efficient methods used, with JC being the least accurate method. The enhanced accuracies in case of NN2 came with more than twice the computational cost when compared with the KHL hardening function. Although, the simple structure of NN (NN1) was reasonably accurate, its computational cost was unreasonably higher than that of the more complex NN (NN2) studied. Hence, NN1 structure network would not be a preferred approach to simulate complex forming processes. Another interesting observation is that although the VM hardening function was able to predict the flow

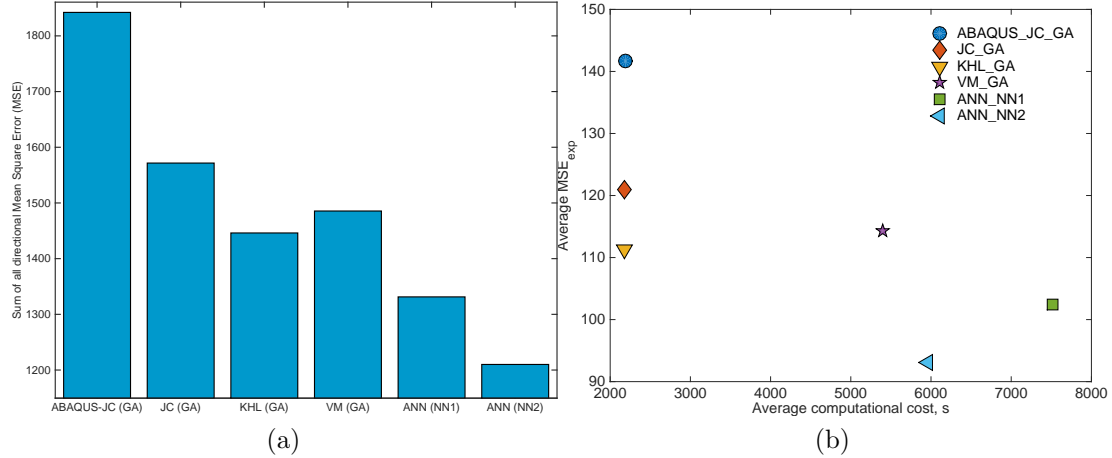


Figure 4.10: (a) Comparison of simulation accuracies and (b) Computational cost vs accuracies.

curves of AA5182-O with much greater accuracy compared to KHL and JC (Fig. 4.5), its accuracy reduced to just below that of the KHL model in the simulations of the tensile tests but with added computation cost. The reason for this reduced accuracy is the intensity of strain localization in the necked region which is more pronounced when the VM hardening function is used, as shown in Fig. 4.8(a). The combination of this extensive localization and the lower strain hardening rate at high strain values and low strain rate deformations (shown in Fig. 4.6(b)) leads to significant reduction in the load measured from the reference point and subsequently VM exhibited reduced accuracy compared to KHL hardening function.

## 4.4 Conclusions

In this study, the flow behaviour of AA5182-O in the strain rate range from  $0.001$  to  $1000\text{s}^{-1}$  and along the three major directions of the sheet (RD, DD, and TD) was investigated using two computational methods; genetic algorithm was used to successfully determine the parameters in commonly used constitutive equations and artificial neural network was used to directly calculate flow stress from experimental variables. The predicted flow curves were then compared to experimental data and the accuracy was evaluated with linear regression method calculations. The following

conclusions can be made;

1. Genetic algorithm is able to solve problems without mathematical limitations and exhibits enhanced performance compared to linear regression analysis. Parameters in the hardening functions calculated by genetic algorithm lead to the most accurate predictions when compared with experimental data.
2. The flow stress of AA5182-O decreases to its minimum at intermediate strain rates (from approximately 10 to 100s<sup>-1</sup>) and then increases with increasing strain rate. Among the hardening models studied, the neural network was the only approach capable to replicate this behaviour. The strain rate term in JC and KHL constitutive equations used were unable to predict such a transition and predicted small negative values of strain rate sensitivity. However, the modified-Voce with logarithmic and exponential strain rate terms exhibited better capability to predict the trend of increasing flow stress at high strain rates. Also, disregarding this small but negative strain rate exponent can lead to considerable inaccuracies in finite element simulations of the tensile tests.
3. Flow stress values calculated using the modified Voce hardening function shows better agreement with experimental data when compared with KHL and JC models. However, KHL results were slightly more accurate when used in finite element simulation.
4. The most accurate calculations of flow stress values for any given direction, strain, and strain rate were predicted using ANN when compared analytically with experimental results or when used in finite element simulation. However, its computational costs were considerable when used in finite element simulation when compared with KHL or JC hardening functions.

## 4.5 Acknowledgements

This research was funded by NSERC's Automotive Partnership Canada program with support from Amino North America Corp., ArcelorMittal Dofasco, Ford Motor Com-



pany, CanmetMATERIALS-Natural Resources Canada and Novelis Inc. Helpful discussions and support received from Dr. Kevin P. Boyle and Prof. Ahmet T. Alpas are also gratefully acknowledged.

## 4.6 References

- [1] W. J. Joost, "Reducing Vehicle Weight and Improving U.S. Energy Efficiency Using Integrated Computational Materials Engineering," *Jom*, vol. 64, pp. 1032–1038, Aug. 2012.
- [2] E. M. Taleff, P. J. Nevland, and P. E. Krajewski, "Tensile ductility of several commercial aluminum alloys at elevated temperatures," *Metallurgical and Materials Transactions a-Physical Metallurgy and Materials Science*, vol. 32, no. 5, pp. 1119–1130, 2001.
- [3] W. Miller, L. Zhuang, J. Bottema, A. Wittebrood, P. De Smet, A. Haszler, and A. Vieregge, "Recent development in aluminium alloys for the automotive industry," *Materials Science and Engineering: A*, vol. 280, pp. 37–49, Mar. 2000.
- [4] E. M. Taleff, P. J. Nevland, and P. E. Krajewski, "Solute-drag creep and tensile ductility in aluminum alloys," in *Creep Behavior of Advanced Materials for the 21st Century*, pp. 349–358, The Mineral, Metals & Materials Society, 1999.
- [5] A. Jenab, A. Karimi Taheri, and A. K. Taheri, "Experimental investigation of the hot deformation behavior of AA7075: Development and comparison of flow localization parameter and dynamic material model processing maps," *International Journal of Mechanical Sciences*, vol. 78, pp. 97–105, Jan. 2014.
- [6] V. Balanethiram, X. Hu, M. Altynova, and G. S. Daehn, "Hyperplasticity: Enhanced formability at high rates," *Journal of Materials Processing Technology*, vol. 45, pp. 595–600, Sept. 1994.
- [7] S. F. Golovashchenko, A. J. Gillard, and A. V. Mamutov, "Formability of dual phase steels in electrohydraulic forming," *Journal of Materials Processing Technology*, vol. 213, pp. 1191–1212, July 2013.
- [8] R. Picu, G. Vincze, F. Ozturk, J. J. Gracio, F. Barlat, a. M. Maniatty, and R. C. Picua, "Strain rate sensitivity of the commercial aluminum alloy AA5182-O," *Materials Science and Engineering A*, vol. 390, pp. 334–343, jan 2005.
- [9] M. Abbadi, P. Hähner, and A. Zeghloul, "On the characteristics of Portevin - Le Chatelier bands in aluminum alloy 5182 under stress-controlled and strain-controlled tensile testing," *Materials Science and Engineering A*, vol. 337, no. 1-2, pp. 194–201, 2002.
- [10] S. T. T. Mukai K. Higashi, T. Mukai, K. Higashi, and S. Tanimura, "Influence of the magnesium concentration on the relationship between fracture mechanism and strain rate in high purity Al-Mg alloys," *Materials Science and Engineering: A*, vol. 176, no. 1-2, pp. 181–189, 1994.
- [11] Y. C. Lin, Y. C. Xia, X. M. Chen, and M. S. Chen, "Constitutive descriptions for hot compressed 2124-T851 aluminum alloy over a wide range of temperature and strain rate," *Computational Materials Science*, vol. 50, no. 1, pp. 227–233, 2010.
- [12] S. A. Hosseini Kordkheili, M. M. Ashrafiyan, and H. Toozandehjani, "A rate-dependent constitutive equation for 5052 aluminum diaphragms," *Materials and Design*, vol. 60, pp. 13–20, 2014.

- [13] T. Rahmaan, A. Bardelcik, J. Imbert, C. Butcher, and M. J. Worswick, "Effect of strain rate on flow stress and anisotropy of DP600 , TRIP780 , and AA5182-O sheet metal alloys," *International Journal of Impact Engineering*, vol. 88, pp. 72–90, 2016.
- [14] L. Chen, G. Zhao, and J. Yu, "Hot deformation behavior and constitutive modeling of homogenized 6026 aluminum alloy," *Materials & Design*, vol. 74, pp. 25–35, 2015.
- [15] A. Jenab and A. Karimi Taheri, "Evaluation of low strain rate constitutive equation of 7075 aluminium alloy at high temperature," *Materials Science and Technology*, vol. 27, no. 6, pp. 1067–1072, 2011.
- [16] D. Trimble and G. O'Donnell, "Constitutive Modelling for elevated temperature flow behaviour of AA7075," *Materials & Design*, vol. 76, pp. 150–168, 2015.
- [17] Y. C. Lin and X. M. Chen, "A critical review of experimental results and constitutive descriptions for metals and alloys in hot working," *Materials & Design*, vol. 32, no. 4, pp. 1733–1759, 2011.
- [18] M. T. Anaraki, M. Sanjari, and A. Akbarzadeh, "Modeling of high temperature rheological behavior of AZ61 Mg-alloy using inverse method and ANN," *Materials & Design*, vol. 29, no. 9, pp. 1701–1706, 2008.
- [19] A. Jenab, A. Karimi Taheri, and K. Jenab, "The Use of ANN to Predict the Hot Deformation Behavior of AA7075 at Low Strain Rates," *Journal of Materials Engineering and Performance*, vol. 22, pp. 903–910, Aug. 2012.
- [20] G. R. Johnson, W. H. Cook, H. S. Rates, and H. Temperatures, "A constitutive model and data for metals subjected to large strains, high strain rates and high temperatures," in *Proceedings of the 7th International Symposium on Ballistics*, vol. 21, pp. 541–547, The Hague, Netherlands: International Ballistics Committee, 1983.
- [21] Y. C. Lin, X. M. Chen, and G. Liu, "A modified Johnson-Cook model for tensile behaviors of typical high-strength alloy steel," *Materials Science and Engineering A*, vol. 527, no. 26, pp. 6980–6986, 2010.
- [22] A. Rohatgi, A. Soulami, E. V. Stephens, R. W. Davies, and M. T. Smith, "An investigation of enhanced formability in AA5182-O Al during high-rate free-forming at room-temperature: Quantification of deformation history," *Journal of Materials Processing Technology*, vol. 214, pp. 722–732, Mar. 2014.
- [23] R. Smerd, S. Winkler, C. Salisbury, M. Worswick, D. Lloyd, and M. Finn, "High strain rate tensile testing of automotive aluminum alloy sheet," *International Journal of Impact Engineering*, vol. 32, pp. 541–560, Dec. 2005.
- [24] D. Banabic and K. Siegert, "Anisotropy and formability of AA5182-0 aluminium alloy sheets," *CIRP Annals - Manufacturing Technology*, vol. 53, no. 1, pp. 219–222, 2004.
- [25] N. Abedrabbo, F. Pourboghrat, and J. Carsley, "Forming of AA5182-O and AA5754-O at elevated temperatures using coupled thermo-mechanical finite element models," *International Journal of Plasticity*, vol. 23, pp. 841–875, May 2007.
- [26] J. W. Signorelli, M. a. Bertinetti, and P. a. Turner, "Predictions of forming limit diagrams using a rate-dependent polycrystal self-consistent plasticity model," *International Journal of Plasticity*, vol. 25, no. 1, pp. 1–25, 2009.
- [27] A. S. Khan, Y. Sung Suh, and R. Kazmi, "Quasi-static and dynamic loading responses and constitutive modeling of titanium alloys," *International Journal of Plasticity*, vol. 20, pp. 2233–2248, Dec. 2004.
- [28] A. S. Khan and M. Baig, "Anisotropic responses, constitutive modeling and the effects of strain-rate and temperature on the formability of an aluminum alloy," *International Journal of Plasticity*, vol. 27, pp. 522–538, Apr. 2011.

- [29] F. Kabirian, A. S. Khan, and A. Pandey, “Negative to positive strain rate sensitivity in 5xxx series aluminum alloys: Experiment and constitutive modeling,” *International Journal of Plasticity*, vol. 55, pp. 232–246, Apr. 2014.
- [30] E. Voce, “The relationship between stress and strain for homogeneous deformation,” *Journal of the Institute of Metals*, vol. 74, pp. 537–562, 1948.
- [31] H. J. Kleemola and M. a. Nieminen, “On the strain-hardening parameters of metals,” *Metallurgical Transactions*, vol. 5, no. 8, pp. 1863–1866, 1974.
- [32] G. Sainath, B. Choudhary, J. Christopher, E. Isaac Samuel, and M. Mathew, “Applicability of Voce equation for tensile flow and work hardening behaviour of P92 ferritic steel,” *International Journal of Pressure Vessels and Piping*, vol. 132-133, pp. 1–9, 2015.
- [33] C. Zhang and B. Wang, “Identification of the hardening behavior of solids described by three-parameter Voce law using spherical indentation,” *Journal of Materials Research*, vol. 27, no. 20, pp. 2624–2629, 2012.
- [34] S.N.Sivanandam and S.N.Deepa, *An introduction to genetic algorithms*. New York: Springer Berlin Heidelberg, 2008.
- [35] J. Lin and J. Yang, “GA-based multiple objective optimisation for determining viscoplastic constitutive equations for superplastic alloys,” *International Journal of Plasticity*, vol. 15, pp. 1181–1196, Jan. 1999.
- [36] M. Zain-ul abdein, D. Nélias, J.-F. Jullien, and A. I. Wagan, “Thermo-mechanical characterisation of AA 6056-T4 and estimation of its material properties using Genetic Algorithm,” *Materials & Design*, vol. 31, pp. 4302–4311, Oct. 2010.
- [37] F. Yin, L. Hua, H. Mao, X. Han, D. Qian, and R. Zhang, “Microstructural modeling and simulation for GCr15 steel during elevated temperature deformation,” *Materials and Design*, vol. 55, pp. 560–573, 2014.
- [38] H. Aguir, H. BelHadjSalah, and R. Hambli, “Parameter identification of an elastoplastic behaviour using artificial neural networks–genetic algorithm method,” *Materials & Design*, vol. 32, pp. 48–53, Jan. 2011.
- [39] K. Elangovan, C. S. Narayanan, and R. Narayanasamy, “Modelling the correlation between the geometrical features and the forming limit strains of perforated Al 8011 sheets using artificial neural network,” *International Journal of Material Forming*, vol. 4, pp. 389–399, Nov. 2010.
- [40] A. Derogar and F. Djavanroodi, “Artificial Neural Network Modeling of Forming Limit Diagram,” *Materials and Manufacturing Processes*, vol. 26, pp. 1415–1422, Nov. 2011.
- [41] A. Forcellese, F. Gabrielli, and M. Simoncini, “Prediction of flow curves and forming limit curves of Mg alloy thin sheets using ANN-based models,” *Computational Materials Science*, vol. 50, pp. 3184–3197, oct 2011.
- [42] Z. Fu, J. Mo, L. Chen, and W. Chen, “Using genetic algorithm-back propagation neural network prediction and finite-element model simulation to optimize the process of multiple-step incremental air-bending forming of sheet metal,” *Materials & Design*, vol. 31, pp. 267–277, Jan. 2010.
- [43] B. S. Kessler, a. S. El-Gizawy, and D. E. Smith, “Incorporating Neural Network Material Models Within Finite Element Analysis for Rheological Behavior Prediction,” *Journal of Pressure Vessel Technology*, vol. 129, no. 1, p. 58, 2007.
- [44] F. Abbassi, T. Belhadj, S. Mistou, and A. Zghal, “Parameter identification of a mechanical ductile damage using artificial neural networks in sheet metal forming,” *Materials and Design*, vol. 45, pp. 605–615, 2013.

- [45] A. C. Thompson, *High Strain Rate Characterization of Advanced High Strength Steels by*. PhD thesis, University of Waterloo, 2006.
- [46] K. Higashi, T. Mukai, K. Kaizu, S. Tsuchida, and S. Tanimura, "Strain rate Dependence on Mechanical Properties in Some Commercial Aluminum Alloys," *Le Journal de Physique IV*, vol. 01, pp. C3-341–C3-346, Oct. 1991.
- [47] K. Higashi, T. Mukai, K. Kaizu, S. Tsuchida, and S. Tanimura, "The microstructural evolution during deformation under several strain rates in a commercial 5182 aluminium alloys," *Le Journal de Physique IV*, vol. 01, pp. C3-347–C3-352, Oct. 1991.
- [48] T. Mukai, K. Ishikawa, and K. Higashi, "Influence of strain rate on the mechanical properties in fine-grained aluminum alloys," *Materials Science and Engineering: A*, vol. 204, pp. 12–18, dec 1995.
- [49] T. Mukai, K. Ishikawa, and K. Higashi, "Strength and ductility under dynamic loading in fine- grained IN905XL aluminum alloy," *Metallurgical and Materials Transactions A*, vol. 26, pp. 2521–2526, oct 1995.
- [50] T. Mukai, M. Kawazoe, and K. Higashi, "Strain-rate dependence of mechanical properties in AA5056 Al–Mg alloy processed by equal-channel-angular-extrusion," *Materials Science and Engineering: A*, vol. 247, pp. 270–274, jun 1998.
- [51] A. Jenab, D. E. Green, A. T. Alpas, and K. P. Boyle, "Formability of AA5182-O Sheet during Electro-Hydraulic Forming : Influence of Input Energy," in *MS&T*, 2015.

## Chapter 5

# Experimental and Numerical Analyses of Formability Improvement of AA5182-O Sheet during Electro-Hydraulic Forming

This chapter discusses the mechanical aspects of formability improvement of AA5182-O using finite element analysis. Factors such as strain rate, stress triaxiality and hydrostatic pressure were calculated from the results of numerical simulation of the EHFF and EHDF process. And in order to verify that the FE model was reliable, simulation results were extensively compared with experimental EHF data.

In order to simulate the loading in EHF, different attempts were made following approaches made in the literature. In each case, deformation, force, acceleration or explosive weight were calibrated based on EHFF experimental results and FE analysis were compared carefully with other EHFF and EHDF experimental results. Since only one of these approaches was selected for publication, the following brief description is worth noting here:

- In a first approach, the effect of the water was neglected by not representing this medium in the EHF simulation. Instead, the EHF pulse was simulated by applying a constant pressure with non uniform distribution on the sheet. This approach was used in earlier attempts to simulate EHF since it was used by Rohathi et al. [32] and Melander et al. [27]. However, it was found that although it gives good correlation between experimental strain measurements and FE analysis, the predicted values of strain rate and velocity were unreasonably high. Besides, the total internal energy had not reached a plateau suggesting that the FE analysis was erroneous.
- In a second approach, FE analysis was performed considering the water in cham-

ber as eulerian material and the effect of EHF pulse was simplified by using an accelerated surface. This attempt was similar to that used by Hassannejad et al. [13] and Maris et al. [26]. This approach gives satisfactory results when compared with experimental strain measurements, and more specifically, more realistic strain rate values were obtained with this approach. However, following discussion with Prof. Golovashchenko, it was noticed that the hydrostatic pressure generated in the sheet upon impact with the die is significantly lower than what would be expected based on the velocity of the sheet.

- Lastly, the FE analysis was performed using the ignition and growth model considering JWL equation of state for an explosive material located inside the water chamber and at the exact location where EHF electrodes were located. It was found that, since this approach closely resembles the EHF process, it leads to more accurate predictions and hence was used to carry out the research that is reported in the following publication.

It is noteworthy that since the latter loading system were based on Coupled Eulerian-Lagrangian (CEL) approach with significantly more elements involved, the computational costs to perform, calibrate and fine-tune the simulations were significant.

Consequently, in this chapter, the formability of electro-hydraulically formed AA5182-O aluminium sheet was investigated by means of experimental testing and numerical modelling. The experimental results were compared with quasi-static, as-received forming limit curve (FLC) and were used to calibrate a finite element model of EHF. It is found that the formability improvement of AA5182-O sheets was insignificant when electro-hydraulically formed without a die. However, when specimens were electro-hydraulically formed with sufficient energy into 34 or 40° conical dies, the effective strain measured in safe grids increased by 40 and 70% respectively when compared with a conservative quasi-static FLC.

Finite element simulation results suggested that a combination of different mechanical parameters contributed to the formability improvement. The increased strain rate in areas close to the apex of the specimen, the negative stress triaxiality just before

specimens contact the die, and significant compressive through-thickness stress generated by high-velocity impact all contributed to the improvement of formability in electro-hydraulic die forming.

∴ This section is accepted for publication: Arash Jenab, Daniel E. Green, Ahmet T. Alpas, Sergey F. Golovashchenko, “Experimental and Finite Element Modelling of Formability Improvement of AA5182-O Sheet during Electro-Hydraulic Forming”, Journal of Materials Processing Technology, December 2017.

## 5.1 Introduction

According to Polmear (2006) the extensive use of Al-Mg alloys (5000-series) in automotive, aerospace and shipbuilding industries is due to their high specific strength, weldability and corrosion resistance. However, Taleff et al. (1999) indicated that in comparison to highly formable steel sheets Al-Mg alloys exhibit lower formability at room temperature. To overcome this limitation, warm forming or hot deformation can be used but forming at elevated temperatures has its own drawbacks, including those associated with additional cost due to the use of specialized lubrication, high energy consumption and post-forming cleaning. An alternative approach is to use high-strain-rate forming techniques such as explosive forming carried out by Balanethiram and Daehn, Balanethiram and Daehn (1992, 1994), electro-magnetic forming (EMF) as performed by Imbert et al. (2005) or Golovashchenko et al. (2013) work on electro-hydraulic forming (EHF). Balanethiram et al. (1994) and Balanethiram (1996) attributed improved formability achieved from these high-rate forming techniques to “*inertial effects*” and changes in material behaviour which stabilize neck formation. To exemplify the improved formability, Seth et al. (2005) observed 30-40% increase in failure strains of different low alloy steels during EMF process. In case of aluminium alloys, Seth (2006) also investigated formability changes of AA6063-T6 during EMF tube expansion and reported that the true strains increased from 8-11% under quasi-static deformation to range of 10-55% in EMF tube expansion tests. Moreover, Oliveira et al. (2005) performed EMF experiments on AA5754(1-1.6mm) and AA5182(1mm) alloys and using numerical simulations estimated the strain rate to be about  $3500\text{s}^{-1}$  and the maximum velocity to be 250-300m/s. Their simulations suggested that higher strains can be reached when the input energy or applied voltage



is increased. Furthermore, Imbert et al. (2005) investigated free and die form EMF (EMFF and EMDF) behaviour of AA5754 sheet. They reported that the major engineering strains in QS condition for the alloy is 20-30% and this number improved to 35-45% in EMDF with an apex angle of 112° apex angle die Imbert et al. (2005) and 65% for the 100° apex angle die).

The effect of high strain rate forming process on forming limit curves (FLC) was also studied by different scholars. Thomas et al. (2007) investigated the changes of forming limit curves of AA6063-T6 aluminium alloy using EMF ring expansion tests and reported two to three-fold increase in the forming limit. Gerdooei et al. (2009) used the Marciniak and Kuczynski model to predict the FLC and increase of 146% in AA6061 formability.

Elimination of matching dies and a decrease in press size are some of the advantages of explosive forming techniques which result in a reduction in initial capital investment. According to Imbert and Worswick (2011), one of the uses for explosive forming is to sharpen corner radii that can be impossible to achieve via conventional forming techniques.

Among all high-strain-rate forming processes, electro-hydraulic forming is of special interest because of the ease which the process can be controlled, the ability to form sheets with lower electrical conductivity, good repeatability (especially with the use of a wire bridge) and the ability to reach high strain rates (i.e. by Hassannejadasl et al. (2014) results  $\sim 15 \times 10^3 \text{s}^{-1}$  for die formed DP590 steel and  $3.9 \times 10^3$  for free formed AA5182-O aluminium alloy with 1mm thickness carried out by Rohatgi et al. (2014).

At the moment of discharge, most of the energy stored in capacitors passes through electrodes and the liquid surrounding the wire bridge vaporizes and produces a high-velocity shock wave that propagates through the chamber and forces the sheet metal into either free space (EHFF) or into a die (EHDF). It is noteworthy that during the deformation the sheet is being formed freely before it reaches the die even when the sheet material is being formed into EHDF.

Golovashchenko et al. (2013) results shows that to obtain the highest improvement

in formability with the EHF process, both high strain rate and high hydrostatic stress are required. The benefit of EHF was demonstrated by Rohatgi et al., Rohatgi et al., Rohatgi et al. (2011, 2012, 2014) on 1mm-thick AA5182-O sheet, who found an increase, relative to the quasi-static FLC, of 150% and 550% in the safe major strains in free-forming and conical die forming, respectively. Evidently, the increase in formability is dependent on the strain path. Due to high inertial forces generated in EHF process, less wrinkling can be observed. Also, Daehn (2006) noted that reduced springback is expected due to high pressure and velocities generated which let the plastic wave propagation through the sheet thickness and eliminating the residual stresses. Another benefit of EHF process explained by Daehn (2006) which is that since there is no friction between the punch and sheet, strain distribution is more uniform.

Rohatgi et al. (2011) measured final strain of EHDF specimens are  $\sim 64\%$  more than EHFF specimens. Rohatgi et al. (2012) performed EHDF and EHFF experiments on AA5182-O sheets with 1mm thickness. The specimens tested was deformed at 21.1kJ (using 7.5kV) and showed a peak strain rate of  $1213\text{s}^{-1}$ . Balanethiram and Daehn (1994) compared quasi-static (QS) and EHDF behaviour of AA6061-T4 in a die with a 90-degree apex angle. Their results show a 568% increase in major strain in near plane-strain conditions: in QS conditions the major engineering strain was observed to be 21.5% whereas it increased to 122.1% in EHDF conditions. Balanethiram (1996) observed around 100% increase in plane-strain as a result of EHF of AA2024-T4 specimens. Golovashchenko et al. (2003) stated that, based on the overall formability can be improved in the range of 11 to 29% while local deformation can be extended in the range of 40 to 90%. They performed EHDF tests on AA6111-T4 in V-shaped dies and measured a major strain of  $\sim 67\%$  as compared to  $\sim 35\%$  in quasi-static conditions. More recently, Maris et al. (2016) studied the effect of EHFF on the FLC of DP600 steel and AA5182-O aluminium sheets by means of experimental and FE simulation studies. They measured the increase of major strain from quasi-static to EHFF forming to be around 8%. Cheng et al. (2017) also studied the effect of EHDF on the FLC of DP600 and reported an increase of 60% in biaxial-tension mode and

120% when specimens were formed into a V-shape die.

It is well known that the strain rate sensitivity of many materials increases significantly at strain rates above  $10^4\text{s}^{-1}$  (i.e. as Daehn (2006) reported). In previous work on high strain rate deformation of AA5182-O, Jenab et al. (2016) studied different phenomenological models and observed that at relatively high strain rate regimes ( $\dot{\epsilon} > 100\text{s}^{-1}$ ), the true flow stress of AA5182-O increases with strain rate. This positive trend is of importance since it helps to postpone neck formation in high strain rate forming.

Previously, Jenab et al. (2015) showed that by increasing the input energy, above a threshold of 8-10 kJ, AA5182-O sheet can be formed to greater safe strains. There are a number of factors that influences sheet formability, including the strain rate, the impact velocity against the die surface and the resulting hydrostatic stress in the material, that are controlled by the input energy. Also, Jenab et al. (2017) studied the microstructure of both safely formed and failed AA5182-O EHFF and EHDF specimens and reported that the area percentage of voids is suppressed by increasing the input energy in the EHF process and more significantly by the presence of a die. Finally, the amount of post uniform deformation in EHF formed specimens is found to be greater than that for quasi-static formed specimens.

A better understanding of the deformation history and material response to high strain rate forming in EHF would help to implement this forming process more broadly in the automotive industry. Hence, in this study, the formability of AA5182-O aluminium sheet is investigated during EHFF and EHDF processes by means of experimental and numerical analysis. The grid analysis results are compared with quasi-static and EHFF forming limit curves and the magnitude of formability improvement is determined. A model to perform finite element (FE) simulation of the EHF process is developed and after validation with experimental results, is used to predict mechanical factors influencing the formability improvement such as strain rate, stress triaxiality and through-thickness stress.

## 5.2 Experimental and Computational Procedures

### 5.2.1 EHF experiments and grid analysis

AA5182-O sheet having a thickness of 1.5mm was provided by Novelis Inc. The chemical composition of the alloy was measured by spectrographic analysis and contained 5.02 Mg, 0.37 Mn, 0.24 Fe, 0.041 Si, and 0.015 wt% Cu with small traces of Cr, Zn and Ti and the balance of Al.

The EHFF experiments, were performed without the use of a die so that the specimens were free to deform. The EHDF experiments used conical dies with die angles of 34 and 40°, noted respectively as EHDF-34° and EHDF-40° in the present work.

The EHF experiments were performed using different input voltages and test conditions. In order to measure the strains in specimens, 20×20 cm square blanks were electro-etched prior to deformation using a 2.54 mm square grid. After forming, major and minor strains were measured at the apex and radially from the apex along the sheet rolling and transverse directions using a grid analyzer with a precision of 0.5% engineering strain. Safe, necked and fractured grids were identified as such prior to being measured. Grids that lay over a crack in the specimens were stitched together by the optical strain measurement system so as to determine the principal strains just prior to fracture. When specimens exhibited worn or missing grid lines either from the friction with the die or by air entrapment, only the readable grids were measured. A formability improvement index was defined in order to compare the forming limit data from the EHF experiments with the quasi-static reference FLCs. Quasi-static FLCs were extracted from Wu et al. (2003) work and from data provided by CanmetMATERIALS, reported in Jenab et al. (2015) work. An experimental EHFF FLC from Maris (2014) was also used for comparison. In order to measure the formability improvement, a consistent linear strain path is assumed between the QS FLC and the true strain data measured on the EHF specimen. The formability improvement was calculated from the difference in magnitudes of in-plane effective plastic strain values from the EHF experiments and the reference FLC for equivalent strain paths.

Considering volume constancy, effective plastic strain values can be calculated using  $\bar{\varepsilon} = 2\sqrt{\frac{1}{3}(\varepsilon_1^2 + \varepsilon_2^2 + \varepsilon_1\varepsilon_2)}$  where  $\varepsilon$  represents the plastic engineering strain for each grid. Consequently, the formability improvement index ( $FI\%$ ) may be expressed as:

$$FI\% = \frac{\bar{\varepsilon}_{\text{EHF}} - \bar{\varepsilon}_{\text{FLC}}}{\bar{\varepsilon}_{\text{FLC}}} \times 100 \quad (5.1)$$

where  $\bar{\varepsilon}_{\text{EHF}}$  and  $\bar{\varepsilon}_{\text{FLC}}$  are the effective plastic strain values at the grid points where strain data were measured and that at the point on the reference FLC that intersects with the experimental strain path, respectively. It is worth emphasizing that Eq. (5.1) determines the percent change in the forming limit along a given strain paths, and not merely the difference in major strain from the QS-FLC, as is more commonly used. To determine the formability improvement index for each specimen, the average value of three safe grids with the greatest effective strains were chosen.

### 5.2.2 Finite element modelling procedure

Due to the cost of carrying EHF experiments, finite element simulation is an essential part of the development and optimization of the EHF process.

ABAQUS<sup>®</sup> 2016 is used to simulate the EHF tests that were carried out on AA5182-O aluminium sheet. The three-dimensional finite element model of the EHF process consisted of an Eulerian mesh to represent the water and void sections, whereas the sheet was modelled using Lagrangian solid elements. The EHF die and water chamber were created as 3D discrete rigid parts. In order to capture the complex non-symmetrical changes in the pressure wave in the EHF chamber, the whole model was simulated without considering symmetry conditions. It is noteworthy that more accurate predictions of velocity, strain rate and impact pressure can be obtained with a formable solid die and EHF chamber. However, using solid die and EHF chamber dramatically increases the computational cost and can be preventive to focus on the main aim of this work. Hence, following previously published works, EHF die and water chamber are simulated using rigid parts.

To obtain accurate simulation results, it is essential to define the mechanical re-

sponse of the sheet material to strain and strain rate precisely. Previously, Jenab et al. (2016) investigated the mechanical properties of AA5182-O using different constitutive equations (Johnson-Cook, Khan-Huang-Liang, Modified-Voce and artificial neural networks (ANN)) and developed different ABAQUS user material subroutines to be used in FE simulations. The benefit of using ANN over conventional hardening functions are three fold:

- It is common to disregard the negative but insignificant strain rate exponent of aluminium alloys during finite element simulations, especially when Johnson-Cook hardening function is being used. Jenab et al. (2016) found that this leads to 14.7% less accuracy in the predicted flow curve in case of AA5182-O.
- The results suggest that ANN provides better agreement with experimental values when compared with analytical calculations and when used in finite element simulations at a given direction, strain and strain rate, even though the computational costs are greater.
- Most importantly, a comparison between ANN outputs and the experimental flow behaviour of AA5182-O shows that, unlike analytical hardening functions, the developed ANN structure is capable to predict the rise of flow stress at high strain rates.

Consequently, instead of using tabular data for flow stress or relying on ABAQUS's built-in hardening functions, the developed ANN VUMAT is used to model the mechanical response of AA5182-O in EHF process.

The water was simulated using the Mie-Gruneisen (Us-Up) equation of state considering a reference speed of sound of  $1450 \times 10^3$  mm/s, a viscosity of  $1 \times 10^{-8}$  MPas, and density of  $1 \times 10^{-3}$  g/mm<sup>3</sup>.

Since the interaction of the sheet with the die generates significant through-thickness compressive stress, the sheet was meshed with 3D Lagrangian solid elements with reduced integration (C3D8R). The sheet had an element size of 1 mm and the thickness of the sheet was divided into 9 elements giving an approximate element height of 0.167mm in the thickness. The Eulerian part consisted of 2 mm 3D elements with

reduced integration and hourglass control (EC3D8R). The Eulerian part was sectioned so that it represents the water beneath the sheet and the void region above the sheet. The total number of elements in the sheet, Eulerian part, explosive material, upper conical die, and water chamber was 123516, 207588, 160, 7654, and 9446, respectively. Since the experimental tests were carried out without the presence of any lubrication, the static and kinetic coefficients of friction between the aluminium sheet and the steel dies were set to 0.61 and 0.47 (i.e. as reported by Serway and Beichner (2000)), respectively instead of commonly used values of 0.15 and 0.05 which are related to lubricated condition. General contact with ABAQUS default properties was assigned to other parts involved in FE simulation, including the interaction between the Eulerian part and the sheet as well as between the Eulerian part and the water chamber. To prevent translational and rotational movements, the sheet edges, the upper conical die and water chamber were encastered.

To simulate pulse formation in the EHF process, Golovashchenko et al. (2013) used energy deposition in the discharge channel. Mamutov et al. (2015) performed a complex multi-physics simulation of the generation of the shock wave in EHF. However, Melander et al. (2011) simulated EHF of different steel grades using a spherical pressure wave originating from the location where the discharge occurs between the electrodes. Rohatgi et al. (2014) used the same approach and used a non-uniform pressure based loading for EHF. Moreover, Hassannejadasl et al. (2014) and Maris et al. (2016) used a pulse acceleration surface instead of time-consuming and complex modelling of EHF pulse formation or discharge itself. Furthermore, another approach to obtain high velocity impact is to use the ignition and growth model based on Jones-Wilkins-Lee (JWL) ( Lee et al. (1968)) equation of state. Hassannejadasl (2014) studied the EHF process using the same approach and with Composition B as the explosive material and a reasonable correlation between simulation and experimental results were obtained in both EHFF and EHDF.

Since the aim of this study is to identify the parameters affecting formability improvement of AA5182-O and not the EHF process itself, the same ignition and growth model was used in this study to simulate the pulse formation. This simplification allows the

authors to focus on material aspect of formability rather than the pulse formation phenomena. Hence, an explosive material was located at the same distance from the sheet as the EHF electrodes and followed the JWL equation of state which can be written in terms of the internal energy per unit mass as:

$$p = A \left( 1 - \frac{\omega \rho_p}{R_1 \rho_0} \right) \exp \left( - R_1 \frac{\rho_0}{\rho_p} \right) + B \left( 1 - \frac{\omega \rho_p}{R_2 \rho_0} \right) \exp \left( - R_2 \frac{\rho_0}{\rho_p} \right) + \omega \rho_p E_m \quad (5.2)$$

where according to Lee et al. (1973),  $p$  is the pressure generated by the release of chemical energy upon the explosion,  $E_m$  is the initial energy per unit mass and  $A$ ,  $B$ ,  $R_1$ ,  $R_2$  and  $\omega$  are explosive material constants;  $\rho_0$  is the density of the explosive material and  $\rho_p$  is the density of the detonation products. Table 5.1 shows the constants for the explosive material used in this study.

Table 5.1: Ignition-and-growth parameters for explosive material.

Detonation Wave Speed [mm/s]	8.53E+06
$A$ [MPa]	5.41E+05
$B$ [MPa]	9.22E+04
$\omega$	0.35
$R_1$	4.5
$R_2$	1.1
$\rho_0$ [g/mm <sup>3</sup> ]	1.74E-03

To calculate the detonation energy density of the explosive material ( $\rho$ ) as a function of input voltage used during EHF experiments, the consistency of energy was considered acknowledging energy loss using an efficiency parameter. Electric potential energy,  $U_{EHF}$ , of a charged capacitor can be calculated from  $U_{EHF} = \frac{1}{2}CV^2$  where  $C$  and  $V$  represent the capacitance and charged voltage of EHF apparatus. The detonation energy density of the explosive material is calculated using  $U_{EHF}$  and its mass considering a multiplicative efficiency factor,  $\eta$ .  $\eta$  is assumed to incorporate energy loss due to wire resistance, heat generation and other factors. The value of  $\eta$  was calibrated so that the difference between the maximum height of the simulated sheet specimen and the maximum height of the safely formed EHFF specimen (at 4.8kJ input energy) is less than 0.01 percent. It was found that, using the parameters for the explosive material that are given in Table 5.1, the EHF numerical model was



calibrated with an efficiency factor of 0.785.

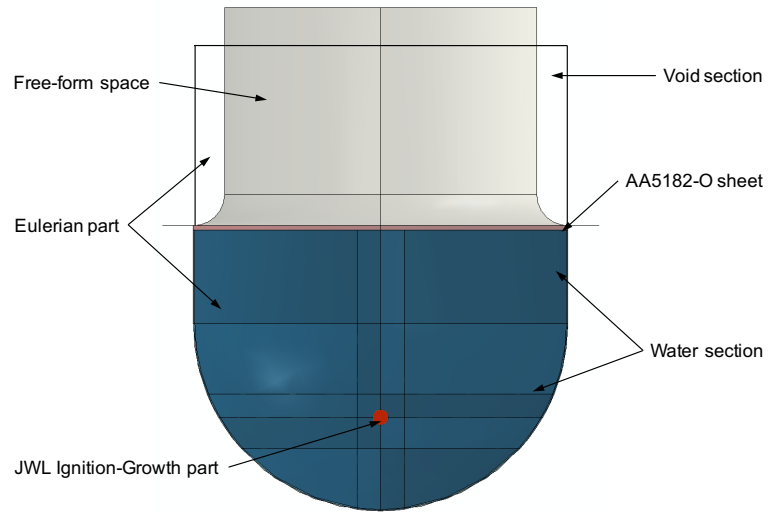
FE simulations were carried out using ABAQUS scripts (instead of GUI) and through MATLAB terminal. In this way, MATLAB controls parameters such as mesh size and input energy and hence the mesh sensitivity and calibration studies were performed automatically in different loops. Codes were developed not only to generate and run FEA but also to extract required data automatically from FE results and imported to MATLAB for post-processing. Fig. 5.1 shows the FE simulation models used in this study for both EHFF (Fig. 5.1(a)) and EHDF (Fig. 5.1(b)).

## 5.3 Results and Discussion

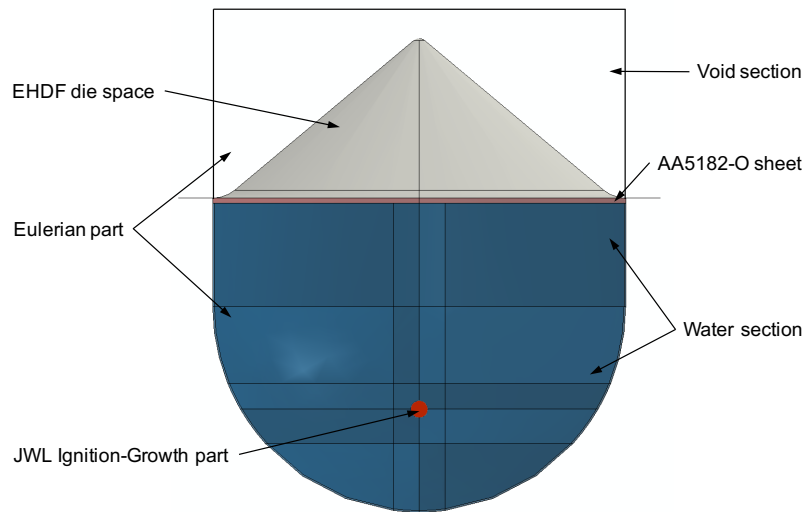
### 5.3.1 EHF experimental results

It is noticed that the EHF experiments are quite sensitive to input voltage. For example, Fig. 5.2(a) shows safely formed and cracked specimens formed under different EHFF condition where an increase of 0.5 kV in input voltage, from 5.5 kV to 6.0 kV, consistently led to failure in EHFF specimens (Fig. 5.2 (a)). However, the sensitivity to the applied voltage decreases significantly with the presence of the die. Fig. 5.2(b) shows two specimens formed using the 34° conical die. Splitting was rarely observed in EHDF-34° experiments and mostly located at the apex area of the conical die (Fig. 5.2(b)-top) since the material could fill the die safely and reach a greater depth compared to EHFF.

Typical specimens deformed using the 40° die are shown in Fig. 5.2(c). All failed specimens showed failure in the apex area and some specimens exhibited signs of concentric circumferential localized deformation on the inside of the conical specimens. However, the measured strain values suggest that much greater safe strains are reached at locations away from these localized deformation areas. It is worth emphasizing that the majority of cracked specimens were formed at lower input voltages (i.e. at 8.0 kV in Fig. 5.2(c)-bottom) and the safe specimens were formed at higher input voltages (i.e. at 12.0 kV in Fig. 5.2(c)-top).



(a)



(b)

Figure 5.1: Schematic of FE model used to simulate (a) EHFF and (b) EHDF-40°.

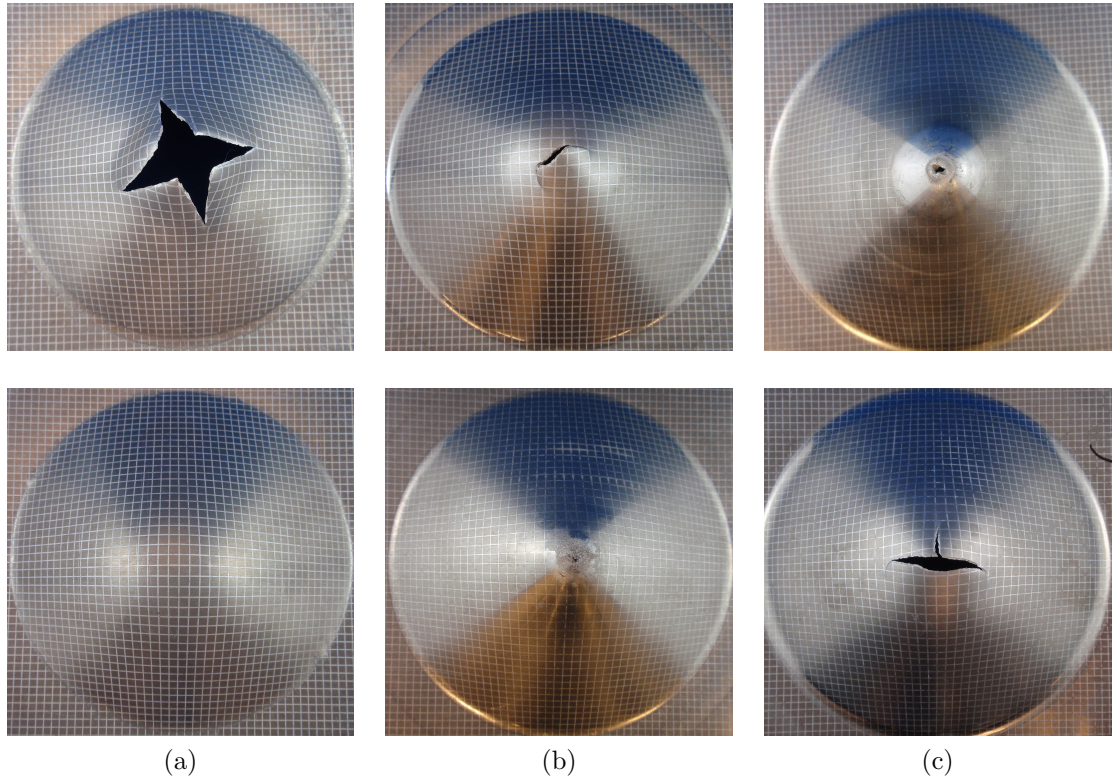


Figure 5.2: Top view of (a) EHFF; top: 6.0 kV, bottom: 5.5 kV, (b) EHDF-34° die; top: 8.4 kV, bottom: 8.0 kV, (c) EHDF-40° die; top: 12.0 kV, bottom: 8.0 kV.

It is noteworthy that in the EHDF experiments and at low voltages, cracks usually nucleate in the apex area and the specimens were unable to completely fill the die cavity (see Fig. 5.2(b) and (c)). Hence, the cracks were formed during the free forming stage of the deformation. Moreover, the apex of the specimen formed in the 40° die was punctured, and can be seen as a hole in Fig. 5.2(c)-top which was due to the die design and not due to failure in the AA5182-O specimen. Furthermore, most of the safely deformed grids in the apex area of EHDF specimens were removed as a result of either generated heat (of compressed air) or due to the friction with the die, as shown in Fig. 5.2(b) and (c).

Table 5.2 shows the calculated formability improvement of selected samples formed in EHFF and EHDF relative to the different FLCs found in the literature for the same alloy. It can be seen that the EHFF specimens do not show significant improvement in formability. The negative values reported in Table 5.2 denotes that not only formability have not improved for the grids with maximum effective strain values, but also

Table 5.2:  $FI\%$  of selected samples compared to different FLCs.

Test Cond.	Voltage, (kV)	Energy, (kJ)	Referenced FLD		
			QS*	QS-Canmet	EHFF
EHFF	5.0	4.0	-54.0	-43.2	-56.5
	5.5	4.8**	-3.7	13.8	0
	6.0	5.8	-6.4	6.1	-12.4
	6.9	4.8	-9.4	12.4	-14.4
EHDF-34°	7.0	4.9	18.3	34.1	10.4
	8.0	6.4**	39.8	54.1	28.8
	9.0	8.1	21.7	35.6	12.9
	10.0	10.0	19.7	32.5	9.2
	10.5	12.1	17.9	30.2	9.5
EHDF-40°	11.0	13.2	19.4	36.6	11.3
	11.5	14.4	45.8	64.0	29.1
	12.0	14.4**	69.7	88.7	53.2

\* QS FLC is derived from Wu et al. (2003), QS-Canmet was used in Jenab et al. (2015) and the EHFF FLC was reported by Maris (2014).

\*\* Safe specimens showing the highest improvement in formability at each testing conditions. EHF condition of such samples are chosen for FE analysis.

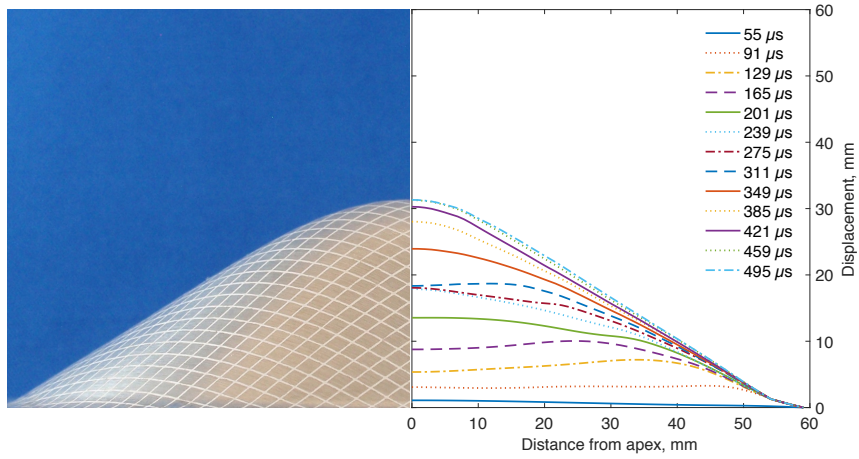
magnitude of the strain values were less than the referenced FLC. However, in case of EHDF, significant formability improvement can be seen. It can also be seen that the maximum  $FI\%$  compared with Wu et al. (2003) for EHDF is 39.8% for specimens formed in the 34° conical die and 69.7% for specimens formed in the EHDF-40° conical die. Finally, it is noteworthy that these formability improvements are less than results reported by Rohatgi et al. (2014), where an increase in safe major strains of 150% and 550% greater than quasi-static FLC were reported for EHFF and EHDF tests, respectively. At each testing condition, EHF conditions where the formed specimens showed the greatest improvement in formability (marked with “\*” in Table 5.2) were further studied.

### 5.3.2 Deformation history

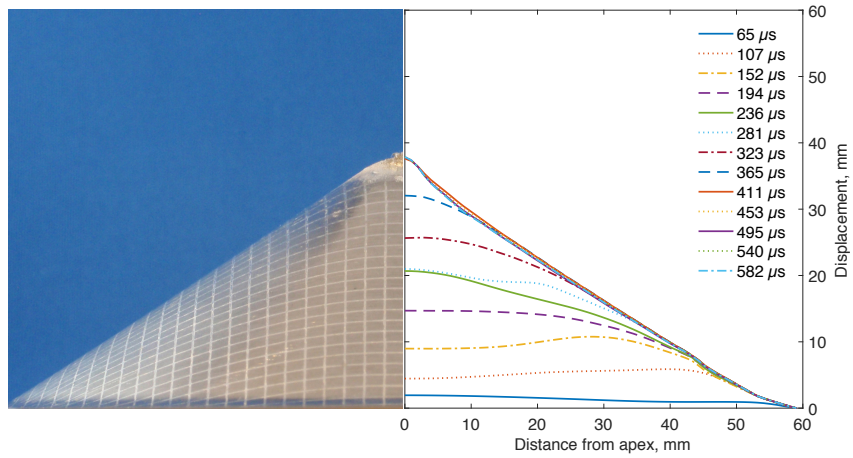
Fig. 5.3 shows the deformation profile and dome height of EHFF (Fig. 5.3(a)) and EHDF (Fig. 5.3(b) and (c)) specimens. The time required to form the EHFF specimen to its final shape is calculated to be less than  $460\mu s$ , and the time required for the specimens to fully fill the EHDF-34° and EHDF-40° dies are about  $410\mu s$  and  $380\mu s$ ,

respectively. Moreover, it can also be seen that for all EHF formed specimens, the vertical displacement of the sheet is delayed at the centre of the specimen relative to the displacement around the periphery. This delay is overcome as the deformation progresses (i.e. between 165 and 201 $\mu$ s for EHFF, 152 and 194 $\mu$ s for EHDF-34° and 159 and 191 $\mu$ s for EHDF-40°) which leads to increased strain rate as a result of a *whiplash* effect as the sheet finally fills the apex of the conical die. It is worth noting that the delay in the central region is also reported in EHDF of steel sheets by Hassannejadasl (2014) and Golovashchenko et al. (2011) using the same chamber geometry and also by Melander et al. (2011) using different die geometries. Imbert et al. (2005) also noticed the same delay in the central region during electromagnetic forming of AA5754 conical specimens. Furthermore, Rohatgi et al. (2012) showed a very slight delay in the central region of deformation for 1 mm thick AA5182 sheets at about 504-548 $\mu$ s, where the entire forming process took about 700 $\mu$ s based on their experimental setup. However, the total time to fill the EHDF specimen is reported to be much longer than what is seen in this study and reported in other EHF literature (i.e. by Cheng et al., Golovashchenko et al., Hassannejadasl et al., Maris et al. (2017, 2013, 2014, 2016)) which is likely due to the difference in the pulse unit that was used.

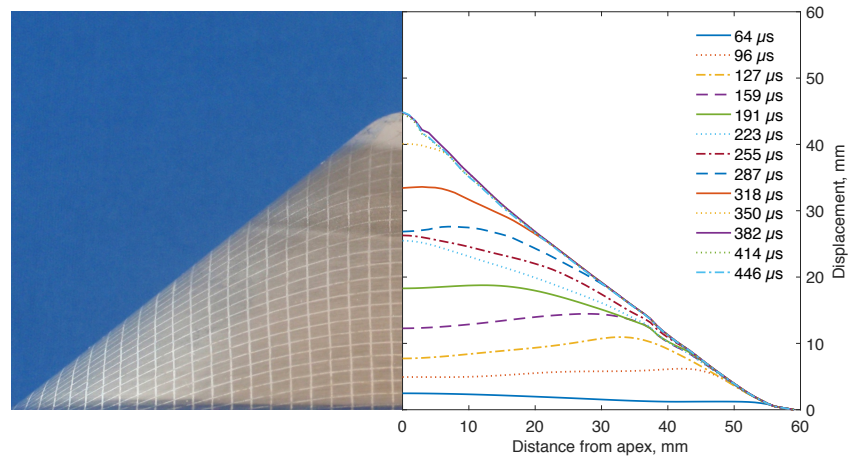
It is also noteworthy that based on the FE simulation, specimens formed under EHDF experienced a more extensive delay as compared to EHFF specimens. This is in agreement with the observations of Hassannejadasl et al. (2014) for DP590 steel sheet subject to EHFF and EHDF conditions. Another observation from Fig. 5.3 is that even in EHDF conditions, the initial stages of forming can be considered as free forming. According to Golovashchenko et al. (2013), the reason is that the sheet material accelerates into the space inside the die cavity without being in contact with the die, and it is not until the end of the process that the sheet fully contacts the apex of the conical die.



(a)



(b)



(c)

Figure 5.3: Progress of EHF deformation at different times, calculated from the FE model, compared with experimental results for (a) EHFF specimen formed with 4.8kJ input energy, (b) EHDF-34° specimen formed with 6.4kJ input energy and (c) EHDF-40° specimen formed with 14.4kJ input energy.

### 5.3.3 Strain distribution and strain path

Fig. 5.4(a)-(c) show a comparison of the experimental and predicted strain distributions for EHFF, EHDF-34° and EHDF-40° specimens, respectively. It can be seen that the FE model is able to predict the major and minor strain values reasonably well at different locations of the specimen for both EHFF and EHDF processes. Major and minor engineering strains measured experimentally along the rolling direction (RD) and transverse direction (TD) of specimens are shown in Fig. 5.4 with hollow square and diamond markers, respectively. Beside the scatter in experimental results for the EHFF specimen formed with 4.8kJ input energy, the FE model was able to predict major and minor strains very accurately. In case of specimens formed into 34 and 40° conical dies with 6.4 and 14.4kJ input energies, shown in Fig. 5.4(b) and (c) respectively, the major strain matches the experimental results for any radial location from the apex. However, in case of the minor strain in the apex region, the FE simulation predicts higher values than the experimental measurements. It is believed that the deviation between the predicted minor strain values and the experimental measurements is due to the isotropic conditions considered in the simulation for AA5182-O sheets.

Fig. 5.5 shows grid analysis results and the predicted strain path compared with the experimental FLC of the alloy taken developed by Wu et al. (2003). In case of the EHFF specimen formed with 4.8kJ input energy, the experimental grid analysis suggests that the strain path is almost equi-biaxial in all measured locations including areas close to the apex, shown in Fig. 5.5(a). Also, FE analysis results confirm the linear equi-biaxial strain path and matches reasonably well with experimental measurements with a slight deviation at the apex. In case of EHDF-34° specimens formed with 6.4kJ, final strains in areas away from the apex are almost linear near to equi-biaxial strain, but after about 20% straining the strain state deviates and moves towards plane strain. However, FE simulation results still suggest a linear balanced biaxial strain path in the apex region which does not match closely with experimental measurements. This discrepancy decreases when the specimen is formed into the 40°

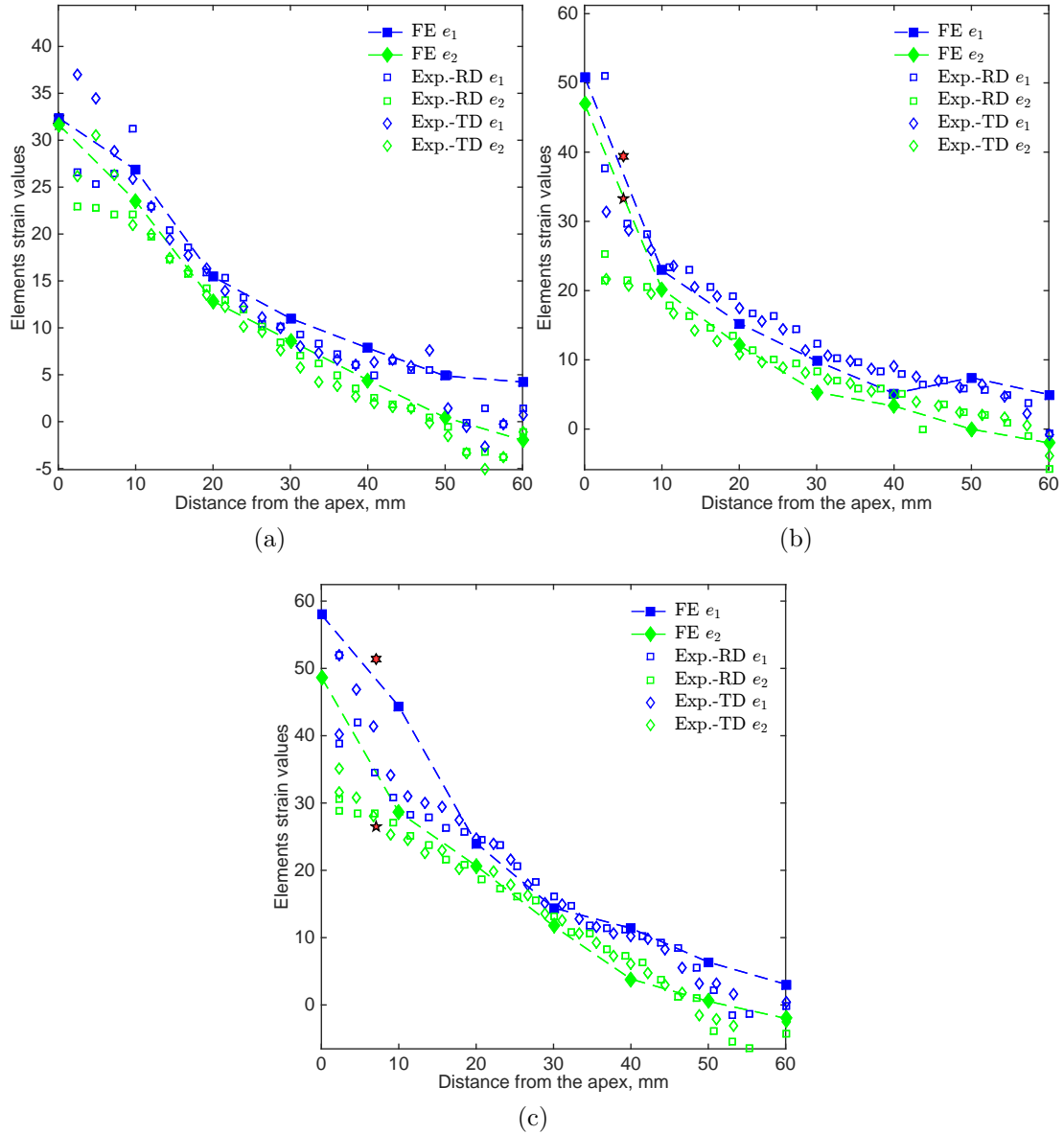


Figure 5.4: Comparison of experimental and predicted strain distributions for (a) EHF specimen formed with 4.8kJ input energy, (b) EHDF-34° specimen formed with 6.4kJ input energy and (c) EHDF-40° specimen formed with 14.4kJ input energy; major ( $e_1$ ) and minor ( $e_2$ ) strains are shown as blue and green points, respectively, where experimental measurements in the RD and TD are shown as square and diamond points.



die mainly since the experimental results tend toward the equi-biaxial region. The fact that strains are close to equi-biaxial near the apex is similar to the experimental strains reported by Rohatgi et al. (2012) at the apex of their conical specimens. Once again, the differences between the FE results and the experimental strain values mainly concern the minor strain values since the major strain values are very well predicted. As mentioned before, since in FE analysis, the sheet was considered to be isotropic, it is believed that the anisotropy of the material is responsible for this discrepancy.

It is noteworthy that strain values of elements selected at different locations across the sheet thickness (i.e. elements at the mid-thickness, elements on the side in contact with the water and elements in contact with the die) are all very similar.

### 5.3.4 Strain rate

One of the main goals of this study was to analyze and understand the different mechanical factors that contribute to the formability improvement of sheet specimens deformed in EHF. Hence, unlike previous studies where sheet specimens were modelled using shell elements (i.e. Hassannejadasl, Maris, Maris et al., Melander et al. (2014, 2014, 2016, 2011)), the sheet material was modelled using 3D elements. Hence, parameters such as strain rate, stress triaxiality and through-thickness stress were calculated not only on one side of the sheet specimens (i.e. side facing the die or the water) but also were derived from elements located across the thickness of the AA5182-O specimen. Fig. 5.6 shows the average value of peak strain rates measured from different elements across the thickness of the AA5182-O specimen: at the die side, at the mid-thickness and at the water side of the specimen. It can be seen that the sheet material experiences significant strain rate at the apex of the EHDF specimens where the peak strain rate decreases as the distance from the apex increases. This reduction of the maximum peak strain rate with the distance from the apex was also reported by Golovashchenko et al. (2013), Hassannejadasl et al. (2014) and Hassannejadasl (2014), and in case of EHDF specimens, is probably correlated to the velocity of the sheet when it impacts the die wall. It can be seen that the sheet

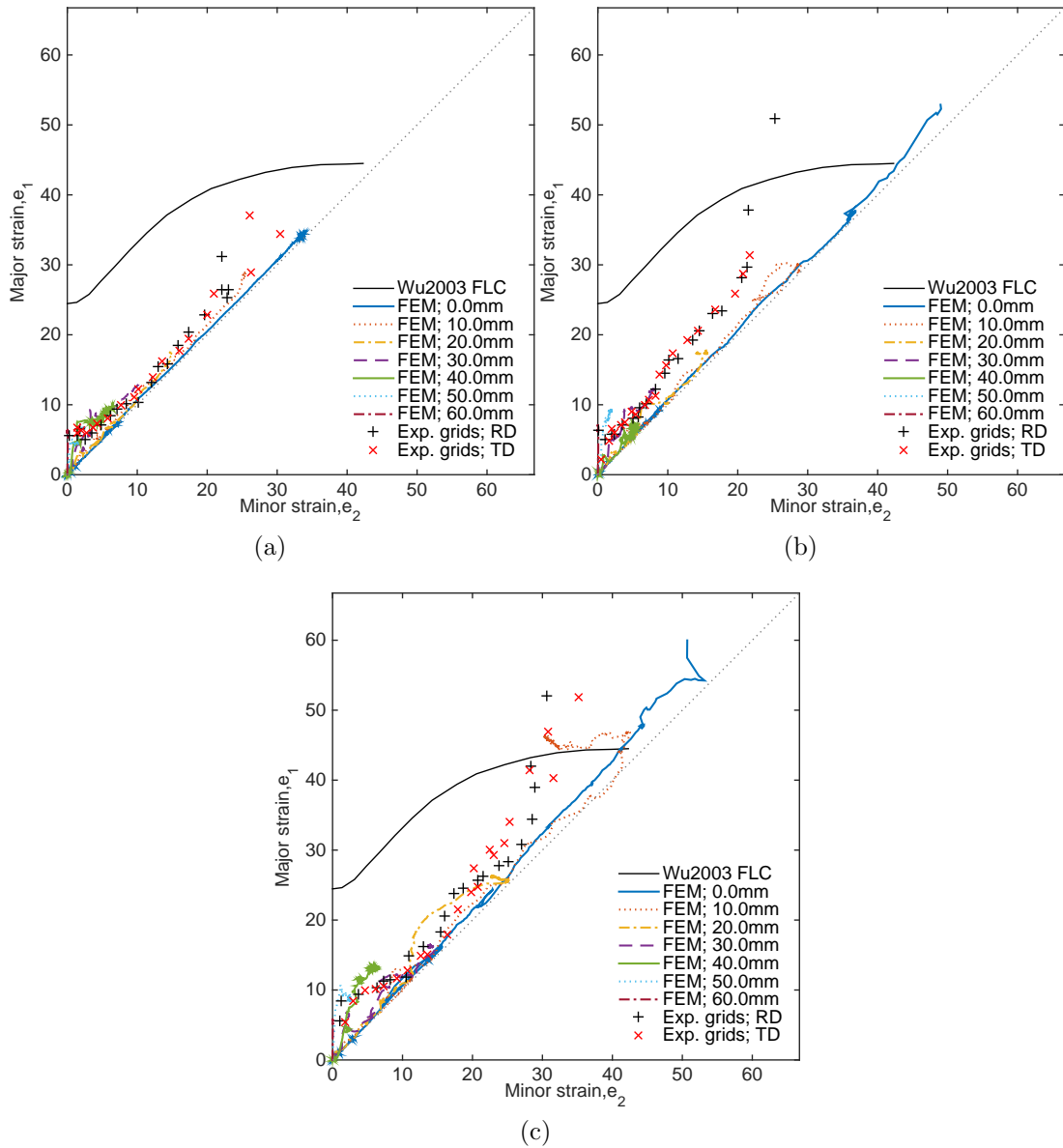


Figure 5.5: Comparison of experimental grid measurement of EHF formed specimens with quasi-static FLC derived from Ref. Wu et al. (2003) and deformation strain path at different locations of (a) EHFF specimen formed with 4.8kJ input energy, (b) EHDF-34° specimen formed with 6.4kJ input energy and (c) EHDF-40° specimen formed with 14.4kJ input energy; + and × denote measurements carried out in the RD and TD directions, respectively. The reported distance on FEM lines is relative to the apex of each specimen.

material formed under EHFF process with 4.8kJ input energy has not experienced significant strain rate as compared to other specimens. Moreover, the peak strain rate for EHFF specimen was recorded during the deformation and not at its final stage of deformation (discussed in Section 5.3.5).

However, the peak strain rate for the apex region of the EHDF-34° specimen formed with 6.4kJ is 3.5 times greater than that of the EHFF specimen (about  $5 \times 10^4 \text{s}^{-1}$ ). It is noteworthy that experimental measurements of Lagrangian strain rate presented by Rohatgi et al. (2012) for AA5182 specimens suggest that the maximum strain rate at the apex of EHDF specimens is about 4 times greater than that in EHFF specimens. Similarly, Hassannejadasl et al. (2014) estimated the peak strain rate in EHDF to be 5.2 times greater than in EHFF. Moreover, this measured value is slightly more than 3 times of the value ( $15,000 \text{s}^{-1}$ ) Hassannejadasl et al. (2014) reported in which 14.4kJ input voltage was used to safely form DP590 steel sheet into the same conical die. Since the density and mass of aluminium specimens used in this study is about one-third that of the DP590 sheet, it was indeed expected to obtain such high strain rate values when the AA5182-O sheet is deformed in EHDF using the same input energy.

Moreover, as the input energy of the EHF process increases (from EHFF at 4.8kJ to EHDF-34 at 6.4kJ and EHDF-40 at 14.4kJ) the peak strain rate increases. Based on the positive trend of AA5182-O flow stress with strain rate, as discussed by Jenab et al. (2016), the effect of such high strain rate deformation should not be ignored as an influencing factor of formability. It is worth noting that the high strain rates calculated by the FE model can promote positive strain rate sensitivity in AA5182-O and consequently enhance the strength of the material as it shows positive relation between flow stress and strain rate at high strain rates. Furthermore, as discussed before, the maximum strain rate in EHFF specimens is much less than that in EHDF specimens. This could be one of the reasons that there is little or no formability improvement in EHFF of AA5182-O, as shown in Table 5.2.

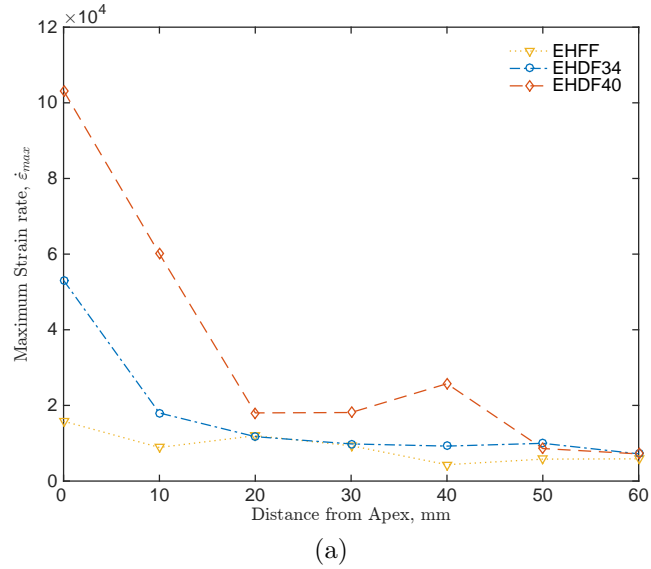


Figure 5.6: Comparison of peak strain rates predicted at different locations from the apex and averaged through the thickness of AA5182-O specimens; EHFF specimen (yellow line) was formed with 4.8kJ input energy, EHDF-34° specimen (blue line) formed with 6.4kJ input energy and EHDF-40° specimen (red line) formed with 14.4kJ input energy.

### 5.3.5 Equivalent strain, stress triaxiality and strain rate history

Fig. 5.7 shows the evolution of normalized values of predicted strain rate, equivalent plastic strain and stress triaxiality in an element located at the apex of the specimen and at the mid-thickness of the sheet during EHF. Small serrations in strain rate and triaxiality values are mainly due to the iterative calculations in explicit FE model. The results show that in case of EHFF (Fig. 5.7(a)), the strain rate increases at a relatively constant rate as the specimen deforms up to its maximum strain rate and then the strain rate reduces to zero in the final stages of the deformation. However, In case of EHDF (Fig. 5.7(b) and (c)), the strain rate suddenly increases as the sheet contacts the die wall and completely fills the die cavity. Moreover, in addition to the peak strain rate at the end of the deformation, in all cases the strain rate also increases to another smaller peak during the deformation and well before the specimen reaches its final shape (around 200-300 $\mu$ s). This observation is due to the effect of first shock wave reaching the specimen and the consequent increase

in the plastic effective strain shown in Fig. 5.7(a)-(c). In case of EHDF specimens (Fig. 5.7(b) and (c)) when the strain rate suddenly increases during the deformation, the stress triaxiality correspondingly decreases to negative values. However, in case of EHFF specimen, the stress triaxiality practically remains positive during the whole deformation process. Many studies showed that once the stress triaxiality decreases, the damage accumulation is suppressed and the fracture strain increases, Golovashchenko et al., Hassannejadasl, Hopperstad et al. (2013, 2014, 2003). More specifically, Shabrov and Needleman (2002) studied the effect of inclusion morphology on void nucleation and observed that, in general, by increasing the stress triaxiality, the effective strain required for void nucleation decreases. Moreover, an effective void nucleation stress depends linearly on the overall hydrostatic stress. Hence, it is thought that the combination of a negative stress triaxiality and increased strain rate influence void formation and coalescence and hence postpone the failure by void nucleation and growth observed by Jenab et al. (2017).

### 5.3.6 Sheet Velocity

The changes in vertical velocity (normal to the sheet surface) of the AA5182-O sheet during EHF at different locations across the specimens is shown in Fig. 5.8. Comparison of Fig. 5.8(a) and (b) shows that the material experiences significant differences in velocity from one location to another as the distance from the apex increases. Fig. 5.8(a) shows that the peak velocity (at about  $100\mu s$ ) of material located at a 40mm radial distance away from the apex reaches 119, 170 and 178m/s in EHFF, EHDF-34 and EHDF-40° specimens, respectively. Moreover, in case of EHDF specimens, similar to the second peak in strain rate mentioned in Section 5.3.5, another smaller peak velocity can be seen in Fig. 5.8(a) where the velocity increases at about  $250\mu s$ . As the distance from the apex decreases, this second velocity peak increases and overcomes the first peak. For the material close to apex, this velocity reaches values much higher than the first peak as shown in Fig. 5.8(b).

At the apex of EHF specimens, the two velocity peaks are very distinguishable. The first peak is the result of the first pressure wave generated by the electrical discharge

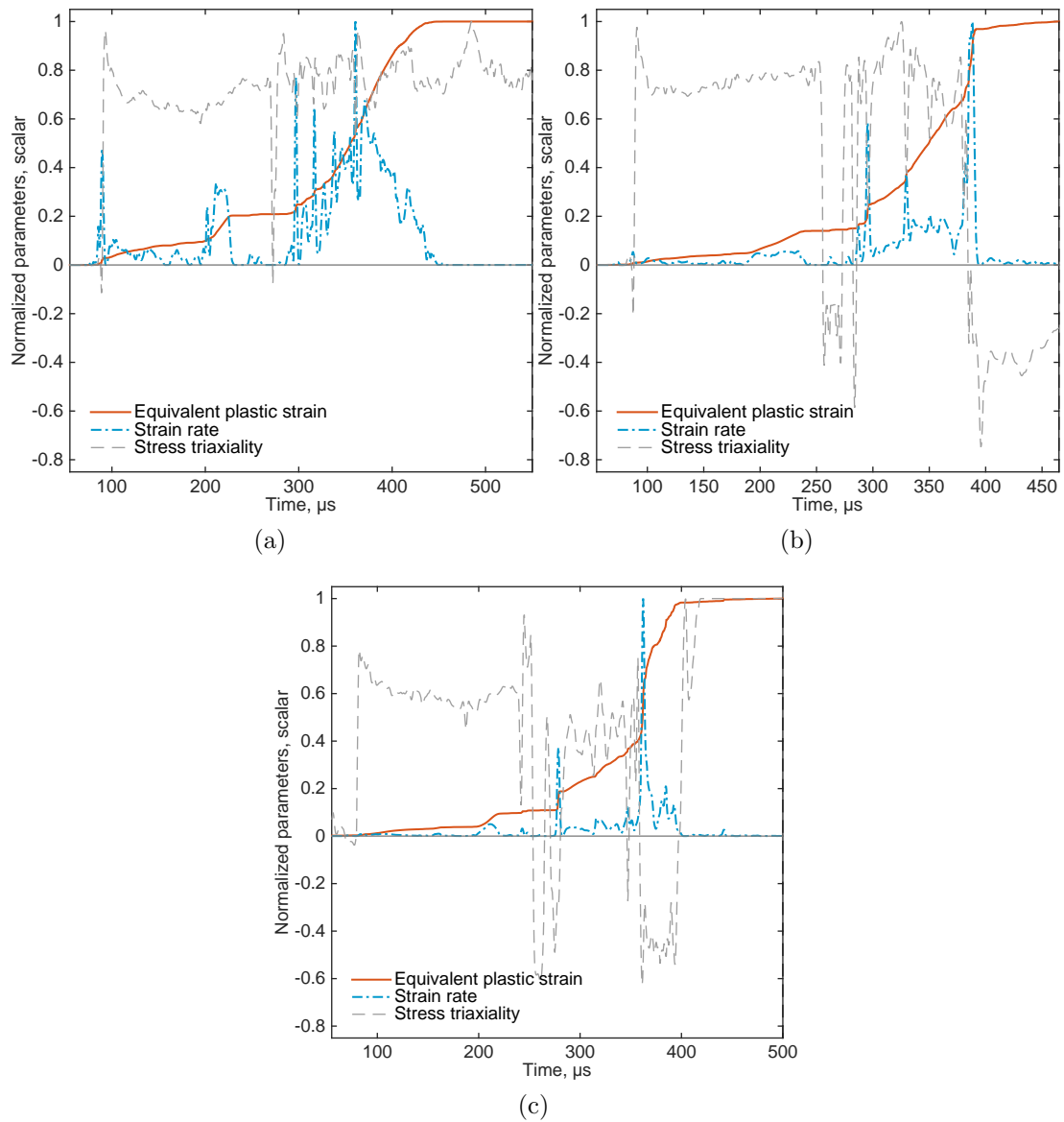


Figure 5.7: Variations of normalized equivalent plastic strain, strain rate and stress triaxiality at the apex for (a) EHFF specimen formed with 4.8kJ input energy, (b) EHDF-34° specimen formed with 6.4kJ input energy and (c) EHDF-40° specimen formed with 14.4kJ input energy.

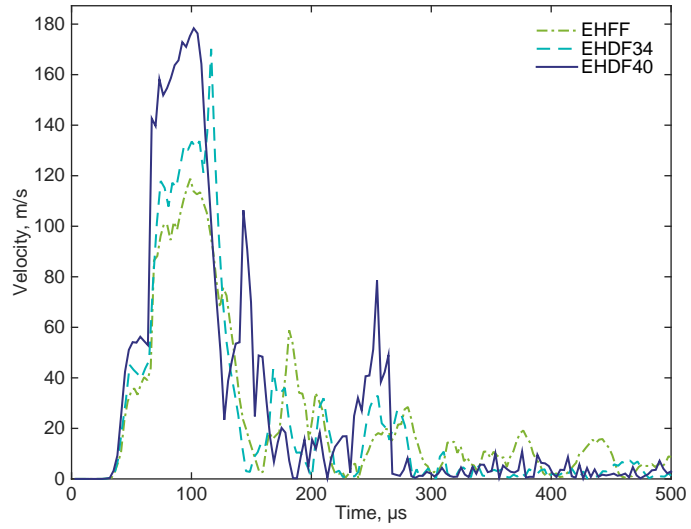
and reaches about 173, 197 and 288m/s for specimens formed in EHFF, EHDF-34 and EHDF-40° conditions, respectively. Emphasizing that not only the die geometry changes in these different test conditions, but also the input energy is different in each case: 4.8kJ in EHFF, 6.4kJ in EHDF-34° and 14.4kJ in EHDF-40°. In case of the second velocity peaks, the difference between the tests is more significant as the peak for the EHFF specimen is about 169m/s, whereas it reaches 332m/s for the EHDF-34 specimen and 446m/s for the EHDF-40° specimen.

It is thought that this second velocity peak is of importance in EHDF tests as it pushes the sheet toward the die at high velocity which leads to the significant compressive stress in the through-thickness direction and the consequent negative stress triaxiality values mentioned earlier. Since the velocity reaches its maximum before the sheet fills the die cavity, the impact pressure generated as a result of this impact contributes to the closure of voids and postpones the failure as observed by Jenab et al. (2017).

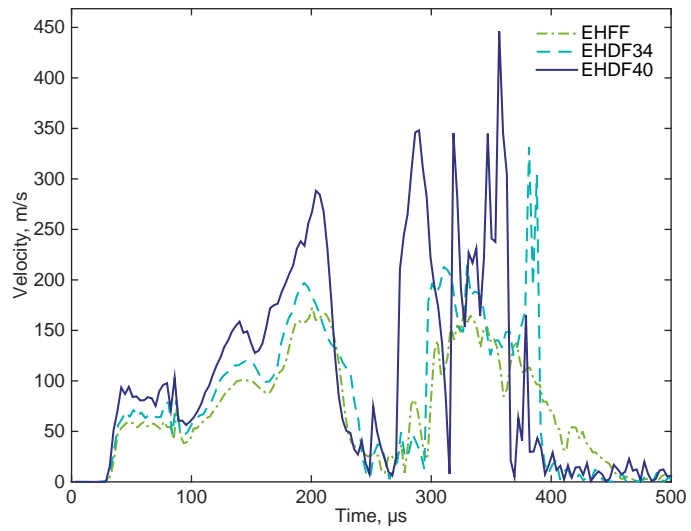
### 5.3.7 Compressive through-thickness stresses

Fig. 5.9(a)-(c) shows the changes of through-thickness stress at different locations of EHFF and EHDF specimens for elements located at the mid-thickness of the AA5182-O sheets. It can be seen that in all three simulated EHF tests, the through-thickness stress reaches negative values (compressive stress state) once at the beginning of the forming process ( 50-100 $\mu$ s) as the first pressure wave forces the sheet to deform, and again several times as the deformation progresses. The magnitude of the through-thickness stress increases significantly when the sheet contacts the die wall. This increased compressive through-thickness stress is of importance as it can postpone the occurrence of failure by void nucleation and growth and has been called the *ironing effect*.

It can be seen from Fig. 5.9(a) that in the case of EHFF conditions, the magnitude of the through-thickness stress remains insignificant at all locations when compared to specimens formed under EHDF conditions (Fig. 5.9(b) and (c)). In EHFF, the maximum compressive stress the material experiences is considerably less than its yield stress (i.e. reported by Jenab et al. (2016)) and hence, this compressive stress



(a)



(b)

Figure 5.8: Variation of velocities for elements located (a) 40mm from the apex and (b) at the apex during EFFF and EHDF processes.



is not sufficient to close the voids or to postpone the onset of failure. This is in agreement with the fact that EHF specimens show insignificant improvement in formability (Section 5.3.1) and as demonstrated by Maris et al. (2016) for AA5182-O sheets.

However, in case of EHDF specimens shown in Fig. 5.9(b) and (c), the through-thickness stress reaches compressive values close to the yield stress of AA5182-O (120-150MPa) at the beginning of deformation (i.e. peak 1 in Fig. 5.9(b)). Then this negative through-thickness stress further increases in magnitude to -300 and -500MPa during EHDF-34 and EHDF-40° deformation, respectively. This significant negative through-thickness stress occurs approximately when the first pressure wave hits the sheet as shown in Fig. 5.7. Finally, just before the specimen contacts the die wall and further on, another peak of significant negative through-thickness stress can be seen which corresponds to the continues pressure generated as the sheet impacts the die. It is believed that these significant compressive stress components could have a major effect on in the closure of existing voids which positively affect AA5182-O formability. To exemplify, the effect of compressive stress components can be seen in Fig. 5.10 which shows a comparison between void percentages in safely formed EHF specimens formed at different input energy. It can be seen from Fig. 5.10 that by increasing the EHDF energy, from 8.1kJ to 19.6kJ, the void percentage in the bulk of AA5182-O sheet reduces from above 0.3% to less than 0.1%.

### **5.3.8 Impact stress**

Fig. 5.11 shows the magnitude of the pressure generated upon impact of the sheet with the die at different locations of the AA5182-O EHF specimens. To plot Fig. 5.11 two approaches were taken; first the maximum compressive stress generated through the thickness of the specimen were measured once the element reaches the die using FE software. The second approach was based on analytical calculations and the predicted sheet velocity. According to Daehn (2006) the pressure generated upon the impact of

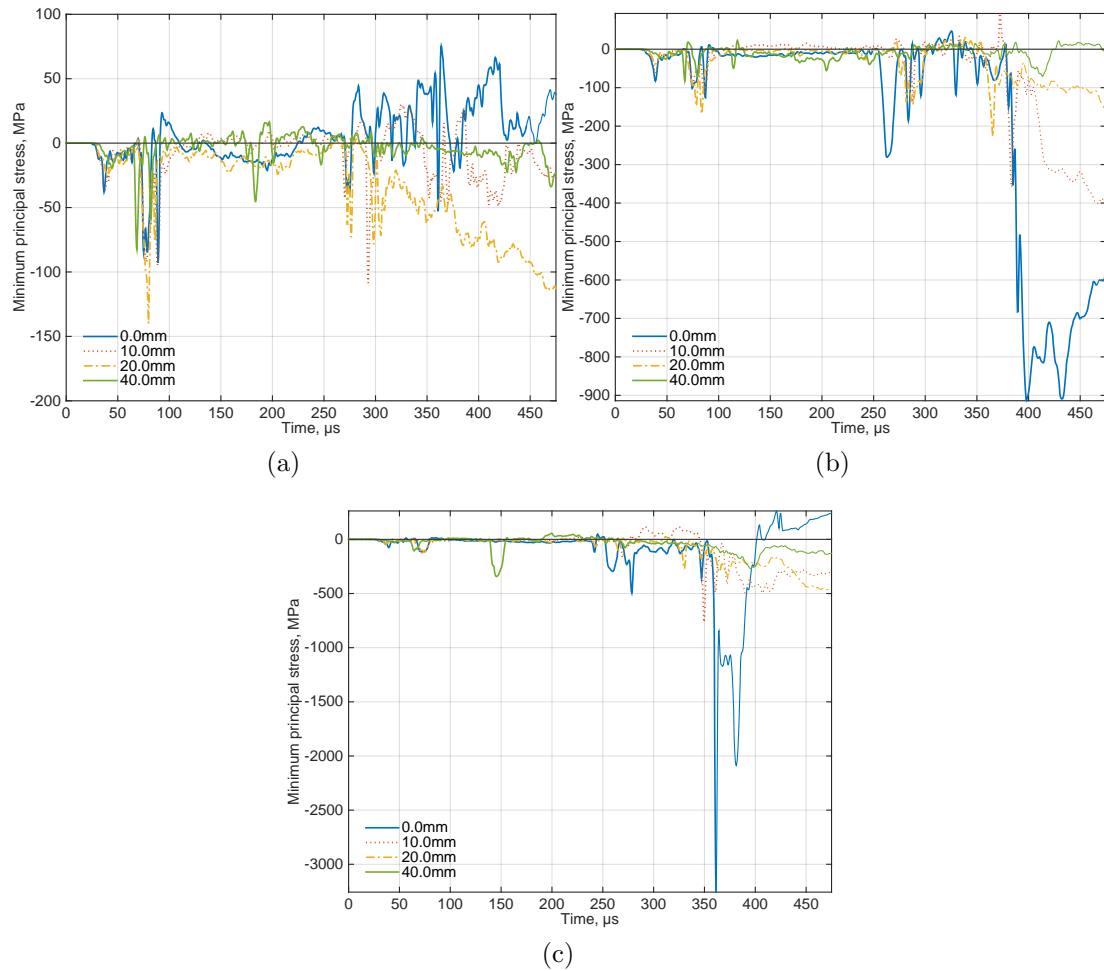


Figure 5.9: Evolution of the through-thickness stress at different radial distances from the apex for (a) EHF specimen formed with 4.8kJ input energy, (b) EHDF-34° specimen formed with 6.4kJ input energy and (c) EHDF-40° specimen formed with 14.4kJ input energy; values were taken from elements located at the mid-thickness of the sheet.

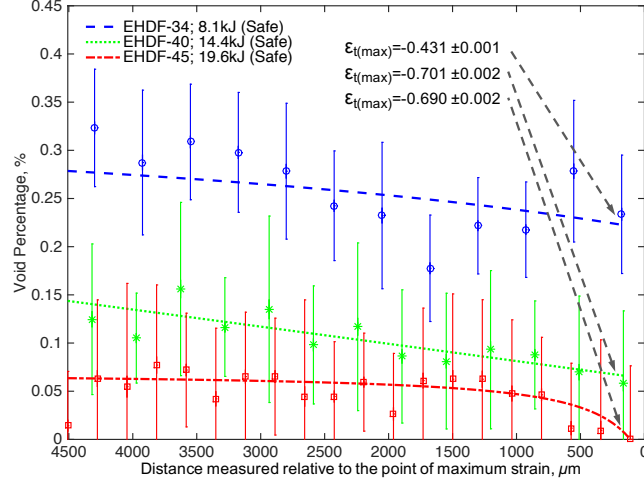


Figure 5.10: The effect of input energy on void evolution in safely formed EHDF specimens brought from Jenab et al. (2017).

the sheet against the matching die ( $P_i$ ) can be estimated using Eq.5.3;

$$P_i = V_i \left( \frac{\rho_{St} \rho_{Al} C_{St} C_{Al}}{\rho_{St} C_{St} + \rho_{Al} C_{Al}} \right) \quad (5.3)$$

where  $V_i$  is the impact velocity,  $\rho_{Al}$  and  $\rho_{St}$  are the density of the aluminium sheet and of the die steel, respectively.  $C_{Al}$  and  $C_{St}$  are the longitudinal wave speed in the aluminium and steel, respectively, which can be calculated based on the bulk modulus ( $K$ ), density ( $\rho$ ) and Poisson's ratio ( $\nu$ ) using Eq.5.4. The values used to calculate the wave speed are shown in Table 5.3.

$$C = \sqrt{\frac{3K(1 - \nu)}{\rho(1 + \nu)}} \quad (5.4)$$

Table 5.3: Steel and aluminium properties.

	Steel	Al.
$\rho$ [kg/m <sup>3</sup> ]	$7.8 \times 10^3$	$2.65 \times 10^3$
$\nu$	0.3	0.33
$K$ [Pa]	$160 \times 10^9$	$E_{Al}/3(1 - 2\nu_{Al})$

It can be seen from Fig. 5.11 that considering all the approximations used to calculate the wave speed, bulk modulus, and simplification made in Eq.5.4 itself, the impact pressure calculated based on analytical and FE analysis are quite close. This is an-

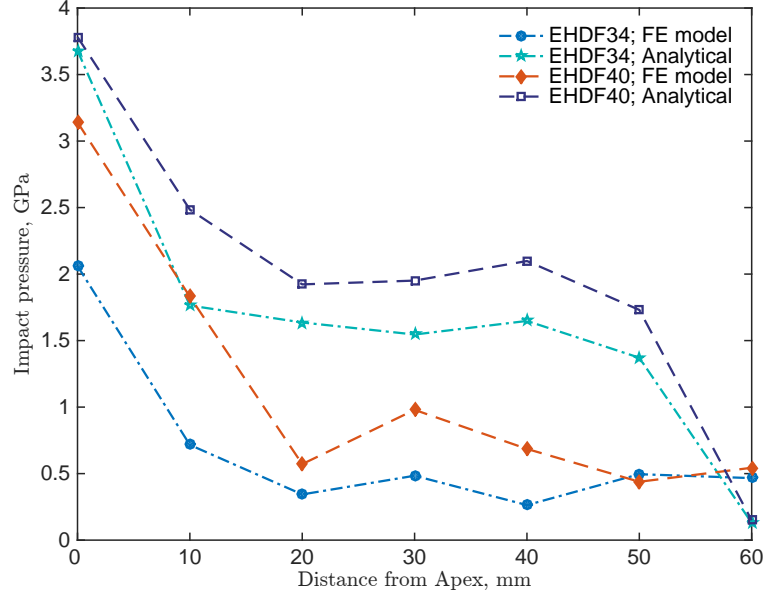


Figure 5.11: Comparison between impact pressure and maximum through thickness stress generated upon impact of the sheet against the die; lines with filled markers are calculated based on the analytical approach, Eq.5.3, and lines with open markers are derived directly from FE model ( $\sigma_{3max}$ ).

other confirmation that the results predicted by the FE model are reasonably accurate. Similar calculations were carried out based on a model developed by Ibrahim et al. (2014) and the same trend was observed, except that at the apex the predicted impact pressures were calculated to be 0.5GPa greater than those obtained from Eq.5.3. Moreover, as shown in Fig. 5.11 elements located at the apex (0mm in Fig.5.9) and close to the apex (10mm from the apex) experience significant compressive stress. According to French and Weinrich (1977) when the superimposed hydrostatic pressure is increased void nucleation and growth can be suppressed and hence localized deformation is postponed. This is also confirmed by Xiang et al. (2017) using molecular dynamics simulations showing that existing void in microstructure collapse under shock compression.

In fact, several high strain rate deformation studies (i.e. Imbert et al. (2005) for AA5754 sheets, Jenab et al. (2017) for AA5182-O sheets, Samei et al. (2014) for DP steel sheets), showed that as a results of the impact of the sheet against the die void growth and coalescence are suppressed. Consequently, the damage accumulation decreases as the impact pressure increases and hence the die effect leads to increased

formability of the sheet material.

Finally, two main mechanisms which contributed to improvement of formability of AA5182-O sheets can be outlined. Firstly, the material response to high strain rate deformation might change when compared to conventional quasi-static or moderate deformation processes. Increased strain rate and deformation velocity could be enough to change constitutive behaviour of AA5182-O as suggested by the slight positive strain rate sensitivity reported by Jenab et al. (2016). Secondly, the combination of EHF process related parameters including compressive through-thickness stresses generated during the deformation could postpone the failure. Also, the increased velocity and significant impact pressure at the final stage of deformation not only prevent material sliding across the die surface and strains localizing, but also helps in further delaying the failure mechanisms. The combination of these mechanical aspects which suppress the damage and positively influence formability were discussed as *tool-sheet interaction* or *ironing effect* to explain such improved mechanical response in earlier high strain rate forming studies.

## 5.4 Conclusions

The purpose of this study was to investigate the formability improvement of commercial AA5182-O sheets during electro-hydraulic forming. Experimental and finite element analyses were therefore carried out on EHFF and EHDF specimens. The effect of different process-related parameters such as strain rate, sheet velocity, stress triaxiality and impact pressure was investigated on the magnitude of formability improvement. And, the following conclusions were obtained:

1. Although, formability improvement during EHFF experiments was insignificant, EHF specimens formed using 34 and 40° conical dies showed 40% and 70% improvement in effective strain values when compared with quasi-static FLC curve.
2. Reasonable correlation between simulation and experimental results were achieved by coupled Eulerian-Lagrangian model and using the ignition and growth model

to simulate the EHF pulse formation. The FE model was able to accurately predict the strain distribution and the shape of deformed specimens. Similar to EHF studies carried out on steel sheets, AA5182-O specimens experience some delay in deformation in the central region relative to the periphery of the specimen. Moreover, experimental results show that AA5182-O sheet was formed in biaxial strain path during EHFF and showed a slight deviation towards plane strain tension after 20-30% engineering strain when EHDF into a conical die.

3. Simulations showed significant peak strain rate values when sheet specimens were formed using EHDF process. In case of EHFF, the peak strain rate occurs during the deformation where triaxiality is positive (tension state). However, when sheet specimens were formed using EHDF, the peak strain rate occurred in the final stage of deformation when the sheet contacted the die at high velocity.
4. Velocity changes during EHFF and EHDF deformation showed that there was a significant difference between velocity changes in the apex region and areas away from the apex. At areas away from the apex, only one peak was seen. However, in the apex region, at least two separate velocity peaks were observed. The peak velocity increased with the input energy when AA5182-O sheet was formed using EHDF.
5. When AA5182-O sheet was formed using EHDF, significant compressive stress was generated through the thickness during the deformation, especially in areas close to the apex. However, in case of EHFF the peak through-thickness stress occurred in the early stages of deformation and was significantly lower than that predicted in EHDF specimens.
6. The impact stress decreased as the radial distance from the apex increased. Moreover, comparison between the FE model predictions and analytical calculations confirms that the FE model is able to adequately predict this compressive impact stress. Furthermore, FE simulation predicted greater impact stress in the EHDF specimens which also showed greater improvement in formability

than the EHFF specimens.

7. Finally, it is thought that the combination of high strain rate, negative stress triaxiality, increased velocity, compressive through-thickness stress and impact pressure all contributed to the formability improvement of AA5182-O in EHDF.

## 5.5 Acknowledgements

This research was funded by NSERC's Automotive Partnership Canada program (APCPJ 418056-11) with support from Amino North America Corp., ArcelorMittal Dofasco, Ford Motor Company, CanmetMATERIALS-Natural Resources Canada and Novelis Inc. Alan Gillard of Ford Research Advanced Engineering is gratefully acknowledged for carrying out the EHF experiments. Also, discussions with Dr. Amir Hassannejadasl were very much appreciated.

## 5.6 References

- [1] Balanethiram, V. S. *Hyperplasticity: Enhanced Formability of Sheet Metals at High Workpiece Velocity*. PhD thesis, 1996.
- [2] Balanethiram, V. S. and Daehn, G. S. Enhanced formability of interstitial free iron at high strain rates. *Scripta Metallurgica et Materialia*, 27(12):1783 – 1788, 1992.
- [3] Balanethiram, V. S. and Daehn, G. S. Hyperplasticity: Increased forming limits at high workpiece velocity. *Scripta Metallurgica et Materialia*, 30(4):515–520, February 1994. ISSN 0956716X.
- [4] Balanethiram, V. S., Hu, X., Altynova, M., and Daehn, G. S. Hyperplasticity: Enhanced formability at high rates. *Journal of Materials Processing Technology*, 45(1-4): 595–600, September 1994. ISSN 09240136.
- [5] Cheng, J., Green, D. E., and Golovashchenko, S. F. Formability enhancement of DP600 steel sheets in electro-hydraulic die forming. *Journal of Materials Processing Technology*, 244:178–189, 2017. ISSN 09240136. doi: 10.1016/j.jmatprotec.2017.01.027.
- [6] Daehn, G. S. High-velocity metal forming. *Metalworking: Sheet Forming (ASM Handbook)*, 14:405–418, 2006.
- [7] French, I. E. and Weinrich, P. F. Tensile Fracture Mechanisms of F.C.C. Metals and Alloys - A Review of The Influence of Pressure. *J Australas Inst Met*, 22(1):40–50, 1977.
- [8] Gerdooei, M., Dariani, B. M., and Liaghat, G. H. Effect of Material Models on Formability of Sheet Metals in Explosive Forming. In *Proceedings of the World Congress on Engineering*, volume II, 2009. ISBN 9789881821010.

- [9] Golovashchenko, S. F., Mamutov, A. V., Bonnen, J. J., and Gillard, A. J. Electrohydraulic forming of sheet metal parts. In *Proceedings of the 10th International Conference on Technology of Plasticity, ICTP 2011*, pages 1170–1175, 2011.
- [10] Golovashchenko, S. F., Gillard, A. J., and Mamutov, A. V. Formability of dual phase steels in electrohydraulic forming. *Journal of Materials Processing Technology*, 213(7): 1191–1212, July 2013. ISSN 09240136.
- [11] Golovashchenko, S., Mamutov, V., Dmitriev, V., and Sherman, A. Formability of sheet metal with pulsed electromagnetic and electrohydraulic technologies. In S.K., D., editor, *TMS Annual Meeting*, pages 99–110, San Diego, CA, 2003.
- [12] Hassannejadasl, A. *Simulation of Electrohydraulic Forming Using Anisotropic , Rate-dependent Plasticity Models*. PhD thesis, 2014.
- [13] Hassannejadasl, A., Green, D. E., Golovashchenko, S. F., Samei, J., and Maris, C. Numerical modelling of electrohydraulic free-forming and die-forming of DP590 steel. *Journal of Manufacturing Processes*, 16(3):391–404, August 2014. ISSN 15266125.
- [14] Hopperstad, O. S., Børvik, T., Langseth, M., Labibes, K., and Albertini, C. On the influence of stress triaxiality and strain rate on the behaviour of a structural steel. Part I. Experiments. *European Journal of Mechanics, A/Solids*, 22(1):1–13, 2003. doi: 10.1016/S0997-7538(02)00006-2.
- [15] Ibrahim, R., Golovashchenko, S. F., Smith, L. M., Mamutov, A. V., Bonnen, J., and Gillard, A. J. Analysis of Dynamic Loads on the Dies in High Speed Sheet Metal Forming Processes. *Journal of Materials Engineering and Performance*, 23(5):1759–1769, 2014. ISSN 1059-9495. doi: 10.1007/s11665-014-0910-2.
- [16] Imbert, J. and Worswick, M. Electromagnetic reduction of a pre-formed radius on AA 5754 sheet. *Journal of Materials Processing Technology*, 211(5):896–908, may 2011. ISSN 09240136. doi: 10.1016/j.jmatprotec.2010.07.021.
- [17] Imbert, J., Worswick, M., Winkler, S., Golovashchenko, S., and Dmitriev, V. Analysis of the increased formability of aluminum alloy sheet formed using electromagnetic forming. *SAE Technical Papers 2005-01-0082*, April 2005.
- [18] Imbert, J. M., Winkler, S. L., Worswick, M. J., Oliveira, D. a., and Golovashchenko, S. The effect of tool-sheet interaction on damage evolution in electromagnetic forming of aluminum alloy sheet. *Journal of Engineering Materials and Technology*, 127(1): 145–153, 2005. ISSN 00944289. doi: 10.1115/1.1839212.
- [19] Jenab, A., Green, D. E., Alpas, A. T., and Boyle, K. P. Formability of AA5182-O Sheet during Electro-Hydraulic Forming : Influence of Input Energy. In *Materials Science and Technology Conference and Exhibition 2015, MS and T 2015*, volume 1, pages 535–542, Columbus, 2015. Association for Iron and Steel Technology, AISTECH.
- [20] Jenab, A., Sari Sarraf, I., Green, D. E., Rahmaan, T., and Worswick, M. J. The Use of genetic algorithm and neural network to predict rate-dependent tensile flow behaviour of AA5182-O sheets. *Materials & Design*, 94:262–273, mar 2016. ISSN 02641275. doi: 10.1016/j.matdes.2016.01.038.
- [21] Jenab, A., Green, D. E., and Alpas, A. T. Microscopic investigation of failure mechanisms in AA5182-O sheets subjected to electro-hydraulic forming. *Materials Science and Engineering: A*, 691(December 2016):31–41, apr 2017. ISSN 09215093. doi: 10.1016/j.msea.2017.03.007.
- [22] Lee, E., Finger, M., and Collins, W. *JWL equation of state coefficients for high explosives*. Livermore, CA (United States), jan 1973. doi: 10.2172/4479737.



- [23] Lee, E. L., Hornig, H. C., and Kury, J. W. Adiabatic Expansion Of High Explosive Detonation Products. Technical report, Lawrence Livermore National Laboratory (LLNL), Livermore, CA (United States), may 1968.
- [24] Mamutov, A. V., Golovashchenko, S. F., Mamutov, V. S., and Bonnen, J. J. F. Modeling of electrohydraulic forming of sheet metal parts. *Journal of Materials Processing Tech.*, 219:84–100, 2015. ISSN 0924-0136. doi: 10.1016/j.jmatprotec.2014.11.045.
- [25] Maris, C. Experimental determination of the forming limits of DP600 and AA5182 sheets in electrohydraulic free forming. Master’s thesis, University of Windsor, 2014.
- [26] Maris, C., Hassannejadasl, A., Green, D. E., Cheng, J., Golovashchenko, S. F., Gillard, A. J., and Liang, Y. Comparison of quasi-static and electrohydraulic free forming limits for DP600 and AA5182 sheets. *Journal of Materials Processing Technology*, 235: 206–219, 2016. ISSN 0924-0136. doi: 10.1016/j.jmatprotec.2016.04.028.
- [27] Melander, A., Delic, A., Björkblad, A., Juntunen, P., Samek, L., and Vadillo, L. Modelling of electro hydraulic free and die forming of sheet steels. *International Journal of Material Forming*, pages 223–231, 2011. ISSN 1960-6206. doi: 10.1007/s12289-011-1080-5.
- [28] Oliveira, D. A., Worswick, M. J., Finn, M., and Newman, D. Electromagnetic forming of aluminum alloy sheet: Free-form and cavity fill experiments and model. *Journal of Materials Processing Technology*, 170(1-2):350–362, dec 2005. ISSN 09240136. doi: 10.1016/j.jmatprotec.2005.04.118.
- [29] Polmear, I. J. *Light Alloys From Traditional Alloys to Nanocrystals*. Butterworth-Heinemann-Elsevier, Oxford, 2006.
- [30] Rohatgi, A., Stephens, E. V., Soulami, A., Davies, R. W., and Smith, M. T. Experimental characterization of sheet metal deformation during electro-hydraulic forming. *Journal of Materials Processing Technology*, 211(11):1824–1833, November 2011. ISSN 09240136.
- [31] Rohatgi, A., Stephens, E. V., Davies, R. W., Smith, M. T., Soulami, A., and Ahzi, S. Electro-hydraulic forming of sheet metals: Free-forming vs. conical-die forming. *Journal of Materials Processing Technology*, 212(5):1070–1079, May 2012. ISSN 09240136.
- [32] Rohatgi, A., Soulami, A., Stephens, E. V., Davies, R. W., and Smith, M. T. An investigation of enhanced formability in AA5182-O Al during high-rate free-forming at room-temperature: Quantification of deformation history. *Journal of Materials Processing Technology*, 214(3):722–732, March 2014. ISSN 09240136.
- [33] Samei, J., Green, D. E., and Golovashchenko, S. F. Analysis of Failure in Dual Phase Steel Sheets Subject to Electrohydraulic Forming. *Journal of Manufacturing Science and Engineering*, 136(October):1–8, 2014. doi: 10.1115/1.4027940.
- [34] Serway, R. A. and Beichner, R. J. *Physics for Scientists and Engineers with Modern Physics*. Physics for Scientists and Engineers with Modern Physics. Saunders College, fifth edition, 2000. ISBN 0-03-022657-0.
- [35] Seth, M. *High velocity formability and factors affecting it*. PhD thesis, The Ohio State University, 2006.
- [36] Seth, M., Vohnout, V. J., and Daehn, G. S. Formability of steel sheet in high velocity impact. *Journal of Materials Processing Technology*, 168(3):390–400, 2005. ISSN 09240136. doi: 10.1016/j.jmatprotec.2004.08.032.
- [37] Shabrov, M. N. and Needleman, A. An analysis of inclusion morphology effects on void nucleation. *Modelling and Simulation in Materials Science and Engineering*, 10(2):163–183, 2002. doi: 10.1088/0965-0393/10/2/305.

- [38] Taleff, E. M., Nevland, P. J., and Krajewski, P. E. Solute-drag creep and tensile ductility in aluminum alloys. In *Creep Behavior of Advanced Materials for the 21st Century*, pages 349–358. The Mineral, Metals & Materials Society, 1999.
- [39] Thomas, J. D., Seth, M., Daehn, G. S., Bradley, J. R., and Triantafyllidis, N. Forming limits for electromagnetically expanded aluminum alloy tubes: Theory and experiment. *Acta Materialia*, 55(8):2863–2873, 2007. ISSN 13596454. doi: 10.1016/j.actamat.2006.12.025.
- [40] Wu, P., Jain, M., Savoie, J., MacEwen, S., Tuğcu, P., and Neale, K. Evaluation of anisotropic yield functions for aluminum sheets. *International Journal of Plasticity*, 19(1):121–138, January 2003. ISSN 07496419.
- [41] Xiang, M., Cui, J., Yang, Y., Liao, Y., Wang, K., Chen, Y., and Chen, J. Shock responses of nanoporous aluminum by molecular dynamics simulations. *International Journal of Plasticity*, 97:24–45, 2017. ISSN 07496419. doi: 10.1016/j.ijplas.2017.05.008.

## Chapter 6

# Microscopic investigation of failure mechanisms in AA5182-O sheets subjected to electro-hydraulic forming

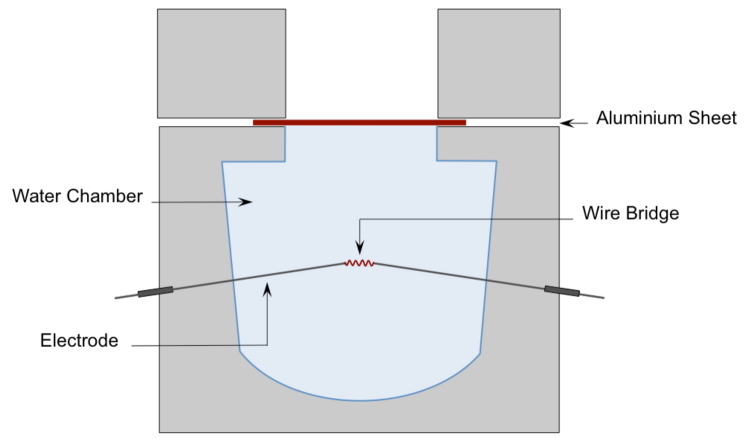
In this chapter, damage mechanisms in AA5182-O aluminium sheets were investigated using quasi-static (QS) Marciniak tests and high strain-rate electro-hydraulic forming (EHF) process. The results confirm that void nucleation, growth and coalescence are the main damage mechanisms of AA5182-O at both high and low strain rates. The EDS analysis suggests that cracking of  $\text{Al}_3(\text{Fe-Mn})$  intermetallic particles is the main source of void nucleation, whereas  $\text{Mg}_2\text{Si}$  particles do not majorly influence void formation. Void growth analysis suggests that specimens deformed under QS conditions contained more voids in areas away from the sub-fracture surface but specimens deformed at high-strain rate exhibit more significant rate of void growth close to sub-fracture areas. Void formation is suppressed by increasing the applied energy in EHF. And more significantly, the growth of voids is suppressed due to the high-velocity impact of the sheet against the die which plays an important role in increasing formability of AA5182-O aluminium sheet in EHF process. When the void percentage increase remains less than about 0.5% AA5182-O can be formed safely. However, when the void percentage increases beyond 0.6-0.8% fracture becomes inevitable.

∴ This section has been published: A. Jenab, D. E. Green, A. T. Alpas, “Microscopic investigation of failure mechanisms in AA5182-O sheets subjected to electro-hydraulic forming”, *Materials Science & Engineering A*, vol. 691, pp. 31-41, Mar 2017.

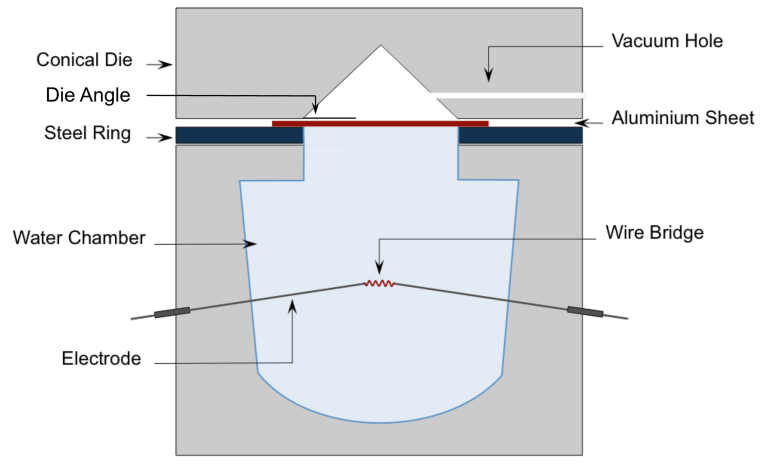
## 6.1 Introduction

Al-Mg alloys (AA5xxx alloys) were developed due to the need for sheet materials with greater strength, weldability, formability and corrosion resistance [1]. Today, AA5182-O aluminium alloys are used extensively for inner-parts of vehicles to reduce body weight and fuel consumption [2]. Aluminium sheets can be formed at elevated temperatures in order to improve their formability and facilitate their implementation in automotive applications. However, high temperature forming has its drawbacks including the application and removal of lubrication and high energy consumption. Alternatively, new forming techniques, mainly at high-strain rates, are of interest. Electro-hydraulic forming (EHF) is one of the most promising high-strain rate forming techniques investigated in recent years in which higher formability was reported for different alloys (i.e. AA6061-T4 in [3, 4], AA5182-O in [5–7], and different dual-phases steels [8–10]). Fig. 6.1 shows a schematic of the EHF process in which a high-voltage current is discharged between two electrodes submerged in water. The pressure pulse generated in the water chamber causes the sheet to deform at high-strain rate, either in free space (Fig. 6.1(a)) or into a die (Fig. 6.1(b)).

Golovashchenko et al. [9] experimentally investigated the effect of the applied energy in electro-hydraulic die forming (EHDF) for different dual phase steels and reported that by increasing the discharge energy of EHF tests, sheet material could safely deform to higher strains and hence fracture strain increases with discharge energy. Moreover, the strain rate of EHDF tests were calculated to be as high as  $20,000\text{s}^{-1}$  in apex regions of  $34^\circ$  conical dies where during electro-hydraulic free forming (EHFF) it reaches  $6900\text{s}^{-1}$ . Hassannejadasl et al. [10] carried out numerical simulation of EHFF and EHDF of DP590 steel sheets using the Johnson-Cook constitutive and damage models and accurately predict the onset of failure in EHF. Their finite element simulation



(a)



(b)

Figure 6.1: Schematic of (a) EHFF and (b) EHDF apparatuses.

estimated the deformation strain rate to be  $3,000\text{s}^{-1}$  during EHFF and  $15,000\text{s}^{-1}$  when EHF into a  $34^\circ$  conical die [10].

Rohatgi et al. [5–7] studied the mechanical response and formability improvement of AA5182-O aluminium during EHFF and EHDF. Their results suggested a significant increase in major strain in the order of 2.5-6.5 times in EHFF and EHDF, respectively. Rohatgi et al. [5] measured the maximum measured in-plane engineering strain-rate of AA5182-O sheets during EHFF to be  $3900\text{s}^{-1}$  and estimated  $4230\text{s}^{-1}$  for EHDF experiments [7]. According to Rohatgi et al. [5] plastic strain with almost proportional relation can be achieved during the EHF process where the strain path at the apex region of specimens is linear and close to equi-biaxial strain state.

During the EHDF deformation, the interaction of die and the workpiece generate super imposed triaxial or hydrostatic pressure. The existence of such hydrostatic pressures, can prevent or postpone the failure [11]; Kao et al. [12] experimentally shown the positive effect of hydrostatic pressure on workability of 1045 steel and Wu et al. [13] numerically showed that void or microcracks nucleation, growth and coalescence can be delayed or completely eliminated by such superimposed pressures.

The term "hyperplasticity" was used to describe the improved formability of sheet materials during the EHF process [3] in which high-strain rate deformation causes "inertial effects" [14] to the specimen and the impact of the sheet against the die causes "die effects" [15, 16]. However, very few researchers have characterized the microstructural phenomena that occur in the material as a result of die impact; most of the research carried out on high-strain rate forming processes only investigated the effects of process related parameters on formability improvement.

Samei et al. [8] studied microstructural changes in DP500 and DP780 steels and correlated the improved formability with the increase in formability of the individual phases (20% for ferrite and 100% for martensite) by using the rule of mixture. Samei et al. [17] also analysed the failure mechanisms prevalent in DP steels in EHDF and concluded that impact of the sheet against the die plays a major role in suppressing voids and delaying the onset of failure.

Previously the authors [18] reported a formability improvement of AA5182-O alu-

minimum in both EHFF and EHDF, however the measured improvement was much less in the case of EHFF. Jenab et al. [19] also studied the tensile behaviour of AA5182-O aluminium at different strain rates and reported that at strain rates above  $10\text{s}^{-1}$  the flow stress increases with strain rate for any level of strain. This may explain why AA5182-O aluminium sheets exhibited higher safe strains when formed at high-strain rate in EHF [18]. However, it is still not well understood how the onset of failure is postponed during EHDF and why in EHFF formability improvement was not significant.

Ductile damage occurs as a result of void nucleation, growth and coalescence. Nucleation of voids mostly occurs at, or around, microstructural heterogeneities. Therefore, alloying elements can significantly influence the damage mechanisms and fracture behaviour. It is well known that the existence of intermetallic particles and precipitates can facilitate the final fracture by either acting as barriers in front of shear zones or by promoting the coalescence of cavities [20].

There are three possible mechanisms for void nucleation around intermetallic particles [20]; decohesion of the particle-matrix interface as shown in Fig. 6.2(a), fracture of a brittle particle (Fig. 6.2(b)), and grain boundary sliding or shear deformation which can cause decohesion of an interface as illustrated in Fig. 6.2(c). The first two lead to spherical and ellipsoidal dimples whereas the last one will lead to parabola-shape dimples [20].

The growth of equiaxed voids leads to a final fracture surface with an array of matching equiaxed dimples with heterogeneities inside them. However, in case of voids nucleated in shear deformation areas (i.e. shear bands) cavities become elongated at an angle of  $45^\circ$  to the applied principal stress which is the direction of the shear bands [20]. This will also lead to parabola-shaped dimples at the fracture surface.

Previously, Spencer [21] investigated the fracture mechanism of AA5182-O aluminium in quasi-static tension and showed that addition of Fe negatively influences the formability of Al-Mg alloys as it reduces the ductility and the fracture strain [21].

Hadianfard et al. [22] studied the damage mechanisms of AA5182-O aluminium using tensile tests at strain rates ranging from  $1.3 \times 10^{-4}$  to  $1500\text{s}^{-1}$  and concluded that void

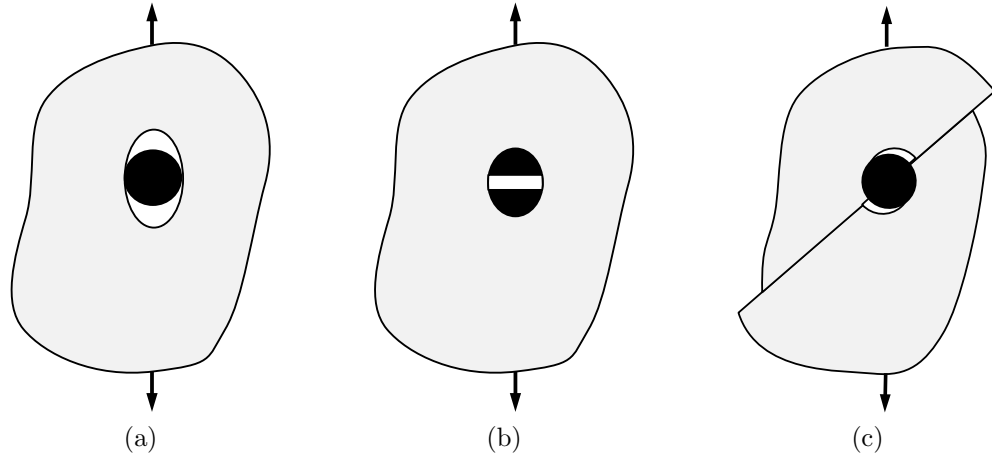


Figure 6.2: Void nucleation around inclusions; (a) matrix decohesion, (b) cracked brittle particles, and (c) shear deformation (adapted from Ref. [20]).

nucleation, growth and coalescence are the dominant damage mechanisms particularly at high-strain rate deformations.

The objective of this study is to identify the microstructural causes of formability enhancement of AA5182-O aluminium during the EHF process so as to facilitate the implementation of this novel forming technique into automotive production. Since AA5182-O aluminium contains Mg, Fe, Mn and Si as alloying elements which form different intermetallic particles of different sizes, the effect of each type of intermetallic particle and the EHF process on its deformation and fracture mechanisms was investigated. More specifically, the damage mechanisms of AA5182-O aluminium were investigated by analysing what occurs at void nucleation sites. Finally, differences in void growth between specimens deformed in biaxial tension under quasi static conditions and in EHDF conditions were analysed in order to understand the effect of the high-velocity impact against the die on the microstructure of AA5182-O aluminium.

## 6.2 Experimental and Analysis Procedures

Table 6.1 shows the optical emissions spectroscopy analysis of as-received AA5182-O aluminium 1.5mm thickness sheets used in this study. The analysis was performed using Baird One-Spark Optical Emissions Spectrometer equipped with tungsten elec-



trode following the ASTM-E1251 [23] standard.

Table 6.1: Chemical composition of the as-received AA5182-O aluminium, wt%.

Mg	Mn	Fe	Si	Cr	Cu	Zn	Ti	Al
5.02	0.37	0.24	0.041	0.004	0.015	<0.01	<0.05	Bal.

Tensile tests were carried out at quasi-static ( $\dot{\epsilon} = 0.001\text{s}^{-1}$ ) and dynamic ( $\dot{\epsilon} = 100\text{s}^{-1}$ ) strain rates. For quasi-static strain rates, specimens were cut by wire EDM following the ASTM-E8 [24] standard and deformed until fracture using an Instron 1331 servo-hydraulic testing machine. For high-strain rate tensile tests, sub-size dog-bone specimens were cut by wire EDM and deformed using a specialized Hydraulic Intermediate Strain Rate apparatus. The reader is referred to Ref. [19, 25–27] for more details about specimen geometries and test conditions.

In order to also consider the equi-biaxial strain domain, quasi-static (QS) Marciniak tests were carried out with a punch velocity of 0.1mm/s leading to a nominal strain rate of 0.01-0.04s<sup>-1</sup>. Interstitial-free (IF) steel sheet having a thickness of 1mm was used to make carrier blanks for the Marciniak tests.

The EHF experiments were performed using a Magnapress pulse unit with 200 $\mu\text{F}$  capacitance and pulses were supplied with different input voltages ranging from 6.8 to 14kV in order to form 200mm by 200mm square gridded AA5182-O sheets. The input energy of EHF can be calculated from  $U = 1/2cv^2$  where  $c$  is the capacitance of the EHF apparatus (capacitors) and  $v$  is the input voltage [9, 28]. The radius of opening of the EHF chamber and hence the area of sheet specimens being deformed is 120mm. EHDF experiments were carried out with different conical dies with die angles of 34, 40 and 45°, and EHFF experiments were carried without any die. Minor and major strains on the surface of the deformed specimens were then measured using an optical strain measurement system. For fractured specimens, only the safe grids close to the crack were measured. Table 6.2 summarizes the specimens used in this study, the status of the location where the subsurface was studied as well as the strain state at each location. It can be seen that all specimens were deformed in a biaxial or near-biaxial strain state, including the QS Maciniak specimens.

A Philips XL30 Scanning Electron Microscope equipped with EDAX Energy Disper-

Table 6.2: Deformation history, status and maximum safe strains measured in studied specimens.

Test	Die angle	Voltage, kV	Energy, kJ	Studied Location	$e_1$	$e_2$
QS Marciniak	-	-	-	Fractured	34.3	33.0
	-	-	-	Safe	29.9	29.5
EHFF	Open	7	4.9	Fractured	36.8	28.2
	Open	13.9	19.4	Fractured	43.6	26.1
EHDF	34°	8.6	7.4	Fractured	37.4	17.9
	34°	9	8.1	Safe, apex	56.4	24.4
	40°	10	10	Fractured	48.8	39.3
	40°	12	14.4	Safe, apex	62.4*	22.8*
	45°	11	12.1	Fractured	56.0	34.2
	45°	14	19.6	Safe, apex	61.0*	24.2*

\* Maximum strains measured in areas where grids were not removed due to impact. In such specimens, the grids at the apex were removed due to the severe impact against the conical die.

sive Spectroscopy was used to investigate the fracture behaviour and chemical analysis of second phases. In order to perform fractography experiments, all specimens were cut by wire EDM and fractured areas apart from cutting edges were examined. Specimens were cleaned in an ultrasonic ethanol bath for at least two minutes before being placed inside the SEM.

Transmission Electron Microscopy (TEM) was carried out on samples cut from safe QS and EHF specimens using a Tecnai Osiris FEI machine with 200kV X-FEG field emission gun equipped with SuperEDS X-ray detection system.

All sub-fracture samples were cut using wire EDM and then cold-mounted to avoid the temperature affecting their microstructure. Sample preparation was carefully performed on mounted samples in order to achieve reproducible results and reduce side effects such as pull-outs, comet tails and embedded abrasive. Abrasive disks were used in successively finer steps. To reduce the amount of deformation, grinding started with 600 SiC papers and was then followed with commercial polishing surfaces from Struder® with successively 9, 6, and 3 $\mu$ m diamond suspension, and finally with 0.5 $\mu$ m OPS abrasive solutions each used with a specific lubricant. Between each step, samples were cleaned with running water, then with an industrial cleaner, and finally in subjected to ultrasonic cleaning in ethanol bath for 5 minutes to remove the residues of previous steps, especially from fine shrinkage gaps in the cold mount that develop

during the curing of the mounts.

To analyse the results, a large-mosaic consisting of at least 10 images (with at least  $200\times$  magnification) taken from sub-fracture surfaces using Clemex<sup>®</sup> motorized stage and specified pattern. The images were digitally enhanced using a pre-defined Adobe Photoshop<sup>®</sup> routine which adjusted the brightness of images and increased the contrast. To measure the void percentage ( $VP$ ) at each location, a specialized MATLAB<sup>®</sup> code was developed. After calculating the pixel density of each image based on the scale bar, areas belonging to the mount were removed and then the large mosaic image was divided into smaller images. After thresholding, the void percentage of each image was calculated using Eq.6.1 and by considering black pixels to be voids and white pixels to be the matrix.

$$VP = \frac{\sum(P^\bullet)}{\sum(P^\bullet) + \sum(P^\circ)} \times 100 \quad (6.1)$$

where  $P^\bullet$  and  $P^\circ$  are black and white pixels, respectively. It is worth noting that the result of this method showed good agreement with Clemex Pro<sup>®</sup> calculation but provides much better flexibility to automatically study  $VP$  changes in large images. Also, using the image enhancing method (i.e. changing the brightness, contrast and thresholding), a void percentage of 0.0054 (0.54%) was determined for this as-received AA5182-O sheet material which is in agreement with 0.5% value reported by Orlov [29]. Finally, all void percentages reported in this work were determined by subtracting the initial void percentage of the as-received material from the void percentage measured from images of the deformed microstructure.

## 6.3 Results and Discussion

### 6.3.1 Strain distribution in EHF specimens

The strain distribution in all studied specimens shows that the strain increases gradually from the bottom to the apex of each specimen. For example, Fig. 6.3(a) and (b) show the strain distribution of EHDF conical specimens deformed with 7.4 and 8.1kJ

input energy, respectively. The specimen in Fig. 6.3(a) cracked in the apex region and hence the apex grids could not be measured. However, as shown in Fig. 6.3(b), the specimen formed successfully with 8.1kJ input energy exhibited higher strains compared to the specimen formed with 7.4kJ. This shows that a threshold energy level must be exceeded in order to obtain enhanced formability in EHDF.

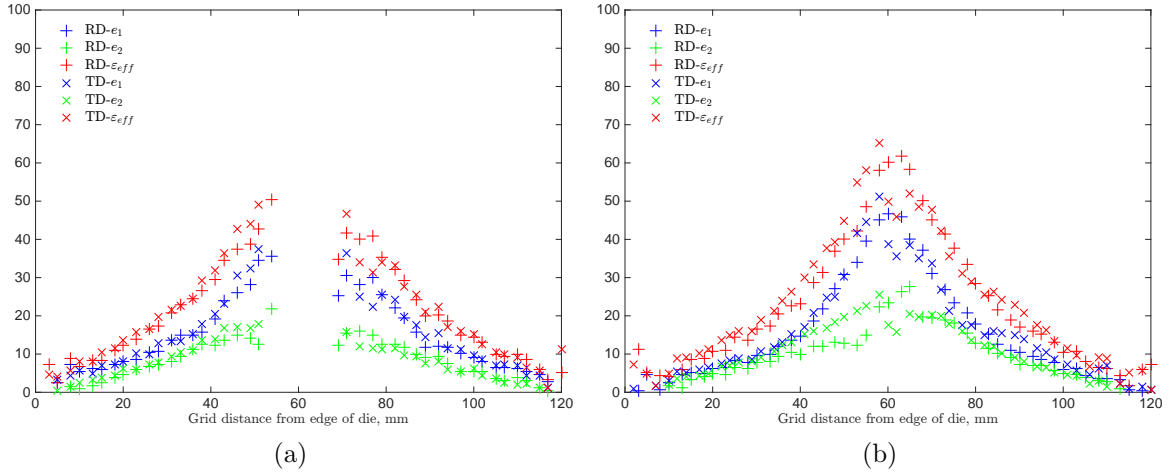


Figure 6.3: Major ( $e_1$ ), minor ( $e_2$ ) and effective ( $\epsilon_{eff}$ ) strain distributions of EHDF-34° specimens deformed at (a) 7.4kJ (fractured) and (b) 8.1kJ (safe) input energies; RD and TD refer to measurements carried out at rolling and transverse directions of the as-received rolled sheet, respectively.

### 6.3.2 Fracture Mechanism

Fig. 6.4 shows subfracture and low magnification SEM images of AA5182-O samples deformed and fractured under QS, EHFF and EHDF conditions. It can be seen that all specimens show similar dimpled fracture topography. Also, Fig. 6.4(a) shows that specimens deformed under QS conditions, did not exhibit significant post-uniform deformation. This can be quantified by the change in thickness strain from  $-0.696 \pm 0.001$  in areas of uniform deformation away from the fracture to  $-0.783 \pm 0.004$  just before fracture. This insignificant through-thickness strain localization is the reason that it was not possible to interrupt the Marciniak tests at the onset of necking. This observation is in agreement with the fact that in the QS strain rate domain, from  $10^{-4}$  to  $1s^{-1}$ , the flow stress of AA5182-O aluminium decreases with increasing strain rate [19].

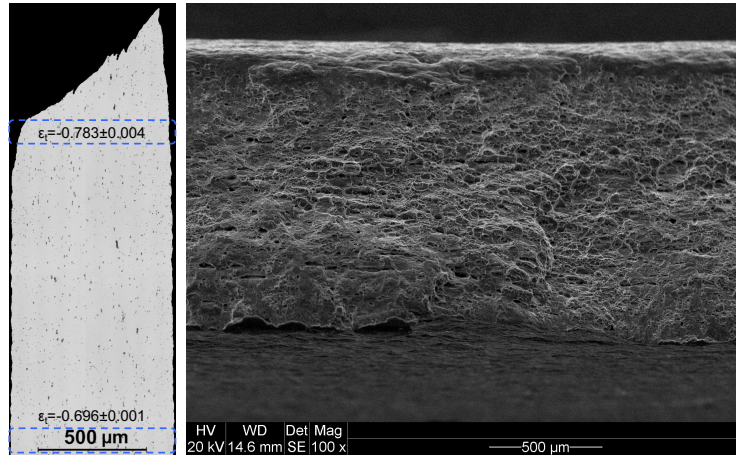
The rapid failure that occurs immediately after reaching the limiting strain was also reported by Spencer [21], who indicated that high rates of shear strain occurring at sub-fracture surface as well as flow softening were reported to be the main reasons for this limited post-uniform deformation. Unlike QS specimens where the failure occurs as a result of a single fracture surface (slip plane), two separated fracture surface were involved in the final failure of EHF specimens. Also, EHF specimens failed with significant through-thickness strain localization and post-uniform deformation as shown in Fig. 6.4(b,c). The thickness strain in the EHFF specimen, Fig. 6.4(b), reduces from  $-0.540 \pm 0.001$  in areas of uniform deformation away from the fracture to about  $-0.940 \pm 0.005$  at the subfracture surface. The same significant post-uniform deformation is also observed in EHDF specimen, Fig. 6.4(c), where the thickness strain reduces from  $-0.528 \pm 0.001$  in areas away from the fracture to  $-1.004 \pm 0.019$  at the subfracture surface.

Fig. 6.5 shows high magnification SEM fractography images of QS and EHF specimens. It can be seen that the fracture surface contains dimples indicating that void nucleation and growth is the major failure mechanism in both high and low strain rate conditions. It is worth emphasizing that due to the through-thickness shearing strain in EHF samples, parabola-shaped dimples can be seen on the fracture surface of AA5182-O aluminium (Fig. 6.5(b)-(d)).

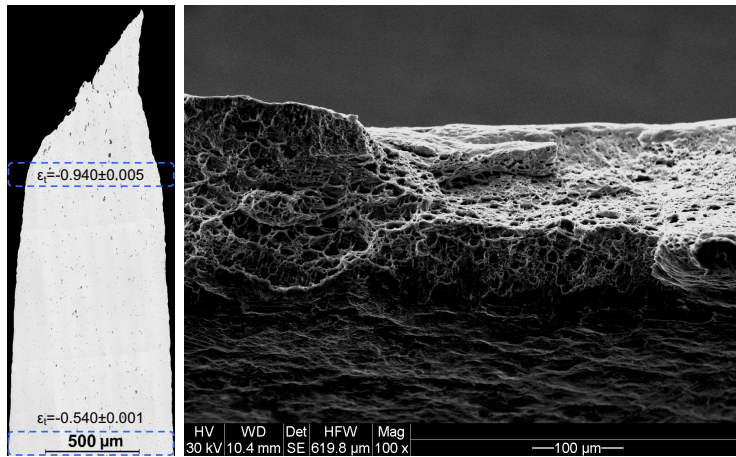
### **6.3.3 Void Nucleation; Intermetallic Particles**

Closer examination of the surface reveals that equiaxed and parabola-shaped dimples coalesce around hard particles. Fig. 6.6(a) and (b) shows the fractography of an EHFF specimen formed at 19.4kJ input energy at  $\times 2000$  magnification. Several second phase particles residing in the dimples can be seen; some are located at the bottom of dimples and some are on the side of the dimples. The EDS analysis confirmed that these particles are mainly (Fe,Mn)- and (Mg,Si)-enriched intermetallic particles and not residues or artifacts of sample preparation.

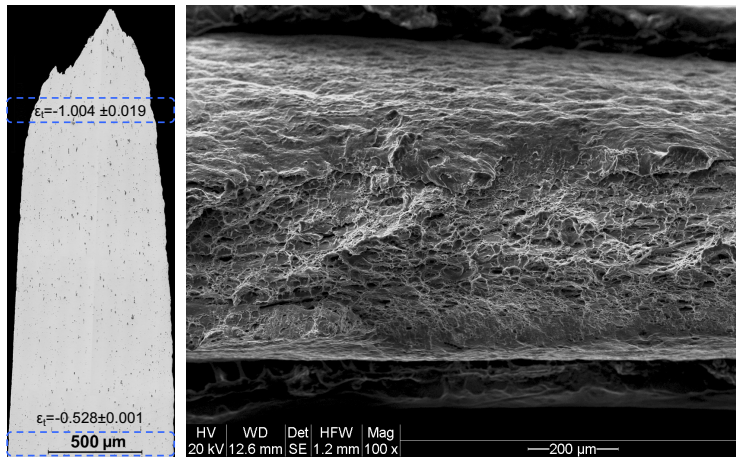
Point EDS analysis was performed on more than 170 particles residing at the bottom and side of the dimples. The results indicate that there are at least two types of



(a)



(b)



(c)

Figure 6.4: Polished subfracture and low magnification fractography of (a) QS Marciniak ( $e_1 = 34.3\%$ ,  $e_2 = 33.0\%$ ), (b) EHFF; 4.9kJ ( $e_1 = 36.8\%$ ,  $e_2 = 28.2\%$ ), and (c) EHDF-40°; 10kJ ( $e_1 = 48.4\%$ ,  $e_2 = 39.3\%$ ).

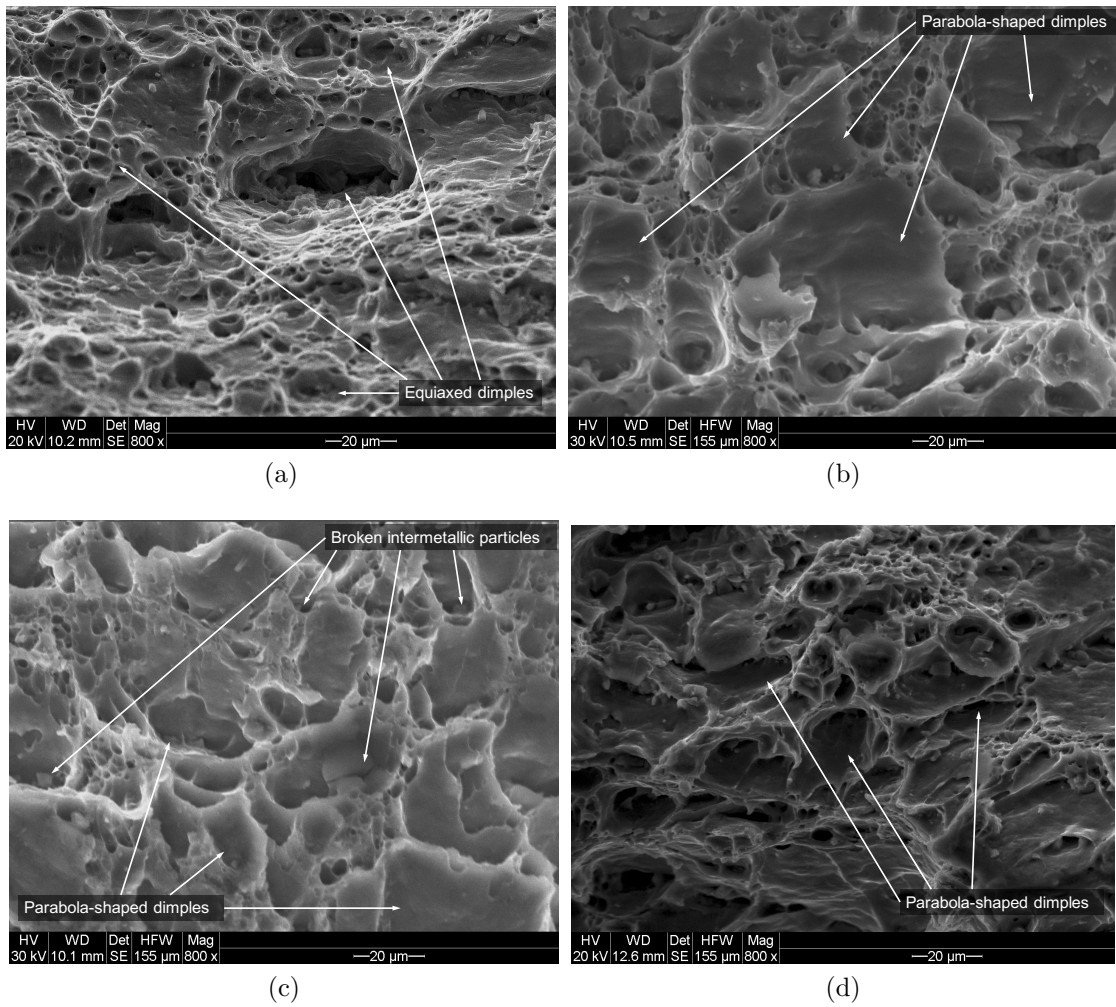


Figure 6.5: Fracture surface of AA5182-O aluminium at 800 $\times$  magnification deformed under biaxial strain state in (a) QS Marciniak, (b) EHFF; 4.9kJ, (c) EHDF-34 $^{\circ}$ ; 7.4kJ, and (d) EHDF-40 $^{\circ}$ ; 10kJ conditions.

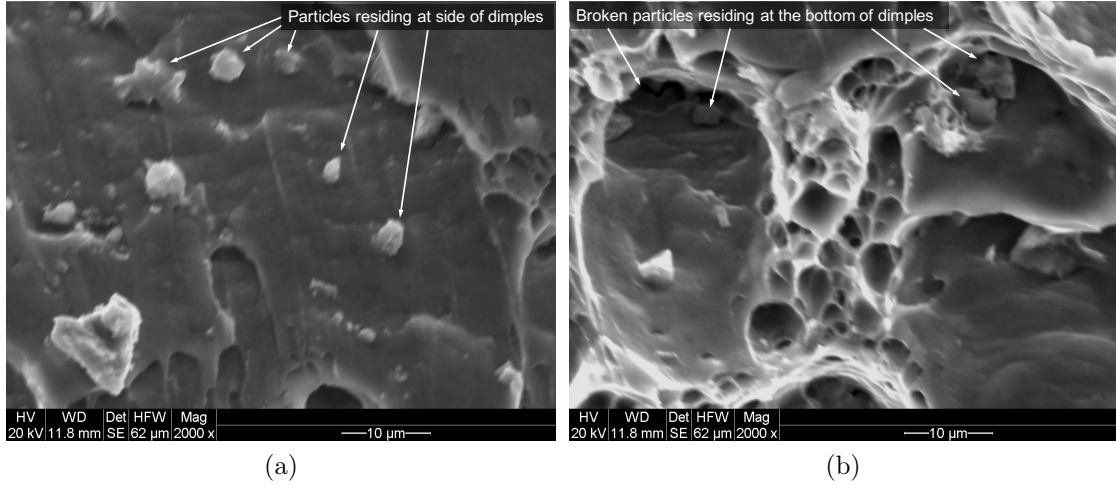


Figure 6.6: Fracture surface of EHFF specimens deformed at 19.4kJ showing different dimple sizes and cracked second phase particles at 2000× magnification; (a) at side of dimples and (b) at the bottom of dimples.

intermetallic particles that contributed to the final failure in AA5182-O. Table 6.3 shows the average quantity of alloying elements, with standard error ( $\sigma_{\bar{p}}$ ) calculated from Eq.6.2, in each type of second phase particle and a description of their typical shape and location.

$$\sigma_{\bar{p}} = t_{\alpha/2} \sqrt{\frac{\sum_{i=1}^n (\bar{p} - p_i)^2}{n(n-1)}} \quad (6.2)$$

where  $t_{\alpha/2}$  is the probability distribution calculated for 95% confidence level,  $n$  is the number of measured particles of each type, and  $p_i$  and  $\bar{p}$  are the individual and mean percentages of alloying element.

Table 6.3: Chemical composition and description of second phases existing on the fracture surface of AA5182-O subject to either quasi-static or high-strain rate forming.

Type	Average alloying elements, wt%					Specification	Position
	Al	Mg	Mn	Fe	Si		
I	71.2±3.6	3.6±0.6	4.1±1.5	21.0±2.9	0.00	broken particles	inside dimples
II	57.4±7.7	23.3±4.3	0.06±0.06	0.1±0.1	18.1±3.9	small, spherical	on dimples' side

The first type (I) intermetallic particles are Fe- and Mn-based particles with average Fe and Mn concentrations of 21% and 4% wt, respectively. Regardless of their size,



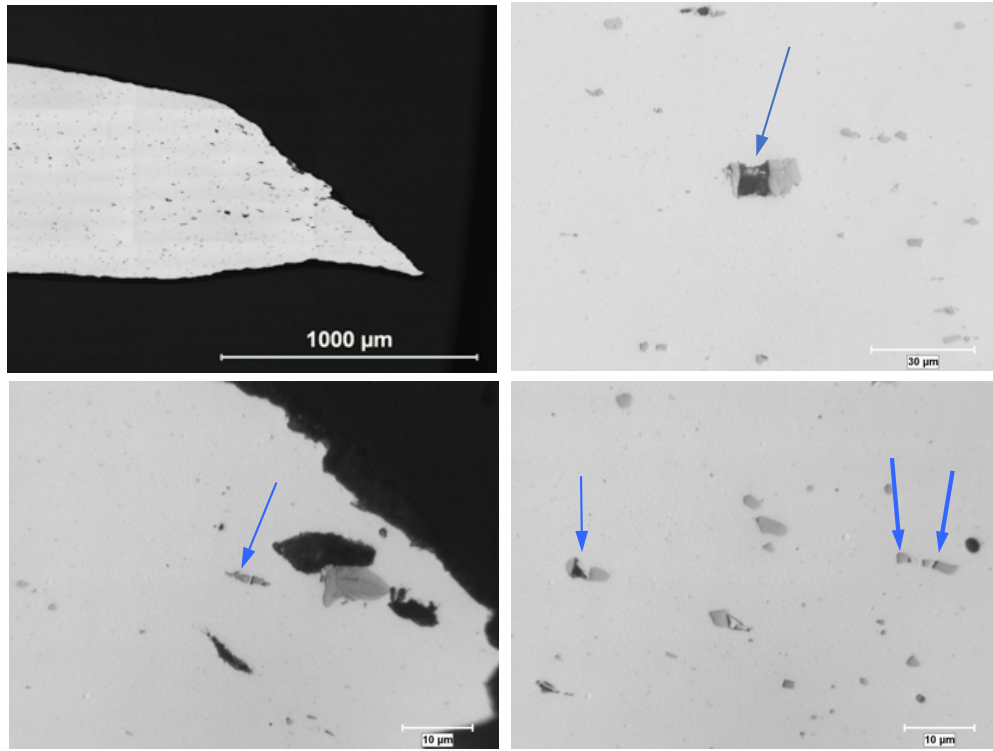
these particles mostly have sharp edges and reside deep inside dimples and were mostly cracked. Typically, relatively larger particles can be seen at the bottom of large dimples, suggesting that the dimple size directly depends on the size of the second phase particle. It is thought that cracking of these intermetallic particles leads to early nucleation of voids. It is worth noting that Fe-Mn containing particles are one of the most important intermetallic particles in AA5182 [30] where coarse particles are undesirable for sheet forming or stamping processes [31]. Depending on the history and heat treatment of the as-received material, AA5182-O aluminium may contain coarse skeletal  $Al_m(Fe,Mn)$  or lamellar shaped  $Al_3(Fe,Mn)$  particles [32]; the former particles can be transformed to the latter by eutectoid process (heat treatment at 470-520°C) and the results will be an increase in the material formability [31].

The second type (II) of intermetallic particle found on fracture surfaces of AA5182-O aluminium contain mainly Mg and Si. It is worth noting that the concentrations obtained by EDS analysis are influenced by the interaction of the X-ray beam with surrounding materials. Hence, the chemical composition of these small intermetallic particles should be  $Mg_2Si$  which is commonly observed in AA5182 alloys [30, 31]. These particles mainly reside at the side of the dimples, and hence it is believed that they most probably were de-bonded from the matrix in the final stages of failure, during void growth and coalescence.

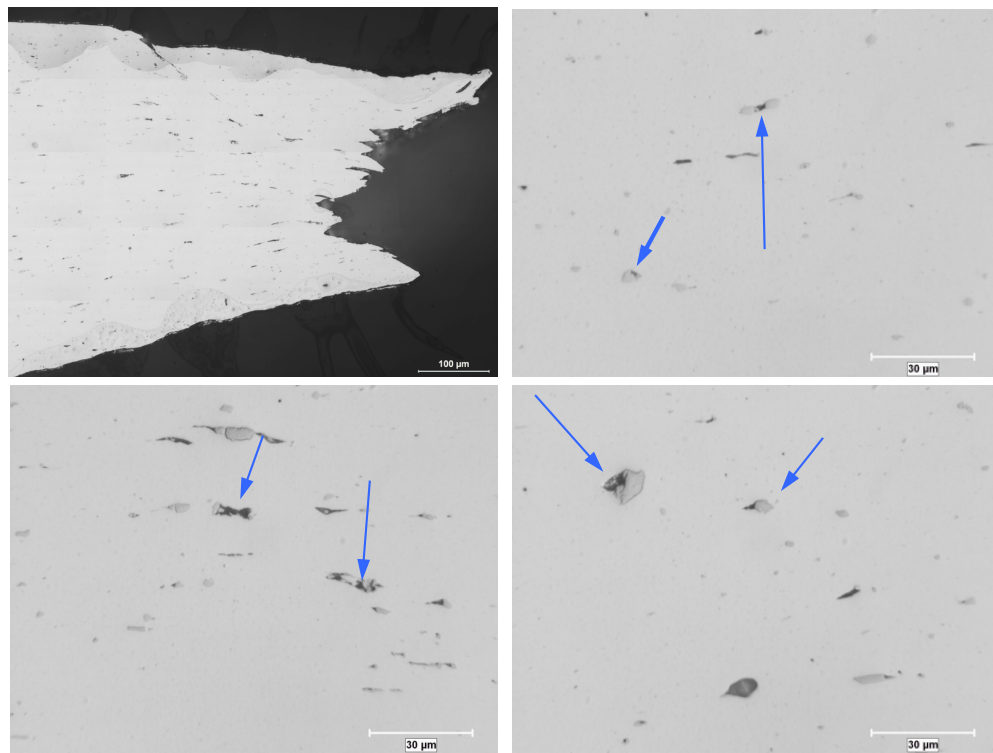
The presence of iron-enriched and silicon-based intermetallic particles was also observed in other aluminium alloys such as in AA7075 [33] and was considered to be the main source of initial void nucleation prior to fracture of AA7075-T651 [34].

These results are in agreement with the assumption of Worswick et al. [35] where voids nucleate more preferentially at particles with larger size and as strain increases the fraction of voids nucleated from smaller particles increases.

Fig. 6.7(a) and (b) show void formation by cracked intermetallic particles in EHFF and EHDF specimens, respectively. The EDS analysis of these particles also confirms that the voids nucleated from (Fe,Mn) enriched intermetallic particles. However, due to their size, void formation from  $Mg_2Si$  particles was not observed in sub-fracture surfaces.



(a)



(b)

Figure 6.7: Void nucleation sites from sub-fracture surface of (a) EHFF; 4.9kJ ( $e_1 = 36.8\%$ ,  $e_2 = 28.2\%$ ) and (b) EHDF-45°; 12.1kJ ( $e_1 = 56.0\%$ ,  $e_2 = 34.2\%$ ) specimens.

More detailed analysis of void formation was achieved from TEM results. Fig. 6.8(a)-(f) show TEM images of specimens safely deformed under QS and EHDF conditions, respectively (see Table 6.2). The samples were selected from areas away from the fracture surface and where the highest level of strains was reached. Fig. 6.8(a), (c), and (e) show the location of nucleated voids using high angle annular dark field images with overlaid bright field images. Fig. 6.8(b), (d), and (f) show scanning TEM (STEM) maps of selected alloying elements at the same locations. Void nucleation from particle cracking can be clearly seen in Fig. 6.8(a) and (b) where an (Fe,Mn) enriched particle cracked in the QS Marciniak specimen. Such void nucleation sites are also observed in EHF specimens. Fig. 6.8(c) and (d) shows an example of particle debonding in a specimen formed under EHDF conical die with 19.6kJ input energy. As mentioned earlier, voids are created when the matrix between a large (Fe,Mn)-containing particles and a small  $Mg_2Si$  particle yields causing a void to form. Fig. 6.8(e) and (f) shows the particle-matrix debonding from an (Fe,Mn)-containing particle which probably was previously broken and subsequently filled by the flow of aluminium during the hot rolling stage of AA5182-O sheet production.

Since (Fe,Mn)-containing intermetallic particles are larger in size than other particles observed, they are more prone to cracking at lower strain values [36]. Cracking of these large particles can be described by a stress-controlled model based on brittle-type fracture [37]. Also, due to their large interface, irregular shapes, and high internal surface defects, these intermetallic particles can cause void nucleation at lower strains when compared to smaller ones.

However, small  $Mg_2Si$  and Al-Mg particles, tend to be spherical or equiaxed in shape and usually participate in the failure by debonding from the matrix. The debonding can occur as a result of dislocation pile-ups which is a strain-controlled process [38] or by separation of the interface which is a stress-controlled process that depends on the hydrostatic stress [39, 40].

It is worth mentioning that the presence of a die in EHDF causes significant hydrostatic stresses to be generated in the sheet upon impact with the die. Imbert et al. [16] performed Electro-Magnetic Forming (EMF) of AA5754 sheets with and

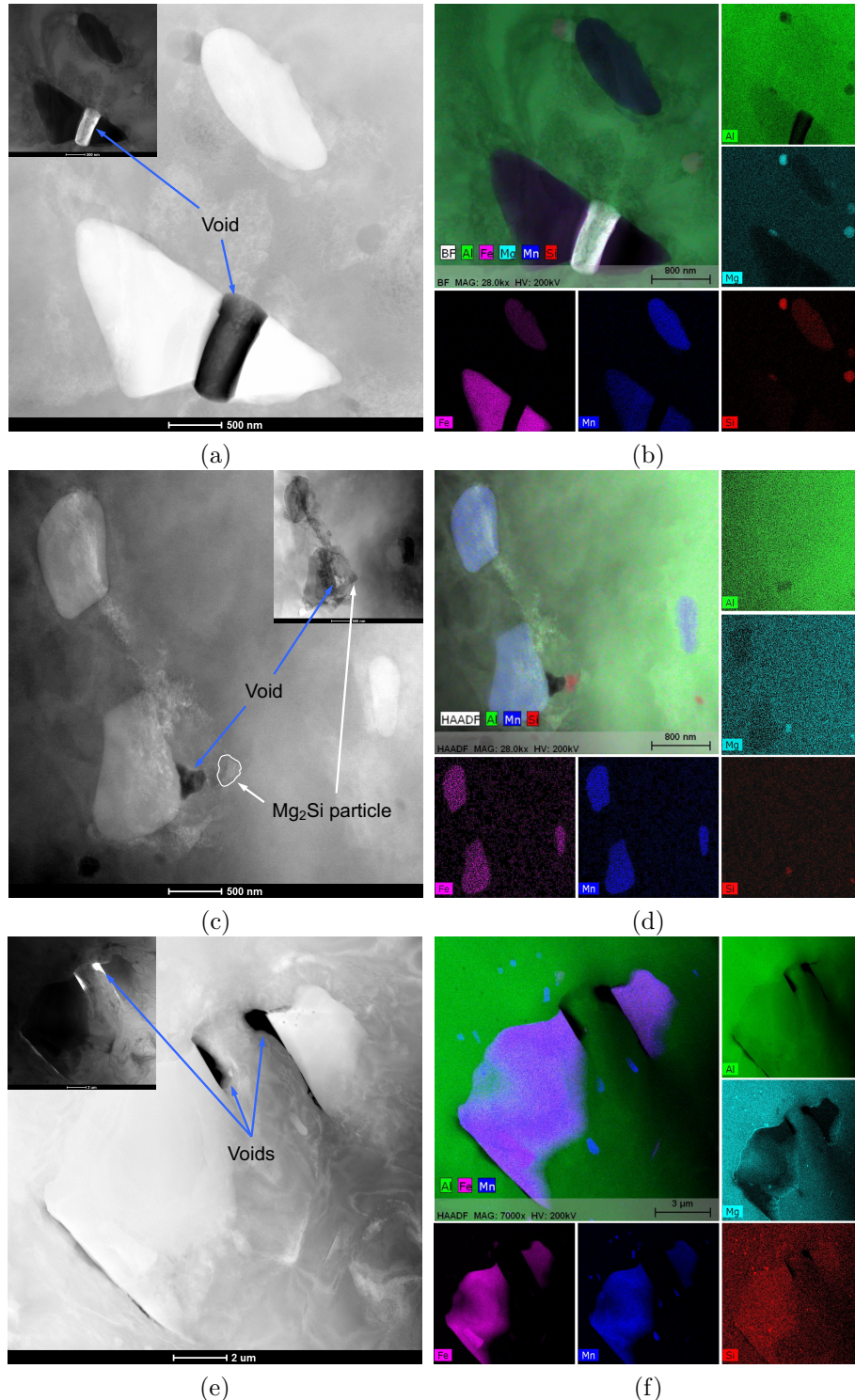
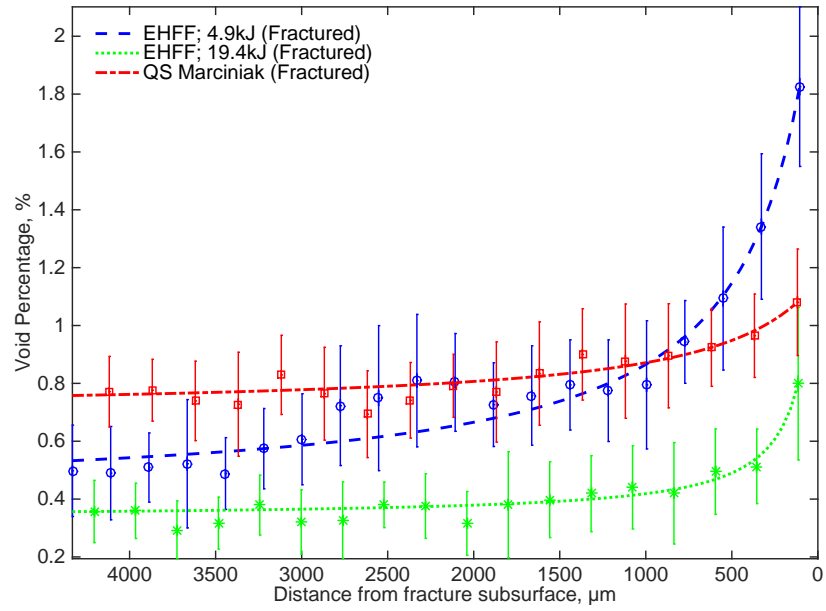


Figure 6.8: Transmission electron microscopy results of AA5182-O aluminium showing void nucleation by (a,b) cracking of (Fe,Mn)-containing particle in QS Marciniak specimen ( $e_1 = 29.9\%$ ,  $e_2 = 29.5\%$ ), (c,d) particle debonding from interface of  $Mg_2Si$  and (Fe,Mn)-containing intermetallic particle in EHDF-45°; 19.6kJ specimen ( $e_1 = 61.0\%$ ,  $e_2 = 24.2\%$ ), and (e,f) particle-matrix debonding in EHDF-40°; 14.4kJ specimen ( $e_1 = 62.4\%$ ,  $e_2 = 22.8\%$ ).

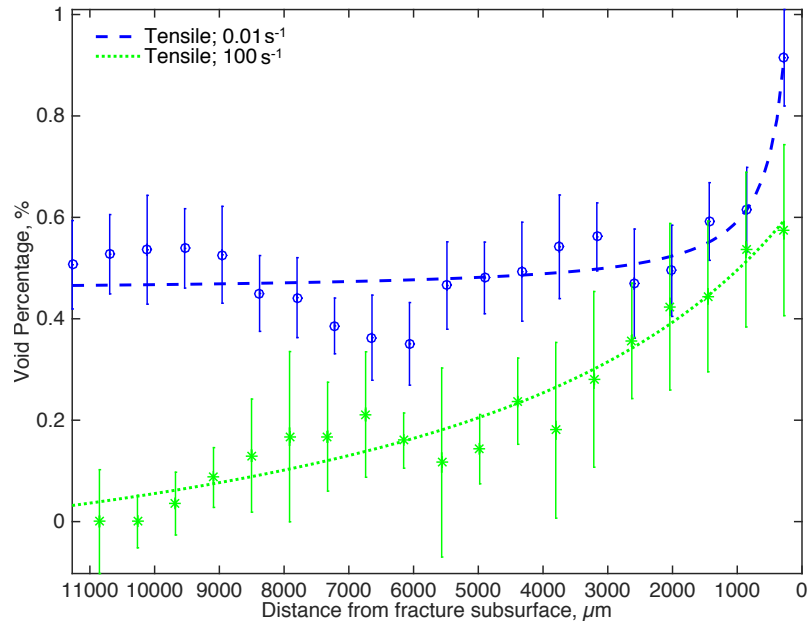
without the presence of a conical die and observed that during free forming EMF formability improves for a narrow region where in case of die forming EMF specimens show a wide range of formability improvement as compared to the QS forming limit curve. They concluded that as a result of die-sheet interaction a complex stress state is created which includes compressive (hydrostatic) stresses that potentially can reduce the effect of damage and suppress the damage evolution. Also, Hassannejad et al. [10] numerically simulated EHDF and showed that once the initial velocity sufficiently high, the specimens experience a negative stress triaxiality upon filling the die. This negative stress triaxiality increases toward the apex region of conical specimens, similar to the safe locations that were studied here.

### 6.3.4 Void Growth

Fig. 6.9(a) shows the void percentage growth as a function of distance from the fracture surface for EHFF and QS Marciniak specimens. It can be clearly seen that void formation is suppressed in the bulk of the material at high-strain rates (EHFF at 4.9kJ and 19.4kJ) compared to QS deformation. However, near to the fracture surface, the specimen deformed at high-strain rates contains more voids as compared with QS specimens. Moreover, by increasing the input energy of EHFF from 4.9kJ to 19.4kJ, lower void percentages can be seen in areas away from the fracture surface and sub-fracture surfaces. This change in material response to increased input energies during EHF of AA5182-O is in agreement with strain measurements which showed that higher values of safe strains were reached in AA5182-O aluminium EHFF specimens formed with greater input energy [18]. The same trend was also seen in case of tensile samples deformed at QS and high-strain rates ( $100\text{s}^{-1}$ ) as shown in Fig. 6.9(b). Fig. 6.10(a) shows the effect of input energy on void suppression in safely formed EHDF specimens. The same void suppression phenomenon can also be seen in safely formed EHDF specimens as shown in Fig. 6.10(a). For safely formed specimens, the distance is measured relative to the point of maximum strain. The maximum thickness strain for specimens formed at 8.1, 14.4, and 19.6kJ input energy were  $-0.431\pm 0.001$ ,  $-0.701\pm 0.002$  and  $-0.690\pm 0.002$ , respectively. Since all samples shown



(a)



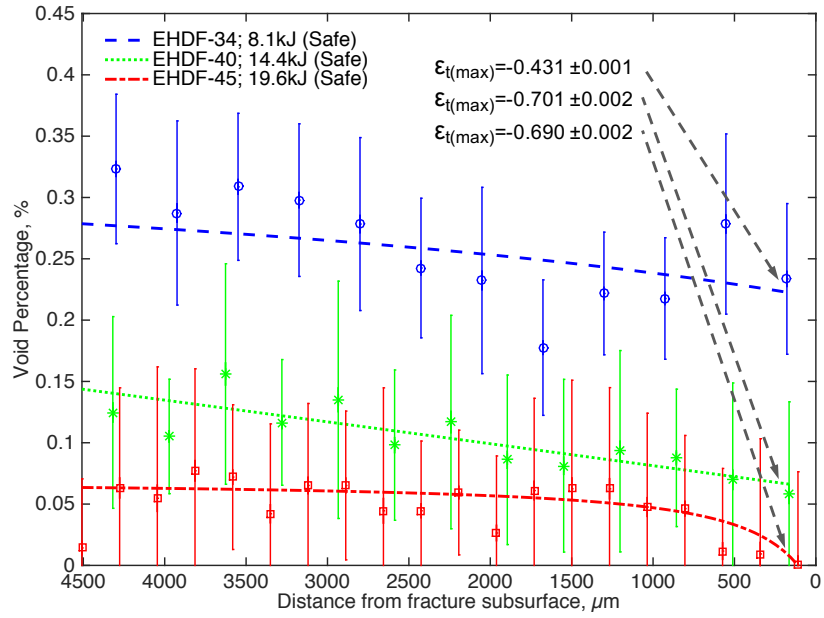
(b)

Figure 6.9: Variation in void percentage with distance from the fracture surface in specimens formed at low and high-strain rates in (a) biaxial and (b) uniaxial tension.

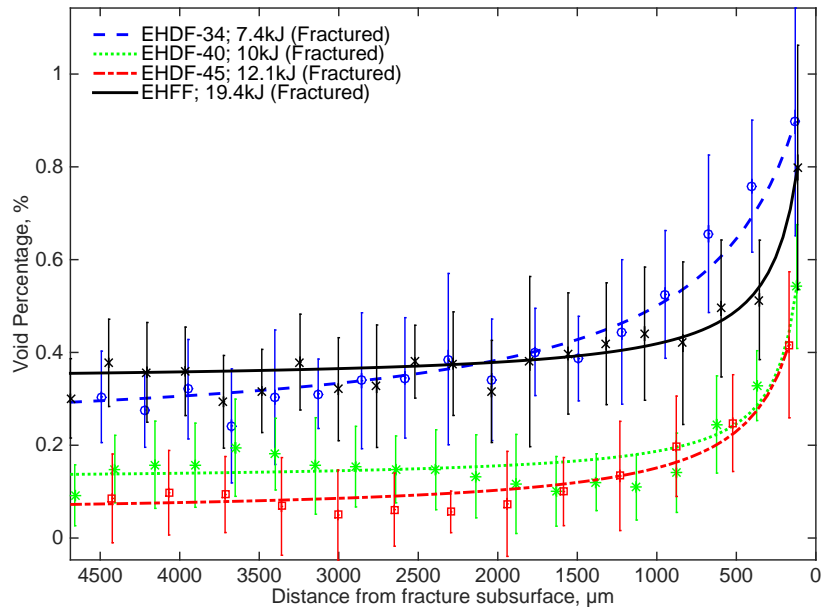
in Fig. 6.10(a) were formed into a die, the significant through-thickness compressive stress generated at the moment of impact against the die leads to closure of voids. It can be seen that the specimens formed with higher energy (14.4 and 19.6kJ) and consequently higher strain rates and impact velocities show lower void percentage. Moreover, even though the thickness strain of 8.1kJ specimen is less than that for 14.4 and 19.6kJ specimens, it exhibited at least twice the void percentage. This confirms the significant effect of the through-thickness compressive stress on void closure in EHF process. It is worth emphasizing that the same non-linear least squares curve fits were used to show the gradient of void percentages. In case of safely formed specimens, the slope of the curves is negative in areas close to the location of maximum strain. Realistically, this confirms that by increasing the strain rate and compressive stresses, void closure increases and less voids should be expected in these specimens. Comparison between void percentages in safely formed and failed samples, as shown in Fig. 6.9(a) and Fig. 6.10(a), suggest that during EHF when the void percentage remains less than 0.5%, AA5182-O aluminium can be formed safely but when the void percentage increases above 0.6-0.8% fracture becomes inevitable. This observation is in agreement with the critical void percentage reported by Chen and Worswick [41] who used a finite element-percolation damage model to predict that the presence of 0.5% of voids would cause final failure in AA5182-O and AA5754 aluminium.

Fig. 6.10(b) shows the effect of the impact against the die on void formation. It can be seen that in the presence of a die in the EHF process, the material exhibited less void formation in areas away from the fracture compared to the EHFF specimen which exhibited the least void percentage (EHFF; 19.4kJ).

It is worth noting that Samei et al. [42] concluded that in case of dual phase steels, the plastic compatibility between different phases improves during the high-strain rate deformation due to their individual formability enhancement and hence, formation of voids is suppressed during the EHDF. However, in case of AA5182-O sheets it is difficult to distinguish between closure of preformed voids and suppression of newly formed voids. Even though, this void suppression effect of EHDF can explain the reason that AA5182-O aluminium shows significant formability improvement when deformed in



(a)



(b)

Figure 6.10: (a) The effect of input energy on void evolution in safely formed EHDF specimens, (b) effect of die presence on void formation in different EHFed specimens.



EHDF condition and very little improvement when formed under EHFF [18]. Since tensile hydrostatic stresses promote void growth [20] it is reasonable to conclude that compressive hydrostatic stresses in EHDF conditions lead to lower void growth rate than EHFF conditions.

Consequently, it is thought that as a result of the large through-thickness compressive stresses that develop due to the high velocity impact of the sheet against the die and improved hardening behaviour of AA5182-O aluminium at high-strain rates, nucleation and growth of voids in EHDF specimens is significantly suppressed.

## 6.4 Conclusions

In this study, the failure mechanisms of 1.5mm AA5182-O sheets were investigated by means of quasi-static Marciniak tests and EHF experiments. The cause of final failure is understood by investigating the void nucleation sites and formability improvement observed during the EHF process was explained by suppression of void growth. The following conclusions were obtained;

1. Ductile damage occurs by void nucleation, growth and coalescence in AA5182-O aluminium sheets deformed in biaxial tension both in QS conditions (Marciniak) and at high-strain rates (EHF).
2. Cracking of large (Fe-Mn)-based intermetallic particles is the main source of void nucleation at lower strains. However, small  $Mg_2Si$  particles can contribute to failure by debonding from the matrix, especially in areas close to (Fe-Mn) containing particles. No significant difference was observed in void nucleation of QS Marciniak and EHF deformed specimens.
3. The specimen formed in QS Marciniak condition exhibited limited post uniform deformation and contained more voids in areas close to, and at distance from, the subfracture surface when compared to EHF specimens.
4. Void formation is suppressed by increasing the applied energy, and more significantly by the presence of a die. By increasing the applied energy, the sheet

reaches greater velocities just prior to the impact against the die wall. As a direct result of large through-thickness compressive stresses, void growth is suppressed and AA5182-O aluminium final failure is postponed.

5. AA5182-O aluminium can be formed safely when the void percentage increase resulting from EHF remains less than 0.5%. However, fracture becomes inevitable when the void percentage increases beyond 0.6-0.8%.

## 6.5 Acknowledgements

This research was funded by NSERC's Automotive Partnership Canada program (APCPJ 418056-11) with support from Amino North America Corp., ArcelorMittal Dofasco, Ford Motor Company, CanmetMATERIALS-Natural Resources Canada and Novelis Inc. Dr. Mark Kozdras, Dr. Kevin Boyle and Dr. Babak Shalchi Amirkhiz of CanmetMATERIALS are gratefully acknowledged for their support and carrying out the TEM analysis.

## 6.6 References

- [1] I. J. Polmear, *Light Alloys From Traditional Alloys to Nanocrystals*. Oxford: Butterworth-Heinemann-Elsevier, 2006.
- [2] W. Miller, L. Zhuang, J. Bottema, A. Wittebrood, P. De Smet, A. Haszler, and A. Vieregge, "Recent development in aluminium alloys for the automotive industry," *Materials Science and Engineering: A*, vol. 280, pp. 37–49, mar 2000.
- [3] V. Balanethiram and G. S. Daehn, "Hyperplasticity: Increased forming limits at high workpiece velocity," *Scripta Metallurgica et Materialia*, vol. 30, pp. 515–520, feb 1994.
- [4] V. Balanethiram, X. Hu, M. Altynova, and G. S. Daehn, "Hyperplasticity: Enhanced formability at high rates," *Journal of Materials Processing Technology*, vol. 45, pp. 595–600, sep 1994.
- [5] A. Rohatgi, E. V. Stephens, A. Soulami, R. W. Davies, and M. T. Smith, "Experimental characterization of sheet metal deformation during electro-hydraulic forming," *Journal of Materials Processing Technology*, vol. 211, pp. 1824–1833, nov 2011.
- [6] A. Rohatgi, E. V. Stephens, R. W. Davies, M. T. Smith, A. Soulami, and S. Ahzi, "Electro-hydraulic forming of sheet metals: Free-forming vs. conical-die forming," *Journal of Materials Processing Technology*, vol. 212, pp. 1070–1079, may 2012.
- [7] A. Rohatgi, A. Soulami, E. V. Stephens, R. W. Davies, and M. T. Smith, "An investigation of enhanced formability in AA5182-O Al during high-rate free-forming at room-temperature: Quantification of deformation history," *Journal of Materials Processing Technology*, vol. 214, pp. 722–732, mar 2014.

- [8] J. Samei, D. E. Green, S. Golovashchenko, and A. Hassannejadasl, “Quantitative Microstructural Analysis of Formability Enhancement in Dual Phase Steels Subject to Electrohydraulic Forming,” *Journal of Materials Engineering and Performance*, vol. 22, pp. 2080–2088, dec 2012.
- [9] S. F. Golovashchenko, A. J. Gillard, and A. V. Mamutov, “Formability of dual phase steels in electrohydraulic forming,” *Journal of Materials Processing Technology*, vol. 213, pp. 1191–1212, jul 2013.
- [10] A. Hassannejadasl, D. E. Green, S. F. Golovashchenko, J. Samei, and C. Maris, “Numerical modelling of electrohydraulic free-forming and die-forming of DP590 steel,” *Journal of Manufacturing Processes*, vol. 16, pp. 391–404, aug 2014.
- [11] R. Smerd, S. Winkler, C. Salisbury, M. Worswick, D. Lloyd, and M. Finn, “High strain rate tensile testing of automotive aluminum alloy sheet,” *International Journal of Impact Engineering*, vol. 32, pp. 541–560, dec 2005.
- [12] A. S. Kao, H. A. Kuhn, O. Richmond, and W. A. Spitzig, “Workability of 1045 spheroidized steel under superimposed hydrostatic pressure,” *Metallurgical Transactions A*, vol. 20, no. 9, pp. 1735–1741, 1989.
- [13] P. D. Wu, X. X. Chen, D. J. Lloyd, and J. D. Embury, “Effects of superimposed hydrostatic pressure on fracture in sheet metals under tension,” *International Journal of Mechanical Sciences*, vol. 52, no. 2, pp. 236–244, 2010.
- [14] X. Hu and G. S. S. Daehn, “Effect of velocity on flow localization in tension,” *Acta Materialia*, vol. 44, no. 3, pp. 1021–1033, 1996.
- [15] V. S. Balanethiram and G. S. Daehn, “Enhanced formability of interstitial free iron at high strain rates,” *Scripta Metallurgica et Materialia*, vol. 27, no. 12, pp. 1783–1788, 1992.
- [16] J. M. Imbert, S. L. Winkler, M. J. Worswick, D. a. Oliveira, and S. Golovashchenko, “The effect of tool–sheet interaction on damage evolution in electromagnetic forming of aluminum alloy sheet,” *Journal of Engineering Materials and Technology*, vol. 127, no. 1, pp. 145–153, 2005.
- [17] J. Samei, D. E. Green, and S. F. Golovashchenko, “Analysis of Failure in Dual Phase Steel Sheets Subject to Electrohydraulic Forming,” *Journal of Manufacturing Science and Engineering*, vol. 136, no. October, pp. 1–8, 2014.
- [18] A. Jenab, D. E. Green, A. T. Alpas, and K. P. Boyle, “Formability of AA5182-O Sheet during Electro-Hydraulic Forming : Influence of Input Energy,” in *MS&T*, pp. 535–542, 2015.
- [19] A. Jenab, I. Sari Sarraf, D. E. Green, T. Rahmaan, and M. J. Worswick, “The Use of genetic algorithm and neural network to predict rate-dependent tensile flow behaviour of AA5182-O sheets,” *Materials & Design*, vol. 94, pp. 262–273, mar 2016.
- [20] D. Hull, *Fractography: Observing, Measuring and Interpreting Fracture Surface Topography*. Cambridge University Press, 1999.
- [21] K. R. Spencer, *Evolution of fracture in an automotive aluminum alloy under plane strain tension*. PhD thesis, University of Waterloo, 2000.
- [22] M. Hadianfard, R. Smerd, S. Winkler, and M. Worswick, “Effects of strain rate on mechanical properties and failure mechanism of structural Al–Mg alloys,” *Materials Science and Engineering: A*, vol. 492, pp. 283–292, sep 2008.
- [23] ASTM-E1251-11, “Standard Test Method for Analysis of Aluminum and Aluminum Alloys by Spark Atomic Emission Spectrometry,” 2011.
- [24] ASTM-E8/E8M11, “Standard Test Methods for Tension Testing of Metallic Materials,” 2016.

- [25] A. C. Thompson, *High Strain Rate Characterization of Advanced High Strength Steels by*. PhD thesis, University of Waterloo, 2006.
- [26] A. C. Thompson, C. P. Salisbury, M. J. Worswick, and R. Mayer, “Constitutive modelling of dual phase steel sheet and tube,” *Journal de Physique IV (Proceedings)*, vol. 134, pp. 281–286, jul 2006.
- [27] T. Rahman, A. Bardelcik, J. Imbert, C. Butcher, and M. J. Worswick, “Effect of strain rate on flow stress and anisotropy of DP600 , TRIP780 , and AA5182-O sheet metal alloys,” *International Journal of Impact Engineering*, vol. 88, pp. 72–90, 2016.
- [28] G. S. Daehn, “High-velocity metal forming,” *Metalworking: Sheet Forming (ASM Handbook)*, vol. 14, pp. 405–418, 2006.
- [29] O. S. Orlov, *A Three-Dimensional Damage Percolation Model*. PhD thesis, Department of Mechanical and Mechatronics Engineering, University of Waterloo, 2006.
- [30] N. Moulin, E. Parra-Denis, D. Jeulin, C. Ducottet, A. Bigot, E. Boller, E. Maire, C. Barat, and H. Klöcker, “Constituent particle break-up during hot rolling of AA5182,” *Advanced Engineering Materials*, vol. 12, no. 1-2, pp. 20–29, 2010.
- [31] Y. Li and L. Arnberg, “A eutectoid phase transformation for the primary intermetallic particle from Al<sub>m</sub>(Fe,Mn) to Al<sub>3</sub>(Fe,Mn) in AA5182 alloy,” *Acta Materialia*, vol. 52, pp. 2945–2952, jun 2004.
- [32] Y. Li and L. Arnberg, “Solidification structures and phase selection of iron-bearing eutectic particles in a DC-cast AA5182 alloy,” *Acta Materialia*, vol. 52, pp. 2673–2681, may 2004.
- [33] Y. Xue, H. El Kadiri, M. F. Horstemeyer, J. B. Jordon, and H. Weiland, “Micromechanisms of multistage fatigue crack growth in a high-strength aluminum alloy,” *Acta Materialia*, vol. 55, no. 6, pp. 1975–1984, 2007.
- [34] J. Jordon, M. Horstemeyer, K. Solanki, J. Bernard, J. Berry, and T. Williams, “Damage characterization and modeling of a 7075-T651 aluminum plate,” *Materials Science and Engineering: A*, vol. 527, no. 1-2, pp. 169–178, 2009.
- [35] M. J. Worswick, Z. T. Chen, a.K Pilkey, D. Lloyd, S. Court, and a.K Pilkey, “Damage characterization and damage percolation modelling in aluminum alloy sheet,” *Acta Materialia*, vol. 49, pp. 2791–2803, aug 2001.
- [36] L. M. Brown and W. M. Stobbs, “Work-hardening of copper of copper - silica -5. Equilibrium Plastic relaxation by secondary dislocations,” *Philos Mag*, vol. 34, no. 3, pp. 351–372, 1976.
- [37] P. F. Thomason, *Ductile Fracture of Metals*. Pergamon Press, 1990.
- [38] F. A. McClintock, “A Criterion for Ductile Fracture by the Growth of Holes,” *Journal of Applied Mechanics*, vol. 35, no. 2, pp. 363–371, 1968.
- [39] A. Needleman, “Continuum model for void nucleation by inclusion debonding,” *Journal of Applied Mechanics, Transactions ASME*, vol. 54, no. 3, pp. 525–531, 1987.
- [40] M. N. Shabrov and A. Needleman, “An analysis of inclusion morphology effects on void nucleation,” *Modelling and Simulation in Materials Science and Engineering*, vol. 10, no. 2, pp. 163–183, 2002.
- [41] Z. Chen and M. J. Worswick, “Investigation of void nucleation in Al–Mg sheet,” *Materials Science and Engineering: A*, vol. 483-484, pp. 99–101, jun 2008.
- [42] J. Samei, D. E. Green, and S. Golovashchenko, “Metallurgical Investigations on Hyperplasticity in Dual Phase Steel Sheets,” *Journal of Manufacturing Science and Engineering*, vol. 136, p. 041010, May 2014.

# Chapter 7

## General Discussion and Conclusions

### 7.1 General Discussion

In this study, the formability of 1.5mm AA5182-O aluminium sheet formed by electro-hydraulic forming was investigated by means of experimental and computational work. Electro-hydraulic forming tests were carried out on sheet specimens using 34, 40 and 45° conical dies and also without any dies (free forming) using different input voltages. Formability improvement was measured as compared to quasi-static forming limit curves. Moreover, a novel approach was used to predict the mechanical response of AA5182-O from low- to high- strain rates along the three major directions of the sheet (RD, DD, and TD): to determine the constants of commonly used hardening equations, instead of non-linear regression, genetic algorithm approach was used and it was shown that it leads to better accuracy compared to non-linear regression fitting procedure. More importantly, the experimental results show that the flow stress of AA5182-O alloys exhibit a positive trend with strain rate at moderate to high strain rates. Consequently, an advanced approach was taken in which artificial neural network was used to describe the hardening of AA5182-O during FE simulations. This step was essential as it provides a reliable description of hardening for FE simulations without disregarding the strain rate exponent, as it is commonly ignored for aluminium alloys during FE simulations. The positive strain rate sensitivity at higher strain rates could potentially postpone failure strain to larger values and contribute to the formability improvement in EHF.

Furthermore, the failure mechanisms of quasi-static Marciniak specimens and of EHF specimens were investigated using optical and electron microscopy, and the results were compared. The cause of final failure can be understood by investigating the void

nucleation sites, and the formability improvement observed during the EHF process was achieved primarily by suppression of void growth. The OM results suggest that the void nucleation sites are mainly large (Fe,Mn)-enriched particles which break during deformation as a result of dislocation pile up. It is found that a threshold of void percentage is necessary to cause failure in AA5182-O specimens during EHF. More importantly, it is found that void percentage in the bulk of sheet material decreases as the strain rate increases or when higher input energies are used to deform the AA5182-O sheet material.

To further investigate the effects of EHF on AA5182-O, the effect of different parameters such as strain rate, sheet velocity, stress triaxiality and impact pressure was investigated using finite element simulations. To do this, the most accurate description of hardening, ANN, is used to simulate EHF using the ignition and growth model and coupled Eulerian-Lagrangian approach with solid elements. It is found that a significant peak of compressive stress occurs in the sheet material during EHDF at the moment of impact and this sudden negative stress triaxiality reduces void growth observed in OM. The impact pressure decreases as the radial distance from the apex increases and hence supports the observation that most of the formability improvement occurred in the apex region of conical specimens.

It is also found that AA5182-O does not show significant formability improvement during EHFF and most of the formability improvement is due to the impact with the EHF dies (EHDF). This is in agreement with work done by Maris [1] who determined the FLC of AA5182-O using EHF experiments. Hence, it is believed that the hardening effect due to positive strain rate sensitivity is not the dominant factor in formability improvement, or at least is not significant to improve formability of AA5182-O during EHFF.

Moreover, numerical simulation results show that peak strain rate achieved during EHFF is significantly lower, by an order of magnitude, than in EHDF. It is noteworthy that in the final stages of EHFF deformation, the strain rate where the final failure is expected to occur, is much lower than during the majority of the deformation process. Hence, the final stages of EHFF are actually closer to a quasi-static

process. Furthermore, the stress triaxiality is positive during the entire EHFF process and therefore cannot prevent void growth. These simulation results explain why the formability improvement of AA5182-O specimens during EHFF is insignificant as compared to quasi-static FLC.

However, the formability of AA5182-O can be improved significantly in EHDF provided the input energy exceeds a certain threshold. Numerical simulation results show that at such high energy levels, not only does the AA5182-O sheet specimens experience higher strain rate deformation, but also significant compressive through thickness stresses at the moment of impact against the die. Also, the specimens reach high velocity just before the sheet material fills the die completely and this generates large impact stress on the sheet. Since OM results show that the void percentage reduction is noticeable during EHDF once a threshold of input energy is exceeded, it is thought that the combination of high strain rate deformation and compressive through-thickness stress, leads to formability improvement in EHDF.

Finally, since the deformation in EHF is carried out at high strain rates, it was necessary to investigate possible changes in deformation mechanisms. The grain structure of AA5182-O EHDF specimens safely formed with a high input energy showed a twin-like microstructure, which according to Gray [2, 3] could be mechanical twinning even in case of high-stacking fault alloys such as Al-Mg alloys. However, further TEM investigation disproved the presence of twinning in AA5182-O specimen formed by EHF. No indication of changes in deformation mechanisms were observed, although the dislocation density increases mildly with increasing strain rate.

## 7.2 Conclusions

The following important conclusions can be drawn from the experimental and FE simulation studies carried out in this research:

- Formability improvement during EHFF was insignificant when compared with quasi-static forming limit curves. Also, AA5182-O sheet specimens were safely formed into 34, 40, and 45° conical dies and showed respectively 40%, 70%, 87%

increase in maximum effective strain values as compared to quasi-static FLC.

- The input energy of EHF should exceed a certain threshold in order to reach significant safe strains in EHDF. It was found that AA5182-O specimens could be successfully formed into conical dies if at least 8-10kJ of input energy was used in the EHF process.
- Flow stress values calculated using the modified Voce hardening function shows better agreement with experimental tensile data as compared with KHL and JC models. However, KHL results were slightly more accurate when used in finite element simulation of the EHF tests.
- Genetic algorithm was successfully used to determine parameters of commonly used constitutive equations. Implementing GA parameters into FE analysis software leads to the most accurate predictions of the rate-dependent hardening functions when compared with experimental data. However, The most accurate calculations of flow stress for any given direction, strain, and strain rate were predicted using ANN when compared analytically with experimental results or when used in finite element simulation. However, its computational cost is considerable when used in finite element simulation when compared with the use of KHL or JC hardening functions.
- The flow stress of AA5182-O decreases to its minimum at intermediate strain rates (from approximately 10 to 100s<sup>-1</sup>) and then increases for strain rates greater than 100s<sup>-1</sup>. Among the hardening models studied, the ANN was the only approach capable to replicate this behaviour. The strain rate term in JC and KHL constitutive equations used were unable to predict such a transition and consistently predicted small negative values of strain rate sensitivity. However, the modified-Voce with logarithmic and exponential strain rate terms exhibited better capability to predict the trend of increasing flow stress at high-strain rates. It is also found that disregarding the small, negative strain rate exponent in FE analysis can lead to considerable inaccuracies in finite element



simulations of the tensile tests.

- AA5182-O aluminium sheets fracture in a ductile manner by void nucleation, growth and coalescence in biaxial tension both in QS conditions (Marciniak) and at high-strain rates (EHF).
- The main source of void nucleation at lower strain values is the cracking of large (Fe-Mn)-based intermetallic particles. However, small  $Mg_2Si$  particles can contribute to failure by debonding from the matrix, especially in areas close to (Fe-Mn) containing particles. No significant difference was observed in void nucleation of QS Marciniak and EHF specimens.
- Specimens formed in QS Marciniak tests exhibited limited post-uniform deformation and contained more voids in areas close to, and at distance from, the subfracture surface when compared to EHF specimens.
- Void formation is suppressed by increasing the applied energy in the EHF process, when the sheet is formed into a die. By increasing the applied energy, the sheet reaches greater velocities just prior to the impact against the die wall. As a direct result of large through-thickness compressive stresses that occur upon impact, void growth is suppressed and AA5182-O aluminium final failure is postponed.
- AA5182-O aluminium can be formed safely when the void percentage increase resulting from EHF remains less than 0.5%. However, fracture becomes inevitable when the void percentage increases beyond 0.6-0.8%.
- Reasonable correlation between simulation and experimental results was achieved by a coupled Eulerian-Lagrangian model when the ignition and growth model was used to simulate the EHF pulse formation. This FE model was able to accurately predict the strain distribution and shape of deformed specimens as a function of time.

- There is a significant difference between velocity changes in the apex region of EHF specimens and in areas away from the apex. In areas away from the apex, only one velocity peak can be seen. However, in the apex region, at least two separate large velocity peaks can be seen. The peak velocity increases with the input energy in both EHFF and EHDF specimens.
- Simulations show significant peak strain rate values when sheet specimens are formed using EHDF. In case of EHFF, the peak strain rate occurs during the deformation where triaxiality is positive (tension state). However, when EHF specimens are formed into a die, the peak strain rate occurs at the final stage of deformation and when triaxiality is negative (compressive state).
- When AA5182-O sheet is formed using EHDF, significant compressive stress is generated through the thickness especially in areas close to the apex when they contact the die. However, in case of EHFF the peak through-thickness stress occurs in the early stages of deformation and is significantly lower than predicted values for EHDF specimens.
- At the moment of the impact between AA5182-O sheet and the EHF die, significant pressure is generated. This impact pressure decreases as the radial distance from the apex increases. Moreover, comparison between FE model predictions and analytical calculations confirms that the FE model is able to reasonably predict this compressive impact stress. Furthermore, FE simulation predicted greater impact pressures for the EHDF specimen which showed most improvement in formability.
- Finally, it is thought that the combination of increased sheet velocity, high-strain rate, compressive through-thickness stress, and negative stress triaxiality all contributed to the formability improvement of AA5182-O.

### **7.3 Originality of the research**

In this study, the formability improvement of commercial AA5182-O sheet formed using EHF process was studied. It was found that AA5182-O sheets exhibit lower formability improvement compared to values previously reported by other researchers, especially in case of free formed EHF.

The root cause of formability improvement during EHF was explained with the help of meticulous and extensive material characterization as well as by varying EHF process parameters. Material flow behaviour was studied in a range of strains. Constants of selected constitutive equations were calculated using genetic algorithm and shown to be more accurate than regression analysis. Moreover, flow behaviour of AA5182-O sheet was further studied by an advanced computational approach, artificial neural network, and the outcome shown to be more accurate than predefined hardening functions. EHF simulations were carried out with coupled Eulerian-Lagrangian approach using the optimum hardening function and the parameters that affect the formability of AA5182-O were studied in detail. It is lucidly shown that a combination of compressive through thickness stress and high strain rate sensitivity lead to formability improvement of AA5182-O in die formed EHF.

Material characterization on both failed and safely formed specimens identified the main source of void nucleation in AA5182-O and showed that void suppression is the main reason AA5182-O exhibits improved formability in EHF process.

The tools developed during this research were shown to be more precise than existing models and offers new insights into the EHF process and the deformation and damage mechanisms that occur during EHF.

### **7.4 Future Work**

1. It would be useful to have experimental stress-strain data of AA5182-O at QS, moderate and high-strain rates up to higher strain values. The reason is that all flow curves used in this work were derived from tensile tests, and the true strain

values remained less than 0.2. This is a relatively low strain value when compared with the strains measured on EHF specimens. Hence, it is suggested to perform biaxial or compression tests at different strain rates. Using stress-strain data up to higher strain values would result in better calibration of hardening functions, and consequently, more accurate finite element simulations of EHF experiments would be achieved.

2. Since high-strain rate deformation imposed by EHF may increase the local temperature to a significant level, it might be useful to perform warm-hot temperature tests on AA5182-O to investigate the effect of temperature on grain microstructure and correlate the temperature-dependant hardening function in the FE model. By having temperature dependant FE simulation, it is possible to study the effect of this important effect on AA5182-O sheet behaviour during EHF.
3. Since ANNs have excellent capabilities to predict mathematically unpredictable relations between various parameters, it is thought that ANN might have the ability to accurately predict the onset of instability of AA5182-O for a given strain path and strain rate.
4. During the grid analysis studies, it was decided to use the conventional North-American method to determine forming limit curves. To develop such diagrams, only safe and necked grids are used and any specimens containing a fracture or crack are dismissed [4]. However, according to the ISO 12004-2 (2008) [5] method grids that contain a crack should also be used to calculate limiting strains. The reasoning behind this approach is that once a fracture occurs in a grid, the load-bearing capacity of such grid becomes zero and hence its strain does not change significantly (i.e. Li et al. [6]). Hence, it would be interesting to perform a comparative study to determine the FLC of AA5182-O sheets using both the ISO and conventional North American approaches with quasi-static Marciniak and bulge test specimens or even EHF specimens.

## 7.5 References

- [1] C. Maris, “Experimental determination of the forming limits of DP600 and AA5182 sheets in electrohydraulic free forming,” Master’s thesis, Windsor, 2014.
- [2] G. Gray, “Deformation twinning in Al-4.8 wt% Mg,” *Acta Metallurgica*, vol. 36, pp. 1745–1754, jul 1988.
- [3] G. Gray, “Deformation substructures induced by high-rate deformation,” *Annual meeting and exhibition of the Minerals, Metals and Materials Society, New Orleans, LA (USA), 17-21 Feb 1991*, jan 1991.
- [4] S. Keeler and W. Backhofen, “Plastic instability and fracture in sheet stretched over rigid punches,” in *ASM Transactions Quarterly*, pp. 25–48, 1964.
- [5] ISO 12004-1:2008(E), “Metallic materials - Sheet and strip - Determination of forming-limit curves Part 1: Measurement and application of forming limit diagrams in the press shop,” 2008.
- [6] J. Li, W. C. Liu, H. Yuan, and Y. K. Gao, “Comparison of earing behavior between continuous cast and direct chill cast AA 5182 aluminum alloys during cold rolling and annealing,” *Journal of Materials Processing Technology*, vol. 210, pp. 2007–2015, nov 2010.

# Appendices

## Appendix A

### Further Microscopic Material Studies; OM, TEM

In this section, further investigations were carried out on the microstructure of AA5182-O sheet formed using QS and EHF by means of optical metallography and transmission electron microscopy. The motivations to perform these investigations are to examine if there is a correlation between micro and macro strain measurements, and to understand if grain structure changes are different between quasi-static and high-strain rate deformation. Moreover, it was necessary to understand if adiabatic heating generated as a result of high-strain rate deformation had any influence on grain structure. Another motivation was to investigate if high-strain rate deformation of AA5182-O could result in different deformation mechanisms such as mechanical twinning. Finally, it was necessary to examine if dislocation density increases significantly beyond conventional cold rolled deformations suggesting new sources of dislocations being activated at high-strain rate deformation.

## **A.1 Microscopic deformation of grains**

### **A.1.1 Polished and anodized surface of as-received AA5182**

Fig. A.1(a) shows polished surfaces of AA5182-O at different orientations to the rolling direction and at 500x magnification. Dark grey areas noticeable in Fig. A.1(a) are second phase particles and black spots are either voids or residue of removed second phase particles. Fig. A.1(b) shows the microstructure of as-received AA5182-O as seen in the orthotropic material orientations. It can be seen from Fig. A.1(b) that for the as-received sheets, the annealing process was successfully done as most of the grains are equi-axed. For more information about sample preparation, polishing steps and anodization solutions please refer to Chapter 6 as well as Appendices B.1 and B.2.

### **A.1.2 Deformed specimens**

The effect of void area percentage change on fracture strain and failure of AA5182-O is discussed in Chapter 6 for both quasi-static and EHF deformation processes. Fig. A.2 shows mosaic images of the subfracture grain structure of (a) a quasi-static Marciniak specimen and (b) a free formed EHF specimen. It can be seen that the quasi-static specimen fractured with 45° angle shear deformation whereas the EHFF specimen showed extensive localized deformation; comparison of thickness strain measurements were discussed in Section 6.3.2 of Chapter 6.

Fig. A.3(a) and (b) show mosaic images at the apex of EHDF specimens formed into 40° and 45° conical die, respectively.

Closer examination of the grain structure of QS and EHF specimens are shown in Fig. A.4. Fig. A.4(a) shows the anodized microstructure of QS deformed specimen. It can be seen that although grains are clearly distinguishable, at large strain values, tracking of grain boundaries is challenging due to the low contrast between each grain. Fig. A.4(b) shows the microstructure of EHFF specimen formed with 6kV input energy using 320 $\mu$ F capacitor. It can be seen that grains are significantly deformed



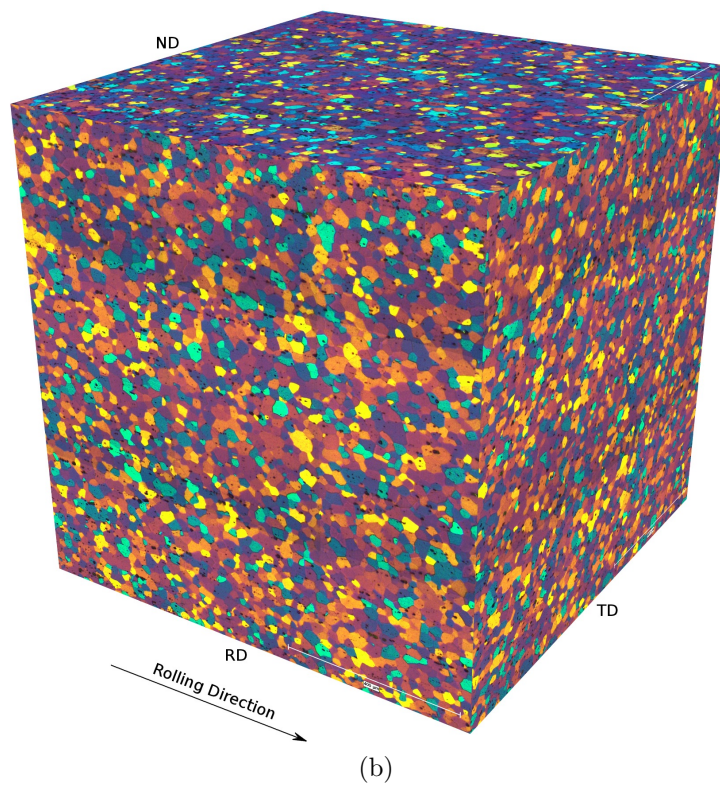
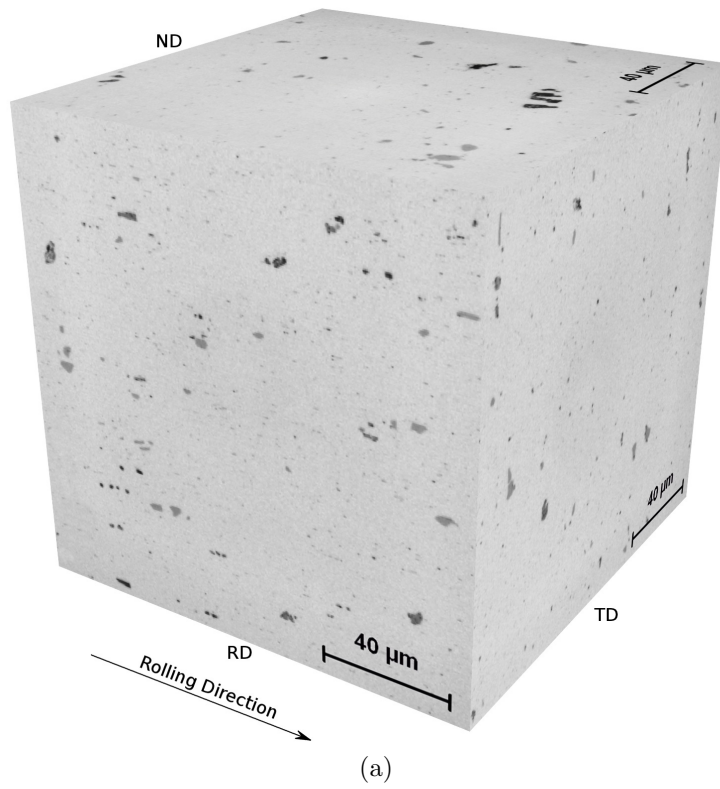
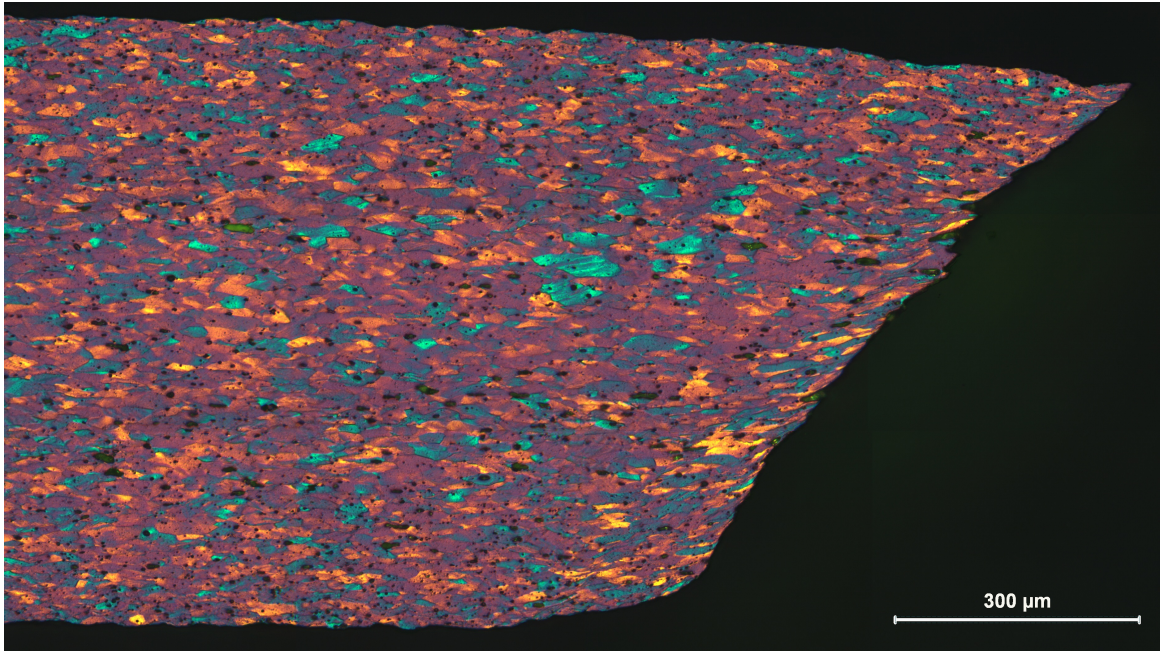
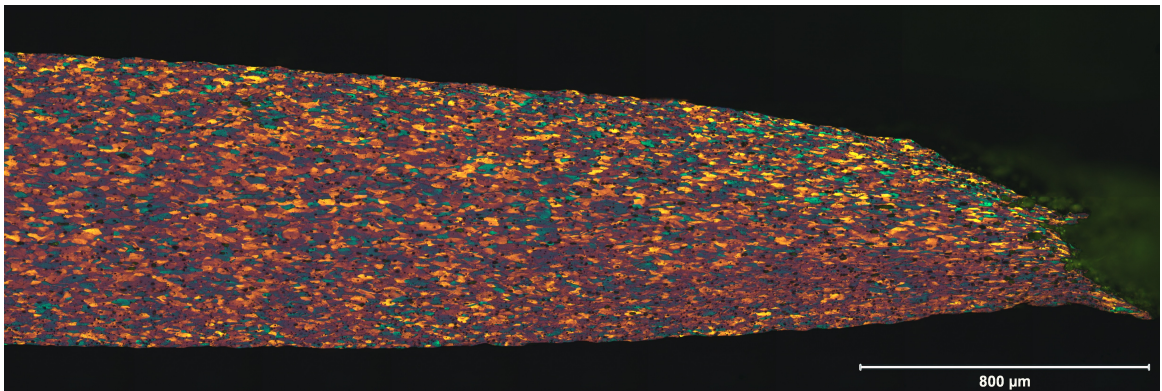


Figure A.1: As-received microstructure of AA5182 in RD, TD, and ND, (a) polished and (b) anodized.

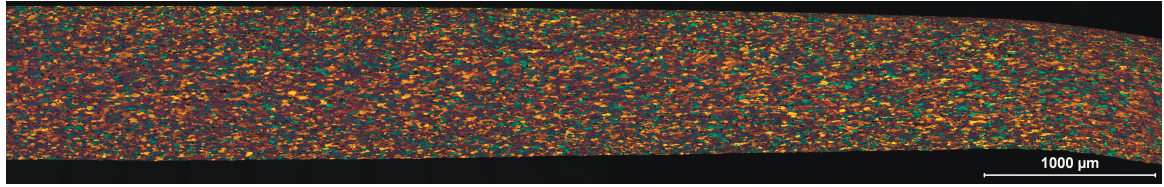


(a)

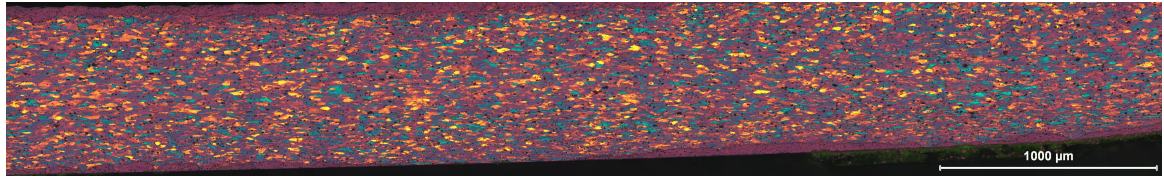


(b)

Figure A.2: Mosaic images of subfracture surface of (a) QS Marciniak specimen and (b) EHFF specimen deformed with at 6.0kV input voltage.



(a)



(b)

Figure A.3: Mosaic images of EHDF specimens formed into (a)  $40^\circ$  conical die with 10kV input voltage and (b) into  $45^\circ$  conical die with 14kV input voltage. Both images were taken at the apex, where greatest levels of major and minor strain were measured.

and patterns of large shear deformation are observable. Fig. A.4(c)-(f) show the microstructure of EHDF specimens formed into  $34^\circ$  (c),  $40^\circ$  (d) and  $45^\circ$  (e,f) conical dies with 9, 10 and 14kV input energies, respectively. Similar to Fig. A.4(b) a shear deformation pattern can be seen among groups of grains. Moreover, the material near the apex of AA5182-O specimens formed by EHF reaches the largest strain values and also exhibits twin-like microstructure (Fig. A.4 (b)-(f)). These twin-like grain structures are of interest due to the fact that, according to Gray [1–3], the occurrence of twinning is possible even in case of high stacking fault energy alloys (including Al-Mg alloys[1, 2]) when the material is deformed at extreme strain rates.

## A.2 Transmission electron microscopy

Transmission Electron Microscopy (TEM) studies were carried out to investigate if the twin-like observations in OM are actual twinning or not. Moreover, since the AA5182-O alloy was safely deformed to larger strain values (as discussed in Chapter 3, 5, and 6.3.2), TEM studies were needed to investigate if dislocation density increases to significantly larger values as a result of new sources being active at high-strain rates.

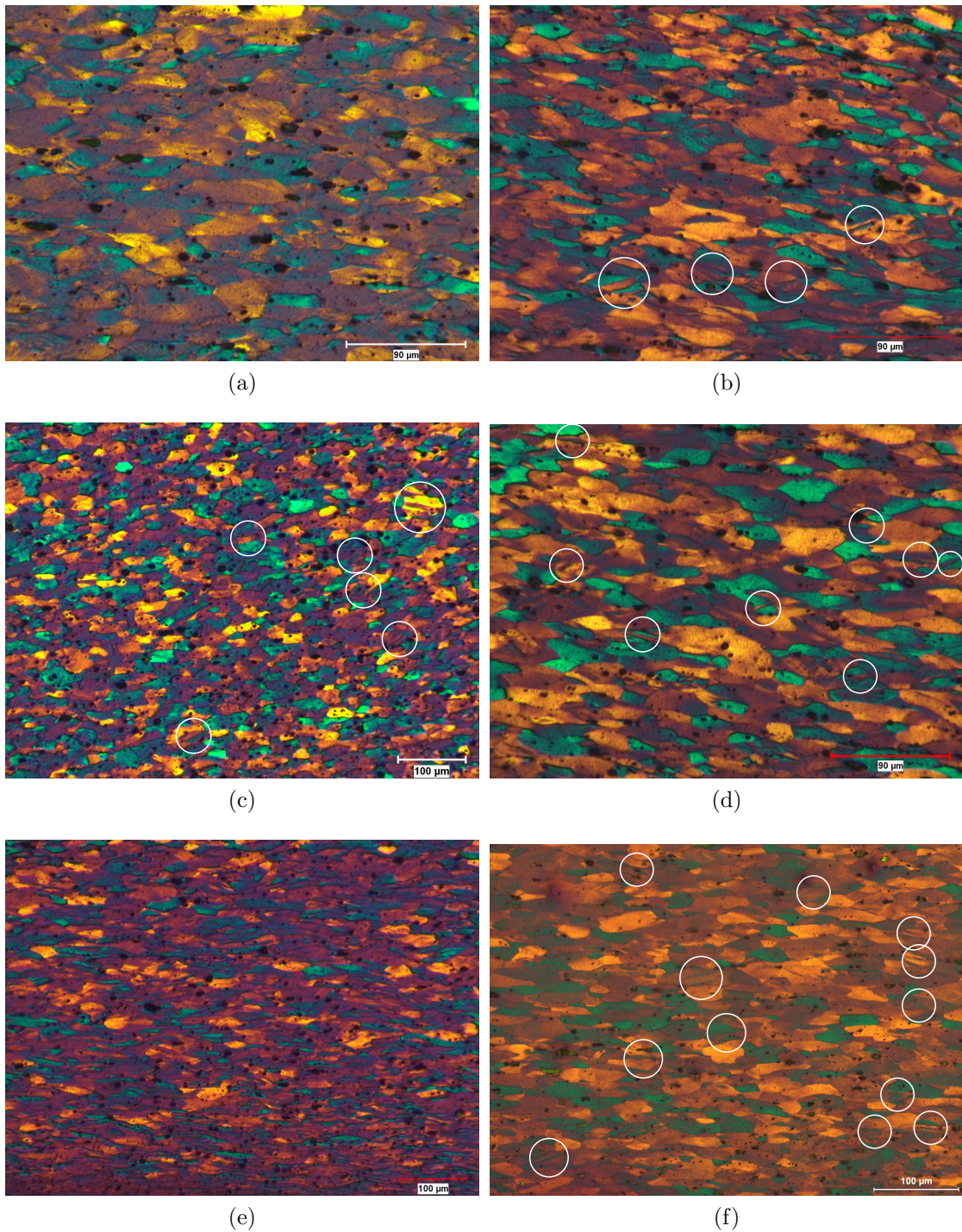


Figure A.4: Microstructure of specimens formed using (a) QS Marciniak, (b) EHFF at 6kV input voltage, (c) 34° die formed EHF using 9kV input voltage, (d) 40° die formed EHF using 10kV input voltage, (e) and (f) 45° die formed EHF using 14kV input voltage. Images were taken at largest values of strain shown in Fig. 3.3 of Chapter 3.

### A.2.1 The effect of beam orientation

To study dislocation densities, care was taken to adjust the beam orientation so that the images are taken where beams are aligned to [110] planes. This alignment is an essential part of a proper TEM analysis. An example of such orientation effect is shown in Fig. A.5. Fig. A.5(a) shows the diffraction pattern in a specimen deformed by EHDF in a 40° conical die with 10kV input voltage and the two selected planes A and B (shown with arrows). Fig. A.5(b) and (c) show the different dark field (DF) images when the beam is aligned on either A or B planes, respectively. Fig. A.5(d) and (e) show the bright field (BF) images taken at [011] orientation at different magnifications. It can be seen that dislocation lines can be seen vividly from Fig. A.5(e) without any bending contour.

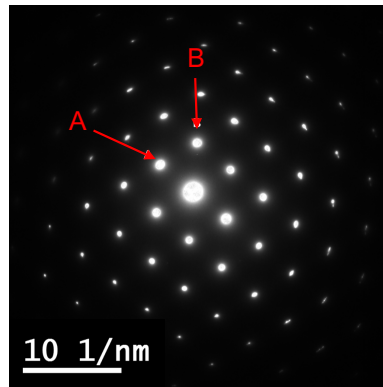
### A.2.2 Dislocation Density Measurements

Since most of the dislocations are visible at low index zone axis ([011] in aluminium), all High Angle Annular Dark Field (HAADF) images were taken in such directions. To measure dislocation densities, at least 5 images were used and local thickness values were measured by electron energy loss spectroscopy (EELS) beam using Malis/Egerton formula. Equation A.1 is used to measure dislocation density. The reported dislocation density values are an average of at least 5 measurements along the vertical and horizontal directions.

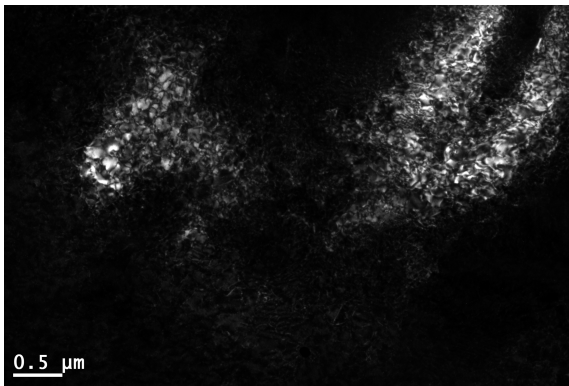
$$\rho = \frac{\sum n_y / \sum L_y + \sum n_x / \sum L_x}{t} \quad (\text{A.1})$$

where  $\rho$  is the dislocation density,  $n_x$  and  $n_y$  are the number of times a horizontal or vertical line crosses dislocation lines.  $L_x$  and  $L_y$  are the length of horizontal and vertical lines and  $t$  is the average thickness of the studied region measured by EELS beam.

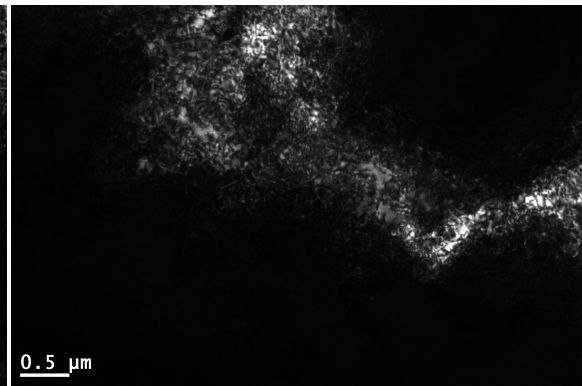
Fig. A.6 illustrates how the mentioned method is used to measure the dislocation density of as-received and deformed AA5182-O sheet specimens.



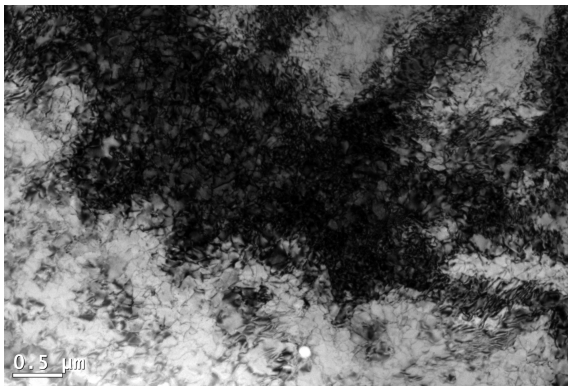
(a)



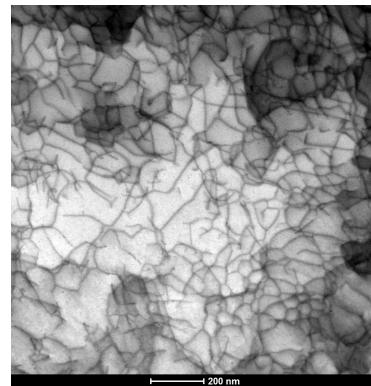
(b)



(c)

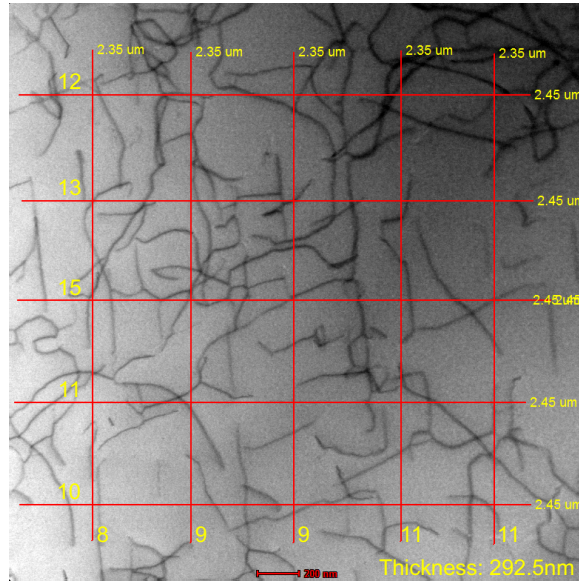


(d)



(e)

Figure A.5: The effect of beam alignment on the observation of dislocation lines; (a) diffraction pattern, (b) DF image at plane A, (c) DF image at plane B, (d) DF image at [011] plane and (e) BF image from [011] plane.



(a)

Figure A.6: Measurement of dislocation densities in as-received AA5182-O

Fig. A.7 shows the dislocation density measured for different studied specimens which showed the highest value of formability improvement (refer to Chapter 5). Fig. A.7 shows the variation of dislocation density with effective strain for selected specimens. All EHF specimens were chosen and TEM specimens were prepared at the exact grid location where the largest strain value was measured. The EHDF-40 specimen was deformed with 10kV input voltage and the EHDF-45 specimen was deformed into the 45° conical die with 14kV input voltage. The QS Marciniak specimen that was selected was deformed along the same biaxial strain path as the EHDF specimens. It can be seen that the dislocation density increases with strain. It can be seen from Fig. A.7 that dislocation density increases by an order of magnitude from as-received to deformed specimens. More specifically, dislocation density increases from  $3.59 \times 10^{13} \text{m}^{-2}$  for as-received AA5182-O sheet to  $3.23 \times 10^{14} \text{m}^{-2}$  for QS specimen. However, the changes of dislocation density with deformation process are insignificant as it increases from  $3.23 \times 10^{14} \text{m}^{-2}$  in quasi-static deformation to  $3.70 \times 10^{14} \text{m}^{-2}$  in high-strain rate deformation. Although dislocation density increases with plastic strain, it seems that either the material experienced a sort of relaxation phenomenon that prevents intense dislocation density increase during EHF process or dislocations

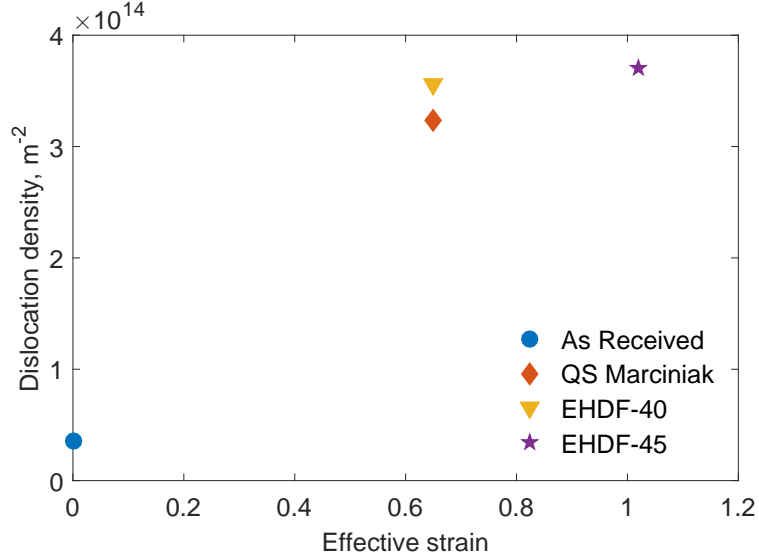


Figure A.7: Variation of dislocation densities of as-received AA5182-O sheet and specimens deformed under QS Marciniak, EHDF-40 safely formed with 10kV input voltage and EHDF-45 safely formed with 14kV input voltage with effective strain in different specimens.

where able to climb over obstacles and keep moving to facilitate further deformation.

### A.2.3 Dislocation-second phase particles interaction

Fig. A.8 shows the interaction of dislocations and intermetallic particles which result in improvement of hardening of the sheet material. It can also be seen that the Fe-Mn enriched particles are larger in size as compared to Mg-Si enriched particles.

Fig. A.9 shows the brittle fracture of an Fe-Mn particle during QS deformation which leads to void nucleation (refer to Chapter 6). The presence of a void can be seen by the dark spot on the bright field image (Fig. A.9(a)) and by the absence of the aluminium matrix in Fig. A.9(b).

According to Horstmeyer et al. [4], deformation at lower temperatures promotes both cracking and debonding due to increased work hardening rates. Small particles (i.e.  $Mg_2Si$ ) tend to be spherical or equiaxed and tend to cause inter-facial fracture due to the pile-up of dislocations at the particle-matrix interface. Also, equiaxed particles are less sensitive to the loading direction [5]. However, they tend to result in void formation by debonding from the matrix [6, 7] which relates to dislocation kinetics and can thus be considered strain-dependent [6]. Particle debonding can also be



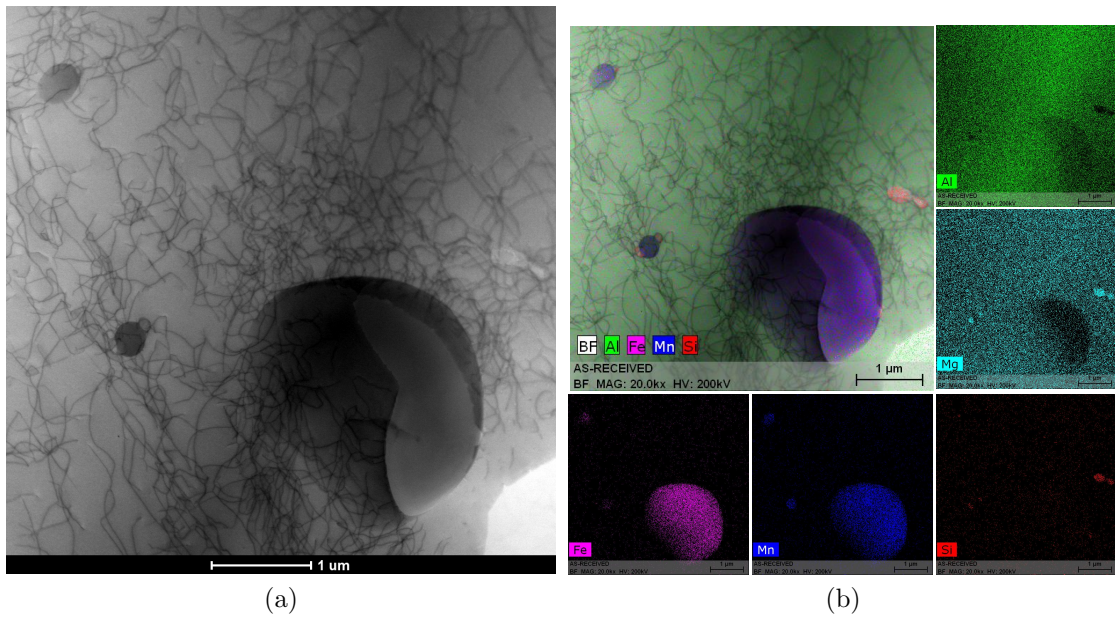


Figure A.8: (a) Dislocations interaction with second phase particles (b) chemical analysis of second phases showing Fe-Mn and Mg-Si enriched second phases.

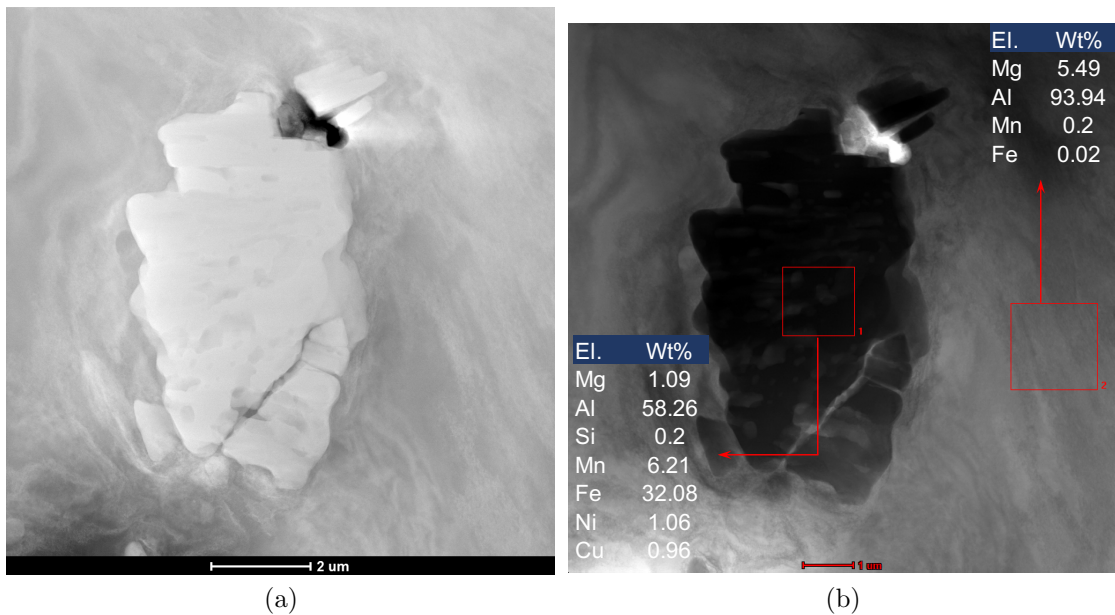


Figure A.9: Initiation of a void by cracking of an Fe-Mn enriched second phase particle; (a) bright field image showing the void as a dark spot and (b) chemical analysis showing the void by the absence of aluminium matrix.

described as stress-controlled since the separation of the interface is dependent upon the hydrostatic stress [8, 9]. It is noteworthy that the existence of particle debonding was scarce in samples prepared either from QS or EHF specimens.

However, large particles with radius greater than  $1\mu\text{m}$  (i.e. containing Fe and Mn) are prone to cracking at lower strains [10] than smaller sub-micron particles (i.e. particles containing Mg and Si). Also, nucleation occurs earlier for these large particles because they contain more internal defects, have a larger interface and have irregular shapes. The nucleation of large particles due to cracking can be described using a stress-controlled model since this is a brittle-type fracture [7].

## Appendix B

### Optical metallography sample preparation

#### B.1 Grinding and Polishing

Abrasive disks were used in successively finer steps so as to remove material mechanically; the abrasive disks, lubricant, force and speed were chosen based on AA5182-O hardness and brittleness. Table B.1 illustrates the steps taken to mechanically polish samples. Care was taken to reduce side effects of pull-outs, comet tails and embedded abrasive; between each step, samples were cleaned with running water, an industrial cleaner and ultrasonic ethanol bath for 5 minutes to remove the residues of previous steps especially from the fine gap made by shrinkage, although very small.

Table B.1: AA5182-O sample polishing steps

Step	Grinding disk, abrasive	Lub.	DP/Lub. ratio	Force, N	Speed, rpm	Time, min
1	SiC-Paper grit #400	Water	-	25	300	until plane
2	MD-Largo, DP 9 $\mu$ m	Blue	10/13	30	150	5
3	MD-Dur, DP 6 $\mu$ m	Blue	10/13	30	150	4
4	MD-Mol, DP 3 $\mu$ m	Red	10/14	25	150	3
5	MD-Nap, OPS 0.5 $\mu$ m	OPS	-	10	150	2

where the Blue, Red and OPS chemical composition is as follows:

- Blue Lubricant: 70-85% Ethanol, 5-15% Propanol, 5-15% Ethanediol.
- Red Lubricant: 70-85% Ethanol, 5-15% Propanol, 5-15% Propylee glycol, 5-15% Ethanediol.
- OPS: 30-50% Butane, 30-50% Ethanol, 5-15% Propane, 1-5% Propanol, <3% Diamond.

## B.2 Anodizing, Etching and Electro-polishing

Table B.2 summarizes the literature survey conducted on the best etchant used for 5xxx-series aluminium alloys. In this dissertation, only Barker solution was used to anodize OM specimens (see Chapter 6 and A).

Table B.2: Most common etchant used for AA5xxx-series metallography observation

Anodize/Etchant Composition	Applying method	Alloy	Ref.
40% (H <sub>3</sub> PO <sub>4</sub> ) (Phosphoric acid)		AA5754-O	[11]
10% (H <sub>3</sub> PO <sub>4</sub> ) (Phosphoric acid)	Temp=50°C, 1-2min, Can be used for HT samples: Shear band decohesion)[12]	AA5182 AA5754	[12, 13]
40ml H <sub>2</sub> O, 32ml H <sub>3</sub> P <sub>4</sub> O <sub>4</sub> , 12ml HF, 68ml Diethylene Glycol Mono- Ethyl Ether (C <sub>6</sub> H <sub>14</sub> O <sub>3</sub> ), 3g Oxalic Acid (powder), 5.2g Boric Acid (powder).	Temp=30°C, 30V DC, 1-2 A, 1-1.5 min	AA5754	[14]
4-5ml HBF <sub>4</sub> (48% conc.), 200ml H <sub>2</sub> O.	Barker's reagent, Same procedure as above, but with 20V DC	AA5754	[15, 16]
6% HCl, 21% HNO <sub>3</sub> , 5% HF.	Modified Keller's reagent Pour on samples, reveal macro-structure	AA5754	[14, 16]

# Appendix C

## Appendix References

### C.1 Appendix References

- [1] G. Gray, “Deformation twinning in Al-4.8 wt% Mg,” *Acta Metallurgica*, vol. 36, pp. 1745–1754, jul 1988.
- [2] G. Gray, “Deformation substructures induced by high-rate deformation,” *Annual meeting and exhibition of the Minerals, Metals and Materials Society, New Orleans, LA (USA), 17-21 Feb 1991*, jan 1991.
- [3] G. T. (Rusty) Gray, “High-Strain-Rate Deformation: Mechanical Behavior and Deformation Substructures Induced,” *Annual Review of Materials Research*, vol. 42, pp. 285–303, aug 2012.
- [4] M. F. Horstemeyer, K. Gall, K. W. Dolan, A. Waters, J. J. Haskins, D. E. Perkins, A. M. Gokhale, and M. D. Dighe, “Numerical, experimental, nondestructive, and image analyses of damage progression in cast A356 aluminum notch tensile bars,” *Theoretical and Applied Fracture Mechanics*, vol. 39, no. 1, pp. 23–45, 2003.
- [5] D. Lassance, D. Fabregue, F. Delannay, and T. Pardoen, “Micromechanics of room and high temperature fracture in 6xxx Al alloys,” *Progress in Materials Science*, vol. 52, pp. 62–129, jan 2007.
- [6] F. A. McClintock, “A Criterion for Ductile Fracture by the Growth of Holes,” *Journal of Applied Mechanics*, vol. 35, no. 2, pp. 363–371, 1968.
- [7] P. F. Thomason, *Ductile Fracture of Metals*. Pergamon Press, 1990.
- [8] A. Needleman, “Continuum model for void nucleation by inclusion debonding,” *Journal of Applied Mechanics, Transactions ASME*, vol. 54, no. 3, pp. 525–531, 1987.
- [9] M. N. Shabrov and A. Needleman, “An analysis of inclusion morphology effects on void nucleation,” *Modelling and Simulation in Materials Science and Engineering*, vol. 10, no. 2, pp. 163–183, 2002.
- [10] L. M. Brown and W. M. Stobbs, “Work-hardening of copper of copper - silica -5. Equilibrium Plastic relaxation by secondary dislocations,” *Philos Mag*, vol. 34, no. 3, pp. 351–372, 1976.
- [11] D. Zdravecky, *Formability and Failure of Automotive Sheet Material AA5754*. Msc, McMaster University, 2007.
- [12] M. Hadianfard, R. Smerd, S. Winkler, and M. J. Worswick, “Effects of strain rate on mechanical properties and failure mechanism of structural Al–Mg alloys,” *Materials Science and . . .*, vol. 492, pp. 283–292, sep 2008.
- [13] M. Hadianfard and M. J. Worswick, “Influence of strain rate on shear localization during deformation and fracture of 5754 and 5182 aluminum alloy,” *Aluminium Alloys 2006, Pts 1 and 2*, vol. 519–521, pp. 1047–1051, 2006.
- [14] K. R. Spencer, *Evolution of fracture in an automotive aluminum alloy under plane strain tension*. PhD thesis, University of Waterloo, 2000.
- [15] G. F. Vander Voort, *Metallography, principles and practice*. ASM International, 1984.

- [16] G. F. Vander Voort, "Color Metallography," *Microscopy Today*, vol. 9, no. November, pp. 22–25, 2005.

## Vita Auctoris

Name: Arash Jenab

Place of Birth: Tehran, Iran

Year of Birth: 1982

Education: Bachelor of Science (BSc)  
Materials Science and Engineering,  
Azad University, Science and Research Campus,  
Tehran, Iran  
2005

Master of Science (MSc)  
Materials Science and EngineeringMetal Forming,  
Sharif University of Technology,  
Tehran, Iran  
2009

Philosophy Degree (PhD)  
Engineering Materials,  
University of Windsor,  
Windsor, Canada  
2017